Fall 2018

Compressive behavior of masonry columns confined with steel reinforced grout (SRG) composite

Sarah Elizabeth Jemison

Department:

COMPRESSIVE BEHAVIOR OF MASONRY COLUMNS CONFINED WITH STEEL REINFORCED GROUT (SRG) COMPOSITE

by

SARAH ELIZABETH JEMISON

A THESIS

Presented to the Faculty of the Graduate School of the

MISSOURI UNIVERSITY OF SCIENCE AND TECHNOLOGY

In Partial Fulfillment of the Requirements for the Degree

MASTER OF SCIENCE IN CIVIL ENGINEERING

2018

Approved by

Dr. Lesley H. Sneed, Advisor
Dr. Mohamed ElGawady
Dr. Guirong Yan

ABSTRACT

In this study, a new type of composite comprised of steel fiber cords embedded in a natural hydraulic lime mortar matrix, known as steel reinforced grout (SRG), is explored for the use in confinement of masonry columns. An experimental study was carried out to understand the behavior of solid clay brick masonry columns confined by SRG jackets. Twenty-four confined and seven unconfined columns with a square cross-section were tested to failure under a monotonic concentric compressive load. Test parameters considered were the column corner condition, number of fiber jacket layers, and number of fiber overlapping faces. SRG confinement improved the compressive strength, ultimate axial strain, and energy absorption of the masonry columns relative to the unconfined condition. Results showed that increasing the number of fiber layers increased the confined compressive strength, however the increase in confined strength was not proportional to the number of fiber layers. Rounding the column corners slightly increased the confined compressive strength. Increasing the number of fiber overlapping faces also increased the confined compressive strength. Models from the literature for FRP-confined masonry were examined for their applicability to predict the strength increase from SRG jackets. Considering the specimens included in this thesis work and supplemented with others collected from the literature, it was found that the model for the Italian CNR-DT 200 provided the closest predictions of the increase in compressive strength provided by the SRG jacket (within 33% of the experimental values). More work is needed to improve the predictions of the increase in compressive strength provided by SRG jackets and to predict the ultimate strain in the jacket.

ACKNOWLEDGMENTS

First, I would like to thank my advisor, Dr. Lesley Sneed. She gave me the opportunity to achieve my goal of receiving my Master of Science degree in Civil Engineering by encouraging me to apply for the Greenberg Scholars Program and later taking me in as her graduate student. She was instrumental in making this project successful, and she has always been there to share her expertise and knowledge. Next, I would like to thank my committee members, Dr. Mohamed ElGawady and Dr. Grace Yan for reviewing my work and being incredible professors throughout my course work.

I would like to thank my family, Tom, Sandy, and Scott Jemison, for their unwavering support of my educational goals. They have always encouraged me to pursue my dreams, and I am proud to have parents and a brother that are such great role-models. I would also like to thank my best friend, Ben Parr, for supporting my decision to pursue this degree program and being a positive support throughout life.

Also, I must thank my research partner on this project, Carolina Senesi, for being the best lab-partner I could have asked for. She was always patient and upbeat through the months of work, while having an amazing work ethic. Also, I would like to thank all my friends that I have met here at Missouri S&T for sharing in this great chapter of our lives. Lastly, it goes without saying that the assistance from fellow graduate students, professors, and department technical staff is sincerely appreciated. A special thank you goes out to John Bullock, Gary Abbott, Greg Leckrone, Brian Swift, and Dr. Christian Carloni for their support and assistance throughout this project.

TABLE OF CONTENTS

Page

APPENDICES

LIST OF ILLUSTRATIONS

Page

LIST OF TABLES

Page

NOMENCLATURE

Symbol	Description
A_{cc}	Transverse Area of Concrete Enclosed by the FRP
ACI	American Concrete Institute
A_e	Area of Effectively Confined Concrete
A_g	Total Cross-Sectional Area
A_m	Total Cross-Sectional Area of Masonry Element
ASTM	American Society for Testing and Materials
b	Width
B-FRCM	Basalt Fiber Reinforced Cementitious Matrix
BFRP	Basalt Fiber Reinforced Polymer
C-FRCM	Carbon Fiber Reinforced Cementitious Matrix
CFRP	Carbon Fiber Reinforced Polymer
CNR	Italian Council of National Research
CoV	Coefficient of Variation
C-TRM	Carbon Textile Reinforced Mortar
D'	Diagonal Dimension of Rectangular Cross-Sectioned Column
DIC	Digital Image Correlation
e	Eccentricity
E_f	Elastic Modulus of Fiber
E_m	Absorbed Energy
E_{mc}	Peak Confined Energy

$E_{mc,u}$	Total Confined Energy
E_{mo}	Peak Unconfined Energy
$E_{mo,u}$	Total Unconfined Energy
EN	European Norm
$f^{*}_{l,eff}$	Effective Lateral Confining Pressure including Fiber Orientation
$f^{''}_{l,eff}$	Effective Lateral Pressure
$f_{c,mat}$	Compressive Strength of Matrix Material
f_c'	Compressive Strength of Unconfined Concrete
f_{cc}	Compressive Strength of Confined Concrete
f_l	Lateral Confining Stress on Concrete Core
$f_{l,eff}$	Effective Lateral Confining Stress
f_{lu}	Confining Stress at Ultimate
f_m	Axial Stress
f_{mc}	Compressive Strength of Confined Masonry
f_{md}	Compressive Strength of Confined Element
f_{mdo}	Compressive Strength of a Well-Made Wall
f_{mo}	Compressive Strength of Unconfined Masonry
f_r	Stress in FRP with the Radii of the Corners
FRCM	Fiber Reinforced Cementitious Matrix
FRM	Fiber Reinforced Mortar
f_u	Ultimate Tensile Strength of Material
f_y	Yield Strength
GFRP	Glass Fiber Reinforced Polymer

GPa	Giga-Pascal
G-TRM	Glass Textile Reinforced Mortar
h	Depth
H	Height
k'	Non-dimensional Coefficient
k_1	Enhancement Coefficient
k_{10}	Ideal Confined Coefficient
k_2	Enhancement Coefficient
k_e	Effective Coefficient
k_H	Horizontal Efficiency Coefficient
k_V	Vertical Efficiency Coefficient
k_θ	Fier Orientation Coefficient
L	Initial height of the column excluding the end caps
LVDT	Linear Variable Differential Transformer
mm	Millimeter
MPa	Mega-Pascal
n	Number of Confining Layers
N	Newton
P	Applied Load
PBO	Polyparaphenylene Benzobisoxazole
RC	Reinforced Concrete
SRP	Steel Fiber Reinforced Polymer
T	Splitting Tensile Strength

t_f	Thickness of Fiber
t_{mat}	Total Thickness of Matrix
TRM	Textile Reinforced Mortar
u_{LVDTi}	Displacement recorded by the ith LVDT
UV	Ultraviolet
α	Shape Factor
β	Constant
γ	Constant
Δu	Average Change in Displacement
Δu_s	Change in displacement from initial stroke head location
ε_{cc}	Ultimate Strain of Confined Concrete
ε_{co}	Ultimate Strain of Unconfined Concrete
ε_{fu}	Ultimate Strain of Fiber
ε_m	Axial Strain
ε_{mc}	Ultimate Strain of Confined Masonry
$\varepsilon_{mc,t}$	Transverse Strain Measurement at Peak Point
$\varepsilon_{mc,t,u}$	Transverse Strain Measurement at Ultimate Point
ε_{mco}	Ultimate Strain of Unconfined Masonry
η	Effectiveness Coefficient
θ	Fiber Orientation
κ_a	Geometric Efficiency Factor
κ_e	Effective Strain Modification Factor
μ	Effectiveness Coefficient

ρ_f	Reinforcement Ratio
ρ_{mat}	Geometric Percentage of the Applied Matrix
σ	Stress
τ	Shape Parameter

1. INTRODUCTION

1.1. PROBLEM STATEMENT

Unreinforced masonry is a common type of construction that has been used throughout the world for hundreds of years and is commonly used for new construction projects today. This type of construction is vulnerable to damage from earthquakes and is sensitive to environmental degradation and increased loading demands due to changes in occupancy. Strengthening and retrofitting techniques are needed to allow historic structures to be preserved for future generations and to reinforce structures that have been damaged. It has been found that strengthening of compression elements is among the upmost importance to prevent catastrophic damage to historic, vertical load bearing structural elements (Krevaikas & Triantafillou 2005; Aiello et al., 2007; Borri et al., 2011; Ombres, 2015).

Compressive elements are often strengthened by providing confinement to the element. Among the techniques available for confining masonry compressive elements, fiber-reinforced polymer (FRP) composite jackets are appealing because of their high strength-to-weight ratio, corrosion resistance, ease of installation, fatigue resistance, protection against ultraviolet (UV) radiation, and relatively short curing time (American Concrete Institute, 2008). FRP jackets have been shown to enhance the strength and deformability of masonry columns under axial load, although the enhancement is dependent on different parameters such as column transverse cross-section, corner radius, aspect ratio, and quantity and type of fiber layers (Krevaikas & Triantafillou, 2005; Corradi et al., 2007; Aiello et al., 2007; Di Ludovico et al., 2010).

However, the use of FRP composite systems poses some disadvantages related to the use of the organic matrix (typically epoxy) including, but not limited to, higher costs of the epoxy resin, poor performance at temperatures above the glass transition temperature, poor compatibility between the epoxy and substrate materials, inability to apply onto wet substrate surfaces, and direct epoxy resin exposure being hazardous to workers.

To avoid some of these problems, inorganic binders such as cement-based mortars, can be used in place of the organic binder to form a new type of composite. Fiber reinforced composites with inorganic matrices are known as fiber reinforced cementitious matrix (FRCM), textile-reinforced mortar (TRM), fiber-reinforced mortar (FRM), or steel reinforced grout (SRG) composite systems. Compared to FRP composite, this type of composite provides good vapor compatibility with masonry substrates, protects against UV radiation, is aesthetically appealing, is cost effective, has reversibility characteristics, performs well under high temperatures, and is easy to apply. As a result, research involving the use of inorganic matrix composites to strengthen masonry structures has increased in recent years.

This study explores the use of a new type of a new type of composite comprised of high-strength steel fiber cords and an inorganic matrix (i.e., SRG composite) for use in strengthening unreinforced clay brick masonry columns. The work presented in this thesis investigates the influence of different parameters, namely the: corner radius, number of fiber layers, and quantity of jacket overlap faces, on the behavior of SRG-confined masonry columns. This study builds upon and expands the database of test

results from studies conducted by Baietti (2017), Fraioli (2017), and Senesi (2018) to gain a better understanding of the behavior and design of SRG-confined masonry.

1.2. GOAL AND OBJECTIVES

The overarching goal of this study was to explore the effectiveness of SRG composite for use in strengthening unreinforced masonry structures. Specific objectives of this thesis work were to:

a) Understand the behavior of SRG-confined masonry columns.
b) Compare the strength and deformability of SRG-confined masonry columns relative to unconfined masonry columns.
c) Determine the influence of different parameters including column corner radius, number of fiber layers, and quantity of jacket overlap faces on the effectiveness of the SRG confinement.
d) Evaluate the applicability of existing models to predict the confined compressive strength of SRG-confined masonry.

1.3. SCOPE

This section outlines the scope of this thesis work in addition to the scope of the project and its multiple phases.

1.3.1. Project Scope. As mentioned in Section 1.1, this thesis work is part of a larger study on confinement of unreinforced clay brick masonry columns using SRG jackets. The first phase of this study was carried out by Baietti (2017) and Fraioli (2017), in which the influence of SRG matrix type, SRG fiber density, and column corner radius

was explored. In the second phase of this study, the test variables were expanded to include the number of SRG jacket layers and number of SRG fiber overlapping faces. The scope of the second phase of this study is discussed in this section.

The second phase of the study project includes 55 unreinforced masonry specimens, 48 of which were confined, and 7 were unconfined for use as the control. All columns were constructed with low-strength, solid clay brick units bonded with a low-strength masonry mortar. The confined columns were wrapped with an SRG jacket comprised of stainless-steel fiber cords embedded in a lime-based mortar matrix. The laboratory work was conducted by two graduate students: Sarah Jemison and Carolina Senesi. Portions of the data were used in separate analyses and are summarized in their respective theses.

The following variables were included in the test matrix:

a) Density of the stainless-steel fiber sheet used in the SRG composite to confine the masonry specimens. The different fiber densities were accomplished by varying the cord spacing. Fiber sheet density was either 670 g/m^2 or 1,200 g/m^2.

b) Corner radius (r) of the masonry columns. The corner was either sharp (r = 0 mm) or rounded (r = 38.1 mm).

c) Number of fiber layers used in the jacket to confine the masonry specimens. For sharp cornered columns, the number of layers was 1, 2, or 3, while for round cornered columns the number of layers was 1 or 2, respectively.

d) Number of fiber overlapping faces. Sharp cornered columns had a single overlap face, whereas round cornered columns had either one or two overlapping faces.

1.3.2. Thesis Scope. Thirty-one of the 55 unreinforced masonry columns considered in the second phase of this study are described in detail in this thesis work. Of the 31 specimens, seven were unconfined so that the strength and deformability enhancement provided by the SRG jacket could be determined. All confined columns presented in this thesis work had an SRG jacket with the same steel fiber density of 1,200 g/m^2. Columns confined with an SRG jacket with fiber density 670 g/m^2 are presented in detail by Senesi (2018).

The confined specimens in this thesis work were divided into six different groups defined by their unique combination of test parameters. The parameter varied for sharp cornered columns was the number of fiber layers (ranging from 1-3 layers) in which each layer was bonded using a 2 mm thick layer of matrix mortar. The parameters varied for round cornered columns include the number of fiber layers (ranging from 1-2 layers) and the number of fiber overlap faces (either 1 or 2 column faces).

1.4. SUMMARY OF THESIS CONTENT

The problem definition, goal, objectives, and scope of this study are defined in Section 1 of this thesis. The background investigation discussed in Section 2 include a review of existing literature on FRP and FRCM confined concrete and masonry. Section 3 describes the experimental program carried out in the second phase of this study in terms of materials, specimen fabrication, and experimental setup. Section 4 summarized

the test results of the 31 specimens included in this thesis work in terms of general behavior, axial stress – axial strain response, axial stress – transverse strain response, and energy absorption. In addition, Section 4 evaluates the influence of the various test parameters considered in this study. Section 5 evaluates the use of existing analytical models to predict the strength increase provided by the confinement system. Section 6 contains a summary, conclusions, and recommendations for future work. Appendix A documents the experimental results for each test specimen included in this thesis work. Appendix B includes documentation of the axial stress – strain relationships for the individual specimens while Appendix C contains figures representing a summary of the experimental results.

2. BACKGROUND

This section describes experimental and analytical studies focused on structural strengthening of compression elements using external reinforcement. The main type of strengthening technique discussed in this section involves confinement of compression elements using fiber reinforced composite jacketing systems in which continuous fibers are wrapped around and externally bonded to the element. Confinement is the application of a material to enclose and restrict the elements transverse dilation upon the application of a compressive load, in this case. The material will restrict the transverse dilation through the development of tensile stresses which causes an offsetting compressive stress in the enclosed material. The resulting state of stress increases the ductility and strength of the confined masonry.

As discussed in Section 1, the composite investigated in this thesis work is a new type of composite referred to as steel reinforced grout (SRG), and very few studies are currently reported in the technical literature on the use of SRG composite to confined masonry compression elements. Therefore, the literature review was broadened to include studies on confinement of concrete and masonry compression members using different types of fiber reinforced composites to lay the groundwork for the research conducted in this study.

Section 2.1 discusses studies involving the strengthening of unreinforced (plain) or internally reinforced concrete compression members using either fiber reinforced polymer (FRP) composite systems or fiber reinforced cementitious matrix (FRCM) composite systems. Section 2.2 discusses experimental and analytical studies involving

the strengthening of masonry compression members using either FRP or FRCM composite systems.

2.1. CONFINEMENT OF CONCRETE

The following section describes existing technical literature that focuses on the effects of FRP and FRCM composites when used as confinement for concrete structures.

2.1.1. FRP Confined Concrete. This section describes experimental and analytical studies focused on concrete elements confined with FRP systems. In recent decades, the use of FRP has grown in popularity for structural strengthening applications. FRP composites provide several advantages over traditional strengthening methods such as steel or concrete jacketing. FRP composites have features such as high strength-to-weight ratio, corrosion resistance, ease of installation, fatigue resistance, protection against UV radiation, and relatively short curing time (American Concrete Institute, 2008).

Regarding compression members, confinement of concentrically or eccentrically loaded columns has become an important means to strengthen existing structures, and several researchers have studied confinement of concrete using FRP jackets. Parameters investigated include the FRP fiber type (carbon, basalt, glass, etc.), FRP fiber orientation (unidirectional or bidirectional jackets), shape of the transverse cross-section of members (circular, rectangular, rectangular with rounded corners), dimensions of the specimens, unconfined concrete compressive strength, internal steel reinforcement, and others (Campione & Miraglia, 2003).

2.1.1.1. Campione Miraglia 2003. Research reported by Campione and Miraglia in 2003 examined the analytical compressive behavior of concrete members confined with FRP jackets in terms of compressive strength and maximum strain of the members. The authors developed analytical models that were calibrated for cases in which the primary failure mode of FRP was rupture of the fibers. To determine the effective lateral confining pressure, fundamental hypotheses were assumed such as 1) all transverse cross-sections of the members were in the same condition along the height due to the presence of continuous FRP reinforcement, and 2) the FRP behaves elastically up to failure. The parameter investigated in this study was the column cross-sectional geometry, which varied from square, square with rounded corners, to circular sections.

The general model used to determine the confined compressive strength for concrete members was developed previously by Mander, Priestly and Park in 1988. The expression is shown in Equation 2.1:

$$f_{cc} = f_{co} + \mathrm{k}' f_{l,eff} \qquad \text{Eq. 2.1}$$

where:

f_{cc} = compressive strength of confined concrete

f_{co} = compressive strength of unconfined concrete

$f_{l,eff}$ = effective lateral confining stress = k_e x f_l

k' = concrete strength enhancement coefficient

k_e = effective coefficient = A_e / A_{cc}

A_e = effective area of confined concrete

A_{cc} = transverse area of concrete enclosed by the centerlines of the perimeter FRP

f_l = lateral confining stress on concrete core from FRP transverse reinforcement (shown in Figure 2.1 and Equations 2.2-2.4 based on the transverse cross section)

$$f_l = \frac{2t_f f_u}{b_d} k_i \text{ (for circular)} \quad \text{Eq. 2.2}$$

$$f_l = \frac{\sqrt{2}t_f f_u}{b_d} k_i \text{ (for square)} \quad \text{Eq. 2.3}$$

$$f_l = \frac{2t_f f_r}{b_d} \text{ (for square with found corners)} \quad \text{Eq. 2.4}$$

f_u = ultimate tensile strength of fiber material

fr = stress in FRP (Equation 2.5) with the radii of the corners, r

$$f_r = f_u \left[\left(1 - \frac{\sqrt{2}}{2} k_i \right) \frac{2r}{b_d} + k_i \frac{\sqrt{2}}{2} \right] \quad \text{Eq. 2.5}$$

b_d = concrete core dimension to centerline of FRP perimeter

t_f = thickness of fiber

k_i = reduction factor of the stress determined experimentally

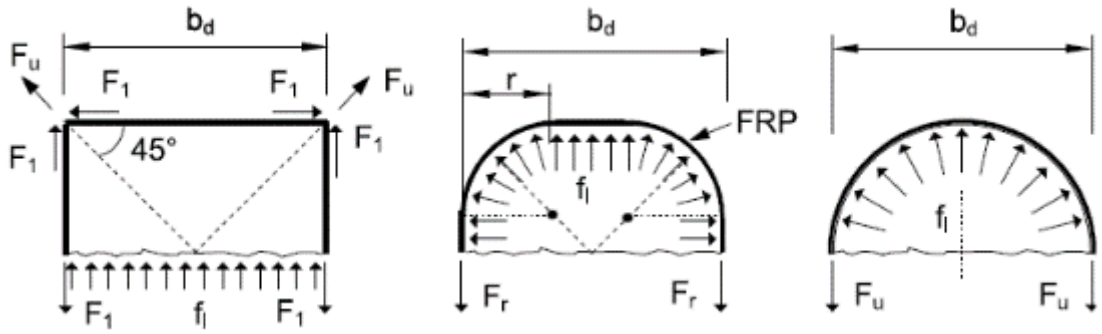

Figure 2.1. Effective Lateral Confining Pressure for FRP-reinforced Cross-sections (Campione & Miraglia, 2003)

Through experimentation, the authors proposed multiple equations for f_l, based on the cross-sectional geometry of the transverse cross-sections due to its evident influence on the compressive behavior of the members. The authors also proposed formulations for the effective coefficient k_e, based on the concrete core dimension (measure from the centerlines of the FRP perimeter) and the corner radius due to the concentration of stresses at the columns corners. The proposed values for k_e were:

k_e = 1 (for circular cross-sections)

k_e = 1/3 (for square cross-sections)

k_e = computed using Eq. 2.6 for square cross-sections with rounded corners:

$$k_e = \frac{\left[b_d^2 - 4\left(r^2 - \frac{\pi r^2}{4}\right)\right] - \frac{2}{3}(b_d - 2r)^2}{b_d^2 - 4\left(r^2 - \frac{\pi r^2}{4}\right)} \qquad \text{Eq. 2.6}$$

2.1.1.2. Bournas Lontou Papanicolaou Triantafillou 2007. Bournas et al. (2007) studied the effectiveness of FRP jackets as a confining system for RC columns. The study included testing of full-scale, FRP confined RC columns subjected to cyclic lateral loading and a constant axial compressive load. Three, full-scale [250 (width) x 250 (depth) x 1600 (length) mm] RC columns with varying strengthening schemes were studied. All specimens were constructed using concrete from the same batch (compressive strength = 25 MPa), longitudinal bars (ultimate tensile strength = 433 MPa), and stirrups (ultimate tensile strength = 444 MPa). The FRP confined column was designed to have equivalent stiffness and circumferential strength as the counterpart specimen confined with TRM described in Section 2.1.2.2.

Flexure controlled the performance and failure mode of the FRP confined columns. The experimental results indicated that FRP confined columns had a peak stress equivalent to the unconfined specimen, however the FRP confinement provided an increased deformation capacity by a factor of 2.0. At a constant axial load, confinement by jacketing limited the axial strain, indicating the FRP confined column was able to maintain the load well compared to the unconfined column. In terms of energy dissipation at failure, the FRP confined column dissipated nearly six times more energy than the unconfined column. Lastly, the stiffness reduction beyond the peak load was considerably lower in comparison to the unconfined specimen.

2.1.1.3. Bournas Triantafillou Zygouris Stavropoulos 2009. In 2009, the authors studied the effectiveness of carbon fiber reinforced polymer (CFRP) composites as a strengthening system, confining “old-type” RC columns subjected to cyclic uniaxial flexure under constant axial load. In total, ten large-scale columns of the same geometry

were constructed using concrete with compressive strength ranging from 25.3-28.9 MPa, three of which were strengthened with an FRP system. The columns were divided into two groups based on the internal reinforcement configuration (continuous longitudinal reinforcement or lap-spliced reinforcing bars at the column's base). The first group of columns contained continuous internal reinforcement and were strengthened with two layers of CFRP at the column ends, (carbon fiber elastic modulus = 225 GPa and tensile strength = 3,800 MPa). The second group of columns had spliced internal reinforcement with different lap lengths (either 20 or 40 bar diameters) and were strengthened with CFRP at the ends.

The experimental results for the first group showed the behavior of the FRP confined specimens was not controlled by buckling of the longitudinal internal reinforcement. Buckling of the longitudinal reinforcement was delayed compared to the unconfined column. The internal bars sustained a significant amount of compressive load after buckling due to the lateral support provided by the FRP jackets. The jackets limited the transverse dilation of the concrete cover and allowed a large amount of strain energy to be stored in the confined concrete. This energy was redistributed to the region of the FRP jacket, where buckling of the longitudinal bars occurred abruptly between the end of the FRP jacket and the next internal stirrup. The authors also found that in columns with continuous longitudinal reinforcement the energy dissipated at failure by the FRP jacketing was about two and a half times greater than the energy dissipated by unconfined specimens.

The experimental results for the second group of specimens showed that for columns with short or long lap splices, FRP confinement was effective in terms of

increasing the deformation capacity. The effectiveness of the confinement decreased with a decrease in lap length. Regardless of the lap length, columns with lap splices dissipated energy at failure nearly two and half times greater than the energy dissipated by unconfined specimens.

2.1.1.4. El-Hacha Mashrik 2012. El-Hacha and Mashrik studied the effectiveness of steel fiber reinforced polymer (SRP) sheets to confine small-scale plain concrete columns tested under monotonic uniaxial compression. The investigation was in terms of peak compressive stress, axial stress – circumferential strain response, and ductility. In total, 84 small-scale concrete specimens were tested. Of the specimens, 36 had circular cross-sections (Phase I), 36 had square cross-sections (Phase II), and the remaining 12 were also square (Phase III). The parameters varied in this study include the concrete compressive strength, transverse cross-sectional geometry, number of fiber layers applied, and the corner radius for columns with square cross-sections. The concrete compressive strength had target values of 25, 30, and 35 MPa. Phase I and Phase II specimens were divided into two groups based off the true concrete compressive strength. For Phase I and Phase II, the quantity of SRP layers ranged from zero (unconfined) to three layers. Phase III studied the effects of corner radius r (r = 3, 6, 10, or 25 mm).

The authors determined that SRP wraps improved the axial capacity and ductility of both square and circular columns, however the effects were more prominent in the circular columns. These results were in accordance with previous studies found in literature. For a constant concrete compressive strength, increasing the number of SRP layers increased the confined axial compressive strength and ductility for both square and circular specimens in a non-linear relation to the number of SRP layers. The authors also

determined that since the confining action of SRP sheets depends on the lateral expansion of concrete, higher concrete compressive strengths reduce the effects of the confinement system. Rounding of the corners improved the axial capacity and ductility of SRP wrapped square specimens with increasing effects as the corner radius increased. Figure 2.2 shows that the authors determined the cross-sectional geometry effected the axial stress – circumferential strain response in that after the peak load, specimens with a circular cross-section showed an ascending branch while specimens with a square cross-section showed a descending branch followed by a plateaued region.

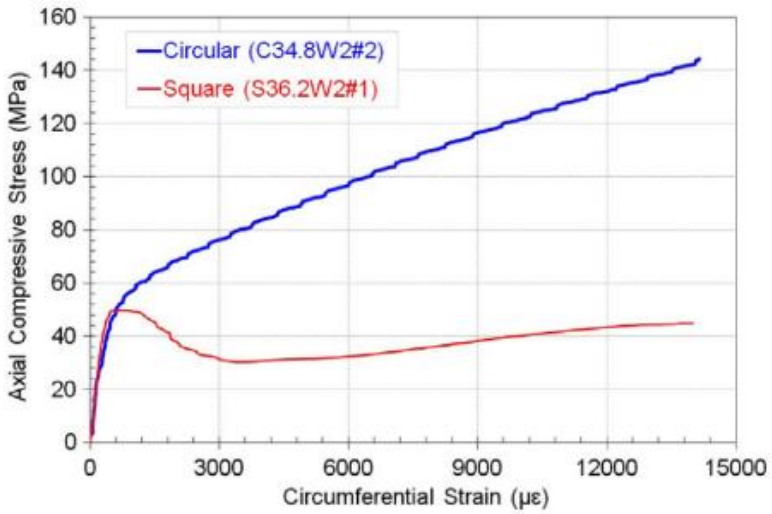

Figure 2.2. Axial Stress - Circumferential Strain Response of Columns with Varying Cross-Section (El-Hacha & Mashrik, 2012)

2.1.1.5. Napoli Realfonzo 2016. Research reported by Napoli and Realfonzo in 2016 studied the effectiveness of SRP on confined concrete cylinders tested under monotonic concentric compressive loading. Models proposed for stress and strain of SRP

confined concrete were compared with models used for GFRP and CFRP confined specimens. In total, 242 small-scale plain concrete cylindrical specimens [150 mm (diameter) x 300 mm (height)] were constructed and divided into five different series based on the average value of the unconfined concrete strength. Parameters investigated were the quantity of confined layers (ranging from 1-3 layers), concrete compressive strength (compressive strengths were 6.88, 14.51, 31.0, 42.15, and 46.10 MPa with varying quantities of specimens for each), and the density of steel tape used (steel tapes densities = 0.157, 0.472, and 0.787 cords per mm; elastic modulus = 190 - 206 GPa; ultimate tensile strength = 3,070 – 3,302 MPa).

The authors determined that for a given SRP layout, the behavior in terms of confined strength and ultimate strain generally reduced with the increase of the concrete compressive strength. In general, the failure mode of the confined specimens was rupture of the SRP tape, which involved the entire specimen height or portions of the height. This failure mode was similar to that of specimens confined with carbon fiber reinforced polymer (CFRP) or glass fiber reinforced polymer (GFRP) systems. Specimens confined with multiple high density SRP layers failed due to a combination of fiber debonding and fiber rupture. The authors determined that by increasing the unconfined concrete strength or quantity of confinement layers, in terms of the axial stress – strain relationship, the number of specimens showing a descending branch after the peak load was reached increased. This descended branch indicated a more ductile failure mode compared to unconfined specimens.

Lastly, predictive models for the confined strength and the ultimate strain of the SRP confined concrete were developed using the experimental results. It was found that

the formula that fitted the test results in terms of ultimate strain was nonlinear, while the relationship for the confinement strength was linear. The proposed formulas are similar to previously proposed models for CFRP and GFRP.

2.1.1.6. Wang Wang Smith Yu 2016. The authors investigated the size effect on the response of CFRP confined square columns loaded with monotonic concentric compression in terms of axial stress-strain and hoop strain responses. In total, 23 confined concrete specimens were constructed and divided into 10 series based on varied parameters. Variables focused on in this study were the specimen geometry (7 different cross-sectional widths *b* ranging from 100 – 400 mm), number of CFRP layers (1-3 layers; elastic modulus = 240 GPa and tensile strength = 4,340 MPa), and the inclusion or exclusion of internal steel reinforcement. Columns were constructed with a constant height-to-cross-sectional width (*H/b*) of 3.0 and a constant corner radius-to-width ratio (*r/w*) of 0.15. All specimens were constructed with the same batch of concrete (compressive strength = 25.4 MPa) and had the same theoretical lateral FRP confining pressure in accordance with ACI 440.2R – (2008).

The failure mode for all confined columns was sudden rupture of the CFRP wraps near the corner regions with no influence of the specimen size. Following the removal of the wraps, it was evident that the columns experienced diagonal failure surfaces with severe concrete crushing. For specimens that were reinforced with internal steel, the internal hoop reinforcement bent outward and the longitudinal bars buckled. In terms of the axial stress – strain response, it was concluded that no size effect existed for small columns ($b < 300$ mm), however there was a difference in large columns due to the decrease in lateral confinement pressure observed for the CFRP. The authors found that

the distribution of FRP hoop strain was non-uniform around the perimeter of the specimens and that the effective rupture strain of FRP generally decreased with an increase in the column cross-sectional size. It was found that the confinement effectiveness decreased with an increase in specimen size in terms of confined strength and ultimate strain.

The authors compared the peak compressive stress f_{cc} determined by the experiments to values determined using the ACI 440.2R – (2008) method shown in Equation 2.7:

$$f_{cc} = f_{co} + \psi_f * 3.3 * \kappa_a * f_l \qquad \text{Eq. 2.7}$$

where:

f_{co} = unconfined cylinder compressive strength of concrete

ψ_f = reduction factor = 0.95

κ_a = geometric efficiency factor, shown in Eq. 2.8

$$\kappa_a = \left[1 - \frac{2(b - r^2)}{3A_g} - \rho_g\right] / (1 - \rho_g) \qquad \text{Eq. 2.8}$$

b = width of cross section

r = corner radius

A_g = gross cross-sectional area

ρ_g = ratio of longitudinal steel to gross cross-sectional area

f_l = effective confinement lateral pressure of FRP shown in Eq. 2.9

$$f_l = \frac{2E_f n t_f \varepsilon_{fe}}{D} \qquad \text{Eq. 2.9}$$

E_f = elastic modulus of FRP

D = external diameter of circular section or the diagonal of non-circular sections

t_f = thickness of fiber

n = number of fiber layers

ε_{fe} = effective lateral strain of FRP at failure (Eq. 2.10)

$$\varepsilon_{fe} = \kappa_e \varepsilon_{fu} \qquad \text{Eq. 2.10}$$

κ_e = effective strain factor shown in Equation 2.11

ε_{fu} = ultimate tensile strain of FRP

It was found that without an effective strain modification factor κ_e, the model proposed by ACI 440.2R overestimated the axial stress capacity for larger sized specimens. After the following effective strain modification factor was applied, the experimental and predicted values correlation improved due to the factor taking the size effect of the rupture strain of FRP into account (Figure 2.3).

$$\kappa_e = 1 - 0.38\left(\frac{b}{100}\right)^{0.41} \qquad 100 \leq b \leq 400 \qquad \text{Eq. 2.11}$$

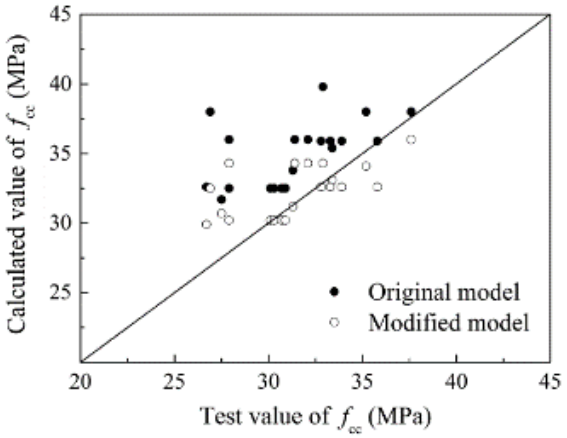

Figure 2.3. Application of Modification Factor

2.1.1.7. Sneed Ravazdezh Santandrea Imohamed Carloni 2017. In this study, the authors investigated the behavior of short plain concrete prisms confined by steel reinforced polymer (SRP) jackets subjected to a monotonic concentric compressive load. In total, 25 concrete prisms [150 mm (width) x 150 mm (depth) x 450 mm (length)] were cast using the same batch of concrete (28-day compressive strength = 25.0 MPa and splitting tensile strength = 2.25 MPa). The confinement system was composed of unidirectional steel fiber sheets (elastic modulus = 190 GPa and tensile strength = 3,000 MPa) embedded in a polymeric matrix (tensile strength = 14 MPa). The authors focused on several different variables including the density of the steel fiber (medium density = 0.314 cords/mm and high density = 0.473 cords/mm), corner radius *r* (sharp *r* = 0 or rounded *r* = 17.5 mm), concrete surface treatment (untreated or sandblasted), SRP jacket height (full-height = 450 mm or quasi full-height = 440 mm), and number of confining layers (1 or 2 layers).

The authors used digital image correlation (DIC) to measure the axial and hoop strains for confined specimens and compared the values determined by other typical techniques (LVDT devices and strain gages). The shown in Figure 2.4 are representative examples of the eight regions used to determine strain.

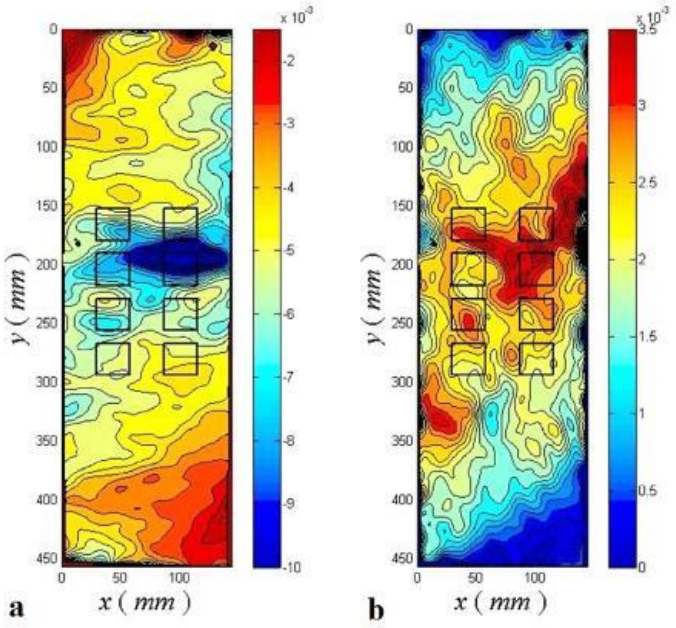

Figure 2.4. Representation of the Strain Calculated using DIC, (a) axial strain, (b) hoop strain (Sneed et al., 2017)

The primary failure mode of confined specimens occurred by separation of the SRP jacket at the vertical overlap region or by rupture of some steel fibers near the corners of the prism. The failure mode of the columns was dependent on the fiber density. Regarding the influence of the corner radius, the peak stress and ultimate strain decreased as the corner radius increased for specimens confined with high density fibers.

This result was due to the sharp corners postponing the opening of the SRP jacket. Contrary for the specimens confined with medium density fibers, as the corner radius increased, the peak stress and ultimate strain increased possibly due to the primary failure mode being fiber rupture before the jacket opening. Concerning the surface treatment, columns with sandblasted surfaces provided greater compressive strength and ultimate strain compared to those with untreated concrete surfaces. The treated surface provided better adhesion between the composite material and the concrete surface.

The authors determined that specimens confined with high density steel provided higher compressive strength and ultimate strain then those specimens confined with medium density steel, however this strength increase was not proportional to the fiber density. When comparing the SRP jacket height, specimens with full jacket height resulted in larger compressive strength, however it decreased in ultimate strain. This behavior could be due to localized deformations for the quasi-full height specimens. Increasing the number of confining layers resulted in increased compressive strength and ultimate strain. However, the increase in strength was not linearly proportional to the number of jacket layers. Lastly, it was found that the energy absorption of the columns increased with increasing composite stiffness caused by increasing the number of confining layers.

2.1.2. FRCM Confined Concrete. This section describes experimental and analytical studies focused on concrete columns confined with FRCM composites. The need for upgrading existing structures has increased in recent years, due to damaged caused by seismic action, non-seismic action, change in occupancy, or the introduction of more stringent design requirements. As discussed in Section 2.1.1, jacketing using an

FRP system to improve the behavior of compression members has been increasing in popularity. FRP systems provide high strength-to-weight ratio, corrosion resistance, ease of application, and minimal change in geometry (Triantafillou et al., 2006). However, the FRP strengthening technique has certain drawbacks attributed to the organic resin used as the bonding matrix or impregnation material. Drawbacks include higher costs for the epoxy resin, poor performance at temperatures above the glass transition temperature, poor compatibility between the epoxy and substrate materials, deterioration of the epoxy by solar generated ultraviolet (UV) light, inability to apply onto wet substrate surfaces, and direct epoxy resin exposure being hazardous to workers (Triantafillou et al., 2006; Ombres, 2015).

To avoid some of the problems associated with organic binders, inorganic binders such as cementitious mortars can be used. Cementitious mortars provide good vapor compatibility with concrete substrate, ease of application, cost effective material, and reversibility characteristics. In this section, experimental and analytical investigations focusing on concrete columns confined with FRCM systems are discussed. Parameters under investigation include the unconfined compressive strength of the concrete, quantity of fiber layers, cross-sectional geometry of the columns, internal reinforcement scheme, and more.

2.1.2.1. Triantafillou et al. 2006. The authors studied the effectiveness of textile-reinforced mortars (TRM) as a means of increasing the axial capacity and ultimate strain of confined concrete specimens subjected to uniaxial compressive loading. The authors also compared the effectiveness of TRM systems to that of FRP systems. Forty-four plain concrete species were divided into three series based on the cross-sectional

geometry and strengthening scheme. All specimens were constructed using the same concrete batch, and the strengthened specimens were confined with a bidirectional carbon fiber fabric (elastic modulus = 225 GPa and tensile strength = 3,350 MPa). The authors investigated the effects of the following parameters: columns cross-sectional geometry (circular or rectangular), matrix mortar type (Type 1 compressive strength = 8.56 MPa; Type 2 compressive strength = 30.61 MPa), matrix type (cement-based mortar or epoxy resin), strengthening scheme (continuous fiber wrapped in helix form embedded within a mortar or resin; unbonded textile not impregnated within matrix but anchored at the column ends using a single layer of transverse wrap), and number of fiber layers (ranging from 2-4 layers).

The author determined that the TRM jackets provided an increase in the column compressive strength and deformation as the number of confining layers increased. This was true for both circular and rectangular cross-sectioned specimens. However, the increase depended on the ultimate tensile strength of the matrix mortar which also controlled the failure mode of the confine specimens. For circular specimens, it was found that FRP confining systems were more effective than TRM systems due to the higher strength and deformability of the resin matrix, allowing for better stress redistribution in the fibers. For rectangular specimens, TRM systems were found to be equally effective as FRP systems in terms of strength and slightly less effective in terms of ultimate strain. It was determined that unbonded textile not impregnated within a matrix but anchored at the column ends behaved nearly as well as those confined with continuous, fully-bonded jackets.

Using the experimental data collected, for both resin-based and mortar-based specimens, simplified models to determine the confined strength f_{cc} (Eq. 2.12), and the ultimate strain ε_{cc}, (Eq. 2.13) were developed:

$$\frac{f_{cc}}{f_{co}} = 1 + k_1 \left(\frac{f_{l,eff}}{f_{co}}\right)^{\beta} \quad \text{Eq. 2.12}$$

$$\varepsilon_{cc} = \varepsilon_{co} + k_2 \left(\frac{f_{l,eff}}{f_{co}}\right)^{\gamma} \quad \text{Eq. 2.13}$$

where:

f_{co} = peak stress of unconfined columns

ε_{co} = unconfined ultimate strain

$f_{l,eff}$ = confining stress at failure shown in Eq. 2.14

$$f_{l,eff} = k_e \frac{b+d}{b*d} t_f E_f \varepsilon_f \quad \text{Eq. 2.14}$$

$$k_e = 1 - \frac{b'^2 + h'^2}{3A_g} \quad \text{Eq. 2.15}$$

β and γ = constants developed based on best fitting experimental data

k_1 and k_2 = measurements of confinement effectiveness shown in Eq. 2.16

$$k_1 = \mu k_{1,R}\ , k_2 = \eta k_{2,R} \qquad \text{Eq. 2.16}$$

μ and η = effectiveness coefficients (dependent on the jacketing system)

k_e = effective coefficient

t_f = thickness of fiber

A_g = total cross-sectional area

b = column width

h = column depth

$b' = b - 2*r$ (Figure 2.5)

$h' = h - 2*r$ (Figure 2.5)

r = corner radius

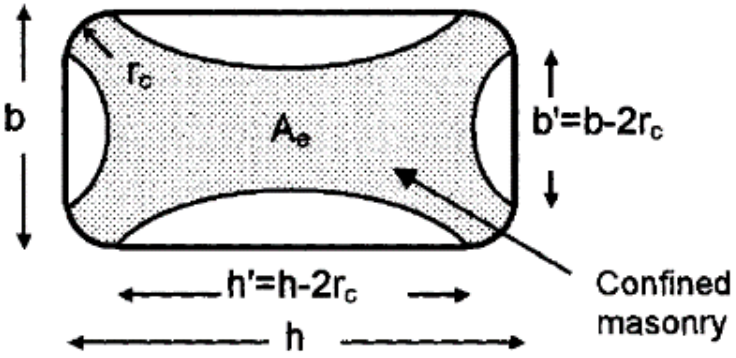

Figure 2.5. Effectively Confined Area of Column with Rectangular Cross-sections (Triantafillou et al., 2006)

The Table 2.1 shows the calibrated values for the constants and coefficients.

Table 2.1. Calibrated Values of Coefficients (Triantafillou et al., 2006)

Strengthening Technique	μ	k_1	η	k_2
Resin-Matrix System	1.00	2.79	1.00	0.08
Continuous Fiber with Mortar-Matrix	0.68	1.90	0.57	0.05
Unbonded Textile with Mortar-Matrix	0.84	2.34	0.82	0.07

2.1.2.2. Bournas Lontou Papanicolaou Triantafillou 2007. Bournas et al**.** (2007) studied the effectiveness of TRM jackets as a confining system for RC columns and compared them with FRP confining systems. This work was divided into two studies: the first focusing on the effectiveness of TRM confining systems on small-scale RC prisms tested under concentric compression, whereas the second study compared the effectiveness of TRM versus FRP systems on full-scale RC columns subjected to lateral cyclic loading and a constant axial compressive load.

The first study included 15 RC specimens [200 (width) x 200 (depth) x 380 (length) mm] divided into three series based on the strengthening scheme. All specimens were constructed using concrete from the same batch (compressive strength = 24.56 MPa) and longitudinal internal reinforcement (ultimate tensile strength = 658 MPa). The strengthening schemes focused on the matrix used (commercial inorganic mortar (compressive strength = 22.13 MPa) or resin adhesive (tensile strength = 70 MPa and elastic modulus = 3.2 GPa)) and the number of fiber layers (ranged from 2-6 layers of

carbon fiber depending on designed stiffness). Internal stirrup spacing varied based on previous and current detailing practices (200 mm or 100 mm, respectively).

The second study tested three, full-scale [250 (width) x 250 (depth) x 1,600 (length) mm] RC columns with varying strengthening schemes. All specimens were constructed using concrete from the same batch (compressive strength = 25 MPa), longitudinal bars (ultimate tensile strength = 433 MPa), and stirrups (ultimate tensile strength = 444 MPa). For all specimens, the strengthening schemes (TRM and FRP) were designed to have equal stiffness and strength in the column circumferential direction.

The results of both studies were compared to those discussed in Section 2.1.1.2. Results of the first study determined that both FRP and TRM systems effectively confine concrete specimens by increasing the strength and deformation while delaying buckling of internal longitudinal bars. For both confining systems, the jacket effectiveness increased with the number of fiber layers but decreased with the increase in confinement provided by stirrups. The authors determined that FRP confining systems were more effective than TRM systems in terms of increasing the strength and ultimate strain due to the nonuniform distribution of stresses in the fibers caused by slippage, local debonding, and microcracking in the matrix mortar.

From the second study, the authors found that flexure controlled the performance and failure mode of the confined columns. The experimental results indicated that FRP and TRM confined columns had nearly equivalent peak stress as the unconfined specimen. The TRM confined specimen provided an increased deformation capacity by a factor greater than 2.0. In terms of energy dissipation at failure, the confined columns (independent of the system) provided nearly six times more energy dissipation than the

unconfined column. Lastly, the stiffness reduction beyond the peak load for retrofitted columns was considerably lower than that of unconfined specimen. Overall, TRM jacketed columns had equivalent results as FRP confined columns in terms of peak stress, cyclic deformation, energy dissipation, and stiffness degradation.

2.1.2.3. Bournas Triantafillou Zygouris Stavropoulos 2009. In 2009, the authors studied the effectiveness of TRM jackets to strengthen "old-type" RC columns subjected to cyclic uniaxial flexure under constant axial load. They also compared the effectiveness of the TRM strengthening system to an FRP strengthening system of equal stiffness and strength. Ten large-scale columns of the same geometry were constructed using concrete with compressive strength ranging from 25.3-28.9 MPa. The columns were divided into two groups based on the internal reinforcement configuration (continuous longitudinal reinforcement or lap-spliced reinforcing bars at the column's base). The first group of columns contained continuous internal reinforcement strengthened by four layers of C-TRM or four layers of G-TRM (carbon fiber elastic modulus = 225 GPa and tensile strength = 3,800 MPa; glass fiber elastic modulus = 70 GPa and tensile strength = 1,700 MPa). The second group of columns had spliced internal reinforcement at different lap lengths (either 20 or 40 bar diameters) and were strengthened with C-TRM. The experimental results obtained were compared to those of CFRP confined columns described in Section 2.1.1.3.

The experimental results for the first group showed that the behavior of carbon and glass TRM jacketed specimens was similar, but it was different from FRP jacketed columns. TRM confined specimens performed better than FRP confined specimens in terms of deformation capacity and drift ratio. TRM jacketed specimens were effective at

increasing the energy dissipation of "old-type" columns by delaying longitudinal bar buckling. The internal reinforcement buckled gradually due to TRM system's ability to deform outward without early fiber rupture, unlike the FRP systems. The results showed that, at failure, columns with continuous longitudinal reinforcement and TRM jackets dissipated almost five times more energy than the unconfined specimens, and two and a half time more than the columns confined with FRP.

The experimental results for the second group of specimens showed that for columns with short lap splices, TRM jackets were slightly less effective in terms of deformation capacity than the FRP confined columns, however they were equivalent for columns with long lap splices. For both TRM and FRP confined columns, the effectiveness of the confinement decreased with a decrease in lap length. Regardless of the strengthening scheme, columns with lap splices dissipated energy at failure nearly two and half times greater than the unconfined specimens.

2.1.2.4. Di Ludovico Prota Manfredi 2010. Di Ludovico, Prota, and Manfredi studied the effectiveness of basalt fibers impregnated with epoxy resin or latex bonded with a cement-based matrix and compared the results with other confinement schemes on concrete cylinders.

Twenty-three concrete cylindrical specimens with a diameter of 150 mm and height of 300 mm were constructed using low-strength concrete. The compressive strength of the concrete was 15 MPa with a water-to-cement ratio of 0.78. The specimens were divided into two series: seven specimens were tested 150 days after casting and sixteen were tested 240 days after casting. In addition to the time at which the specimens were tested, other test parameters included the type of confinement fiber, number of fiber

layers, and the type of matrix bonding the fiber to the concrete substrate. The confining fibers used were as follows: uniaxial GFRP laminates: (elastic modulus = 65.6 GPa and tensile strength = 1,370 MPa), primed alkali-resistant fiberglass grids: (elastic modulus = 72.0 GPa and tensile strength = 1,440 MPa), and bidirectional basalt laminates: (elastic modulus = 91.1 GPa and tensile strength = 1,814 MPa). The matrix used was a cement-based mortar or epoxy resin, while the impregnation material for the basalt fibers was either epoxy resin or latex.

Failure of confined specimens occurred when the reinforcement system ruptured in the hoop direction or the debonding of the fiber jacket. Transverse strain around the perimeter of confined specimens was proven to be non-uniform and the distribution was affected by the type of reinforcement and matrix used. It was also determined that the use of mortar as a bonding agent significantly influenced the effective lateral reinforcement strain at failure as demonstrated by cracking of the mortar, which indicated it was less homogeneous than the epoxy resin. For all strengthening systems, the compressive strength and ultimate strain increased as the number of fiber layers increased, but the increase was not linearly proportional to the number of jacket layers.

Regarding the basalt confining systems, the use of resin or latex as the impregnation material provided substantial increases in both compressive strength and ductility of concrete members compared to other systems using mortar matrix. Basalt confined specimens using mortar as the matrix failed due to debonding of the fiber jacket. The jacket failure resulted from the slow propagation of cracks in the axial direction of the column. The failure mode of GFRP laminate specimens was attributed to brittleness caused by fiber rupture. Specimens confined with primed glass-fiber grid bonded with

cement-based mortar did not perform as well as those confined with basalt in terms of peak stress and ultimate strain obtained. In terms of ultimate axial strain, GFRP laminate confined specimens provided the largest increase compared to the unconfined specimens. Using the experimental results collected, the authors used models from literature to predict the confined strength (Eq. 2.17) and ultimate axial strain (Eq. 2.18) of confined specimens:

$$\frac{f_{cc}}{f_{co}} = 1 + k_1 \left(\frac{f_{lu}}{f_{co}}\right)^{\beta} \quad \text{Eq. 2.17}$$

$$\varepsilon_{ccu} = \varepsilon_{co} + k_2 \left(\frac{f_{lu}}{f_{co}}\right)^{\gamma} \quad \text{Eq. 2.18}$$

where:

f_{lu} = confining stress at failure

f_{co} = peak stress of unconfined columns

β and γ = constants developed based on best fitting experimental data

k_1 and k_2 = measurements of confinement effectiveness

ε_{co} = unconfined ultimate strain

υ and ψ = effectiveness coefficients based on each specific confinement system

$k_{1,M}$ and $k_{2,N}$ = confinement effectiveness coefficient shown in Eq. 2.19

$$k_{1,M} = \upsilon k_1 \, , k_{2,N} = \psi k_2 \quad \text{Eq. 2.19}$$

The constants β, γ, k_1, and k_2 were developed using the experimental results for the FRP and basalt confining systems, shown in the Tables 2.2 and 2.3.

Table 2.2. Analytical Results in Terms of Strength Increase (Di Ludovico et al., 2010)

	β = 1						β = 0.85					
Confinement Technique	$k_{1,M}$	R^2	υ	$\Delta f_{cc}/f_{co}$ (%)	SD	COV (%)	$k_{1,M}$	R^2	υ	$\Delta f_{cc}/f_{co}$ (%)	SD	COV (%)
GFRP	2.94	1.00	1.00	0.60	0.001	16.6	2.68	1.00	1.00	1.28	0.002	15.2
GFRP grid (mortar)	3.45	0.76	1.17	6.10	0.051	83.5	2.35	0.73	0.88	6.48	0.056	86.8
BRM (resin)	4.60	0.61	1.56	7.00	0.056	79.9	3.35	0.71	1.25	5.80	0.05	87.4
BRM (latex)	3.75	0.64	1.27	7.10	0.065	91.5	2.72	0.66	1.01	7.29	0.064	87.6

Table 2.3. Analytical Results in Terms of Ultimate Axial Strain Increase (Di Ludovico et al., 2010)

	γ = 1						γ = 0.85					
Confinement Technique	$k_{2,M}$	R^2	ψ	$\Delta\varepsilon_{cc,u}$ (%)	SD	COV (%)	$k_{2,M}$	R^2	ψ	$\Delta\varepsilon_{cc,u}$ (%)	SD	COV (%)
GFRP	0.037	0.99	1.00	4.1	0.01	24.2	0.034	0.99	1.00	5.0	0.011	22.8
GFRP grid (mortar)	0.026	0.11	0.69	29.8	0.13	43.8	0.018	0.19	0.53	29.3	0.121	41.5
BRM (resin)	0.029	0.55	0.78	17.7	0.193	109	0.021	0.59	0.62	16.6	0.189	113.7
BRM (latex)	0.029	0.78	0.78	24.0	0.205	85.5	0.022	0.73	0.64	28.2	0.312	110.6

2.1.2.5. Ombres 2014. Ombres studied the effectiveness of polyparaphenylene benzobisoxazole (PBO) confinement on plain concrete prisms loaded under uniaxial monotonic compressive loading. Twenty small-scale, cylindrical concrete specimens were constructed and divided into two series based on the concrete mixture used (Series I cured for 120 days with compressive strength = 15.40 MPa and Series II cured for 270 days with compressive strength = 29.26 MPa). The confinement system included bidirectional PBO fibers (elastic modulus = 270 GPa and tensile strength = 5,800 MPa) and a cement-based matrix (compressive strength = 30.40 MPa and elastic modulus = 6.10 MPa). Parameters in this study included the number of fiber layers (ranging from 1-4 layers) and fiber orientation (θ = 30°, 45°, or 90° relative to the column cross section).

The failure modes observed included a combination of PBO sheet rupture and debonding at the fiber-matrix interface or a reduction in confining action due to damages to the confining jacket at the ends. The failure modes were dependent on the concrete compressive strength and fiber orientation. The author found that the peak stress increased for all confinement configurations while increasing with the number of PBO layers. The peak stress was influenced by the unconfined concrete compressive strength in which the confining action of the jackets was more apparent with lower strength concrete. The author also found that the stress increase was more prominent for specimens confined fibers oriented at 90° than those confined with fibers oriented at 30° or 45°.

Regarding hoop strains, the study demonstrated that these strains were non-uniform along the specimen height. Due to this, premature failure of the reinforcement occurred by local rupturing of the fibers. In terms of ductility, the author quantified this

using the “energy index” which was the area under the axial stress - axial strain curves until the ultimate stress point was reached. For the same concrete compressive strength, the ductility increased as the number of PBO layers increased. For the same number of PBO layers, the ductility decreased as the concrete compressive strength increased.

The author compared the experimental results to values predicted using existing models in literature for FRP confined concrete. Most models overestimated the peak stress of PBO-FRCM confined concrete. The models were ineffective in predicting the ultimate axial strain of the experimental specimens. In turn, the author developed a simplified model based on the experimental data to determine the normalized confining strength $\frac{f_{cc}}{f_{co}}$ shown in Eq. 2.20:

$$\frac{f_{cc}}{f_{co}} = 1 + 5.268\frac{f^*_{l,eff}}{f_{co}} \qquad \text{Eq. 2.20}$$

where:

f_{co} = unconfined compressive strength of concrete

$f^*_{l,eff}$ = effective lateral confining pressure taking fiber orientation into account shown in Equation 2.21

$$f^*_{l,eff} = k_e f_l = k_e k_\theta \rho_f E_f \varepsilon_f \qquad \text{Eq. 2.21}$$

k_e = strain efficiency coefficient

k_θ = fiber orientation coefficient shown in Eq. 2.22

$$k_\theta = \frac{1}{1 + 3\tan\theta} \quad \text{Eq. 2.22}$$

ρ_f = reinforcement ratio

$$\rho_f = \frac{4t_f}{D} \quad \text{Eq. 2.23}$$

t_f = thickness of fiber

D = specimen diameter

E_f = elastic modulus of fiber

ε_f = ultimate strain of fiber

2.1.2.6. Cascardi Longo Micelli Aiello 2017. The authors conducted a state-of-art review involving fiber reinforced mortar (FRM)-confined columns subjected to uniaxial compression. Two databases were developed by collecting data from the literature and then analyzed: one including 231 concrete specimens, and the other including 45 masonry specimens. Specimens in the database varied in terms of specimen geometry (sizes ranging from small-scale specimens to large-scale specimens; transverse cross-section al geometry included circular, square, and rectangular sections). The authors also focused on the type of fiber used in the FRM-confining systems including the use of basalt, carbon, glass, steel, and PBO. The elastic modulus of the fiber materials ranged from 52 GPa (basalt) to 270 GPa (carbon).

The authors used multiple linear regression analysis to determine the parameters that influenced the confining pressure. The parameters with the highest influence for

concrete specimens were the elastic modulus of the fiber, mechanical properties of the matrix material (elastic modulus and compressive strength), and the mechanical properties of the concrete. The authors concluded the use of inorganic matrix for FRM-confined concrete specimens resulted in increased cracking as the applied load increased, reducing the stress distribution from the column to the fiber jackets, ultimately decreasing the confining strength.

Cascardi et al. proposed a simplified model to determine the confined stress f_{cc} (Eq. 2.24), in which the fiber influence was considered as well as the strength and quantity of the matrix applied:

$$f_{cc} = f_{co}\left(1.0 + k'\left(\frac{f_{l,eff}}{f_{co}}\right)^{\frac{2}{3}}\right) \quad \text{Eq. 2.24}$$

where:

f_{co} = compressive strength of unconfined concrete

k' = non-dimensional coefficient shown in Eq. 2.25

$$k' = 4\rho_{mat}\frac{f_{c,mat}}{f_{co}} \quad \text{Eq. 2.25}$$

$f_{l,eff}$ = effective lateral pressure calculated using Eq. 2.26:

$$f_{l,eff} = \frac{nt_f E_f \varepsilon_f}{D'} \quad \text{Eq. 2.26}$$

ρ_{mat} = geometric percentage of the applied matrix in the FRM-system (Eq. 2.27):

$$\rho_{mat} = \frac{4t_{mat}}{D'} \quad \text{Eq. 2.27}$$

$f_{c,mat}$ = compressive strength of matrix material

n = number of confining layers

t_f = thickness of fiber

E_f = elastic modulus of fiber

ε_f = ultimate tensile strength of the fiber (ε_f = 0.004 mm/mm)

D' = diagonal dimension of rectangular cross-sectioned column

t_{mat} = (total) thickness of matrix

2.2. CONFINEMENT OF MASONRY

The following section describes existing technical literature that focuses on the effects of FRP and FRCM composites when used as confinement for masonry structures.

2.2.1. FRP Confinement Methods. In this section, investigations focused on masonry columns strengthened with FRP systems are discussed. Structural strengthening of masonry elements built with natural or man-made units is a common need. Compression members, such as columns, are prone to brittle failure under seismic loads or from overloading due to a change in occupancy. Traditional techniques include filling

cracks with grout, confining weak areas with brick elements or concrete regions, external post-tensioning of steel ties, and more (Krevaikas & Triantafillou, 2005). More recently, the use of FRP strengthening systems has been explored, including using fiber strips or sheets bonded externally to the masonry compression member.

This section discusses experimental and analytical investigations reported in literature that are focused on the use of fiber reinforced polymers as external or internal strengthening systems for masonry columns.

2.2.1.1. Krevaikas Triantafillou 2005. Research conducted by Krevaikas and Triantafillou (2005) studied the axial capacity of FRP confined masonry columns tested under uniaxial compression. Forty-two clay brick masonry column specimens were constructed and divided into four series based on the following parameters: number of fiber layers (1-3 or 5 based on FRP type), corner radius r (r = 10 or 20 mm), cross-sectional aspect ratio (ranged from 1:1 to 2:1 shown in Figure 2.6), and type of fiber (CFRP with elastic modulus = 230 GPa and tensile strength = 3,500 MPa; GFRP with elastic modulus = 70 GPa and tensile strength = 2,000 MPa). The specimens were analyzed in terms of axial stress-strain response and failure mode.

Krevaikas and Triantafillou concluded that FRP confined masonry behaves similar to FRP confined concrete in that the failure mode included vertical (axial direction of the column) cracks that widened followed by crushing of the substrate material. In this study, FRP jackets generally enhanced the strength and deformability of the masonry under axial load, but GFRP was more effective in deformability compared to the CFRP jackets. Other conclusions include the strength and strain capacity for

rectangular masonry columns was improved by increasing the corner radius or decreasing the cross-sectional aspect ratio.

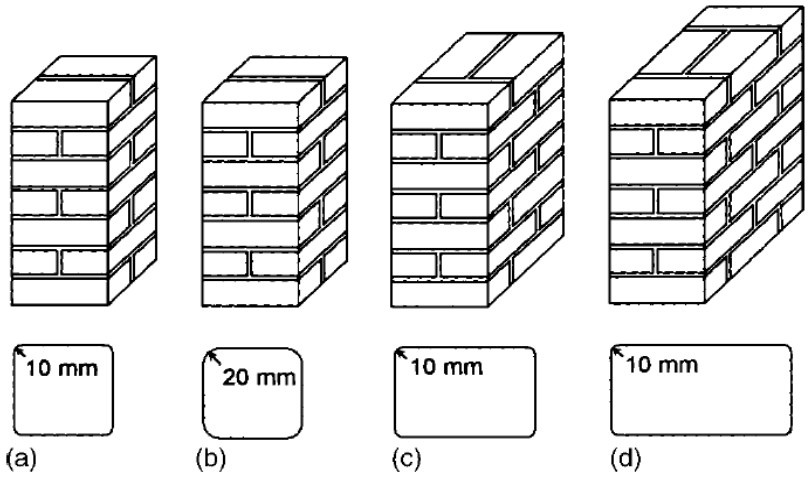

Figure 2.6. Configuration of Masonry Specimens tested: (a) Square Cross-Section, *r* = 10 mm, (b) Square Cross-Section, *r* = 20 mm, (c) Rectangular Cross-section with Aspect Ratio 1.5:1, *r* = 10 mm, (d) Rectangular Cross-Section with Aspect Ratio 2:1, *r* = 10 mm. (Krevaikas & Triantafillou, 2005)

The authors proposed a model determining the confined compressive strength of masonry, f_{mc} using the Equations 2.28-2.29:

$$f_{mc} = f_{mo}\,;\ if\ \frac{f_{l,eff}}{f_{mo}} \leq 0.24 \qquad \text{Eq. 2.28}$$

$$f_{mc} = f_{mo}\left(0.6 + 1.65\frac{f_{l,eff}}{f_{mo}}\right);\ \ if\ \frac{f_{l,eff}}{f_{mo}} \geq 0.24 \qquad \text{Eq. 2.29}$$

where:

f_{mo} = compressive strength of unconfined masonry

$f_{l,eff}$ = confining stress at failure (ultimate) given by equations found in Section 2.1.2.1

According to the model, the ultimate strain ε_{mc}, could be expressed as Eq. 2.30:

$$\varepsilon_{mc} = \varepsilon_{mo} + 0.034\frac{f_{l,eff}}{f_{mo}} \quad \text{Eq. 2.30}$$

where:

ε_{mo} = unconfined ultimate strain

2.2.1.2. Corradi Grazini Borri 2007. Corradi, Grazini, and Borri (2007) studied the effects of CFRP jackets on solid brick masonry columns. Twenty-four solid clay brick columns were divided into eight different series and tested under uniaxial compression. Variables focused on in this study included the cross-section geometry (square or octagonal), CFRP type (high-strength CFRP with elastic modulus = 417.6 GPa and tensile strength = 3,388 MPa or "very high modulus" CFRP with elastic modulus = 673.2 GPa and tensile strength = 1,955 MPa), and the number of fiber layers (1-2 fiber layers). The corners of square cross-sections were rounded to *r* = 20 mm to prevent fiber rupture caused by concentrated stresses. The authors evaluated the increase in compressive strength, the axial stress-strain response, and the failure mode of the columns.

In this study, the primary failure mode for columns with square cross-sections was the crushing of the masonry followed by the failure of the carbon fibers at the corners. Regarding both types of CFRP, the confinement strength and axial deformation capacity increased as well as column stiffness compared to the unconfined columns. The authors determined that the increase in capacity could be attributed to the rounding of the corners. The primary failure mode for the confined octagonal columns was due to transverse dilation which led to the crushing of masonry. With the use of high-ultimate tensile strength CFRP, a significant increase in confined strength and deformation was observed for both one and two layered specimens.

The authors proposed a simplified model to determine the confined compressive strength, f_{md}, shown in Eq. 2.31:

$$f_{md} = f_{mdo} + \left(k' * f_{l,eff}\right) \quad \text{Eq. 2.31}$$

where:

f_{mdo} = compressive strength of a "well-made wall"

$f'_{l,eff}$ = effective confinement stress computed using Eq. 2.32:

$$f_{l,eff} = k_e * f_l \quad \text{Eq. 2.32}$$

$$k_e = \frac{A_c}{A_m} \quad \text{Eq. 2.33}$$

k_e = effective confinement coefficient shown in Eq. 2.33

f_l = equivalent confinement stress

A_c = effective confined area

A_m = cross-sectional area of the masonry element

k_1 = confinement coefficient based on the material and typology of the applied reinforcement determined using Eq. 2.34:

$$\mathrm{k}' = k_{10} * \frac{f_{\mathrm{l,eff}}}{f_{m\mathrm{do}}}^{-\alpha} \qquad \text{Eq. 2.34}$$

α = shape parameter depending on the plastic characteristics of the material approximately -0.17 for masonry material

k_{10} = ideal confinement coefficient approximately 2.4 for masonry material

2.2.1.3. Aiello Micelli Valente 2007. The authors performed this study to understand the mechanical behavior of circular masonry columns confined with FRP and subjected to axial compression. Eighteen calcareous stone columns were constructed using two construction schemes and three different strengthening techniques. The strengthening techniques included using continuous and discontinuous (along the column longitudinal axis) CFRP wrapping (elastic modulus = 200 GPa and tensile strength = 1,800 MPa) and using transverse internal GFRP reinforcing bar (elastic modulus = 38.6 GPa and tensile strength = 879 MPa) throughout the cross-section. The GFRP reinforcing bars were used as internal confinement by drilling holes in the constructed columns and

bonded using epoxy paste. Another parameter varied was pre-cracking specimens to simulate pre-existing damage to the columns.

The authors concluded that the use of continuous CFRP sheets was more effective in column strengthening and axial deformability than discontinuous wrapping. Regarding the discontinuous strengthening technique, the use of three, 100 mm wide sheets showed higher increases in mechanical properties than two, 150 mm wide sheets. The authors noted that the damage caused by overloads applied in the pre-cracking stage before strengthening did not reduce the mechanical properties of the FRP confined columns.

The authors used the design equations proposed by the Italian Council of National Research (2004) to compare with the experimental results for this study. It was concluded that the use of these equations provided conservative results for continuously wrapped columns, unconservative results for discontinuously wrapped specimens, and reasonably consistent results for the GFRP strengthened specimens. The equation used for determining the confined strength for columns given by CNR-DT 200 (2004) is:

$$f_{mc} = f_{mo} + k' * f_{l,eff} \qquad \text{Eq. 2.35}$$

where:

f_{mo} = characteristic strength of unconfined masonry

k' = hardening factor for compressive strength using Eq. 2.36

$$k' = \frac{g_m}{1000} \qquad \text{Eq. 2.36}$$

g_m = specific weight of masonry

$f'_{l,eff}$ = effective lateral pressure of masonry column shown in Eq. 2.37

$$f_{l,eff} = k_H k_V f_1 \quad \text{Eq. 2.37}$$

k_H = horizontal coefficient of efficiency

k_V = vertical coefficient of efficiency

$$f_l = \frac{1}{2}\rho_f E_f \varepsilon_{fd,rid} \quad \text{Eq. 2.38}$$

ρ_f = reinforcement ratio calculated using Eq. 2.39:

$$\rho_f = \frac{4t_f b_f}{Dp_f} \quad \text{Eq. 2.39}$$

b_f = width of FRP strips along the vertical direction

t_f = thickness of FRP

E_f = Elastic modulus of FRP

ε_f = circumferential FRP strain

D = diameter of the column

p_f = distance between two successive FRP strips measures by two axes

2.2.1.4. Aiello Micelli Valente 2009. Aiello, Micelli, and Valente (2009) studied the effectiveness of GFRP systems on strengthening clay brick and calcareous unit columns subjected to uniaxial compressive load. Thirty-three square prismatic specimens [250 mm (width) x 250 mm (depth) x 500 mm (length)] were constructed using either clay brick units (compressive strength = 23.26 MPa) or calcareous units (compressive strength = 13.61 MPa). Variables focused on in this study were strengthening scheme (external reinforcement using unidirectional GFRP sheets, internal GFRP bars with varied spacing, or a combination of external and internal reinforcement), column corner radius *r* (*r* = 10 mm or 20 mm), construction scheme (hollow-core or full-core specimens), and material of masonry units (calcareous or clay brick units).

The experimental results indicated that the most effective strengthening scheme was a combination of external GFRP reinforcement with internal reinforcement spaced less than the maximum allowed by ACI 440 - 2004. These specimens provided a significant increase in confining strength and axial deformability. It was found that the effectiveness of FRP confinement was dependent on the materials used as the substrate and that the FRP was more effective with materials of lower compressive strength. Regarding the quantity of GFRP used, as the quantity of GFRP (sheets or bars) increased, the column compressive strength increased. Also, the corner radius significantly affected the behavior of columns in that as the radius increased the column compressive strength increased. Lastly, the authors determined that the GFRP reinforcement was more efficient on hollow-core columns when compared to full-core columns.

Using the experimental results obtained, the authors calibrated models developed by CNR-DT 200 (2004) and Krevaikas and Triantafillous (2005) to predict the strength

of FRP confined masonry columns. The study showed that equations reported by CNR-DT 200 (2004) were reliable in describing the behavior of the FRP confined specimens even with several parameters being varied. Regarding the model developed by Krevaikas and Triantafillous, the model did not agree well with the experimental results due the relationship between the confined strength and the lateral pressure, which varied in terms the substrate material and construction scheme for which model was originally calibrated.

2.2.1.5. Di Ludovico D'Ambra Prota Manfredi 2010. Research reported by the authors in 2010 studied the effectiveness of FRP confinement on Tuff unit and clay masonry brick columns. Tuff units were researched due to their use in historic construction in Western Europe. Eighteen prismatic columns with square cross sections were tested under monolithic compression until failure. The parameters varied in this study were the column material (Tuff units or Clay brick shown in Figure 2.7) and the FRP fiber applied (GFRP with elastic modulus = 69 GPa and tensile strength = 1,371 MPa, CFRP with elastic modulus = 228 GPa and tensile strength = 3,377 MPa, or BFRP with elastic modulus = 91 GPa and tensile strength = 1,814 MPa). It is important to note that the Tuff unit columns were considered to have a hollow core due to the material within being non-homogeneous, shown in Figure 2.7 (a).

The experimental outcomes showed that GFRP and CFRP wraps led to similar compressive strength gains on tuff masonry columns. For clay brick columns, GFRP and BFRP systems led to similar compressive strength gains, however BFRP was found to be more effective in terms of ultimate strain gained, even though its mechanical external reinforcement ratio was lower than GFRP. Comparing the performances of tuff and clay

brick specimens, the overall effectiveness of FRP wrapping was more significant on clay brick than tuff masonry.

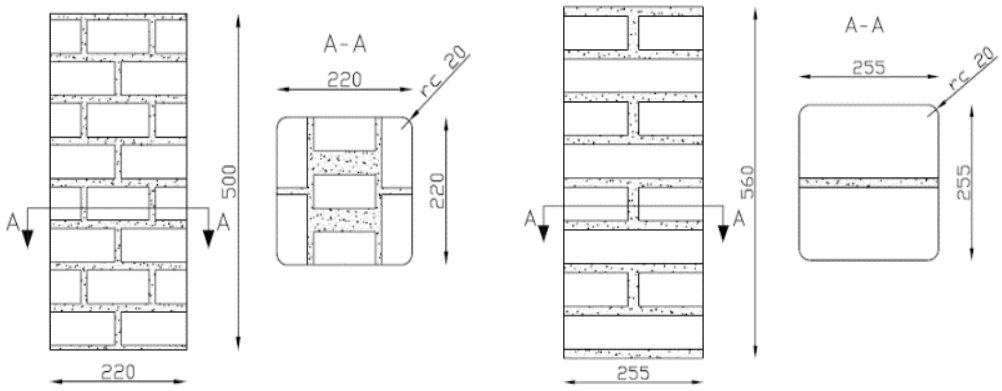

(a) (b)

Figure 2.7. Column Cross-section, (a) Tuff Unit Columns, (b) Clay Brick Columns

The authors also performed a comparative study using analytic models found in the CNR-DT 200 (2004) to determine the compressive strength of confined masonry columns, f_{mc}. Through this study, the authors determined values for the ideal confinement coefficient (k_1) and the shape parameter depending on the plasticity characteristics of the material (β), ultimately to determine the value of a non-dimensional coefficient (k'). The following general expression (Eq. 2.40) was used to determine the compressive strength:

$$f_{mc} = f_{mo} * (\alpha + k' * \frac{f_{l,eff}}{f_{mo}}) \qquad \text{Eq. 2.40}$$

where:

f_{mo} = compressive strength of unconfined masonry

$f_{l,eff}$ = effective lateral pressure calculated using Eq. 2.41

α = non-dimensional coefficient

k' = non-dimensional coefficient (Eq. 2.42)

$$f_{l,eff} = k_H k_V f_1 \quad \text{Eq. 2.41}$$

$$k' = k_1 \left(\frac{f_{l,eff}}{f_{m0}}\right)^{\tau} \quad \text{Eq. 2.42}$$

k_H = horizontal coefficient of efficiency (using the same formulation for k_e in Equation 2.8)

k_V = vertical coefficient of efficiency (equal to 1.0 for continuously confined specimens)

k_1 = ideal confinement coefficient

τ = shape parameter based on plastic characteristics of the material

f_1 = lateral confinement pressure determined using Eq. 2.43

$$f_l = \frac{b+d}{b*d} t_f E_f \varepsilon_f \quad \text{Eq. 2.43}$$

b = column width

d = column depth

t_f = thickness of FRP

E_f = elastic modulus of FRP

ε_f = circumferential FRP strain

Calibrating the equations with the gathered data, Table 2.4 indicates the non-dimensional coefficient *k'*, determined for tuff and clay brick columns and the refined equations to predict strength gains of confined masonry columns.

Table 2.4. Refined Equations Proposed by the Writers to Predict Strength Gains of Confined Masonry Columns

Material	Analytical expression
Tuff	$f_{mc} = f_{m0} \cdot \left(1 + k' \cdot \frac{f_{l,\text{eff}}}{f_{m0}}\right)$ where $k' = 1.09 \cdot \left(\frac{f_{l,\text{eff}}}{f_{m0}}\right)^{-0.24}$
Clay brick	$f_{mc} = f_{m0} \cdot \left(1 + k' \cdot \frac{f_{l,\text{eff}}}{f_{m0}}\right)$ where $k' = 1.53 \cdot \left(\frac{f_{l,\text{eff}}}{f_{m0}}\right)^{-0.10}$

2.2.1.6. Borri Castori Carradi 2011. Borri, Castori, and Carradi (2011) studied the application of unidirectional steel fiber reinforced polymer (SRP) as a means of increasing the capacity of masonry columns. Twenty-three clay masonry columns were subjected to uniaxial monotonic compressive loading. Of the 23 specimens, 13 had an octagonal cross-section and 10 had a square cross-section. Other parameters varied include the steel cord type and the reinforcement scheme. The first type of steel cord

(elastic modulus = 160 GPa and tensile strength 3,199 MPa) included three steel filaments wound together by a single external filament of a smaller diameter. The second type (elastic modulus = 143 GPa and tensile strength 2,396 MPa) resulted from twisting five individual filaments together using three straight filaments wrapped by two filaments at a high twist angle. Columns were wrapped either continuously or discontinuously using three, 100 mm wide fiber strips.

The investigation of the columns was in terms of axial stress-strain relationships and failure mode. The failure mode of the square columns was rupture of the SRP jacket after masonry crushing. For the octagonal columns, the failure mode was due to progressive transversal dilation followed by failure of the sheets. Figure 2.8 shows the idealized dilation of the cross-sections under investigation. Regarding the reinforcing scheme, the authors concluded that continuous wrapping was effective in terms of increasing both strength and deformation capacity. For both square and octagonal columns, Type 1 steel cords provided larger strength and deformation increases.

The authors provided analytical formulations to predict the behavior of the strengthened columns including the design compressive strength (f_{mcd}) for confined masonry columns. The formulations were based on the CNR-DT 200 (2004) model and revealed good agreement between the experimental data and theoretical predication for the corresponding load-carrying capacity.

2.2.1.7. Borri Castori Corradi 2013. Research reported by the authors in 2013 studied the effectiveness of steel cords (with and without epoxy resin) to strengthen masonry columns. Forty-eight solid clay brick columns were constructed and divided into four series.

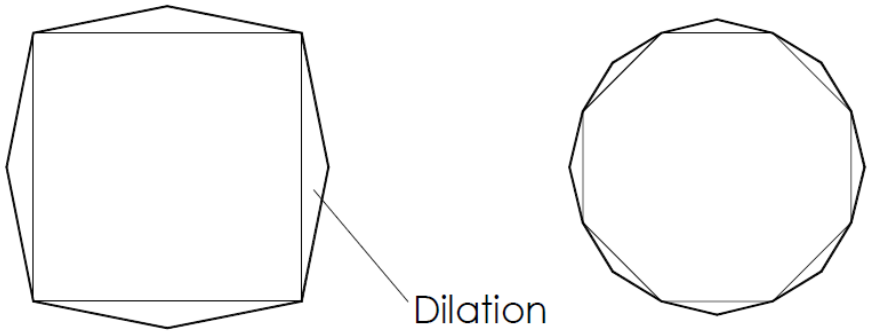

Figure 2.8. Idealized Dilation of Square and Octagonal Cross-sectioned Columns

The series were varied based on the parameters which included the cross-sectional aspect ratio, strengthening scheme, and the application of the steel cords. The cross-sectional aspect ratio ranged from 1:1 to 2:1 and varied between rectangular and octagonal cross-sections. The strengthening schemes included in this study were the use of continuous or discontinuous SRP, or hooping with steel cords. The types of steel cords used varied between three types; Type 1 was made by twisting three ultra-high-strength steel filaments together at a longer than usual lay length and then overwrapping the bundle with a single filament. Types 2 and 3 were made by twisting 49 and 19 stainless steel filaments together, respectively. The mechanical properties of the steel cords are summarized in Table 2.5. The final parameter varied was the application procedure of the steel cords, where some were pre-tensioned.

Regarding the experimental outcomes for octagonal specimens, both continuous and discontinuous wrapping schemes provided similar compressive strength increases

and ultimate displacements, with displacements being approximate three times that of the unconfined specimens.

Table 2.5. Mechanical Properties of Reinforcement

	High-strength steel cord	Stainless steel cords	
Property	Type 1	Type 2	Type 3
Cord Diameter (mm)	1.02	1.60	3.00
Cross-sectional area (mm^2)	0.561	0.904	5.372
Elastic Modulus (MPa)	143,000	73,500	117,000
Tensile Strength (MPa)	2,396	1,470	1,211
Strain to Failure (%)	1.16	2.00	1.03

For square columns, the continuous wrapping scheme provided greater strength gains when compared to the discontinuous wrapping. For rectangular columns, overall continuous and discontinuous strength and ultimate displacement gains were lesser than those of square and octagonal specimens. In addition, columns strengthened by steel hooping exhibited lower mechanical properties but did provide effective confining results. Lastly, the authors determined that pre-tensioning of the steel cords appeared to have a nontrivial influence on the column behavior.

2.2.1.8. Fossetti Minafò 2016. Fossetti and Minafò (2016) studied the compressive behavior of masonry columns reinforced with different strengthening systems and tested under uniaxial compression. Sixteen masonry columns [230 mm (width) x 230 mm (depth) x 930 mm (length)] were constructed using solid clay bricks

and varying grades of mortar. The parameters focused on in this study were the masonry mortar types [low strength mortar (compressive strength = 0.55 MPa) and medium strength mortar (compressive strength = 4.54 MPa)] and strengthening techniques used (using CFRP, B-FRCM, and steel wires). The FRP system included one ply of unidirectional carbon fibers (elastic modulus = 240 GPa and tensile strength = 4,100 MPa) bonded with an epoxy resin. Characteristics of the specimens confined with B-FRCM and steel wire are discussed in Section 2.2.2.5.

Regarding the FRP confined specimens, the experimental results indicated that the confinement efficiency depended on the masonry mortar grade and that the FRP system was effective for low-grade masonry mortar specimens. The behavior of FRP confined columns was characterized by a long initial stage in which the column sustained large loads. After the "half-peak load", delamination initiated between external wrap and the masonry column. After the peak load, failure occurred due to FRP tensile rupture at the column corners followed by compete crushing of the masonry core in a brittle manner. FRP confined systems provided an increased strength enhancement as the mortar compressive strength decreased. FRP confined columns with low-strength mortar provided an increase of nearly four times the unconfined strength. Regarding energy absorbed, specimens confined by FRP provided a substantial increase averaging 505% compared to the unconfined specimens. This increase was attributed to the increased peak stress and ascending branch of the axial stress-strain relationship.

The authors also compared the experimental results with predicted values calculated using models available in literature. The models used to predict the confined strength of specimens were developed by Campione and Miraglia (2003), Krevaikas and

Triantafillou (2005), Corradi et al (2007), Di Ludovido et al (2010), and CNR-DT 200 (2013). The process in which Krevaikas and Triantafillou (2005), Di Ludovido et al (2010), and CNR-DT 200 (2013) were developed is discussed in Section 5.3. It was found that the expressions available resulted in conservative predictions of the confined strength with respect to the experimental results obtained. The model that provided the best agreement was developed by Corradi et al. (2007) for FRP confined members.

2.2.2. FRCM Confined Masonry. As discussed in Section 2.2.1, a common strengthening technique used for masonry compression elements includes the use of FRP systems. These systems provide high strength-to-weight ratios, however the system does not have good compatibility with masonry substrates. A solution to this issue is to replace the organic matrix with an inorganic matrix material, such as cement-based mortar, which provides good compatibly with masonry and can be applied onto wet substrates. This system, called fiber reinforced cementitious matrix composites, is ideal for the preservation of historical masonry structures.

This section describes investigations reported in the literature that are focused on the strengthening of masonry columns using FRCM composite systems, many in comparison to their FRP counterparts.

2.2.2.1. Carloni Mazzoti Savoia Subranmaniam 2014. Research reported by the authors in 2014 investigated the influence of FRCM confinement and the brick patterns on the load-carrying capacity of confined columns subjected to uniaxial compression. This study was divided into two experimental works: the first to study the effects of the confining system, and the second to study the effects of the brick patterns. For the first study, six columns comprised of six bricks placed directly on the other were

constructed. Three of the columns were wrapped with a single layer of PBO-FRCM using an inorganic matrix. Regarding the second study, 18 columns were constructed using three different construction schemes. The columns were constructed with varying the aspect ratio (1:1, 1.5:1 and 2:1 shown in Figure 2.9) and wrapped with a single layer of PBO-FRCM with a 100 mm overlap length on one column face.

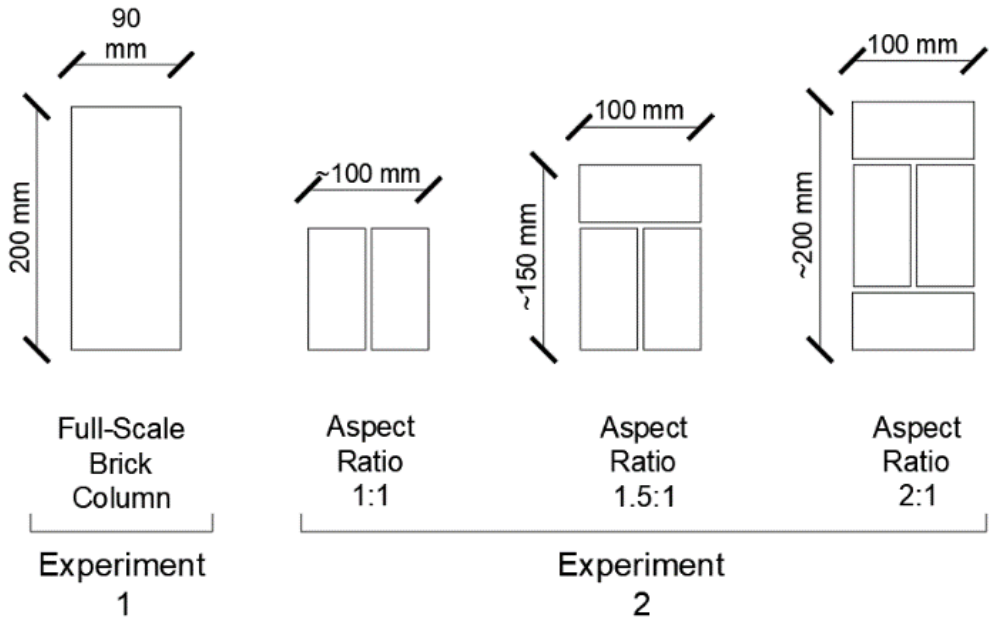

Figure 2.9. Brick Construction Configuration (Carloni et al., 2013)

Experimental results regarding the effectiveness of the FRCM system (Experiment one) showed that for the confining configuration used, the reinforcement did not significantly enhance the load-carrying capacity under axial load. Failure of the control specimens failed in a brittle manner, while the confined specimens failed due to

rupture of the fibers and the formation of cracks at the fiber overlap. The effects of the construction scheme (Experiment Two) were more evident and showed that the brick pattern affected the load-carrying capacity significantly due to the presence of mortar joints. The failure mode of the confined columns was the formation of vertical cracks at the fiber overlap followed by fiber rupture at the corners and slippage of the fibers within the inorganic matrix.

Regarding the axial stress – strain response, the curves of confined specimens featured a softening branch after the peak load due to the slippage of the fibers within the matrix. The curves also indicated that they were dependent on the cross-sectional aspect ratio. After column failure, arching effect was observed for columns with aspect ratios of 1:1 and 1.5:1. Columns with an aspect ratio of 2:1 did not show clear arching effect (Figure 2.10). As shown in Figure 2.11, the cracking patterns in the transverse and longitudinal direction were influenced by the presence of vertical mortar joints. The authors concluded that the compressive strength of confined specimens may be controlled by slippage of the fibers and that longer overlaps may be required for future tests.

Figure 2.10. Representative Cross-sectional Crack Pattern of Specimens, (a) Square 1:1, (b) Rectangular 1.5:1, (c) Rectangular 2:1 (Carloni et al., 2013)

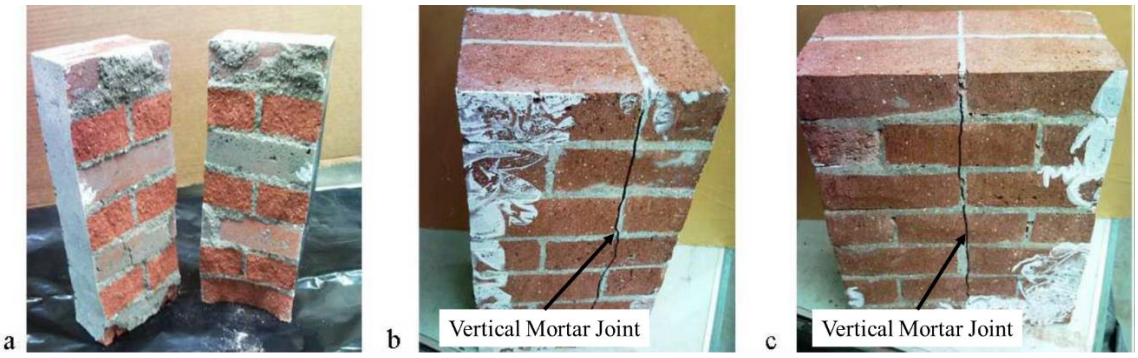

Figure 2.11. Images of Unconfined Specimens, (a) Square 1:1, (b) Rectangular 1.5:1, (c) Rectangular 2:1 (Carloni et al., 2013)

2.2.2.2. Ombres 2015. In this study, the author analyzed the effectiveness of carbon fiber reinforced cementitious matrix (C-FRCM) composite as a confinement system for masonry columns in terms of structural response, geometric parameters, and mechanical parameters. Five masonry columns were tested under concentric and eccentric axial loading until failure. Two columns were unconfined and used as control specimens. Two of the remaining columns were confined with one layer of C-FRCM (elastic modulus = 240 GPa and tensile strength = 4,800 MPa) and the other column was confined with two layers of C-FRCM. The parameters varied included the number of confining layers and the eccentricity of the applied load. The eccentricities (e) considered were $e/H = 0$ (concentric loading) and $e/H = 0.20$, with H being the height of the section. Of the specimens, one unconfined column and one column confined with a single layer of FRCM were tested under concentric loading conditions while the remaining were tested under eccentric loading conditions.

Regarding the specimens tested under concentric conditions, the failure mode of the confined specimens was rupture of the fibers due to significant lateral expansion of

the masonry. The confinement system provided an increase in strength, lateral deformation, and axial deformation compared to the control specimen. Overall, the confinement system was effective by improving the masonry column's ductility. Regarding the specimens tested under eccentric conditions, the columns confined by one and two C-FRCM layers failed due to fiber rupture at the corners. It was observed that the failure mode of the confined specimens due to fiber rupture was gradual, unlike the unconfined specimens which showed a brittle failure. The author found that as the confinement ratio increased, so did the confinement effectiveness in terms of increasing the column strength and lateral displacement.

2.2.2.3. Cevallow Olivito Codispoti 2015. The authors performed an experimental investigation to determine the effectiveness of flax fiber reinforced cementitious matrix (Flax-FRCM) composite and polyparaphenylene benzobisoxazole fiber reinforced cementitious matrix (PBO-FRCM) composite on solid clay brick columns loaded under eccentric compression. Twenty-seven masonry columns were constructed using three different construction configurations. Eighteen of the specimens were unreinforced, nine of which were loaded concentrically, while the remaining nine were loaded eccentrically. The remaining nine specimens were pre-damaged using extreme eccentric loading and later repaired using FRCM on the extreme tensile side. The parameters varied included the column construction configurations and the type of FRCM repair system used. The construction configurations (see Figure 2.12) included the following: Type "P": five bricks were piled on top of each other. Type "M": 40 bricks using a Flemish bond. Type "C": 34 bricks built using two bricks per row. The types of bidirectional FRCM used were Flux-FRCM (elastic modulus = 4 GPa and tensile strength

= 292 MPa) and PBO-FRCM (elastic modulus = 155 GPa and tensile strength = 3,730 MPa).

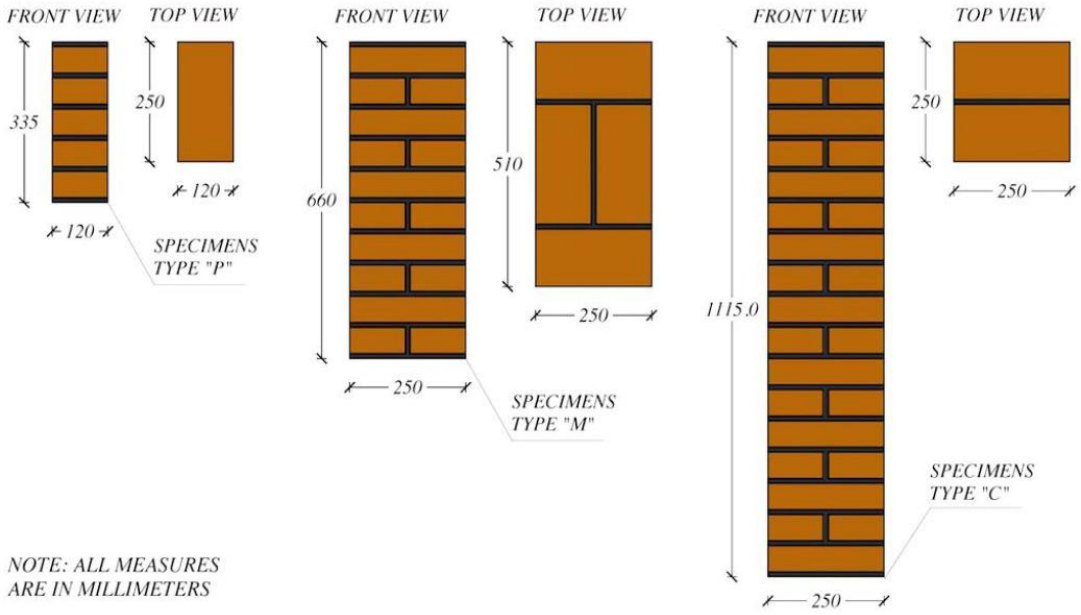

Figure 2.12. Construction Configuration of Tested Specimens (Cevallos et al., 2015)

The authors analyzed the results in terms of failure mode, load-displacement relationships, and moment-curvature responses. The failure mode of the eccentrically loaded unreinforced specimens was debonding of the mortar/brick at a mortar joint due to the formation of finer detachment fractures on the compressed surface. In general, both FRCM systems studied distributed the load and increased the column's load-bearing capacity. Columns strengthened with flax fibers exhibited a more ductile behavior and lower stiffness than those strengthened with PBO fibers, improving the deformation

capacity of the repaired elements. Flax-FRCM composites released the absorbed energy through the formation of cracks in the matrix, preventing debonding and improving the ductility of the masonry element. Columns strengthened with PBO-FRCM composite produced a lower strain capacity, which effected the ductility of the strengthened column. The lower strain capacity allowed for an increase in stresses between the composite and masonry substrate which led to debonding of the strengthening system.

2.2.2.4. Campione Cavaleri Papia 2016. Campione, Cavaleri, and Papia (2016) investigated the effectiveness of internal steel reinforcement on the compressive behavior of masonry columns under concentric and eccentric loading conditions. Twenty-six clay brick columns were tested of which 11 specimens were unreinforced, while the remaining 15 were reinforced with one or two layers of steel grid applied in the horizontal mortar joints during the construction phase. The specimens were constructed using solid clay brick and cement mortar with the following dimensions: 250 mm (width) x 250 mm (depth) x 400 mm (length). Variables focused on in this study included the number of steel grids applied [1 or 2 grids (f_y = 700 MPa) with no additional mortar between layers, shown in Figure 2.13] and the loading scenario (concentric loading (e = 0) or eccentric ($e = b/6$, b being the width of the column)).

The unconfined, concentrically loaded specimens exhibited a failure mode of masonry crushing after the formation of large vertical cracks along the length of each column face. The confined specimens loaded concentrically failed due to the formation of fine cracks that did not form at the vertical mortar joints. The authors determined that the energy dissipated from reinforced specimens increased with respect to the unconfined specimens.

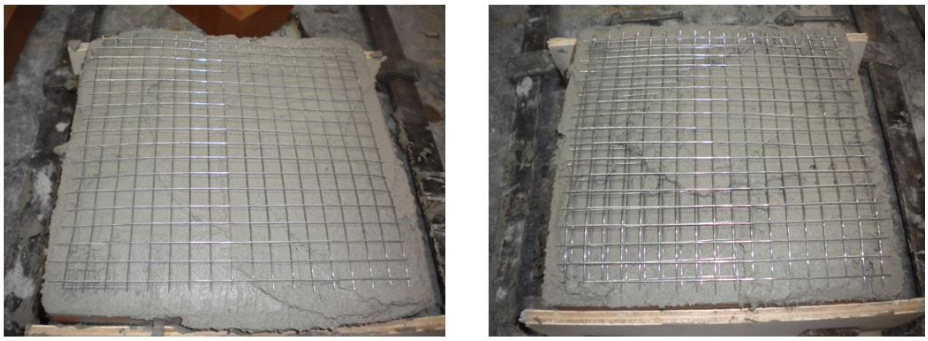

(a) (b)

Figure 2.13. Steel Grid Configuration (Campione et al., 2016)

Eccentrically loaded columns produced drastically different failure modes when compared to concentrically loaded specimens. Unconfined columns produced large vertical cracks through the mortar joints and finer cracks beneath the applied load. Specimens confined with one steel grid layer developed cracks beneath the applied load near the mortar joints while specimens confined with two steel grid layers developed cracks beneath the applied load near both the mortar joints and the column's edge. The results for both concentric and eccentric compressive tests indicated that the effectiveness in terms of flexural rigidity and bearing capacity increased as the number of steel grids increased. Figure 2.14 shows the axial load - axial shortening curves for eccentrically loaded masonry columns. The curves in Figure 2.14 show that the bearing capacity increased as the quantity of steel grids used increased.

2.2.2.5. Fossetti Minafò 2016. Fossetti and Minafò (2016) studied the compressive behavior of masonry columns reinforced with different strengthening systems tested under uniaxial compression.

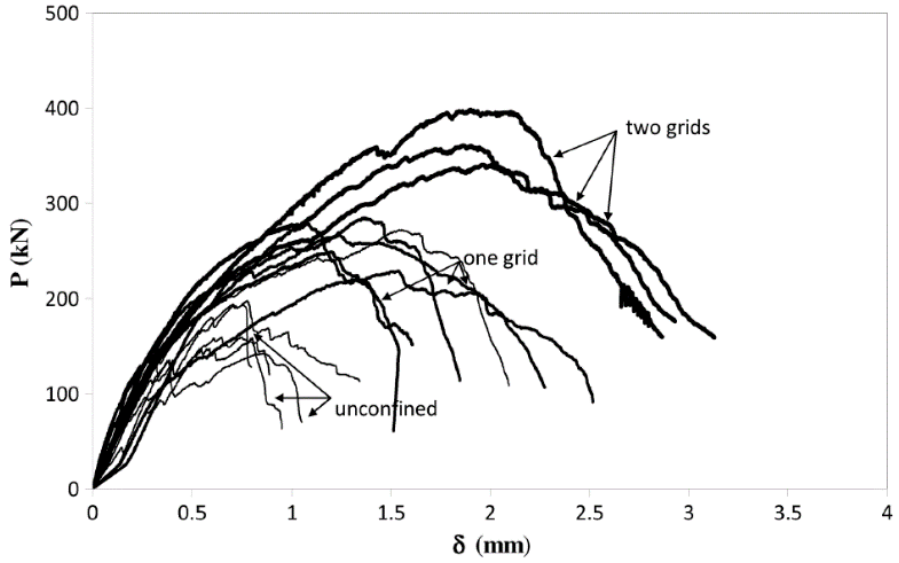

Figure 2.14. Load-Axial Shortening Curves for Eccentrically Loaded Masonry Columns (Campione et al., 2016).

Sixteen masonry columns [230 mm (width) x 230 mm (depth) x 930 mm (length)] using solid clay bricks and varying grades of mortar were included in this study. The parameters focused on in this study were the masonry mortar types [low strength mortar (compressive strength = 0.55 MPa) and medium strength mortar (compressive strength = 4.54 MPa) and strengthening technique (CFRP, B-FRCM, and steel wires). The strengthening techniques were as follows: one layer of bidirectional basalt mesh (elastic modulus = 90 GPa and tensile strength = 1,800 MPa) used with a high-strength cement-based mortar, reinforced with glass fibers, and the use of steel wires (diameter = 1.8 mm, elastic modulus = 200 GPa, tensile strength = 1,900 MPa) collaring each horizontal mortar joint. Characteristics of the specimens confined with FRP are discussed in Section 2.2.1.8.

The experimental results indicated that for each strengthening technique, the efficiency depended on the masonry mortar grade. All techniques were more effective for low-grade masonry mortar specimens. The authors determined that large strength increases could be obtained using FRP (Section 2.2.1.8), however this system produced brittle failure modes. The use of B-FRCM jacketing only provided effective strength enhancements for low-grade masonry specimens while the results for medium-grade masonry specimens were negligible. The failure mode of this system was debonding of the FRCM jacket from the masonry or the rupture of the basalt due to concentrated stresses at the corners. The steel wire strengthening technique provided significant increases in ultimate strain and absorbed energy, thereby enhancing the masonry columns ductility. The failure mode of this system was rupture of wires in the horizontal mortar joints due to the transverse dilation of the vertical cracks which propagation along the column length.

The authors compared the experimental results with predicted values calculated using models available in literature. The models used to predict the confining strength of specimens were developed by Campione and Miraglia (2003), Krevaikas and Triantafillou (2005), Corradi et al (2007), Di Ludovido et al (2010), and CNR-DT 200 (2013). The process in which Krevaikas and Triantafillou (2005), Di Ludovido et al (2010), and CNR-DT 200 (2013) were developed is discussed in Section 5.3. It was found that the expressions available resulted in conservative predictions with respect to the experimental results obtained, as shown in Table 2.6. The model that provided the best agreement was developed by Corradi et al. (2007) for FRP confined members, while

formulations developed by Di Ludovico et al. (2010) resulted in good predictions for B-FRCM confined specimens and columns collared with steel wires.

Table 2.6. Experimental vs. Predicted Results (Fossetti & Minafo, 2017)

	Experim	Campione and Miraglia		Krevaikas and Triantafillou		Corradi et al.		Di Ludovico et al.		CNR-DT 200 2013	
	f_{mc}/f_{m0}	f_{left}/f_{m0}	f_{mc}/f_{m0}	f_{left}/f_{m0}	f_{mc}/f_{m0}	f_{left}/f_{m0}	f_{mc}/f_{m0}	f_{left}/f_{m0}	f_{mc}/f_{m0}	f_{left}/f_{m0}	f_{mc}/f_{m0}
M1_F	3.73	0.25	1.50	0.75	1.84	0.75	2.90	0.75	2.18	0.18	1.71
M3_F	2.31	0.13	1.25	0.37	1.22	0.37	2.06	0.37	1.63	0.09	1.50
M1_BF	1.74	0.06	1.12	0.18	1.00	0.18	1.57	0.18	1.77	0.04	1.32
M3_BF	1.14	0.03	1.06	0.09	1.00	0.09	1.32	0.09	1.17	0.02	1.23
M1_SW	1.33	0.25	1.49	0.25	1.01	0.25	1.75	0.25	1.43	0.10	1.55
M3_SW	1.18	0.12	1.25	0.12	1.00	0.12	1.42	0.12	1.23	0.05	1.39

2.2.2.6. Cascardi Longo Micelli Aiello 2017. The authors conducted a state-of-art review involving FRM-confined columns subjected to uniaxial compression. Two databases were developed by collecting data from the literature and then analyzed: one including 231 concrete specimens, and the other including 45 masonry specimens. Specimens in the database varied in terms of specimen geometry (sizes ranging from small-scale specimens to large-scale specimens; transverse cross-section al geometry included circular, square, and rectangular sections). The authors also focused on the type of fiber used in the FRM-confining systems including the use of basalt, carbon, glass, steel, and PBO. The elastic modulus of the fiber materials ranged from 52 GPa (basalt) to 270 GPa (carbon).

The authors used multiple linear regression analysis to determine the parameters that influenced the confining pressure. The parameters with the highest influence for

masonry specimens were the elastic modulus of the fiber and the thickness of the matrix layers. The authors concluded the use of inorganic matrix for FRM-confined masonry specimens resulted in increased cracking as the applied load increased, reducing the stress distribution from the column to the fiber jackets, ultimately decreasing the confining strength.

Cascardi et al. proposed a simplified model to determine the confined stress f_{mc} (Eq. 2.44), in which the fiber influence was considered as well as the strength and quantity of the matrix applied:

$$f_{mc} = f_{mo}\left(1.0 + k'\left(\frac{f_{l,eff}}{f_{mo}}\right)^{0.5}\right) \quad \text{Eq. 2.44}$$

where:

f_{mo} = compressive strength of unconfined masonry

k' = effectiveness coefficient shown in Eq. 2.45

$$k' = 6\rho_{mat}\frac{f_{c,mat}}{f_{mo}} \quad \text{Eq. 2.45}$$

$f_{l,eff}$ = effective lateral pressure calculated using Equation 2.46:

$$f_{l,eff} = \frac{nt_f E_f \varepsilon_f}{D'} \quad \text{Eq. 2.46}$$

ρ_{mat} = geometric percentage of the applied matrix in the FRM-system:

$$\rho_{mat} = \frac{4t_{mat}}{D'} \qquad \text{Eq. 2.47}$$

$f_{c,mat}$ = compressive strength of matrix material

n = number of confining layers

t_f = thickness of fiber

E_f = Elastic modulus of fiber

ε_f = ultimate tensile strength of the fiber (ε_f = 0.004 mm/mm)

D' = diagonal dimension of rectangular cross-sectioned column

t_{mat} = (total) thickness of matrix

2.2.2.7. Santandrea Quartarone Carloni Gu 2017. The authors studied the behavior of square cross-sectioned masonry prisms confined by basalt and steel-FRCM composites subjected to a monotonic concentric compressive load. The analysis of the confinement effectiveness was in terms of load-bearing capacity with respect to the unconfined specimens. Twenty-one masonry columns were tested under concentric compressive loading. Of the 21 specimens, 6 were unconfined columns, while the remaining 15 were confined with an FRCM system. The parameters studied included the type of fiber used in the confining system and the column corner radius. The composite system was composed of fibers (steel or basalt) embedded in a hydraulic mortar matrix made of lime and mineral binder. The steel fibers (elastic modulus = 190 GPa and tensile strength = 3,000 MPa) were unidirectional sheets made of high-strength galvanized

twisted steel micro-cords held together by a glass fiber micro-mesh. The basalt fibers (elastic modulus = 70 GPa and tensile strength = 1,700 MPa.) were in the form of a balanced bi-axial mesh made of low-density basalt fibers spaced at 17 mm on-center in both directions. The corner radius for one of the confined series with basalt fibers was ground down to a 20 mm radius.

The results were analyzed in terms of the axial stress –strain behavior. All specimens showed a linear response until the peak load. After the peak load, the confined specimens continued to deform under decreasing applied load until failure. The unconfined specimen failure mode was brittle, indicated by wide longitudinal cracks along the full length of each column face. Regarding specimens confined with basalt fibers, the failure mode was rupture of the fibers after the formation of longitudinal cracks near the corners. On average, the basalt system did provide a slight increase in compressive strength when compared with the unconfined specimens. It was noted that nearly half of the specimens confined with basalt fibers had a compressive strength that was equal to or less than the average value of the control specimens, and therefore the effectiveness was unclear. For this series, the axial stress – strain response after the peak was similar to that of the unconfined specimens.

Regarding specimens confined with steel fibers, the failure mode observes was detachment of the FRCM jacket at the overlapping region. This system provided an average compressive strength increase of 33% compared to the unconfined specimens. The axial stress - axial strain response after the peak had a more gradual slope than the unconfined specimens.

2.2.2.8. Sneed Carloni Baietti Fraioli 2017. The authors investigated the effectiveness of steel reinforced grout (SRG) confining system on clay masonry columns subjected to monotonic concentric compressive load. Eighteen solid clay masonry columns with a square cross-section were analyzed in this study. The dimensions of each column were 250 mm (width) x 250 mm (depth) x 720 mm (length) using solid clay bricks bonded together using a natural hydraulic lime mortar (compressive strength determined through testing = 13.1 MPa). Fifteen of the specimens were confined with the SRG system, while the remaining three were unconfined for use as control specimens. Parameters focused on in this study were the density of the steel fiber jackets (elastic modulus = 205 GPa and tensile strength = 2,900 MPa, sheet densities of 670 g/m^2 and 1,200 g/m^2) and the column corner radius *r* (*r* = 0 mm, *r* = 9.5 mm, and *r* = 38.1 mm).

The authors analyzed the specimens in terms of the failure modes and the axial stress – axial strain relationships. Regarding the axial stress – axial strain response of unconfined columns, the initial response was linear. After the peak load, the response declined rapidly due to the brittle nature of the masonry columns. The axial stress – axial strain response of confined columns followed an initial linear response. After the peak load, the descending branch was non-linear and had a gradual slope, indicating an increase in column ductility.

The authors concluded that the application of SRG jackets increased the compressive strength of masonry columns compared to the unconfined specimens. The compressive strength of the confined specimens increased with increasing corner radius and fiber density. It is important to note that the increase in compressive strength did not appear to be proportional to the increase in fiber density.

2.2.2.9. Baietti 2017. The author investigated the effectiveness of steel reinforced grout (SRG) confining system on clay masonry columns subjected to monotonic concentric compressive load. This study was part of a larger project which included results found in Section 2.2.2.8. Nineteen solid clay masonry columns with a square cross-section were analyzed in this study. The dimensions of each column were 250 mm (width) x 250 mm (depth) x 720 mm (length) using solid clay bricks bonded together using a mineral mortar with a crystalline reaction geobinder base (compressive strength determined through testing = 47.1 MPa). Sixteen of the specimens were confined with the SRG system, while the remaining three were unconfined for use as control specimens. Parameters focused on in this study were the density of the steel fiber jackets (elastic modulus = 205 GPa and tensile strength = 2,900 MPa, sheet densities of 670 g/m^2 and 1,200 g/m^2) and the column corner radius r (r = 0 mm, 9.5 mm, and 38.1 mm).

The authors analyzed the specimens in terms of the failure modes and the axial stress – axial strain relationships. Regarding the axial stress – axial strain response of unconfined columns, the initial response was linear. After the peak load, the response declined rapidly due to the brittle nature of the masonry columns. The axial stress – axial strain response of confined columns followed an initial linear response. After the peak load, the descending branch was non-linear and had a gradual slope followed by a plateaued region until failure, indicating an increase in column ductility.

The author concluded that the application of SRG jackets increased the compressive strength of masonry columns compared to the unconfined specimens. The compressive strength of the confined specimens increased with increasing corner radius and fiber density. It is important to note that the increase in compressive strength did not

appear to be linearly proportional to the increase in fiber density. The primary failure mode for confined specimens was the separation of the fibers at the overlap along a limited portion of the column length. The results from the study were similar to those found in Section 2.2.2.8, indicating that the influence of the compressive strength of the matrix mortar had little effect on the results in terms of peak axial stress and ultimate axial strain.

3. EXPERIMENTAL PROGRAM

3.1. OVERVIEW

As discussed in Section 1.3.1, this study was part of a larger research project that aimed at understanding the behavior of unreinforced brick masonry columns confined with SRG jackets and subjected to a monotonic concentric compressive load. The test variables considered in the overall study included column corner radius, density of the steel fibers in the SRG jacket, number of confinement layers, and number of overlapping faces. For each combination of test parameters, four replicate specimens were built, resulting in a total of 55 specimens, including a series of seven control specimens. Thirty-one of the 55 total specimens are included in this thesis.

The SRG-confined specimens included in this thesis work all had the same density of steel fibers in the SRG jacket. Parameters that were the focus of this thesis work were the corner radius [either r = 0 (sharp corners) or r = 38.1 mm (rounded corners)]; the number of layers of confinement, (1, 2, or 3 for the sharp corner columns; 1 or 2 for the rounded corner columns); and number of overlapping layers (1 for the sharp corner columns; 1 or 2 for the round cornered columns with 1 layer of confinement; 1 for the round cornered columns with 2 layers of confinement).

All columns were designed to have the same nominal dimensions: 245 mm (width) x 245 mm (depth) x 705 mm (height), resulting in a height-to-side ratio of approximately 2.9. The cross-sectional dimensions are shown in Figure 3.1. The cross-sectional area of the masonry columns with sharp corners was A_m=60,025 mm^2, and the cross-sectional area of the columns with rounded corners was A_m=58,778 mm^2

After all specimens were constructed and allowed the allotted time to cure, half of the columns' corners were grinded, resulting in two different cross-sectional shapes: a square cross-section with a sharp corner radius of 0 mm and a rounded cross-section with a corner radius of 38.1 mm (Figure 3.1).

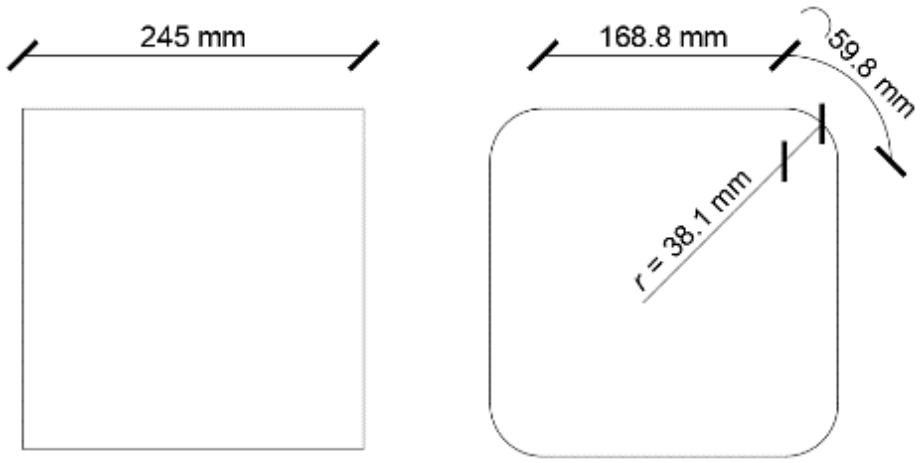

(a) (b)

Figure 3.1. Dimensions of Cross-Sections with (a) Sharp Corners, (b) Rounded Corners

As noted, seven columns were left unconfined and used as control specimens to define the increase in strength provided by the confinement. The unconfined specimens were named following the designation UC-Z:

- UC indicates that the specimen is unconfined;
- Z indicates the specimen number, 1, 2, 3, 4, 5, 6 or 7.

The confined specimens were classified according to the variables introduced previously, following the designation C-X-R-Y(a)-Z:

- C indicates that the specimen is confined;
- X differentiates the fiber fabric densities: 6 for GeoSteel G600, 12 for GeoSteel G1200;
- R differentiates the corner radii: 0 for r = 0 mm for sharp corner specimens, 38 for r = 38.1 mm for rounded specimens;
- Y differentiates the number of confinement layers, 1, 2, 3;
- a, where present, indicates that two overlapping faces were provided at the end of the jacket (unless noted, one overlapping face was provided);
- Z indicates the specimen number within a group: 1, 2, 3, or 4

Table 3.1 summarizes the specimens included in this thesis work:

The following sections summarize the materials (Section 3.2), fabrication of test specimens (Section 3.3), and experimental setup (Section 3.4). The general procedures described herein were conducted in the same time period (2017-2018) and by the same students. The construction and testing of the specimens took place in the High Bay Structural Engineering Research Laboratory in Butler-Carlton Hall at Missouri University of Science and Technology (Missouri S&T).

3.2. MATERIALS

This section provides details regarding the materials used in construction of the unreinforced masonry columns and the materials used for the SRG confinement system.

Table 3.1. Specimen Naming System and Test Variables

Group	Specimen	Composite Matrix	Composite fiber density (g/m^2)	Corner radius (mm)	Number of fiber layers	Number of overlapping faces
Control	UC-1	-	-	0	-	-
	UC-2					
	UC-3					
	UC-4					
	UC-5					
	UC-6					
	UC-7					
1	C-12-0-1-1	Lime-based Mortar	1,200	0	1	1
	C-12-0-1-2					
	C-12-0-1-3					
	C-12-0-1-4					
2	C-12-0-2-1	Lime-based Mortar	1,200	0	2	1
	C-12-0-2-2					
	C-12-0-2-3					
	C-12-0-2-4					
3	C-12-0-3-1	Lime-based Mortar	1,200	0	3	1
	C-12-0-3-2					
	C-12-0-3-3					
	C-12-0-3-4					
4	C-12-38-1-1	Lime-based Mortar	1,200	38.1	1	1
	C-12-38-1-2					
	C-12-38-1-3					
	C-12-38-1-4					
5	C-12-38-1(2)-1	Lime-based Mortar	1,200	38.1	1	2
	C-12-38-1(2)-2					
	C-12-38-1(2)-3					
	C-12-38-1(2)-4					
6	C-12-38-2-1	Lime-based Mortar	1,200	38.1	2	1
	C-12-38-2-2					
	C-12-38-2-3					
	C-12-38-2-4					

3.2.1. Masonry Columns. This section describes the materials used for the construction of the unreinforced masonry columns. Included for each material are its mechanical properties provided by the manufacturer and determined through laboratory testing as well as the test methods used.

3.2.1.1. Brick. The Rosso Vivo solid clay bricks used to construct the masonry columns were provided by San Marco – Terreal Italian Company. The brick units had nominal dimensions of 120 mm (width) x 55 mm (height) x 250 mm (length). Vivo brick is the first facing brick with a finish without sand on the surface (Figure 3.2). This finish is the result of the brick removal process from its mold in which sand is not used, leaving the surface clean. The bricks were selected to represent the behavior of historical masonry having lower mechanical properties than modern day brick.

Figure 3.2. *Rosso Vivo Brick,* San Marco - Terreal Italia Company

The physical and mechanical properties reported by the manufacturer (SanMarco) are summarized in Table 3.2. In addition, the compressive strength of the bricks was

determined from the average of 10 specimens tested in accordance with UNI EN 772-1 (2011), resulting in a coefficient of variation of 0.184 MPa.

Table 3.2. Brick Properties

Properties Reported by the Manufacturer[(1)]	
Dimensions (mm)	120 x 250 x 55
Unitary Weight (kg)	2.40 - 2.80
Compressive Strength (MPa)	18
Properties Determined by Testing	
Compressive Strength (MPa) (CoV)	20.8 (0.184)

Note (1): reported by manufacturer (San Marco)

3.2.1.2. Masonry mortar. The mortar used to bind the facing bricks was a natural plaster made with pure lime NHL (natural hydraulic lime) according to EN 459-1 (2015) (Figure 3.3). This mortar is highly breathable and protects masonry over time, making it ideal for use in historic restorations (Kerakoll, 2017).

The mixture proportions recommended by the manufacturer were 5.1 L of clean water per one 25 kg bag of mixture. However, in this study, 5.15 L of water was used for each mixture to achieve the propter mortar consistency. Following the manufacturer's instructions, the mortar was mixed by first adding the mortar into a cement mixer and then gradually adding the water. The mixing process was continued at a constant rate for five minutes or until the mixture was smooth. Each batch of mortar was sufficient to construct one column.

Figure 3.3. BioCalce Plaster Mortar

The compressive strength after 28 days provided by the manufacturer was greater than 1.5 N/mm^2 using the test method provided by EN 998-1 (2016) (Table 3.3). Compressive strength and splitting tensile strength tests were also determined experimentally for each batch of BioCalce mortar used to construct the masonry columns.

Table 3.3. Masonry Mortar Properties

Properties Reported by the Manufacturer[1]	
Density of Wet Mortar (kg/dm^3)	~1.61
Compressive Strength (28 day) (MPa)	1.5 - 5.0
Properties Determined by Testing	
Compressive Strength (28 day) (MPa)	3.4

Note 1: reported by manufacturer (Kerakoll)

Figure 3.4. BioCalce Mortar Cube

Compression tests were conducted on cubes (Figure 3.4) with dimension of 50.8 mm that were constructed using brass or steel cube forms (Figures 3.5). The forms were cleaned prior to their use with a steel wire brush and metal tools. Once the forms were assembled, the interior and top surfaces were lubricated using a generic form-oil to allow for easy form removal. The mortar was placed in the forms in two equal layers, each of which was consolidated using the rodding technique in accordance with ASTM C192-16a (2016). Each layer was consolidated using a 10 mm diameter rod, 25 strokes per layer. The cubes were finished using a smooth metal tool or trowel. The cubes remained in the forms for approximately 24 hours before they were removed. Once removed, the cubes were covered with a damp cloth and cured in controlled temperature and humidity conditions for 28 days. After the allotted time, the cubes were uncovered and left in the same room until they were tested. All cubes were tested for compressive strength in accordance with ASTM C109/C109M (2016).

Compression tests were performed in the Load Frame Laboratory in Butler-Carlton Hall at Missouri S&T using an 800 kN capacity servo-controlled Tinius Olsen, Universal Compression/Tension Machine with a data acquisition PC workstation (Figure 3.6). All cubes were tested at a rate of approximately 900 N/s.

Figure 3.5. Cube Formwork

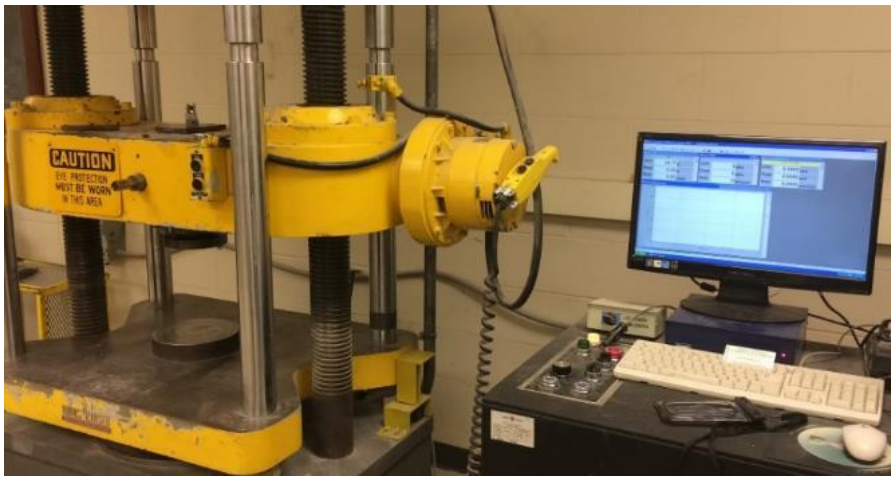

Figure 3.6. Tinius-Olsen Load Frame (Baietti, 2017)

Each cube was placed in the testing machine and centered below the loading head. A small gap was left above the cube prior to testing to prevent damage to the cube. The test began by applying a 100 N preload to the cube before the load was applied at a constant rate. The test completion was automatic once the cube failed and the load head returned to its original position. Figure 3.7(a-c) provides images of the basic phases during cube testing.

The peak load *P* (N) was recorded by the testing machine, and the compressive strength σ, was computed as:

$$\sigma = \frac{P}{A} \quad (MPa) \qquad \text{Eq. 3.1}$$

where "*A*" is the cross-sectional area of the cube in mm^2.

Then mean value of the peak compressive strength of the masonry mortar for each column was computed using the average value of the three cubes for each batch. The average compressive strength and the coefficient of variation (CoV) are reported in Table 3.4. Considering the 31 specimens included in this thesis work, the average compressive strength of the masonry mortar was 3.4 MPa (CoV = 0.185). Considering all 55 specimens included in the overall study (including those in this thesis work and those reported by Senesi 2018), the average compressive strength was also 3.4 MPa (CoV = 0.177). In both cases, the values exceeded the manufacturer's minimum value of 1.5 MPa (Table 3.3).

(a) (b)

(c)

Figure 3.7. (a) Compression Test Set-up, (b) Mortar Cube Compression Application, (c) Failure Mode

The splitting tensile strength was determined for some batches of masonry mortar. The splitting tensile strength was determined by the average of three 50.8 mm diameter, 101.6 mm long cylinders tested at a rate of approximately 90 N/s using the Tinius-Olsen Universal Compression/Tension Machine described previously. Masonry mortar cylinders were made in accordance with ASTM C192-16a (2016) using a nonabsorbent

plastic material as the mold. Similarly, to the cube construction, the interior of the mold was lubricated using form-oil to allow easy removal. The mortar was placed in the molds in two equal layers and consolidated using the rodding technique (Figure 3.8). Each layer required 25 strokes using a 10 mm diameter smooth rod. The cylinders were finished by rolling the smooth rod across the top in multiple direction until the surface was level and the access material was removed (Figure 3.9). The cylinders were not disturbed for approximately 24 hours before being removed from the molds. Once removed, each cylinder was numbered and placed next to its correlating column in an environmentally controlled space (Figure 3.10). The cylinders were covered with a damp cloth for 28 days prior to being tested. After 28 days, the damp cloths were removed, and the cylinders were left in the same space until tested.

Figure 3.8. Masonry Mortar Layering (Baietti, 2017)

The splitting tensile strength test was performed in accordance with ASTM C496 (2017). Each cylinder was marked with a line on its length and on one of the circular faces to aid in the test set-up.

Table 3.4. Masonry Mortar Compressive Strength

Group	Specimen	Average compressive strength (MPa)	CoV
Control	UC-1	3.4	0.242
	UC-2	3.7	0.080
	UC-3	2.9	0.121
	UC-4	3.8	0.243
	UC-5	3.5	0.316
	UC-6	3.2	0.233
	UC-7	3.7	0.207
1	C-12-0-1-1	3.9	0.074
	C-12-0-1-2	3.2	0.224
	C-12-0-1-3	3.1	0.238
	C-12-0-1-4	3.5	0.144
2	C-12-0-2-1	3.3	0.130
	C-12-0-2-2	3.0	0.170
	C-12-0-2-3	3.9	0.082
	C-12-0-2-4	2.7	0.351
3	C-12-0-3-1	3.7	0.141
	C-12-0-3-2	3.5	0.051
	C-12-0-3-3	3.4	0.241
	C-12-0-3-4	3.6	0.115
4	C-12-38-1-1	3.7	0.157
	C-12-38-1-2	4.2	0.232
	C-12-38-1-3	3.2	0.165
	C-12-38-1-4	3.7	0.592
5	C-12-38-1(2)-1	3.7	0.164
	C-12-38-1(2)-2	3.2	0.104
	C-12-38-1(2)-3	2.6	0.144
	C-12-38-1(2)-4	3.1	0.175
6	C-12-38-2-1	4.0	0.183
	C-12-38-2-2	3.7	0.101
	C-12-38-2-3	3.7	0.201
	C-12-38-2-4	2.8	0.064
Average (MPa)		**3.4**	**0.185**

Figure 3.9. Masonry Mortar Cylinder Construction

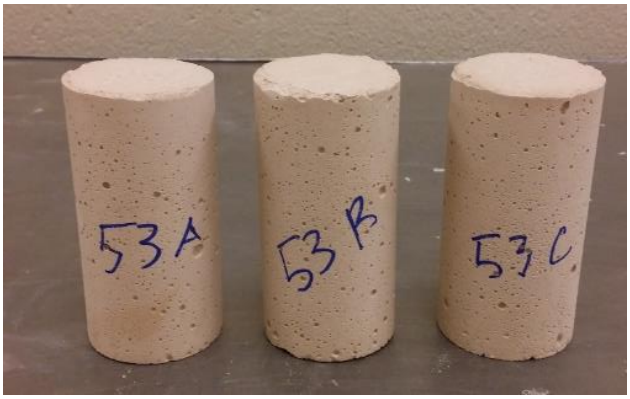

Figure 3.10. Masonry Mortar Cylinders

The specimen was placed on a plywood strip, lengthwise, within the testing machine. Another plywood strip was placed lengthwise at the top of the cylinder. The line marked on the circular face was aligned vertically, contacting the center of each plywood strip (Figure 3.11). Once aligned, a preload of 100 N was applied to the cylinder until the test was able to run at an approximate rate of 90 N/s. The test was complete once

a vertical crack formed across the full diameter of the specimen, splitting the cylinder in two pieces (Figure 3.12).

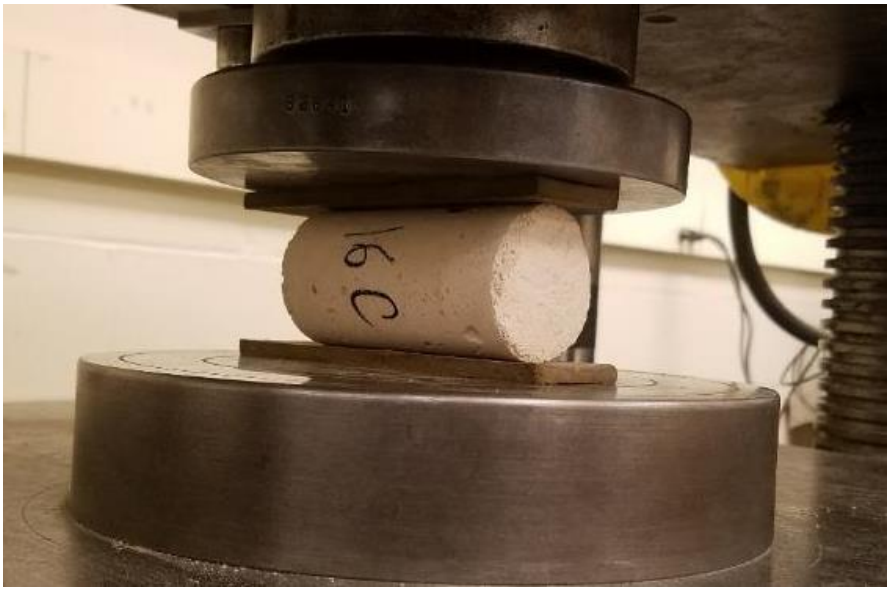

Figure 3.11. Splitting Tensile Test Set-up

Figure 3.12. Masonry Mortar Splitting Tensile Failure Mode

The splitting tensile strength *T*, was computed as:

$$T = \frac{2P}{\pi l d} \quad (MPa) \qquad \text{Eq. 3.2}$$

where:

P = maximum applied load indicated by the testing machine (N)

d = diameter of the cylinder equal to 50.8 mm

l = length of cylinder equal to 101.6 mm.

Mean values of the splitting tensile strength were computed on three cylinders per batch and the coefficient of variation are reported in Table 3.5. The average splitting tensile strength for all specimens tested was 0.39 MPa (CoV = 0.027).

Table 3.5. Splitting Tensile Strength

Specimen	**Average splitting tensile strength (MPa)**	**CoV**
C-6-0-1-1	0.25	0.018
C-6-0-1-2	0.42	0.054
C-6-0-3-1	0.33	0.006
C-6-38-1-1	0.45	0.015
C-6-38-1(2) -2	0.40	0.012
C-12-0-1-1	0.44	0.032
C-12-0-1-2	0.37	0.037
UC-5	0.43	0.045
Average (MPa)	**0.39**	**0.027**

3.2.2. SRG Composite. This section describes the steel reinforced grout (SRG) composite that was externally bonded to the unreinforced masonry columns. The SRG system in this study was composed of steel fiber sheets embedded within a lime-based mortar matrix. The composite material used in this study was produced by Kerakoll Company.

3.2.2.1. Steel fibers. As discussed in Section 3.1, different steel fiber sheet densities were considered in the overall research study that included this thesis work. In the overall study, two different steel fabrics were considered, namely GeoSteel G600 and GeoSteel 1200, consisting of the same fibers but different spacings resulting in different fiber densities. All confined specimens included in this thesis were confined with GeoSteel 1200. For completeness, both steel fabrics are described in this section.

GeoSteel is a unidirectional sheet made of extra-high strength galvanized steel micro-cords, fixed to a fiberglass micromesh to facilitate installation. Each steel chord is obtained by joining five filaments, of which three are straight and two are wrapped using a high torque angle. The cross-sectional area of the cord A_{cord}, was 0.538 mm^2. The galvanization of each wire protects the steel reinforcement from harsh environmental conditions allowing good mechanical and installation properties to be obtained. The sheets can be shaped using a bender provided by the manufacturers, allowing for easy application without altering the mechanical properties of the steel (Figures 3.13 and 3.14).

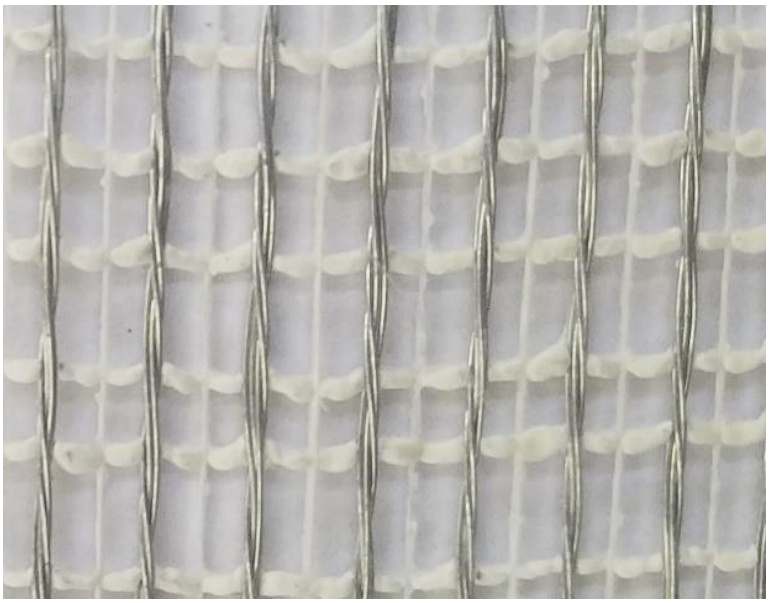

Figure 3.13. Close-up of GeoSteel G600

Figure 3.14. Close-up of GeoSteel G1200

The structural and mechanical properties guaranteed by GeoSteel Hardwire are higher than traditional carbon, glass, and aramid fabrics, and are particularly effective in applications for structural reinforcement and seismic upgrading. The fabric can be used with different composite matrices provided by Kerakoll Company including GeoLite Gel, GeoLite matrix, GeoCalce Fino, which is the one used in the present study. The main uses and characteristics of the GeoSteel fibers are:

- High durability, due to the galvanization process of the steel wires, tested in a chloride, freeze-thaw and high humidity environment;
- Structural strengthening of elements made of brick, natural stone, and tuff masonry when used with GeoCalce Fino. This combination allows for both breathability and high mechanical adhesion;
- Structural strengthening of elements made of reinforced concrete, pre-stressed reinforced concrete, and good consistency masonry when used with GeoLite;
- Structural strengthening of sections made of reinforced concrete, pre-stressed reinforced concrete, wood and steel when used with GeoLite Gel.
- No requirement of advanced impregnation of the sheet or particular precautions, it can be tensioned to create structural reinforcement, or anchored and fastened with metal plates;
- Easy to be shaped with GeoSteel Bender, without reducing the mechanical properties.

The geometrical and mechanical properties, as provided by the manufacturer, are summarized in Table 3.6:

Table 3.6. GeoSteel Geometric and Mechanical Properties Provided by the Manufacturer (Kerakoll, 2017)

	GeoSteel G600	**GeoSteel G1200**
Wire characteristic tensile stress	> 2900 MPa	> 2900 MPa
Wire Elastic Modulus	> 205 GPa	> 205 GPa
Sheet break deformation	> 2%	> 2%
n° of strands/cm	1.57 strands/cm	3.14 strands/cm
Sheet Density (including heat-sealing)	≈ 670 g/m^2	≈ 1200 g/m^2

3.2.2.2. Matrix. The mortar used as the composites matrix was GeoCalce F Antisismico (Figure 3.15). This mortar is a breathable, structural geo-mortar made from pure natural hydraulic lime (NHL) and geo-binder. This material is designed specifically to be used with GeoSteel galvanized steel sheets and is classified with M15 resistance according to EN 998-2 (2016). The matrix is ideal for use in historic renovations according to Kerakoll.

The physical and mechanical characteristics provided by the manufacturer (Kerakoll, 2017) are summarized in Table 3.7.

Table 3.7. GeoCalce Matrix Mortar Properties Provided by the Manufacturer (Kerakoll, GeoCalce F Antisismico, 2017)

Density of Wet Mortar (kg/dm^3)	~1.73
Compressive Strength (28 day) (MPa)	> 15 (EN 1504-3)

Figure 3.15. GeoCalce F Antisismico

Similar to the masonry mortar, experimental tests were performed to verify the properties reported by the manufacturer and determine more accurate properties given the laboratory conditions. Compressive strength and splitting tensile strength tests were performed on each batch of GeoCalce mortar used for the composite application. A minimum of three cubes were made from each batch of matrix mortar. One batch of mortar included one 25 kg bag of GeoCalce with the appropriate amount of water and was sufficient to apply the SRG jacket for one column. According to the manufacturer, the recommended quantity of clean water was 5.3 L per 25 kg bag of mortar. The mortar proportions used in this study were consistent with the manufacturer's required values.

The mixing procedure for the matrix mortar was similar to that used by the masonry mortar. Each batch was mixed for approximately 4-5 minutes until the mixture was smooth. Each cube had the dimension of 50.8 mm and was constructed using brass or steel cube forms.

The cube construction and test procedure for compressive strength was consistent with the procedure previously described in Section 3.2.1.2. Table 3.8 indicates the average compressive strength of three matrix mortar cubes, tested for each batch used. The average compressive strength for specimens tested in this study was 12.7 MPa (CoV = 0.683).

The average compressive strength of the composite matrix mortar in this study was less than the manufacturer's stated minimum of 15 MPa, with values ranging from 11.1 to 16.8 MPa. Reasons for variation could include the humidity in the laboratory and the exterior climate in the area. At times, the large garage doors to the laboratory were opened, allowing for the exterior conditions to fill the space and change the temperature and humidity levels. Regarding the cubes tested, the compressive strength failure mode observed was similar to that of the masonry mortar as shown in Figure 3.16.

Splitting tensile tests were performed for all batches of matrix for the composite. Cylinders were constructed and tested using the same procedures described in Section 3.2.1.3. The splitting tensile failure mode was similar to that of the masonry mortar, however due to its higher strength, the cylinder began to crush at times before failure or before the vertical crack began to form, as shown in Figure 3.17.

The splitting tensile strength was computed using Equation 3.2. The splitting tensile average strength of three cylinders made for each matrix batch is summarized in Table 3.9.

Table 3.8. Compressive Strength of Matrix Mortar

Group	Specimen	Average compressive strength (MPa)	CoV
1	C-12-0-1-1	16.8	1.485
	C-12-0-1-2	14.3	1.255
	C-12-0-1-3	11.5	0.167
	C-12-0-1-4	11.4	0.495
2	C-12-0-2-1	11.2	0.299
	C-12-0-2-2	11.1	0.820
	C-12-0-2-3	12.4	0.507
	C-12-0-2-4	14.8	0.983
3	C-12-0-3-1	12.4	0.788
	C-12-0-3-2	12.9	0.883
	C-12-0-3-3	14.5	0.630
	C-12-0-3-4	11.1	0.446
4	C-12-38-1-1	12.0	0.168
	C-12-38-1-2		
	C-12-38-1-3	14.8	1.033
	C-12-38-1-4		
5	C-12-38-1(2)-1	13.4	0.528
	C-12-38-1(2)-2	11.9	1.334
	C-12-38-1(2)-3	12.8	0.630
	C-12-38-1(2)-4	12.8	0.387
6	C-12-38-2-1	11.1	0.226
	C-12-38-2-2		
	C-12-38-2-3	12.3	1.045
	C-12-38-2-4	11.6	0.231
Average (MPa)		**12.7**	**0.683**

Figure 3.16. Matrix Mortar Failure Mode

Figure 3.17. Matrix Mortar Splitting Tensile Failure Mode

Table 3.9. Matrix Mortar Splitting Tensile Strength

Group	Specimen	Average splitting tensile strength (MPa)	CoV
1	C-12-0-1-1	2.2	0.031
	C-12-0-1-2	1.9	0.148
	C-12-0-1-3	1.5	0.101
	C-12-0-1-4	1.7	0.198
2	C-12-0-2-1	1.6	0.076
	C-12-0-2-2	1.6	0.193
	C-12-0-2-3	1.3	0.247
	C-12-0-2-4	1.2	0.066
3	C-12-0-3-1	1.4	0.199
	C-12-0-3-2	1.9	0.112
	C-12-0-3-3	2.1	0.032
	C-12-0-3-4	1.3	0.187
4	C-12-38-1-1	1.5	0.099
	C-12-38-1-2		
	C-12-38-1-3	1.8	0.233
	C-12-38-1-4		
5	C-12-38-1(2)-1	1.6	0.144
	C-12-38-1(2)-2	1.6	0.169
	C-12-38-1(2)-3	1.4	0.180
	C-12-38-1(2)-4	1.2	0.123
6	C-12-38-2-1	1.2	0.101
	C-12-38-2-2		
	C-12-38-2-3	1.5	0.101
	C-12-38-2-4	1.6	0.097
Average (MPa)		**1.6**	**0.141**

3.3. FABRICATION OF TEST SPECIMENS

This section provides details regarding the fabrication of the unconfined masonry columns and the process used to confine the columns with the SRG system.

3.3.1. Masonry Column Construction. The construction of all masonry specimens followed the same sequence of steps described in this section.

As recommended by the manufacturer, the bricks were saturated with water prior to their use to prevent debonding between bricks and mortar. The bricks were porous and were highly absorbent. Undamaged bricks were placed in large, rubber containers to prevent damage when being handled within the containers. Water was continuously added to the containers when a portion of brick became un-submerged (Figure 3.18). The bricks were submerged in clean water for a minimum of one hour before use.

Figure 3.18. Brick Saturation

One batch of masonry mortar was used to construct each column. Each batch included one bag of BioCalce mortar. Differing from the manufacturer's instructions, each 25 kg bag of mortar, was mixed with approximately 5.15 L, instead of 5.1 L, of clean water determined by the weight conversion of 1 L of clean water equals 1000 grams (Figure 3.19). The instructions stated that for each batch of mortar, one bag of BioCalce should be completely used with the recommended amount of water. As discussed in Section 3.2.1.2, the compressive strength of the masonry mortar was slightly lower than expected based on data collected in a previous study (Baietti, 2017) but still above the manufacturer's provided values.

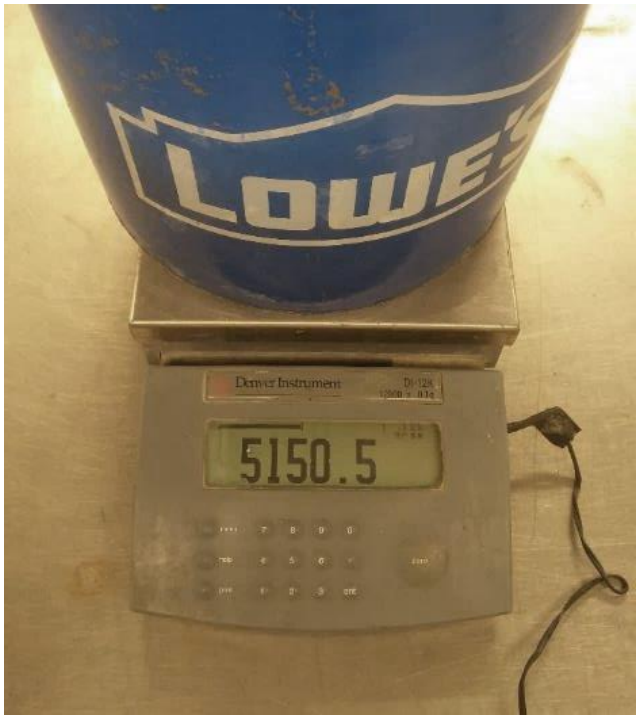

Figure 3.19. Weighing of Required Water

The manufacturer's instructions recommended that the water be poured first into a clean cement mixer and then the powder be added in one operation. Due to limitations of the laboratory, the powder was added to the cement mixer after dampening the interior of the drum using water in addition to the required quantity, then the water was slowly added while the mixer was in operation. The water was added slowly to clean the interior of the mixer to ensure that the full bag of powder was in solution. The mortar was mixed at a constant rate for approximately five minutes or until the mixture was homogeneous and smooth. Then the mortar was removed from the mixer using a trowel and placed into a rubber container (Figure 3.20). The interior of the rubber container was lubricated with form-oil for easy removal of un-used mortar. Once the mortar was completely removed, the cement mixer was thoroughly cleaned using clean water and a plastic bristle brush.

Figure 3.20. Masonry Mortar Prior to Use

Immediately after mixing the masonry mortar, column fabrication took place within the following hour, which was within the mortars workable time limit. A lubricated, wood base frame was used to apply a base layer of mortar before positioning the first layer of bricks. The first mortar layer was used to ensure that the first layer of bricks would bond together. Each layer of mortar was shaped utilizing two steel frames that were 1.27 cm thick. The two steel frames were composed of two, smooth steel rods that were 1.27 cm in diameter and approximately 25.4 cm in length. This length was selected since the summation of the two brick widths and the vertical joint was approximately 25.4 cm. The steel frames are shown in Figure 3.21 a and b.

The mortar was placed using a brick and block trowel and then spread using a texturing and polishing trowel (Figure 3.21). Once the layer of flat, smooth mortar was equal to the thickness of the steel frame, one saturated brick was placed on the edge of the steel frame. Next, a 1 cm thick smooth bar used as a spacer to ensure the second brick was placed at the proper distance. Mortar was applied to the interior facing side of the second brick and then placed next to the spacer. The mortar spacer was then removed and the gap between the bricks was filled with additional mortar (Figure 3.22).

Once the vertical gap was filled and the excess mortar was removed, the steel frames beneath the bricks were removed, and 10 mm diameter steel spacers made of short segments of reinforcing bars were placed at each corner of the column layer. The spacers were used to prevent the mortar joints from compressing excessively as brick layers were added to the column. Before proceeding, the horizontal levelness was verified. The flatness was checked in multiple locations and directions to determine if modifications were needed (Figure 3.23a). If modifications were required, a rubber mallet was used to

gently tap the top surface of the brick layers in multiple locations until the layer was level and the mortar joint at the underside of the layer was 10 mm (Figure 3.23b). Excess mortar that was exposed through the adjustment was removed and discarded.

(a) (b)

Figure 3.21. (a) Wood Base, (b) First Mortar Layer Placement

(a) (b)

Figure 3.22. (a) Placement of First Brick, (b) Filling Gap with Mortar

(a) (b)

Figure 3.23. (a) Checking the Horizontal Level of the Layer, (b) Leveling the Layer

The remaining ten brick courses were placed in an alternate stretcher and header bond configuration (Figure 3.24 a-c). Generally, after the placement of the 8th or 9th course, the vertical alignment was verified using a vertical level. Corrections were made to the vertical alignment of the column using a rubber mallet, if required.

Once all the layers were complete, the column was not disturbed for approximately 30-45 minutes to allow the mortar to begin to cure. After the allotted time, the corner spacers were removed (Figure 3.25a). At this point, all corners and joints that needed more masonry mortar were filled in using a mortar bag and mortar paste (Figure 3.25b). The mortar used to fill in the joints was the same mortar used to construct the

column, however water was added to this mortar to increase its workability. All joints were finished with a jointer or by hand and all excess mortar was removed as the final step.

(a) (b) (c)

Figure 3.24. (a) Laying of the Mortar, (b) Placement of First Brick, (c) Horizontal Level Check

After the joints were finished, the column was left in the same location in the laboratory for a minimum of 12 hours. After the allotted time, the column was removed from the wood base board via a specially made frame in combination with the 20 ton overhead crane located within the laboratory. The specially made frame simulates an ice grabber where, when the crane begins to lift the column upward, it allows for the hooked ends supporting the column to tightly clamp together (Figure 3.26).

(a) (b)

Figure 3.25. (a) Spacers in Corners, (b) Filling in the Corners and Joints

Figure 3.26. Specialty Frame Used to Move Columns

To characterize the masonry mortar material properties, three masonry mortar cubes were constructed using steel or brass forms for each column (Figure 3.27). Three masonry mortar cylinders were made for eight of the batches using plastic forms (Figure 3.28). The processes used to make the cubes and cylinders are discussed in Section 3.2.1.2.

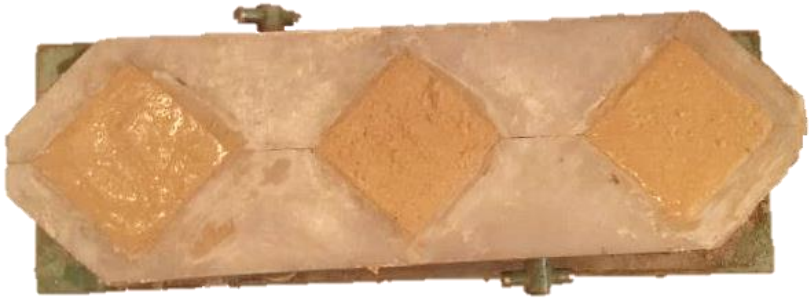

Figure 3.27. Fresh Masonry Mortar Cubes

Figure 3.28. Masonry Mortar Cylinders

After fabrication, all specimens were allowed to cure for a minimum of 12 hours. Following that, all specimens were relocated to a more permanent location for the curing process. Once relocated, the columns were wrapped with several wet clothes (Figure 3.29). The cubes and cylinders were demolded and placed on top of the correlating column and covered with a wet cloth. All specimens were hydrated daily for 28 days. After the curing time was complete, the specimens were uncovered and kept in the same laboratory location until the SRG jacket was installed.

Figure 3.29. Curing of the Specimens

After curing for 28 days in a temperature and humidity-controlled environment, the cubes were tested for their compressive strength and the cylinders were tested to obtain the splitting tensile strength. The test procedures and results are described in Section 3.2.1.2/3.

3.3.2. SRG Jacket Installation. This section describes the procedures used to install the SRG jackets to the column specimens. The installation procedure followed the sequence of steps described in the sections that follow.

3.3.2.1. Column surface cleaning. Due to the finishing technique used during column construction, mortar residue was left on the surface of the brick faces. According to the manufacturer's instructions, the composite should be applied to a substrate that is clean and solid, as well as free from loose debris, dust, and mold (Kerakoll, 2017). To prepare the columns, each face was cleaned using a steel wired brush (Figure 3.30). In addition, the mortar layers located at the top and bottom of each column were removed using a hammer and chisel. The layers were removed so that a high strength mortar cap could be applied, which would allow for the load to be evenly distributed to the bricks during testing. During the mortar removal process, the columns were gently laid on their longitudinal side to facilitate removal of the bottom layer. The bottom layer was also wire brushed to create a flat, clean surface.

3.3.2.2. Column corner preparation. Twelve of the columns in this thesis work required the corners to be rounded to a specific radius before installing the composite. The corners were ground using a Stadea grinding wheel to obtain the required corner radius of 38.1 mm (Figure 3.31a). The tool utilized was a Black & Decker 7"/9" H.D. Angle Sander (Figure 3.31b). Two columns were transported at a time while laying

on their longitudinal sides. The columns remained on their sides during the grinding operation, and when two of the four corners were complete, each column was gently rolled in order to complete grinding on the other two corners. Figure 3.32 shows the grinding process. Figure 3.33 and 3.34 show photographs of representative column specimens with sharp and rounded corners.

Figure 3.30. Cleaning of a Specimen

(a)

(b)

Figure 3.31. (a) Stadea Grinding Wheel, (b) 7”/9” H.D. Angle Sander

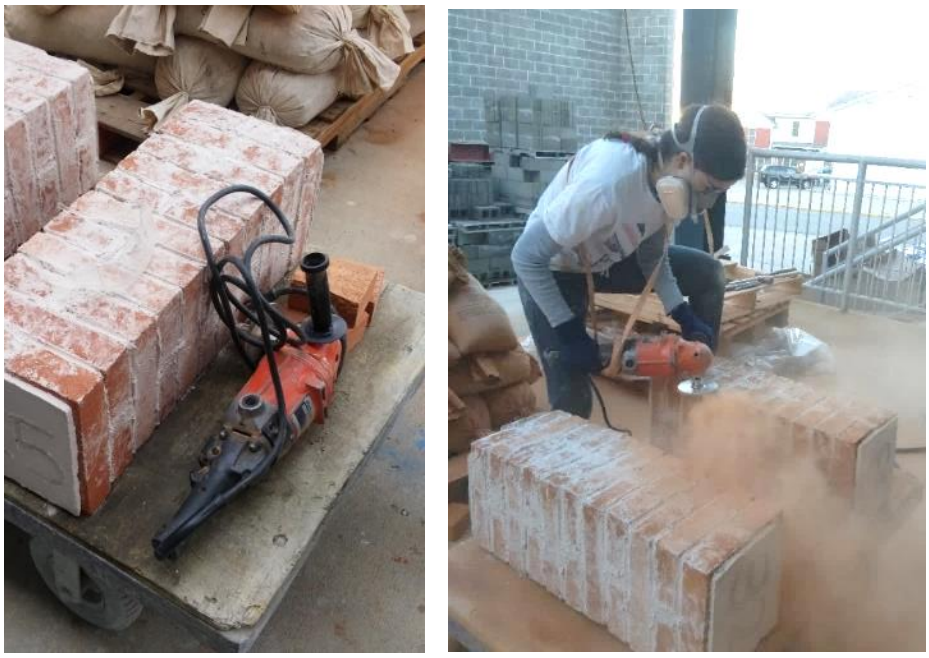

(a) (b)

Figure 3.32. (a) Specimen and Grinder before Grinding, (b) Specimen in Grinding Process

(a) (b)

Figure 3.33. (a) Specimen with Sharp Corners, (b) Specimen with Rounded Corners

(a) (b)

Figure 3.34. (a) Cross-Section of Specimen with Sharp Corners, (b) Cross-Section of Specimen with Rounded Corners

3.3.2.3. Steel fiber sheet preparation. The GeoSteel sheets were pre-bent to conform to the column surface. For each layer of confinement, three sheets were needed to cover the entire column length. The sheet heights, starting at the base of the column were, 30 cm, 30 cm, and 10.5 cm. The jacket preparation included measuring the steel fibers, cutting the fibers sheets to length, and bending the fiber sheets at the corner marks. Due to the two different column corner radii considered (sharp r = 0 mm and rounded r = 38.1 mm), two different bending machines were used to obtain the proper bent angles. For the columns with sharp corners, each corner was bent using a sheet-metal bender (Figure 3.35 and 37a). For each fiber layer, an overlap of 19 cm was provided to be overlapped on one face of the column.

For the columns with rounded corners, the corners were bent using a GeoSteel bender provided by Kerakoll (Figure 3.36). Each corner required three different bends of

approximately 30 degrees each (Figure 3.37b). The rounded columns were provided with an overlap of fibers on either one or two column faces and for the final overlap face, the fiber length provided was 17 cm.

Figure 3.35. Sheet metal Bender for Sharp Cornered Specimens

Figure 3.36. GeoSteel Bender for Rounded Cornered Specimens

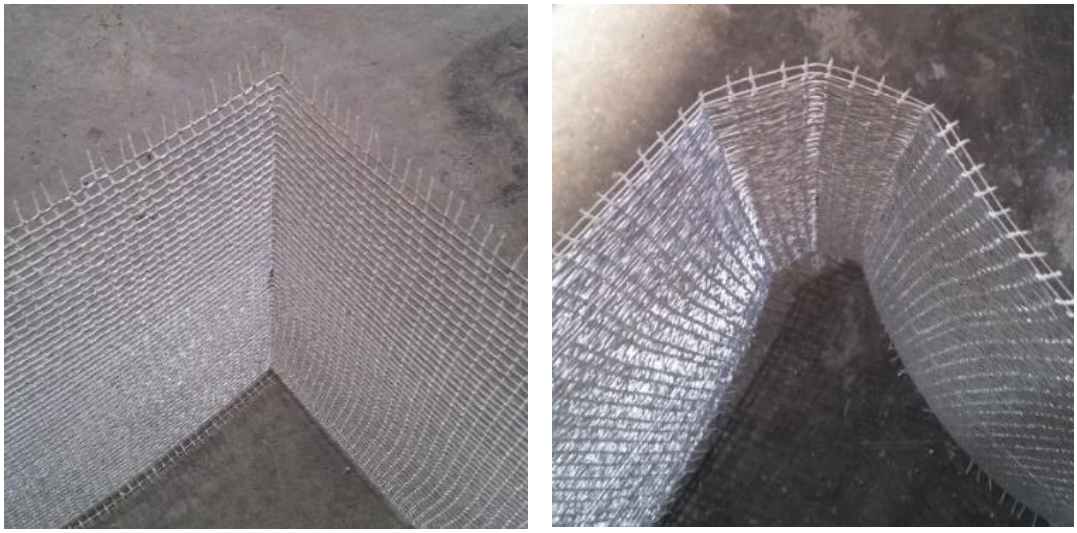

(a) (b)

Figure 3.37. (a) Bent Fibers for Sharp Cornered Specimens, (b) for Round Cornered Specimens

Figure 3.38 shows the dimensions followed to cut the fiber sheets. It was suggested to consider 4 mm of mortar between the first layer of fibers and the bricks and 2 mm of mortar between consecutive layers of fibers. The numbers in the interior of the

column represent the layer of fibers, and the location of the number represents the position of the overlap. The specimen showing 2 overlap areas represents the specimens with two overlap faces (Group 5). Shown in Figure 3.39 are pre-bent fibers for specimens with three layers.

Strain gages were mounted to the steel fibers for certain specimens. The strain gages were mounted to the steel fiber sheets before applying the SRG jacket. Installation of the strain gages is discussed in Section 3.4.3.2.

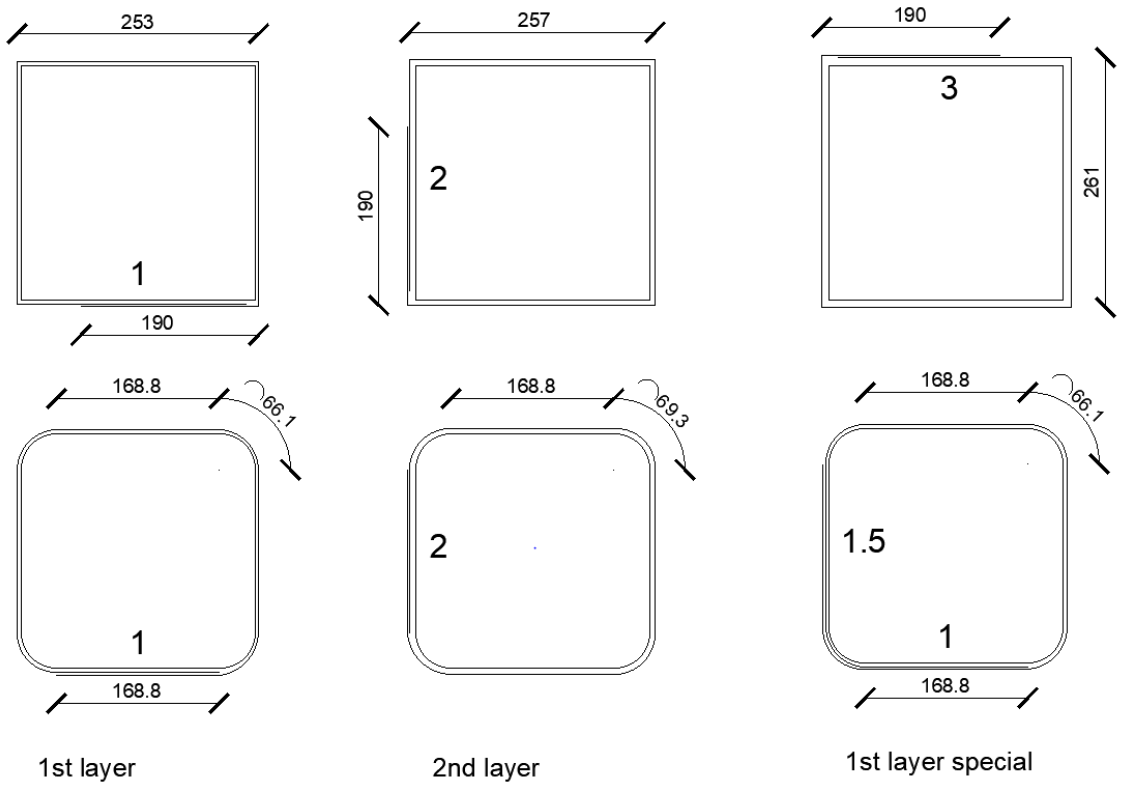

Figure 3.38. Dimensions of Fiber Sheets (mm)

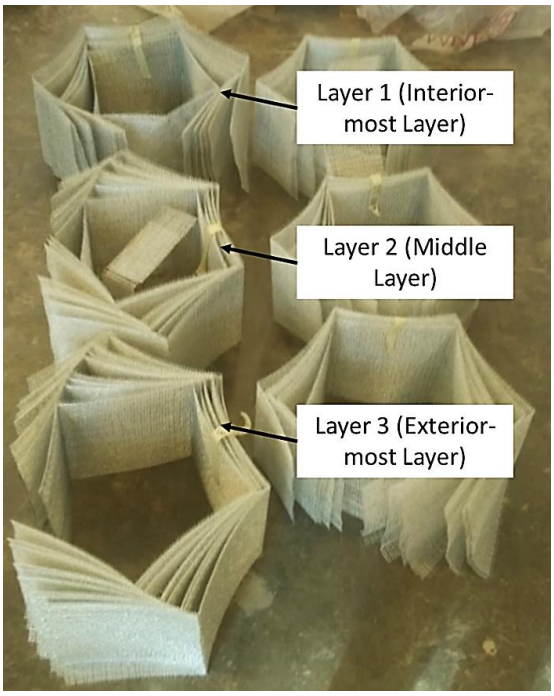

Figure 3.39. Pre-Bent Fibers for Three Layered Specimen

3.3.2.4. SRG jacket application. The application of the SRG jacket onto each confined specimen followed the same sequence of steps described in this section.

A single bag of GeoCalce F Antisismico mortar (25 kg) could be used for up to two columns, depending on the number of layers of confinement being applied. One batch of mortar (25 kg bag) required 5.3 L of clean water according to the manufacturer's instructions (Figure 3.40). The same procedure that was used to mix the masonry mortar mixing was used, however the matrix mortar was only mixed for 4 minutes or until the mixture was smooth and homogeneous.

(a) (b)

Figure 3.40. (a) Weighing of Required Water, (b) Mixed GeoCalce

After mixing, the matrix mortar was placed into rubber containers similar to previous procedures (Figure 3.40b). Then the cement mixer was cleaned thoroughly to prepare it for the next mortar batch.

After mixing the mortar, the jacket was installed within 30 minutes while the mortar was still workable. Prior to matrix application, the column was relocated to an open area in the laboratory and sprayed with water, to ensure a proper bond between the bricks and the matrix (Figure 3.41a). All layers were applied using texturing and polishing trowels (Figure 3.41b). The first layer of matrix was 4 mm thick, to provide an even surface to the fiber sheets and to fill any underlying voids. The thickness was measured using a thin rod that was marked at 4 mm at one end.

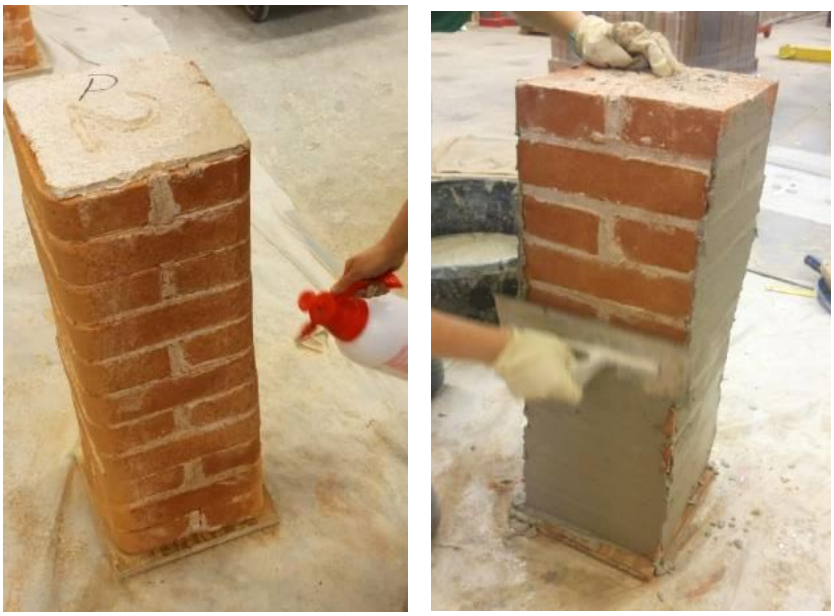

(a) (b)

Figure 3.41. (a) Hydration of Specimen, (b) First Layer of Matrix Mortar

Immediately after the application of the first matrix mortar layer, the fiber sheets were applied beginning at the bottom of the column with the steel fibers facing inwards. The three sheets were positioned to avoid an overlap in the transverse direction of the column. For each layer of fibers, the sheets were lightly pressed into the first layer of mortar using a trowel or by hand to ensure proper bond (Figure 3.42). To ensure proper bond on the overlapping face and to prevent movement during the application process, a thin layer of mortar was applied to the first layer of fiber on the side the overlap was to take place. The overlap length was pressed into the added mortar layer to ensure proper bond. For the columns with rounded corners, the matrix mortar was applied by hand because no tool was able to apply the mortar properly to the corners. The matrix mortar

thickness at the corners was slightly larger than 4 mm due to limitation of the bending machines.

After positioning the three sheets, they were covered with an even 2 mm thick layer of matrix mortar shown in Figure 3.43.

(a) (b)

Figure 3.42. (a) Pressing Fibers into First Mortar Layer, (b) Additional Mortar to Ensure Proper Bond

For specimens with more than one confining layers, the application of the second and third layers of sheets followed the procedure described in the previous step with slight variances. The differences included the length of the fiber sheets, which was

adjusted to take into consideration the added layers of mortar between each layer, and the thickness of the mortar layer between each subsequent fiber sheet, which was 2 mm thick.

Figure 3.43. Fibers Covered with 2 mm Mortar Layer

During the application of each mortar layer, the total mortar thickness was measured using a thin rod marked at 4 mm, 6 mm, 8 mm and 10 mm. For the columns with rounded corners, the matrix mortar at the corners was applied by hand, and the thickness at the corners was greater than 2 mm. Figure 3.44 shows the application of a second layer of fibers and the finished specimen.

(a) (b)

Figure 3.44. (a) Second Layer of Fibers, (b) Final Matrix Mortar Layer

Cubes and cylinder specimens were cast from each batch of matrix mortar to characterize the mechanical properties. For each batch of matrix mortar, three cubes and three cylinders were fabricated while the mortar was still fresh. The procedures used to cast the specimens are described in Sections 3.2.1.2 and 3.2.1.3.

After the jacket installation was complete, the columns were left undisturbed for a minimum of 12 hours. After the allotted time, the columns were relocated and then wrapped in wet cloths for 28 days. The columns were hydrated daily for 28 days, and then they were uncovered and left in the laboratory until testing (Figure 3.45).

Figure 3.45. Curing of the Confined Specimens by Wet Cloth

3.4. EXPERIMENTAL SETUP

This section described the methods used to test each specimen in terms of its preparation, instrumentation, and testing procedure.

3.4.1. Specimen Preparation. Before testing, the top and bottom faces of the columns needed to be flat and parallel to avoid stress concentrations and non-uniform loading conditions. This was achieved by applying a 25-30 mm thick layer of USG Hydro-Stone Brand Gypsum Cement to each end. Once dried, the USG Hydro-Stone Gypsum Cement was extremely hard, had a high compressive strength, and was highly water resistant. During testing, the extra layer also ensured that the plates did not begin to bear load on the confinement system.

For each cap, the Hydro-Stone material was made by slowly sifting 1.89 kg of Hydro-Stone powder into a container with 0.63 kg of clean water. Once all the powder was in the water, the mixture was allowed to soak for three minutes according to the manufacturer's instructions. Next, the Hydro-Stone was mixed with the water using a small paint mixer at a constant rate. Once the mixture was homogeneous, it was poured into a frame that was attached to the top of a column.

The frames used to form the caps were made from 0.64 cm x 5.1 cm steel bars. The interior dimensions of the frame were approximately 24.25 cm x 24.25 cm. The frame was attached to the face of the column using quick drying, silicone caulk, which then contained the liquid Hydro-Stone mixture. The mixture was left uncovered for a minimum of two hours or until hardened. Once complete, the frames were removed and cleaned of caulking material (Figure 3.46).

Figure 3.46. Hydro-Stone Cap

3.4.2. Specimen Positioning. After capping, the column was positioned in the front of the testing machine. A forklift was used to gently pick-up and place the column into position. To pick up the column, custom holders were bolted and strapped to the perimeter of the column, allowing the forks of the fork lift to slowly lift and move the column (Figure 3.47). To prevent damage to the column by the holders, cloths were placed between the column and the holders.

The forklift operator was guided by one individual while another told the directions in which the forks should move. A square was marked on the base plate to indicate the proper placement of the column. Once the column was in position, it was gently placed into position by the forklift.

Figure 3.47. Custom Holder to Place Columns into Machine using Forklift

3.4.3. Instrumentation. The following sections provide details regarding the instrumentation used to measure the axial displacement and transverse strain during the testing procedure.

3.4.3.1. Linear Variable Differential Transformer (LVDT). Axial displacements between the top and bottom pressing plates were measured using four linear variable differential transformers (LVDTs) installed at each corner of the plate, as shown in Figure 3.48. Custom made LVDT holders were clamped to the stationary bottom pressing plate while securing the LVDTs above the top pressing plate. The axial displacements were measured from the top of the top pressing plate. The gauge length of the LVDTs was 50.8 mm, and the initial reading was set to 21 mm in compression (-21 mm). This allowed for a maximum measurable displacement of 46.4 mm. The average displacement of two of the LVDTs located on opposite corners was used to control the machine stroke to maintain a loading rate of 0.2 mm/min. The average displacement of the four LVDTs were not used to control the machine's stroke due to limitations of the software used. Axial strains were calculated considering the average displacements measured by the four LVDTs divided by the total height of the specimen, not including the caps on either end.

3.4.3.2. Strain gauges. Uniaxial electrical resistance strain gauges were applied to four of the columns in this thesis work. Columns that were instrumented with strain gages were two columns from each category of specimens with one layer of confinement (C-12-0-1 and C-12-38-1 series).

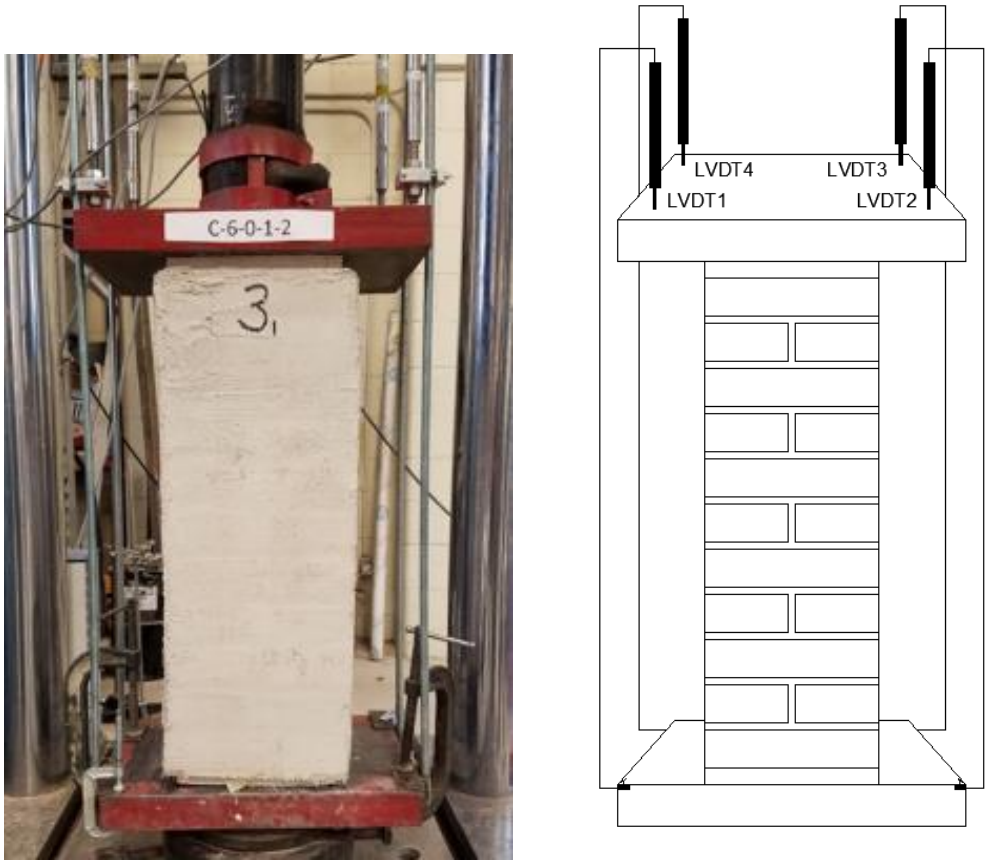

Figure 3.48. Positioning of LVDTs

The strain gauges used were type CEA - 06 - 125UN - 120 from Micro Measurements. All gauges had a gage factor of 1.2 and a grid resistance of 120.0 Ohms. All materials used to install the strain gages were from the same manufacturer. All strain gauges were applied to the steel fibers on the outside surface of the fiber sheet after removing the plastic backing on the fiber sheet (Figure 3.49). One strain gauge was applied to each face of the column at mid-height in the longitudinal direction, as shown in Figure 3.50. In the transverse direction, the gauges were located approximately 10 mm in one direction from the center to avoid the vertical mortar joints. Regarding the overlap

side of a fiber jacket, the strain gauge was located on the outer-most layer of fibers as shown in Figure 3.49 and Figure 3.53.

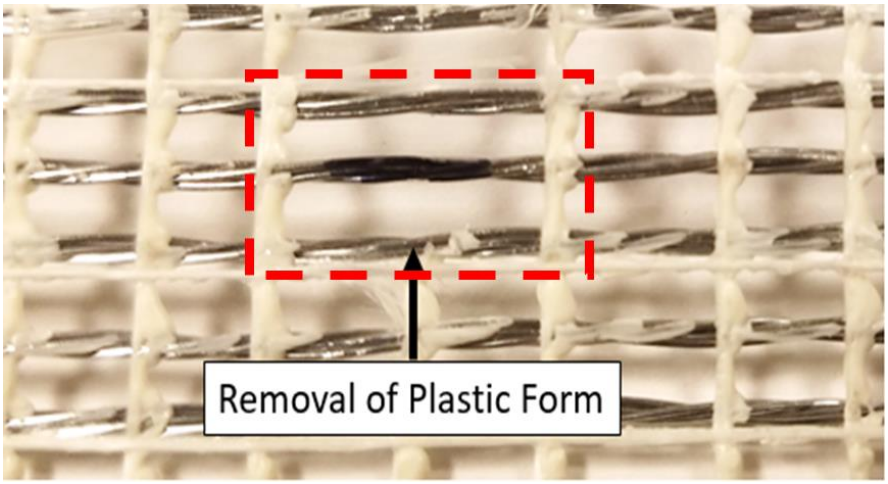

Figure 3.49. Removed Plastic on Steel Fiber Sheet for Epoxy Patch Preparation

Since the steel chords had a very small diameter, an epoxy patch was created on the steel chords using GeoLite Gel epoxy (provided by Kerakoll), and the strain gauges were applied onto the epoxy patch (Figure 3.51). The epoxy patches were placed to bond no more than three steel chords together to prevent altering the mechanical behavior. The strain gauges were positioned on top of one fiber chord.

Once the epoxy patch hardened, it was sanded using different grit sand paper until smooth. Sanding began using 100-Grit sand paper and was completed using 400-Grit sand paper.

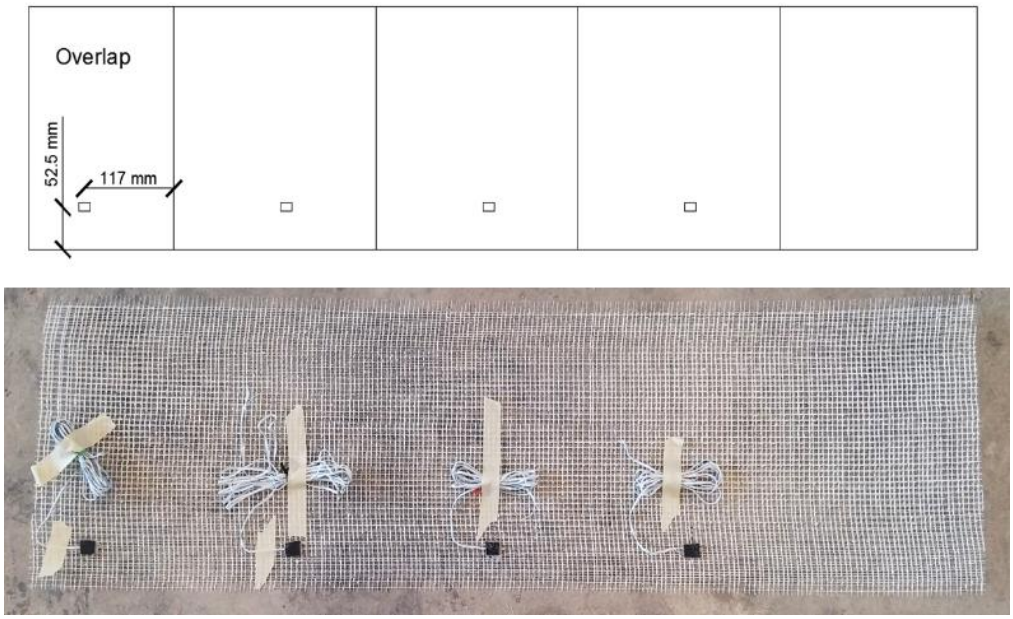

Figure 3.50. Positioning of the Strain Gauges

Figure 3.51. GeoLite Gel (Epoxy)

Once the surface was uniform and smooth, a line perpendicular to the fiber chord under consideration was drawn on the patch to indicate the location of the center of the strain gauge (Figure 3.53 a). The patch was then conditioned and neutralized to remove all particles and dust (Figure 3.52). Next, the strain gauges were removed from the packaging and placed on tape that had anti-static properties. Finally, the strain gauge was then positioned and placed on the clean epoxy patch so that the direction of the strain reading would be perpendicular to the line drawn (Figure 3.53 b).

The tape was then carefully lifted upward only to the point of exposing the strain gauge. A thin coat of 200 Catalyst-C was applied to the gauge and undisturbed for one minute to allow for better bondage with the adhesive (Figure 3.54 a). The gauge was then bonded to the epoxy patch using M-Bond 200 Adhesive and undisturbed for more than one minute (Figure 3.54 b). After the adhesive provided ample bondage, the tape was removed, and anti-static scotch tape was placed over the portion of the strain gauge for protection (Figure 3.55 a).

The strain gauge wires were composed of three individual cables. Each cable contained seven wires. Each cable was stripped of the rubber casing and then twisted together until all wires were in contact with one another. When all three wires were twisted together, two of the three wires were then again twisted together.

Next, using 361A-20R solder and a temperature-controlled soldering iron, the exposed wires were lightly coated in solder and a small bead of solder was carefully placed on the terminals (Vishap Precision Group, 2014).

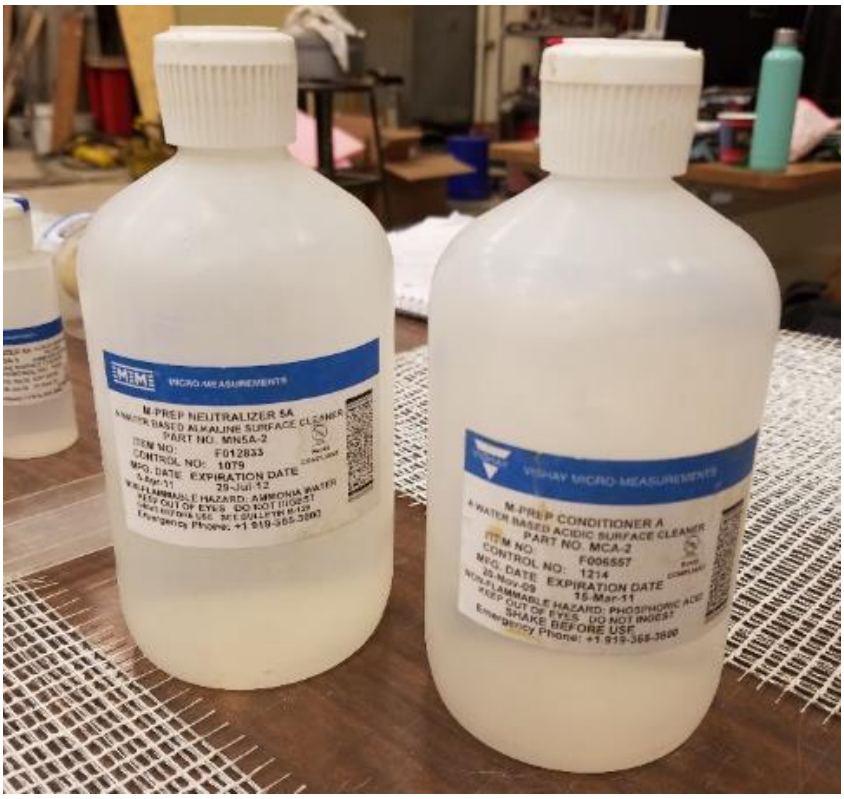

Figure 3.52. Conditioner and Neutralizer for Cleaning

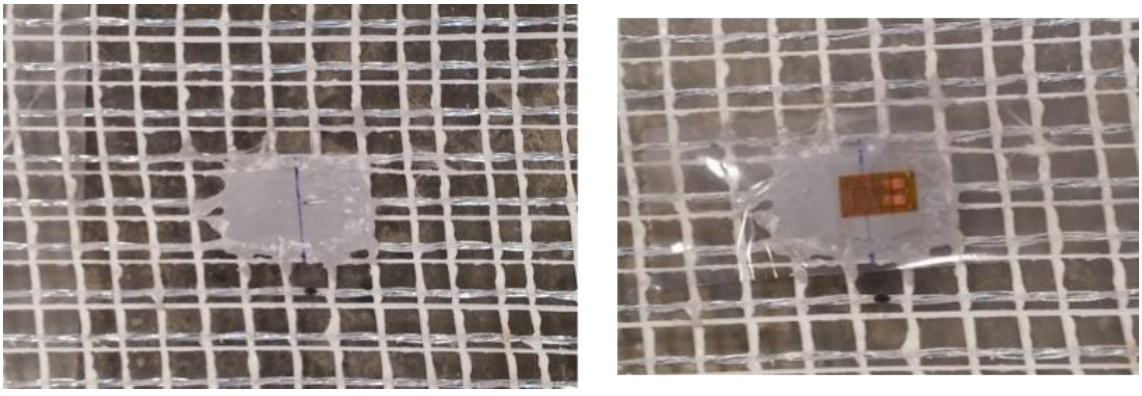

(a) (b)

Figure 3.53. (a) Sanded Epoxy Patch on G600 GeoSteel, (b) Strain Gauge Taped to Patch

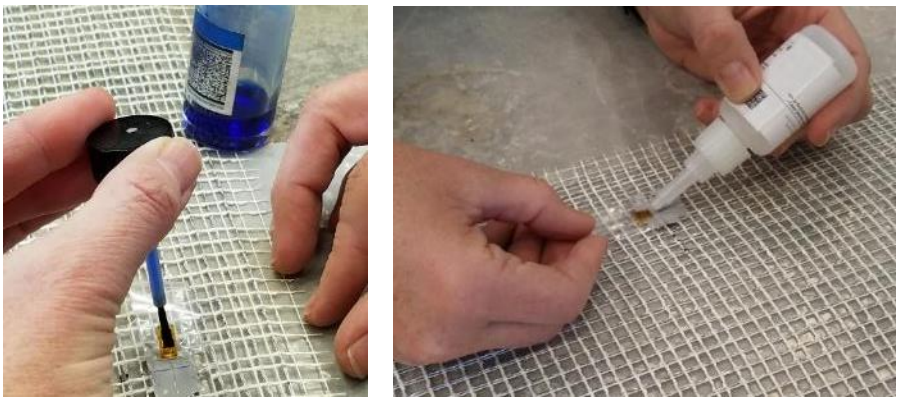

(a) (b)

Figure 3.54. (a) 200 Catalyst C Application, (b) M-Bond 200 Adhesive Application

The wires were then connected to the terminals (Figure 3.55 b). Once connected, the strain gauge resistance was tested to ensure the connection was complete using a digital multimeter as shown in Figure 3.56a. Once the wires were properly connected to the strain gauge, the strain gauge and exposed wires were protected using a polyurethane coating and mastic patch (Figure 3.56 b and 3.57).

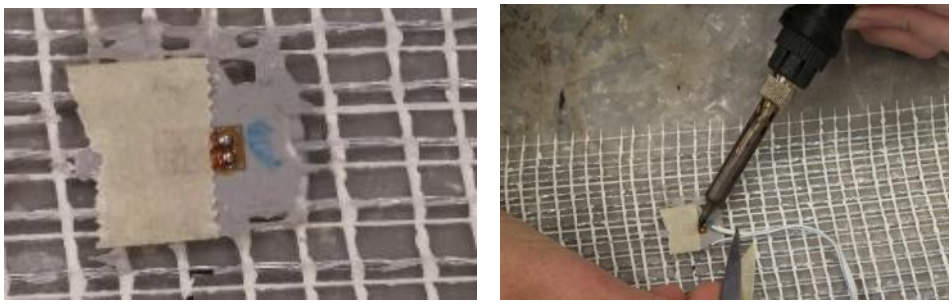

(a) (b)

Figure 3.55. (a) Preparing Terminals, (b) Soldering Wires to the Terminals

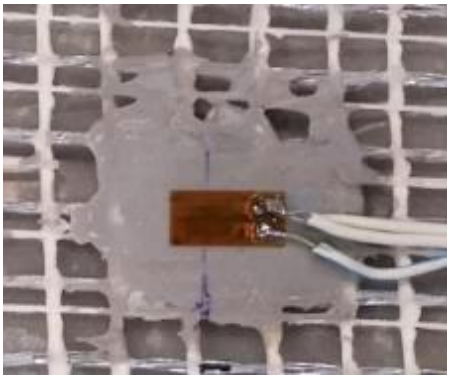

(a) (b)

Figure 3.56. (a) Digital Multimeter and Probes, (b) Polyurethane Coating

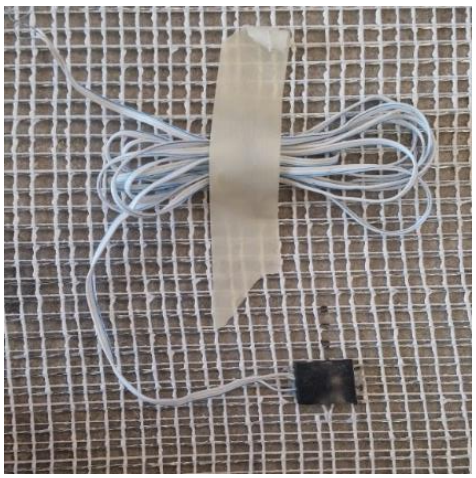

Figure 3.57. Completed Strain Gauge

3.4.4. Testing Procedure. The columns were subjected to a monotonically increasing concentric uniaxial compression load that was distributed uniformly across the top and bottom surfaces of the column. The columns were tested in a servo-hydraulic material testing system (MTS) machine, with a 2,450 kN (550 kip) capacity. The system was equipped with a data acquisition PC workstation that recorded the applied load,

machine displacement (stroke), and displacement of the four LVDTs, and readings from the strain gages (where applicable). The test set-up included a swivel head ball bearing system beneath the bottom pressing plate, allowing it to be adjusted when the specimen was placed. Figure 3.58 provides an image of the described test set-up. The testing procedure used for each column followed the same steps summarized in this section:

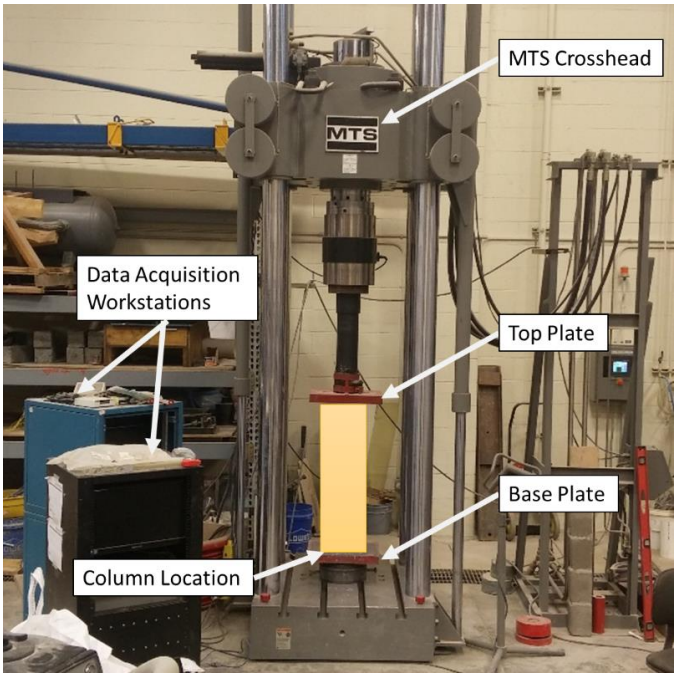

Figure 3.58. MTS Machine and Test Setup

Using a meter-long ruler and level, the base plate position was altered in the transverse direction and rotated until the column was leveled. Once the base plate was positioned, a layer of sand was applied to the top Hydro-Stone layer and carefully leveled

using a flat level. Then, the crosshead of the machine was slowly lowered until it was in contact with the top of the column and then locked in place.

Once locked, a pre-load of 4.448 kN (1,000 lbs) was applied to prevent movement during the rest of the set-up procedure. This pre-load was less than 1% of the estimated peak load of a confined column.

After the specimen was leveled, the attached frame was removed. The initial conditions were documented by taking photos of all faces of the column and recording its initial dimensions relative to the base pressing plate. The dimensions recorded included the longitudinal height and the transverse width of two faces of the column.

The instrumentation described in Section 3.4.3 was set in place and connected to the data acquisition system. The four custom LVDT holders were secured on the baseplate, next to the four corners of the column using C-clamps. Once secure, the individual LVDTs were placed on the holders so that the reading would be taken from the upper pressing plate, with an initial reading set to 21 mm in compression (-21 mm). This allowed for a maximum displacement of 46.4 mm.

A plexi-glass barrier was placed next to the front face of the column (i.e., towards the interior of the laboratory). This barrier was secured using straps at its top and anchors at its base.

The target load rate was 0.2 mm/min. The average displacement between two LVDTs located at opposite corners was used to ensure that the displacement of the machine (stroke) maintained a constant rate during testing and could be manually modified if needed. Next, the LVDT displacements and the stroke position were zeroed. The machine measuring the LVDT displacements was set to record measurements one

every second during the duration of the test. After all required checks were complete, the test was initiated.

While the test was operating, sounds and cracks were observed and documented. During the test, a graph was continuously being updated that plotted the Applied Load verses Stroke Displacement. When the curve showed unusual or interesting behavior, such as a drop in the curve, the load at which this behavior occurred was documented along with the corresponding behavior of the column. During some of the tests, the loading plate began to bear on the composite system; this point was documented, but the test was allowed to proceed to determine the overall behavior of the column.

The tests were determined to be complete when there was a significant and rapid drop in applied load, the load reached at least 85% of the peak load value, or when fragments of columns began to dislodge. The main reason for test termination was when a significant and rapid drop in applied load occurred.

Once terminated, the load was removed until only 2.22 kN (500 lbs) remained to maintain the columns position. The safety measures and LVDTs were removed from the test set-up including the LVDT holders. Final documentation began by photographing each face of the column and the longitudinal and transverse measurements. If the failure mode of the column was debonding of the composite jacket, the jacket was removed to expose the interior column while the specimen was secured by the machine. Once exposed, major cracks and effects were documented and measured. If possible, some of the upper layers of brick were removed to observe the condition of the masonry near the

mid-height of the column. At completion of testing, the specimen was removed from the machine by hand and placed in the laboratory. The machine area was cleaned of all column fragments to prepare for the next test.

4. SUMMARY OF RESULTS

4.1. OVERVIEW

This section summarizes the behavior of each column group including the unconfined (control) specimens, and confined specimens in Groups 1-6. The groups and their characteristics are defined in Table 3.1. The general behavior described in Section 4.2 includes the failure mode observed, damage to the column and confining system observed during the test, and damage to the masonry column after completion of the test. Section 4.3 contains a discussion of the axial deformations measured by the individual LVDTs, while Section 4.4 presents the axial stress - axial strain responses of each specimen group. Section 4.5 discusses the energy absorbed, and Section 4.6 presents the transverse strain measured in the composite fibers for certain confined specimens. Based on the test results, the influence of the different test parameters included in this study are summarized in Section 4.7. Finally, Section 4.8 highlights the key test results.

4.2. GENERAL BEHAVIOR

This section describes the physical behavior observed throughout testing of the unconfined columns.

4.2.1. Unconfined Specimens. Seven unconfined masonry columns were tested under concentric uniaxial compression until failure. The results obtained were used as a basis of comparison to determine the efficacy of the confinement system with the varied parameters.

The unconfined specimens failed in a brittle manner due to masonry crushing and increasing transversal displacement. Prior to the peak load, small vertical cracks formed on the column faces, i.e., in the longitudinal direction of the column, which propagated through the mortar joints and clay brick units. Once the peak load was reached, the cracks widened and became apparent on all four column faces. For some specimens, other vertical cracks formed near the corners of the column, at the top or bottom, which then propagated towards the mid-height of the column as shown in Figure 4.1. Images depicting the failure mode of the individual specimens are found in Appendix A, Table A1 -Table A7.

Testing was terminated when portions of the unconfined column began to break off from the column and dislodge or when the applied load decreased significantly from the peak applied load.

Figure 4.1. Failure Mode of Unconfined Column

4.2.2. Confined Specimens. This section describes the behavior observed for the confined column groups.

4.2.2.1. Group 1. For the specimens of Group 1 (G1200 fibers, corner radius = 0 mm, 1 fiber layer), vertical cracks formed on the surface of the composite at the column corners and end of the fiber overlap prior to the peak load. Horizontal cracks also formed at the mid-height of the column, near the location of a masonry mortar joint. After the peak load was reached, the vertical cracks along the overlap widened significantly, indicating that the composite was beginning to debond due to the tensile stresses created. The exterior matrix layer began to detach from the fibers and either spalled off the column or remained attached to the outer surface of the fibers (see Figure 4.2). Once the interior of the column was exposed, large vertical cracks were observed in the longitudinal direction of the column. These vertical cracks were similar to those of the unconfined specimens. Once the fiber overlap layer detached from the fiber layer beneath, the load applied to the column decreased rapidly, similar to the failure of the unconfined specimens.

Testing was terminated after the fiber overlap face detached completely (see Figure 4.3a), causing a rapid decrease in the applied load. After testing was complete, the single fiber layer of Group 1 specimens was removed. The behavior resembled that of the unconfined columns with vertical cracks propagating through the mortar joints and brick faces. The crack size ranged from 2 mm to 8 mm in width for the columns of Group1. Additional vertical cracks were observed near the corners of the columns as shown in Figure 4.3b. It was also noted that the column corners were slightly crushed. Images depicting the failure mode of specimens of this group are in Appendix A, Table A7-A11.

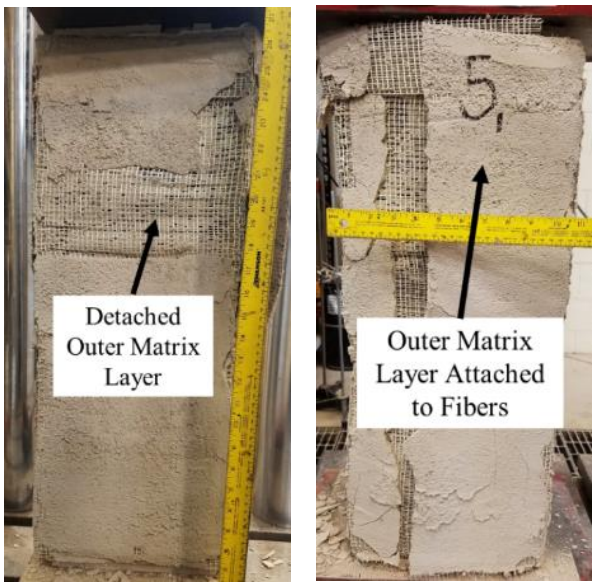

(a) (b)

Figure 4.2. Column C-12-0-1-2 (a) Detached Outer Matrix Layer, (b) Outer Matrix Layer Attached to Fibers

(a) (b)

Figure 4.3. Group 1 Failure Mode, (a) Fiber Debonding at Overlap, (b) Vertical Cracks in Matrix and Column

4.2.2.2. Group 2. For the specimens of Group 2 (G1200 fibers, corner radius = 0 mm**,** 2 fiber layers), small vertical cracks formed at the mid-region of the fiber overlap prior to the peak load. Horizontal cracks also formed at the location of masonry mortar joints near the top of the column and at the mid-height, indicating crushing if the masonry mortar at those joints (Figure 4.4). Once the peak load was reached, the vertical crack along the fiber overlap began to widen and increase in length, exposing the inner-most fiber layer of the jacket. At this point, the inner-most fiber layer of the jacket was detaching from the outer-most fiber overlap layer due to spalling of the matrix mortar. As the fiber overlap region detached from the overlap face, the load decreased rapidly until the load began to plateau. The primary failure mode of the specimens in this group was fiber debonding at the overlap (Figure 4.4a).

Testing was terminated once one fiber layer or multiple fiber layers detached from the column faces, causing a significant decrease in load capacity. Once testing was complete, the outer-most layer of fibers was removed and in some cases, the inner-most fiber layer was removed, exposing the masonry column. Once the column was exposed, the top layers of brick were removed to observe the damage towards the mid-height of the column. All cross-sections exhibited visible arching effect on all sides, some being more pronounced than others, as shown in the Figure 4.5. The arching effect displayed on these specimens were often asymmetrical, being more pronounced on one side verses the opposing side. Additional images depicting the failure mode of specimens within this group are found in Tables A12-A15 in Appendix A.

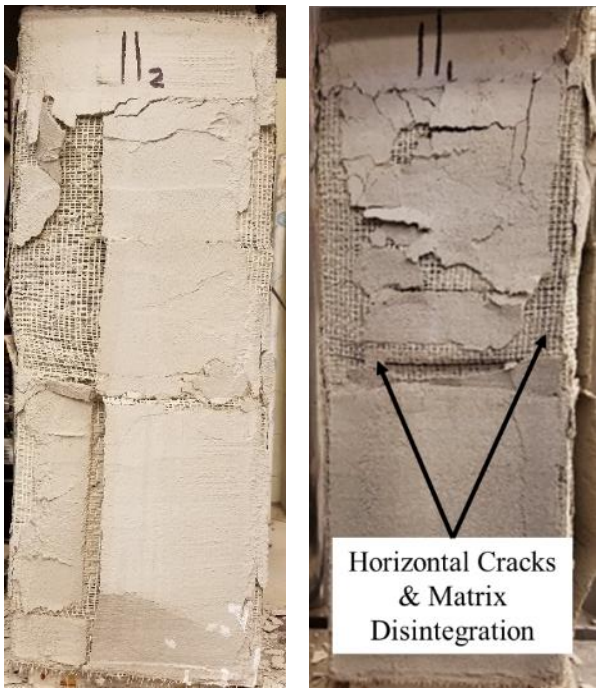

(a) (b)

Figure 4.4. Column C-12-0-2-2 Failure (a) Fiber Debonding at Overlap, (b) Horizontal Cracks and Matrix Disintegration on Jacket Surface

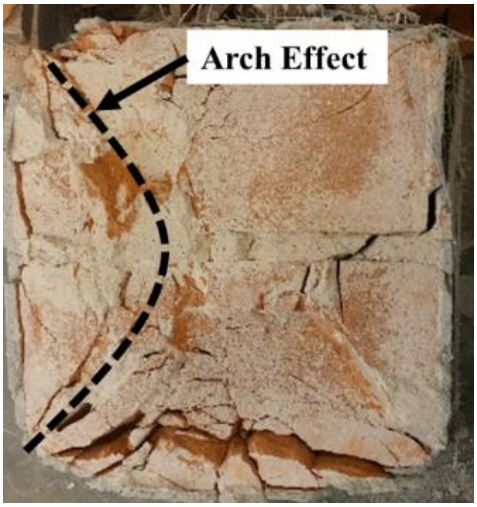

Figure 4.5. Cross Section of Column Showing Asymmetric Arching Effect Due to Confining Stresses

4.2.2.3. Group 3. For the specimens of Group 3 (G1200 fibers, corner radius = 0 mm, 3 fiber layers), horizontal cracks formed at the mid-height of the columns on each face and towards the top or bottom of the column on multiple faces prior to the peak load. Additionally, small vertical cracks formed along the exterior-most overlap in the longitudinal direction. During testing, the outer-most layer of matrix was disintegrated in regions of damaged bricks or at the top and bottom regions of the columns. The term, disintegrated is defined herein as a material breaking into small pieces or dust like particles. Once the peak load was reached, the outer-most fiber layer began to detach, exposing the second layer of fibers. It was observed that the second layer began to detach after the ultimate load was reached (corresponding to 85% of the peak load). In certain cases, the outer-most layer of fibers completely detached from three of the column faces, including the face with the overlap portion. Due to the varying overlap locations of each fiber layer, the second layer overlap did not completely detach from the column, and therefore was able to continue to provide confinement. Also, in the post-peak response, it was noted that the sharp corners of the columns crushed due to the concentrated stresses at the corners, resulting in rounding of the corners, as shown in Figure 4.7.

Testing for Group 3 specimens, was terminated after the ultimate load was reached or when load began to bear on the composite system. The latter occurred on three of the specimens after the ultimate load was reached. At this point, the failure mode was inconclusive other than the second and third fiber layers did begin to detach from these columns. It is likely that the failure mode would have been fiber debonding. Figure 4.6 shows a representative failure response of a Group 3 specimen. After testing, the three fiber layers were removed from the top half of the column, exposing the mid-region. The

cross section of all Group 3 specimens exhibited visible arch effect on all faces, particularly towards the mid-height of the columns. The top and bottom brick layers completely crushed due to the confinement or the high-strength capping material. The cross section shown in Figure 4.7 illustrates the symmetric arching effect that occurred for all specimens in the group. Images depicting the failure mode of specimens within this group are found in Appendix A, Tables A16-A19.

(a) (b) (c)

Figure 4.6. Column C-12-0-3-4 Failure Mode (a) Third (Outer) Layer Fiber Debonding, (b) Jacket Detachment, (c) Horizontal Cracking and Bulging

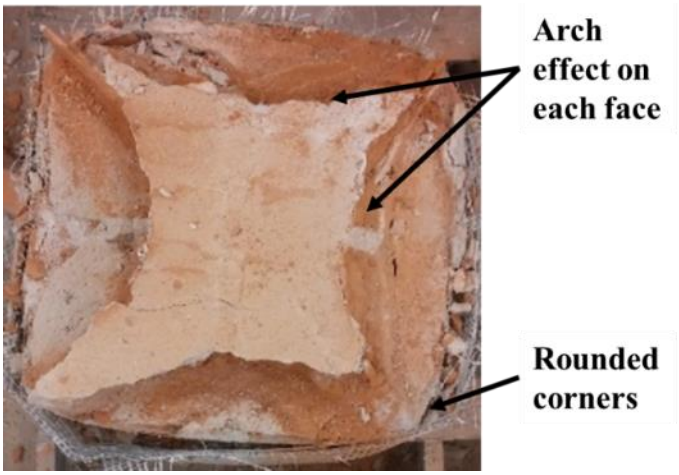

Figure 4.7. Cross Section of Column Showing Symmetric Arching Effect and Crushed Column Corners

4.2.2.4. Group 4. For the specimens of Group 4 (G1200 fibers, corner radius = 38.1 mm, 1 fiber layer), vertical cracks formed at the column corners prior to the peak load. The formation of these cracks was attributed to the articulated shape of the fiber sheet around the curved corners (discussed in Section 3.3.2.3). The outer-most matrix layer disintegrated from the specimen, starting at the corners and progressing inwards toward the center of the column faces. Throughout the test, crackling noises were noticed, which was the result of matrix pieces falling off the column, as shown in Figure 4.8. Prior to reaching the peak load, a small vertical crack was visible at the fiber overlap location. Once the peak load was reached, the overlap crack width increased significantly. The post-peak behavior of the columns was similar to the unconfined specimens in which the rapid drops in load occurred due to the formation of large vertical cracks within the masonry column, or detachment of the fibers from a column face. This failure mode is depicted in Figure 4.8.

Testing of Group 4 specimens was terminated when a layer of fiber detached from one or multiple column faces, causing a significant decrease in confinement capacity. After testing, the fiber layer was removed, exposing the masonry column. It is important to highlight that while removing the fiber layer, the composite was still well attached to three of the rounded corners. Large vertical cracks oriented in the column's longitudinal direction were noticeable on all column faces, shown in Figure 4.9. Similar to the unconfined columns, the large cracks passed through mortar joints and brick units and were apparent near the column corners. The primary failure mode of specimens in this group was fiber debonding. Additional images depicting the failure mode of specimens within this group are found in Tables A20-A23 of Appendix A.

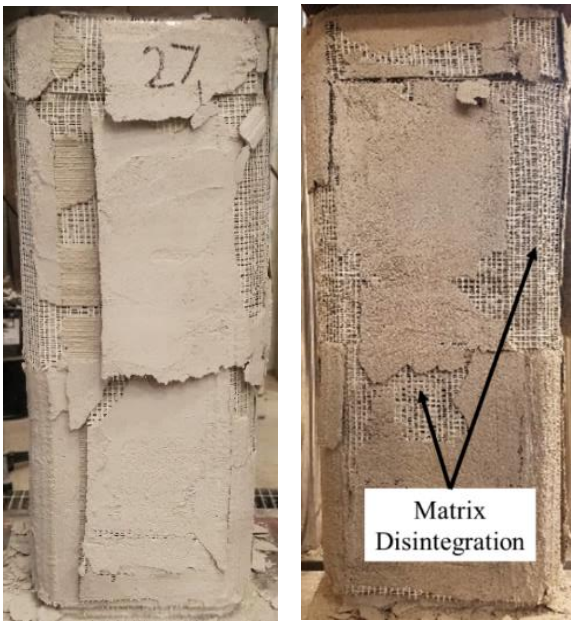

(a) (b)

Figure 4.8. Column C-12-38-1-2 Failure (a) Fiber Debonding at Overlap, (b) Exterior Matrix Layer Disintegration

Figure 4.9. Column C-12-38-1-2 Exposure of Vertical Cracks in Masonry Column

4.2.2.5. Group 5. For the specimens of Group 5 (G1200 fibers, corner radius = 38.1 mm, 1 fiber layer, 2 overlapping faces), vertical cracks formed at the column corners prior to the peak load. Similar to Group 4 specimens, the formation of these cracks was attributed to the articulated shape of the fiber sheet around the curved corners (discussed in Section 3.3.2.3). Small vertical cracks began to form along the fiber overlap and widened once the peak load was reached. For all specimens, after the peak load, the fibers on the first overlap face debonded causing a significant drop in the applied load. Soon after, the ultimate load was reached for all specimens. Significant drops in the applied load were caused by the first overlap face completely debonding followed by the second overlap face. Throughout the test, crackling sounds were heard, which were the result of the outer-most matrix layer falling off the specimen.

Testing was terminated when the fibers either partially or completely debonded along the column length for the two overlapping faces (Figure 4.10). After testing was complete, the fibers were removed from the top half of the column exposing the damaged masonry. Large vertical cracks were observed on all longitudinal faces, ranging from 2 mm to 12 mm in width (Figure 4.11). It is important to note that some of the cracks exposed were wider than those of a typical unconfined column, demonstrating that the confined column can withstand larger transverse dilation before failure. Also, crushing of some of the mortar joints was observed. Images depicting the failure mode of specimens within this group are found in Tables A24-A27 in Appendix A.

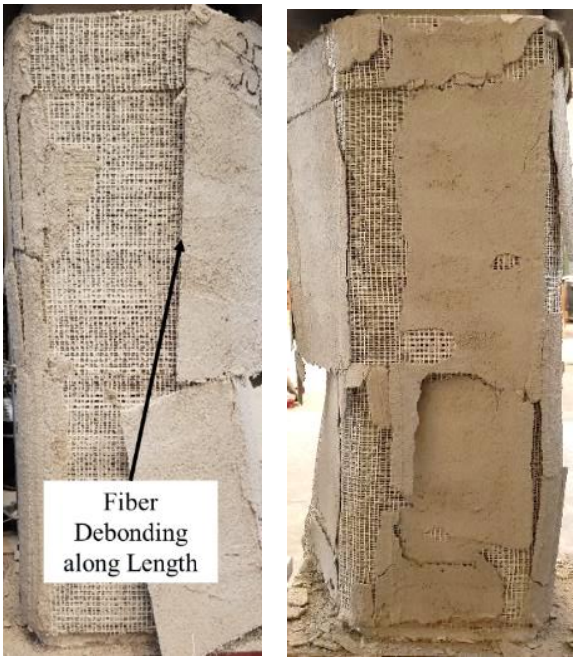

(a) (b)

Figure 4.10. Column C-12-38-1(2)-4 Failure (a) Fiber Debonding along Length, (b) Fiber Debonding and Matrix Disintegration at Corners.

(a) (b)

Figure 4.11. Column C-12-38-1(2)-4 (a) Wide Vertical Crack, (b) Crack at Column Corners and Middle of Face

4.2.2.6. Group 6. For the specimens of Group 6 (G1200 fibers, corner radius = 38.1 mm, 2 fiber layer), vertical cracks formed at the column corners followed by a small vertical crack located at the end of the fiber overlap prior to the peak load. In addition, horizontal cracks formed on multiple column faces (Figure 4.12b). Once the peak load was reached, the crack at the end of the fiber overlap widened until sudden detachment occurred, causing a rapid decrease in confinement capacity. When the detachment occurred, a loud popping sound was heard, most likely due to widening of the vertical cracks. Throughout testing, crackling sounds were noted that were due to the outer-most layer of matrix crumbling off the specimen at the corners. When the second (i.e., outer-most) fiber layer detached, the outer-most matrix layer remained attached to the fibers.

Testing was terminated after the ultimate load was reached and when the second fiber layer detached from at least one column face, causing a significant decrease in applied load. Fiber detachment is shown in Figure 4.12a. After testing, the two fiber layers were removed, exposing the large vertical cracks on each column face as shown in Figure 4.13. Arching effect was observed on the cross section and was primarily asymmetric (Figure 4.14), located on only two faces; except for one column in which it was apparent on all column faces. Images depicting the failure mode of specimens within this group are found in Tables A28-A31 in Appendix A.

(a) (b)

Figure 4.12. Column C-12-38-2-4 Failure (a) Debonded Jackets, (b) Horizontal Cracking

(a) (b)

Figure 4.13. C-12-38-2-4 Column (a) Small Vertical Crack, (b) Large Vertical Crack and Arching Effect

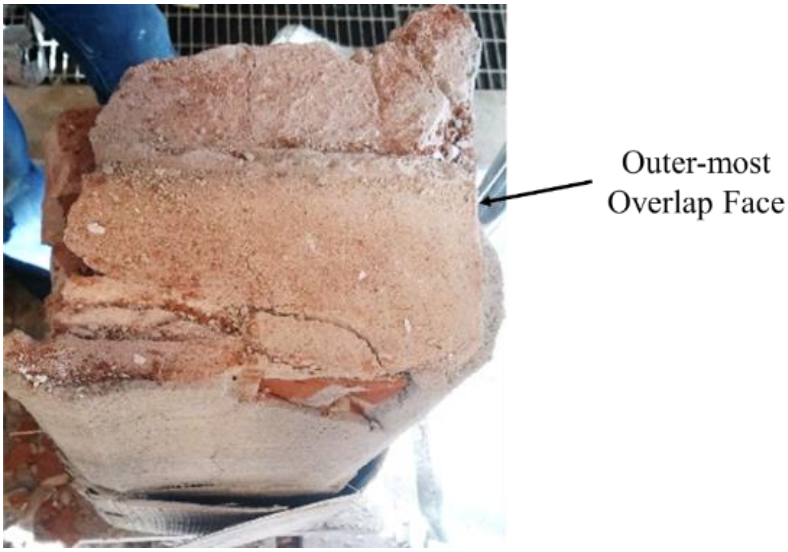

Figure 4.14. Asymmetric Arching Effect of Group 6 Specimens

4.3. DETERMINATION OF AXIAL DEFORMATION

During testing, the displacement was measured using four LVDTs, one placed at each corner of the top pressing plate. Figure 4.15 identifies the locations of the LVDTs about the front face of the column (Face 1). The measured displacements were used to determine if the specimens deformed symmetrically or asymmetrically. Since the bottom pressing plate was positioned on a swivel-head ball bearing system, rotation was allowed during testing. A column was determined to deform either symmetrically or asymmetrically by plotting measured displacements of the four LVDTs verses time and verses axial stress. Two general types of asymmetric responses were observed 1) deviation in displacement measurements before the peak stress was reached, or 2) deviation in displacement measurements after the peak stress was reached. Asymmetric response indicates nonuniform compression was applied to the columns, which in turn could influence the values of stress and strain, which are global values. This could explain the larger standard deviations of values reported for groups with one or more columns that exhibited asymmetric response.

Figure 4.16 shows an example of a symmetric response which created uniform deformation duration testing. Figure 4.17 shows the axial load verses axial displacement response of the corresponding specimen. As shown in Figures 4.16 and 4.17, the individual LVDT responses were parallel to the others, indicating uniform displacement throughout testing. It should be noted that values of the displacement resulting from compression are designated as positive in this study.

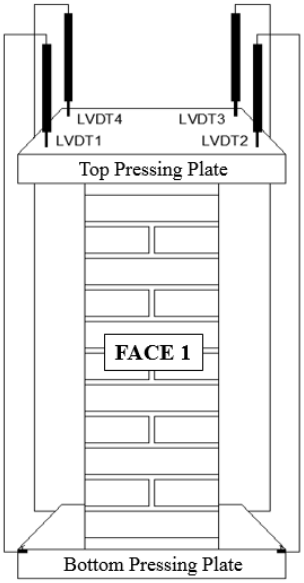

Figure 4.15. LVDT Locations

For columns that did not exhibit a symmetrical response, in general, included two different types of asymmetric responses – those that were asymmetric before the peak stress was reached (A1) and those that became asymmetric after the peak stress was reached (A2). Often, for specimens that had an A2 response, significant deviation occurred between the peak and ultimate stress points. Figure 4.18 shows an example of a specimen that did not deform uniformly beginning early in the test. In this case, the front face (Face 1) of the column deformed more than the back face of the column (Face 3). This non-uniformity could be due to many different reasons including the column not being perfectly level prior to testing, the column not being centered with the load cell potentially causing more damage to one face, or due to human error resulting in nonuniform column construction. Figure 4.19 shows the applied axial load – axial displacement response for the corresponding specimen.

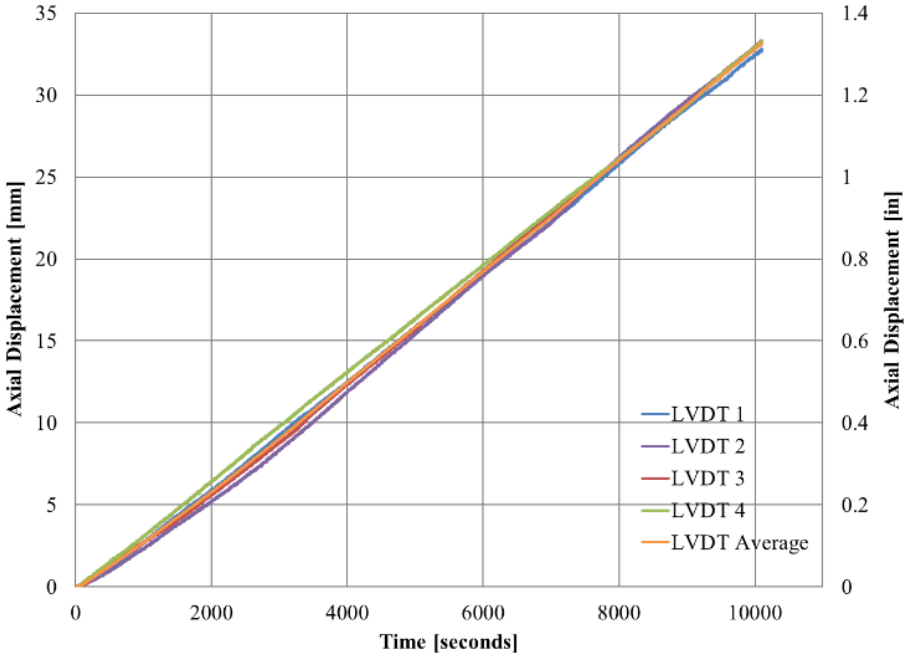

Figure 4.16. Example of Symmetric Axial Displacement Measured by LVDTs (Column C-12-0-2-3)

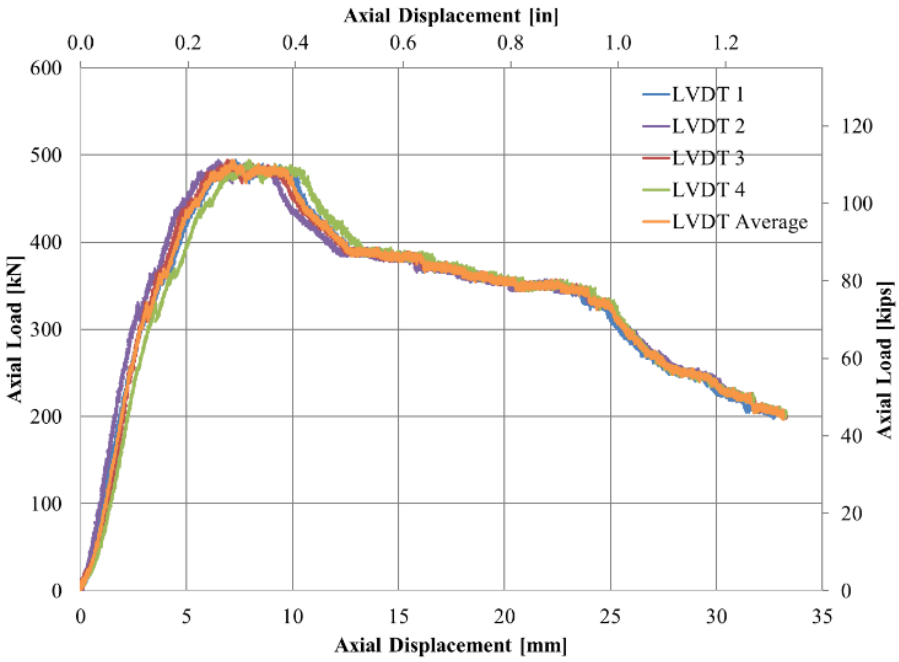

Figure 4.17. Axial Load vs. Axial Displacement Response of Specimen with Symmetric Axial Displacement Measured by LVDTs (C-12-0-2-3)

Figure 4.20 shows an example of a column that displaced uniformly until the ultimate applied load was reached. In general, the overlap region of confined column began to debond significantly for load levels between the peak load and ultimate load, allowing the column within to become disturbed and the transverse cracks to widen, thus allowing the tensile stresses within the composite systems to no longer be transferred from the substrate material to the reinforcing fiber within that particular region. Figure 4.21 shows the corresponding applied axial load – axial displacement response for the column of the same asymmetrical response. The shown response indicates increased compression at the locations of LVDT 3 and 4 (near the back face of the column).

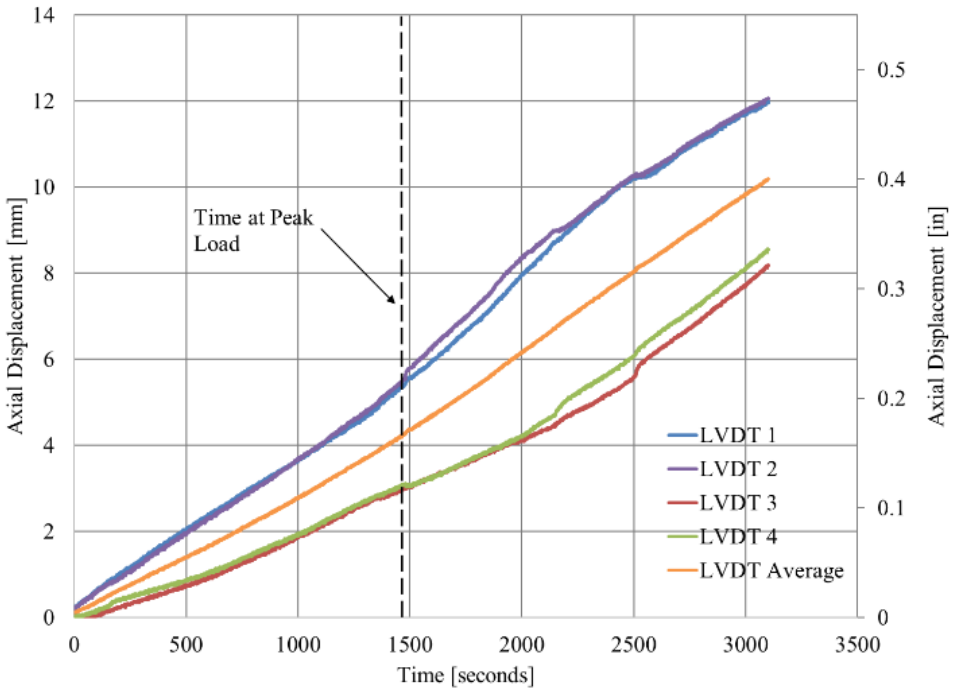

Figure 4.18. Example of Asymmetric (A1) Axial Displacement Measured by LVDTs (Column C-12-0-1-3)

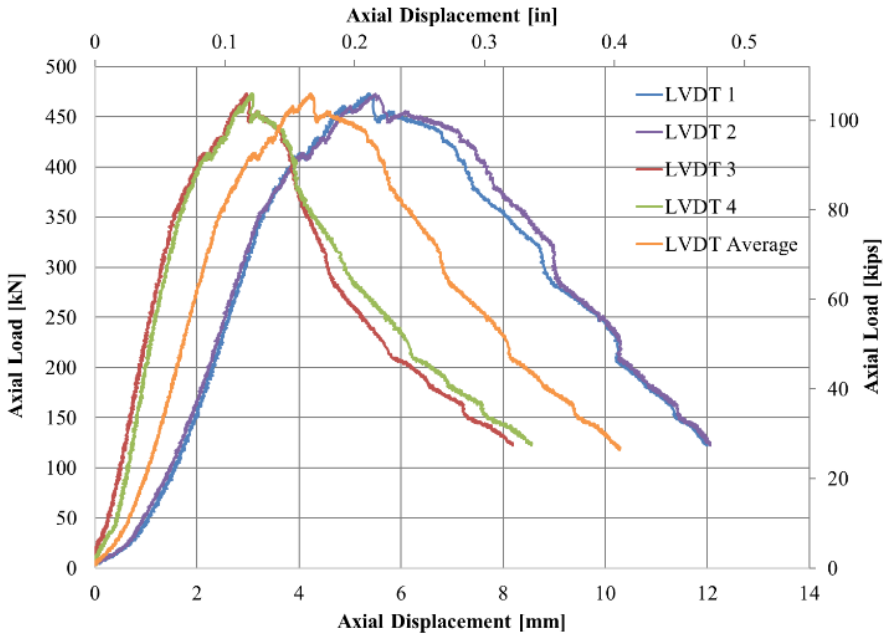

Figure 4.19. Axial Load vs. Axial Displacement Response of Specimen with A1 Asymmetric Axial Displacement Measured by LVDTs (C-12-0-1-3)

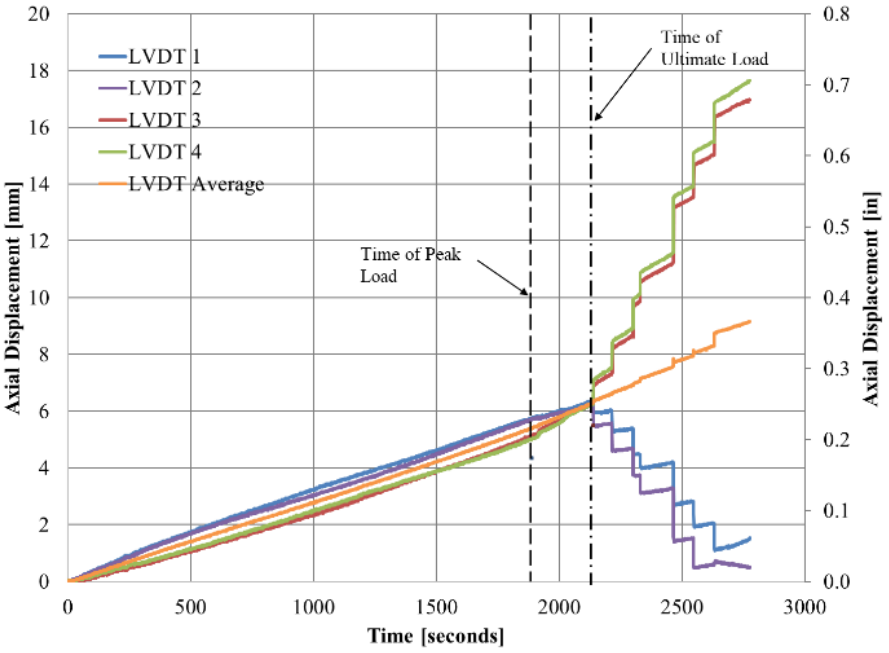

Figure 4.20. Example of Asymmetric (A2) Axial Displacement Measured by LVDTs (Column C-12-38-1(2)-3)

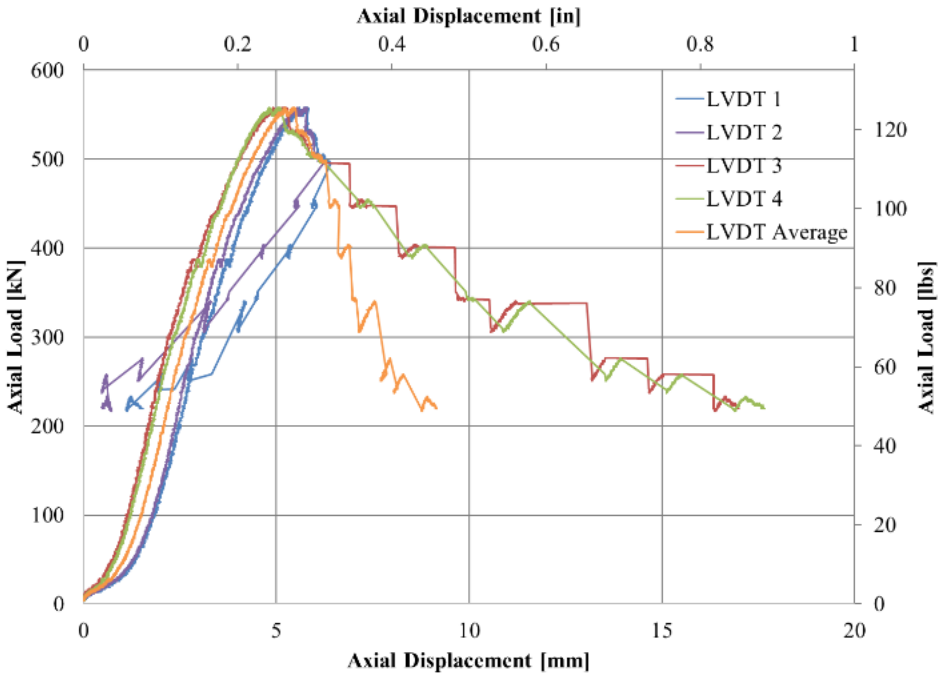

Figure 4.21. Axial Load vs. Axial Displacement Response of Specimen with A2 Asymmetric Axial Displacement Measured by LVDT (C-12-38-1(2)-3)

4.4. AXIAL STRESS - AXIAL STRAIN RESPONSE

This section presents the axial stress - axial strain responses for each specimen. The axial stress (f_m) was computed from the applied axial load measured by the load cell using Equation 4.1:

$$f_m = \frac{P}{A} \ (MPa) \qquad \text{Eq. 4.1}$$

where:

P is the applied axial load;

A is the cross-sectional area, equal to 60,025 mm^2 for the sharp cornered columns and 58,778 mm^2 for the rounded cornered columns

The axial strain (ε_m), was determined from the LVDT displacements (discussed in Section 4.3) using Equation 4.2:

$$\Delta u = \frac{u_{LVDT1} + u_{LVDT2} + u_{LVDT3} + u_{LVDT4}}{4} \rightarrow \varepsilon_m = \frac{\Delta u}{L} \qquad \text{Eq. 4.2}$$

where:

Δu = average change in displacement from initial displacement

L = initial height of the column excluding the caps at each end

u_{LVDTi} = displacement recorded by the i^{th} LVDT

The stroke displacement (ε) was compared to the axial displacement measured by the LVDTs to verify the columns behavior under applied axial compression. The stroke displacement was converted to strain using Equation 4.3:

$$\varepsilon = \frac{\Delta u_s}{L} \qquad \text{Eq. 4.3}$$

where:

Δu_s = change in displacement from initial stroke head location

In the sections that follow, the axial stress – axial strain relationship is reported for each group of specimens. Each group is plotted separately, and for the confined specimen Groups 1-6, the response of representative control specimens is also included

for comparison purposes. The ultimate axial stress – axial strain point, which corresponds to the point at which that applied load dropped to 85% of the peak applied load, is identified with a bolded "**X**" along the curves. For many specimens, the ultimate axial stress – axial strain point represents the point in which the jacket began to detach or deform significantly. This point also relates to the ductility of the specimen or its ability to withstand deformation beyond the column yield point without a significant loss in strength (Wight J. K., 2016).

The axial stress - axial strain relationships were used to compare the different specimens in the same group and to determine key values of axial stress and axial strain. Additionally, average values of peak axial stress and ultimate axial strain were determined for each group. These values are used to determine the efficacy of the confining system in improving the masonry column's strength and ductility compared to the unconfined condition. Using the same axial stress – axial strain curves, the energy absorbed by the specimens was computed as the area under the developed curve, as discussed in Section 4.5.

Table 4.1 summarizes the key values from the axial stress – axial strain responses. For the unconfined specimens, the peak stress and strain at peak stress are denoted as f_{mo} and ε_{mo}, respectively. The ultimate stress and ultimate strain of the unconfined specimens are denoted as $f_{mo,u}$ and $\varepsilon_{mo,u}$, respectively. For the confined specimens, the peak stress and strain at peak stress are denoted as f_{mc} and ε_{mc}, respectively. The ultimate stress and ultimate strain of the confined specimens are denoted as $f_{mc,u}$ and $\varepsilon_{mc,u}$, respectively. Average values for each series are also computed and are denoted with and overbar.

Table 4.1. Summary of Results

Specimen		f_{mo} or f_{mc}	$\overline{f_{mo}}$ or $\overline{f_{mc}}$	STD	CoV	$f_{mo,u}$ or $f_{mc,u}$	$\overline{f_{mo,u}}$ or $\overline{f_{mc,u}}$	ε_{mo} or ε_{mc}	$\overline{\varepsilon_{mo}}$ or $\overline{\varepsilon_{mc}}$	$\varepsilon_{mo,u}$ or $\varepsilon_{mc,u}$	$\overline{\varepsilon_{mo,u}}$ or $\overline{\varepsilon_{mc,u}}$	STD	CoV	Failure Mode	Axial Disp.
Group	**Name**	**MPa**	**MPa**	**MPa**	**%**	**MPa**	**MPa**	**mm / mm**	**mm / mm**	**mm / mm**	**mm / mm**	**mm / mm**	**%**	**C/O[1]**	**S/A1/ A2[2]**
Control	UC-1	7.65	6.62	0.73	11.0	6.50	5.59	0.0061	0.0061	0.0074	0.0078	0.0013	16.6	C	A1
	UC-2	6.16				5.21		0.0071		0.0079				C	S
	UC-3	6.47				5.48		0.0050		0.0051				C	A2
	UC-4	6.28				5.33		0.0063		0.0080				C	S
	UC-5	5.64				4.78		0.0056		0.0090				C	A1
	UC-6	6.61				5.48		0.0056		0.0087				C	A2
	UC-7	7.52				6.37		0.0072		0.0082				C	A2
Group 1	C-12-0-1-1	7.28	7.59	0.32	4.2	6.19	6.43	0.0093	0.0068	0.0102	0.0080	0.0015	18.3	O	S
	C-12-0-1-2	7.34				6.23		0.0062		0.0075				O	A1
	C-12-0-1-3	7.87				6.66		0.0052		0.0073				O	A1
	C-12-0-1-4	7.86				6.65		0.0066		0.0070				O	A1
Group 2	C-12-0-2-1	8.31	8.45	0.68	8.1	7.05	7.17	0.0081	0.0090	0.0103	0.0125	0.0024	18.9	O	S
	C-12-0-2-2	7.83				6.63		0.0072		0.0117				O	A1
	C-12-0-2-3	8.23				7.00		0.0099		0.0158				O	S
	C-12-0-2-4	9.42				8.00		0.0108		0.0121				O	S
Group 3	C-12-0-3-1	9.36	9.32	0.59	6.3	7.95	7.92	0.0112	0.0099	0.0374	0.0275	0.0.014	49.4	O	S
	C-12-0-3-2	10.05				8.53		0.0076		0.0142				O	S
	C-12-0-3-3	9.22				7.84		0.0114		0.0176				O	S
	C-12-0-3-4	8.63				7.35		0.0095		0.0409				O	S

Table 4.1. Summary of Results (Cont.)

Group 4	C-12-38-1-1	7.09	7.73	0.59	7.7	6.02	6.54	0.0071	0.0065	0.0081	0.0077	7E-04	9.6	O	A2
	C-12-38-1-2	7.96				6.76		0.0065		0.0075				O	A2
	C-12-38-1-3	8.43				7.17		0.0056		0.0067				O	A2
	C-12-38-1-4	7.42				6.22		0.0067		0.0084				O	A1
Group 5	C-12-38-1(2)-1	9.70	8.73	1.01	11.5	8.20	7.32	0.0081	0.0066	0.0099	0.0087	1E-03	11.1	O	A2
	C-12-38-1(2)-2	7.78				6.58		0.0057		0.0081				O	A1
	C-12-38-1(2)-3	9.50				7.76		0.0062		0.0078				O	A2
	C-12-38-1(2)-4	7.95				6.76		0.0066		0.0092				O	A2
Group 6	C-12-38-2-1	8.83	9.08	0.49	5.4	7.49	7.67	0.0064	0.0073	0.0074	0.0086	1E-03	11.1	O	A2
	C-12-38-2-2	8.66				7.32		0.0084		0.0096				O	A1
	C-12-38-2-3	9.77				8.18		0.0078		0.0092				O	A2
	C-12-38-2-4	9.06				7.70		0.0068		0.0082				O	A1

Note: (1) C = masonry crushing, O = jacketing opening
(2) S = All Corners Symmetric, A1 = Asymmetric before peak axial stress was reached, A2 = Asymmetric after peak axial stress
Conversions: 1 MPa = 145.038 psi, 1 mm/mm = 1 in/in

4.4.1. Unconfined (Control) Group. The axial stress – axial strain behavior of the unconfined specimens was characterized by an initial linear response followed by a non-linear descending branch after the peak load was achieved. During the descending branch, sharp drops in load were observed, which represent large cracks forming or growing while testing. The columns were considered to have failed based on the size of the cracks, the quantity of drops in the curve, and if the ultimate load had been reached. The responses are shown in Figure 4.22 and 4.23. The average peak stress of the Control Group was 6.62 MPa (STD = 0.73 MPa) and the average axial strain at peak stress was 0.0061 mm/mm (STD = 0.0008 mm/mm). The average ultimate stress of the Control Group was 5.59 MPa (STD = 0.62 MPa), and the average axial strain at ultimate stress was 0.0077 mm/mm (STD = 0.0013 mm/mm). The varying responses of the unconfined specimens shown in Figure 4.23 could be, in part, due to the different ages of the columns at testing. The age of the columns ranged from 56 days to 83 days. All columns were cured for 28 days and left uncovered for the remainder of the time until tested, as discussed in Section 3.3.2.

Figure 4.24 shows the idealized stress – axial strain relationship for masonry proposed by (Kaushik et al., 2007). The axial stress – axial strain curves of the confined specimens are similar in shape to the proposed idealized relationship, however the idealized relationship overestimates the strain in the descending branch of the curve for mortar with lime. The descending branch which correlates with mortar without lime better represents the behavior of the unconfined specimens in this study. Axial stress – axial strain responses for individual specimens are found in Appendix B, Figure B.1-B.8.

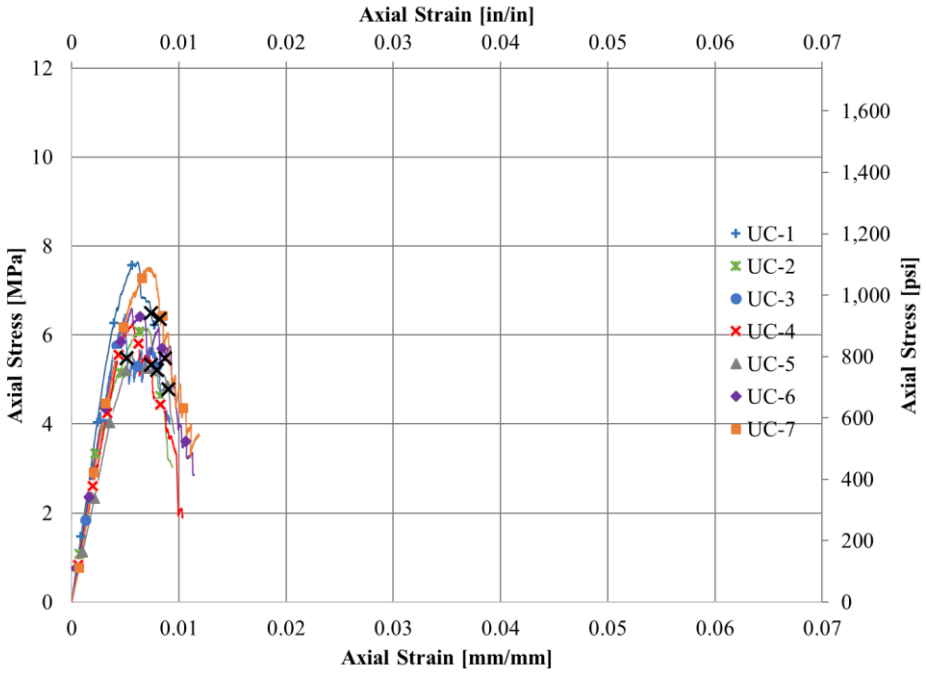

Figure 4.22. Control Group: Axial Stress - Axial Strain Response

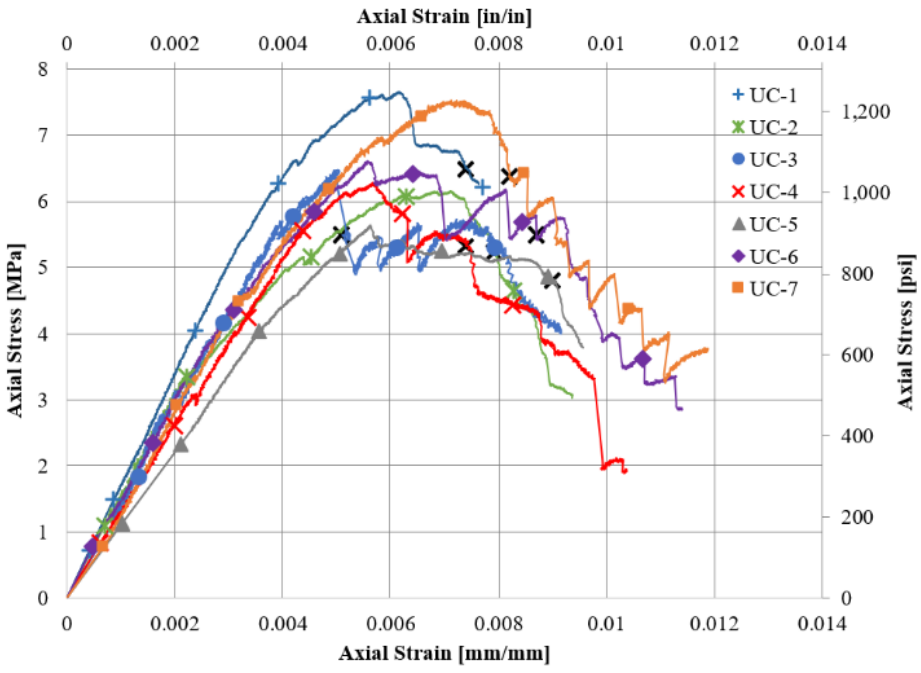

Figure 4.23. Control Group: Axial Stress - Axial Strain Response (Revised Scales)

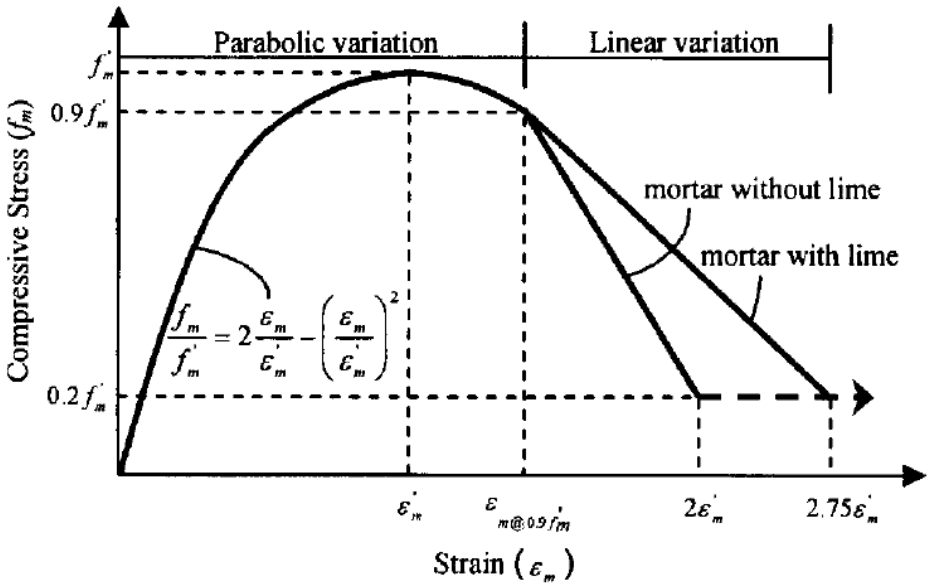

Figure 4.24. Idealized Stress - Strain Curve for Masonry (Kaushik et al., 2007)

4.4.2. Group 1. The axial stress - axial strain relationships for specimens in Group 1, were similar to those of the unconfined specimens. The curves showed an initial linear response. Immediately after the peak load a sharp drop was observed, representing the opening of the overlap fibers, followed by a rapid descent until failure (Figure 4.25). The average peak axial stress and average axial strain at the peak stress for Group 1 specimens was 7.59 MPa (STD = 0.32 MPa) and 0.0068 mm/mm (STD = 0.0017 mm/mm), respectively. The average ultimate axial stress and average axial strain for Group 1 specimens was 6.43 MPa (STD = 0.26 MPa) and 0.0080 mm/mm (STD = 0.0015 mm/mm), respectively. The average increase in peak confining axial stress compared to the control specimens was 15%, and the average increase in ultimate axial strain was 3%. These results indicate that the addition of the confining system, slightly improved the overall compressive strength and ductility of the columns. Axial stress –

axial strain responses for individual specimens are found in Appendix B, Figure B.9-B.12.

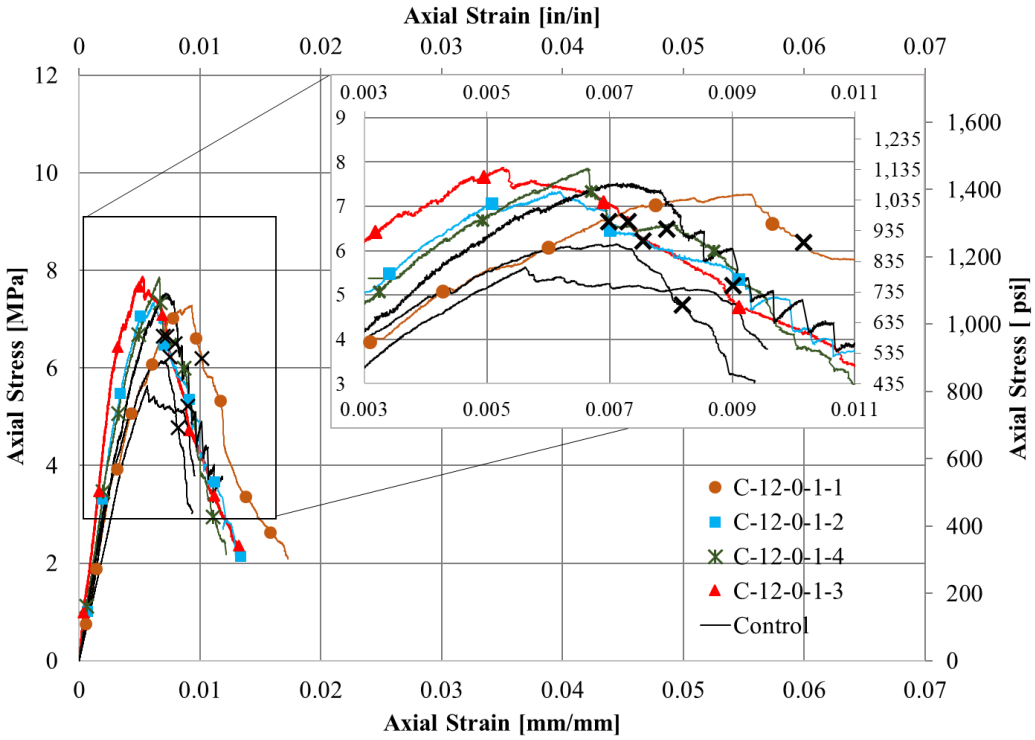

Figure 4.25. Group 1: Axial Stress - Axial Strain Response

4.4.3. Group 2. The axial stress - axial strain relationships for the specimens in Group 2 showed a significant increase in ultimate axial strain relative to the unconfined specimens, thus increasing the ductility of the columns. The initial response was linear, similar to the unconfined specimens. The post-peak response included a sharp drop due to detachment of the outer-most layer of fibers at the overlap, however most of the responses were followed by a plateaued region until column failure, as shown in Figure

4.26. The average peak axial stress and average axial strain at the peak stress for Group 2 specimens was 8.45 MPa (STD = 0.68 MPa) and 0.0090 mm/mm (STD = 0.0017 mm/mm), respectively. The average ultimate axial stress and average axial strain for Group 2 specimens was 7.17 MPa (STD = 0.59 MPa) and 0.0125 mm/mm (STD = 0.0024 mm/mm), respectively. The average increase in peak axial stress compared to the control specimens was 28%, and the average increase in ultimate axial strain was 61%. These results indicate that the confinement system, in this case, improved the overall compressive strength and ductility of masonry columns. Axial stress – axial strain responses for individual specimens are found in Appendix B, Figure B.13-B.16.

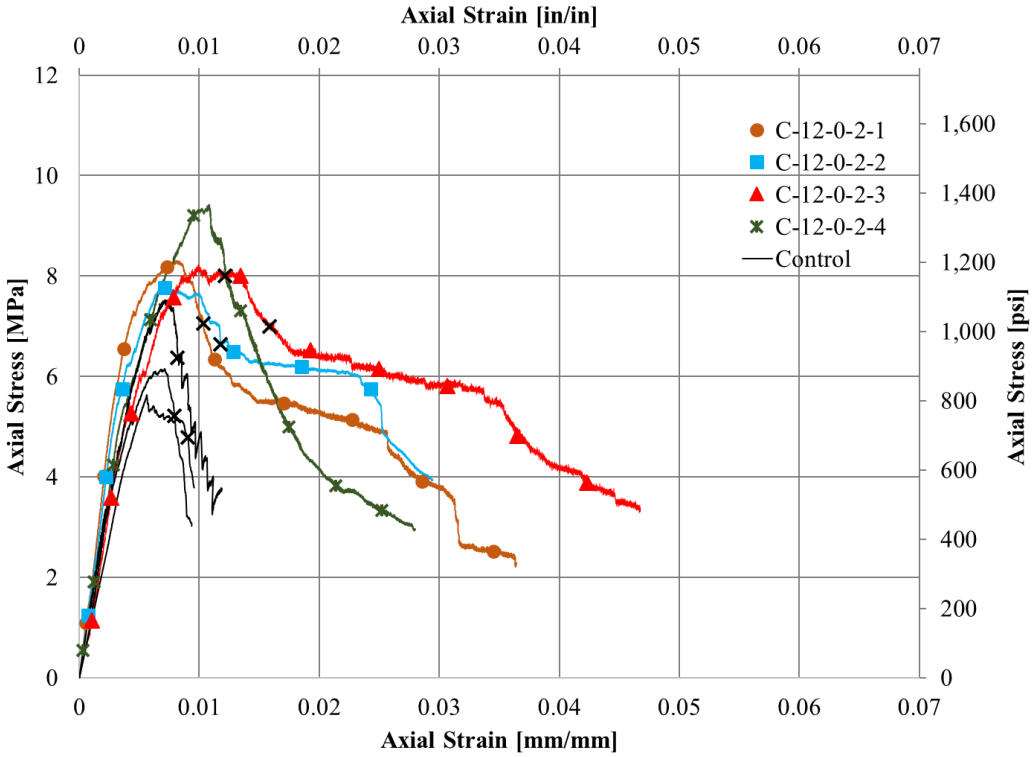

Figure 4.26. Group 2: Axial Stress - Axial Strain Response

4.4.4. Group 3. The axial stress - axial strain relationships for specimens in Group 3 showed an initial linear response. After the peak load was reached, the post-peak response included a sharp drop in the curve caused by debonding of the third (outer-most) fiber layer, followed by a plateaued region. This region allowed for a significant increase in the ultimate axial strain compared to the Control Group specimens. At the end of the plateaued region there was a sharp drop in stress caused by partial detachment of the second fiber layer (Figure 4.27). The average peak axial stress and average axial strain at peak stress for Group 3 specimens was 9.32 MPa (STD = 0.59 MPa) and 0.0099 mm/mm (STD = 0.0017 mm/mm), respectively. The average ultimate axial stress and average ultimate axial strain for Group 3 was 7.92 MPa (STD = 0.48 MPa) and 0.0275 mm/mm (STD = 0.0136 mm/mm), respectively. The average increase in peak compressive stress compared to the control series was 41%, and the average increase in ultimate axial strain was 258%. These results indicate that the confinement system significantly improved the overall compressive strength and ductility of the masonry columns. Axial stress – axial strain responses for individual specimens are found in Appendix B, Figure B.17-B.20.

4.4.5. Group 4. The axial stress - axial strain relationships for specimens in Group 4 were similar to those of the unconfined specimens. The initial response was linear followed by a post-peak response of a rapid descending branch. Drops in the descending branch were due to the fiber jacket debonding from multiple column faces (Figure 4.28). The average peak axial stress and average axial strain at peak stress for Group 4 specimens was 7.73 MPa (STD = 0.59 MPa) and 0.0065 mm/mm (0.0007 mm/mm), respectively.

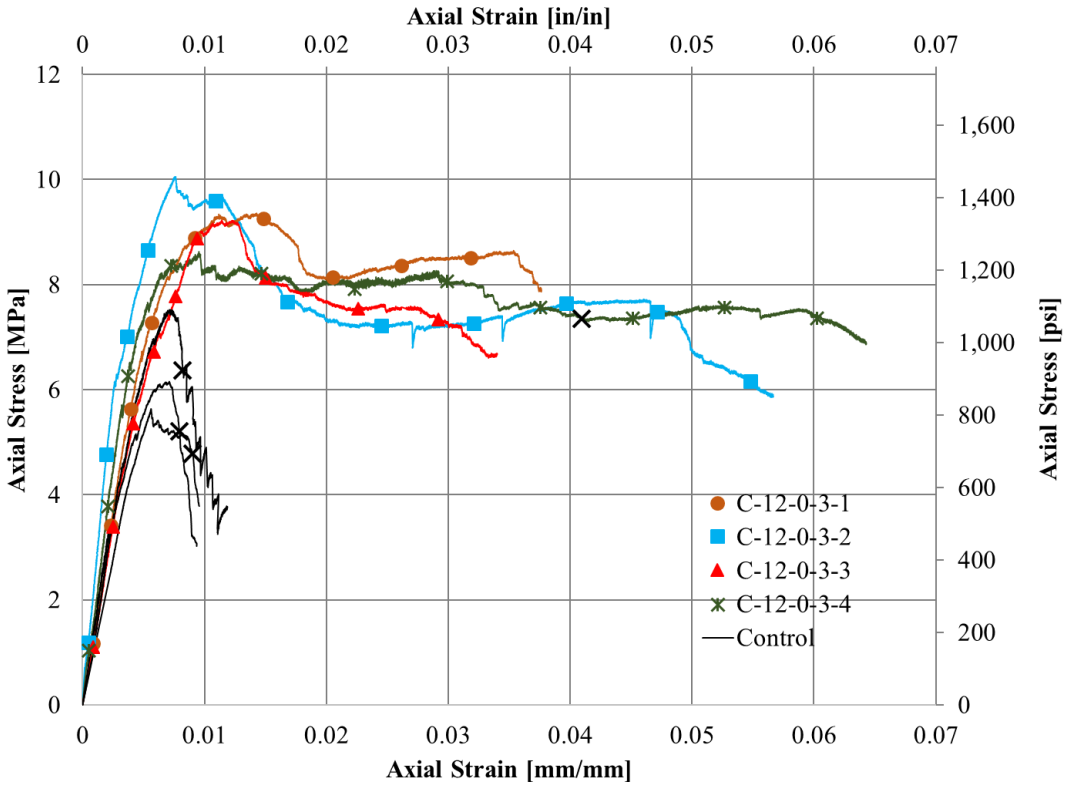

Figure 4.27. Group 3: Axial Stress - Axial Strain Response

The average ultimate axial stress and average ultimate axial strain for Group 4 was 6.54 MPa (STD = 0.52 MPa) and 0.0077 mm/mm (STD = 0.0007 mm/mm), respectively. The average increase in peak axial stress compared to the control group was 17%, but the average ultimate axial strain did not increase from the results of the control specimens. These results indicate that the confining system for Group 4 improved the overall compressive strength of the column but did not improve the ductility in terms of axial strain. Axial stress – axial strain responses for individual specimens are found in Appendix B, Figure B.21-B.24.

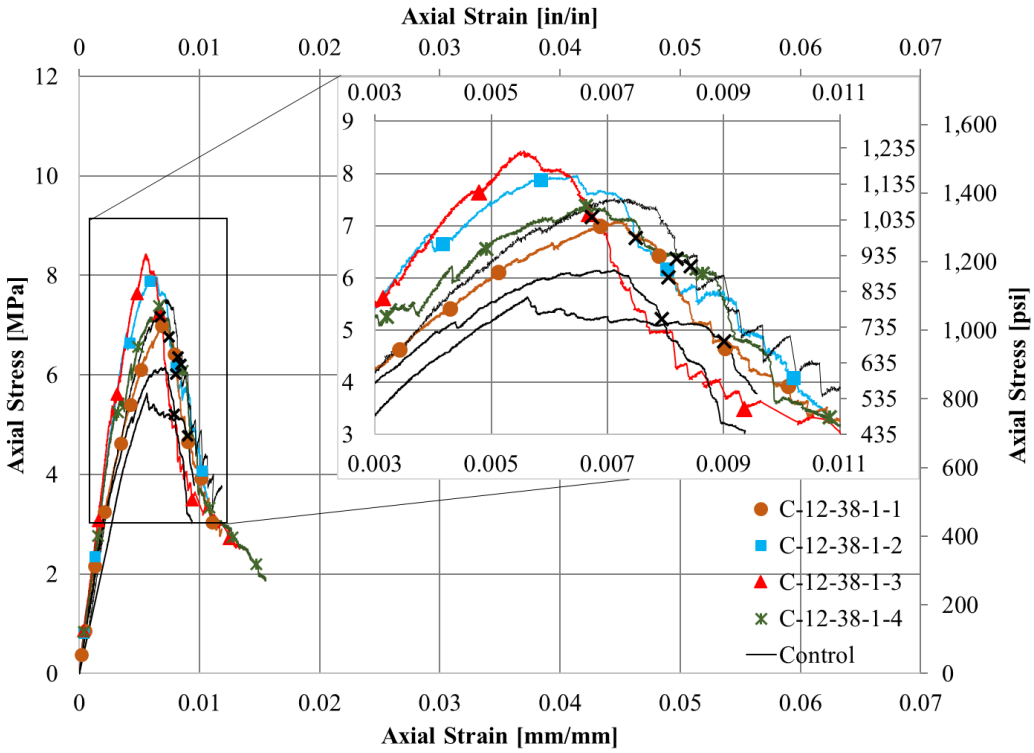

Figure 4.28. Group 4: Axial Stress - Axial Strain Response

4.4.6. Group 5. The axial stress - axial strain relationships for specimens in Group 5 were similar to those of the unconfined specimens, but overall had larger peak axial stress. The initial response was linear followed by a post-peak response including frequent drops in the curve. The drops were due to the fiber jacket debonding on multiple faces (Figure 4.29).

The average peak axial stress and average axial strain at peak stress for Group 5 specimens was 8.73 MPa (STD = 1.01 MPa) and 0.0066 mm/mm (STD = 0.0011 mm/mm), respectively. The average ultimate axial stress and average ultimate axial strain for Group 5 specimens was 7.32 MPa (STD = 0.78 MPa) and 0.0087 mm/mm (STD = 0.0010 mm/mm), respectively. The average increase in peak compressive strength

compared to the control group was 32%, and the average increase in ultimate axial strain was 14%. These results indicate that the confining system in this group, improved the overall strength and ductility of the column. It is important to note there was a larger standard deviation (STD) for the peak strength results compared to other confined masonry columns with rounded corners. The large STD is likely due the asymmetric axial displacement response of the columns according to the LVDT readings, similar to that described in Section 4.3 and shown in Figure 4.20 and 4.21. Axial stress – axial strain responses for individual specimens are found in Appendix B, Figure B.25-B.28.

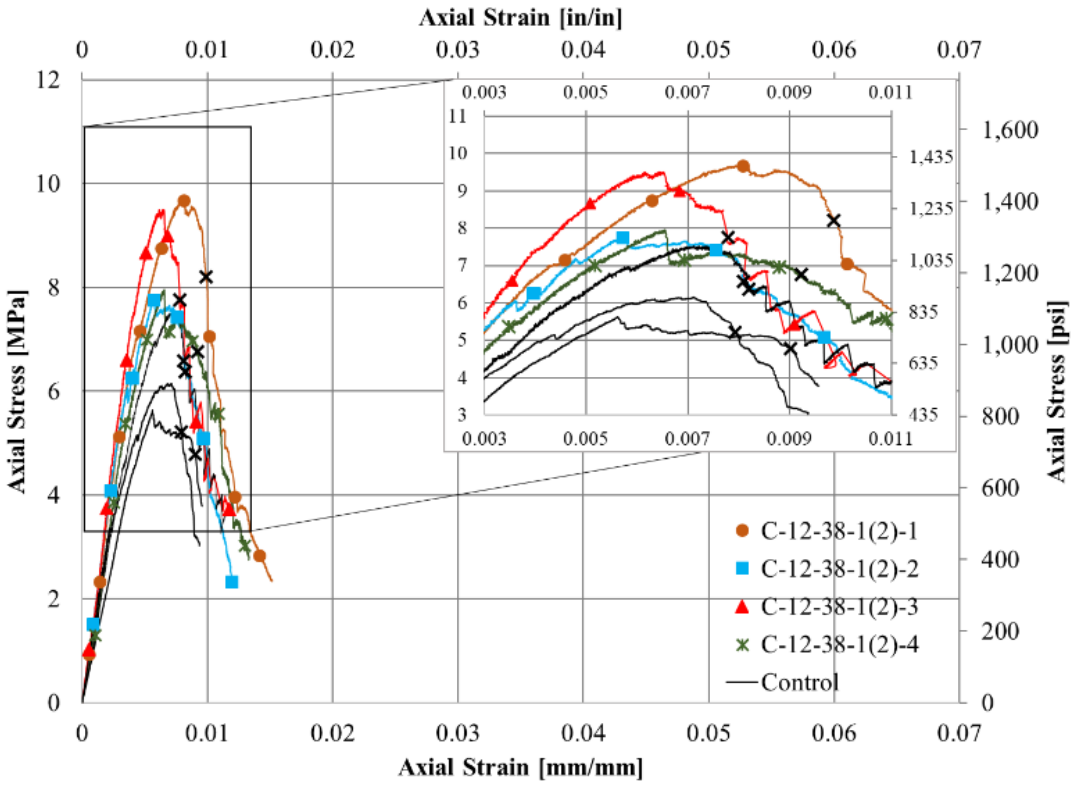

Figure 4.29. Group 5: Axial Stress - Axial Strain Response

4.4.7. Group 6. The axial stress - axial strain relationships for specimens in Group 6 were similar to the unconfined specimens, however they had a higher peak axial stress and ultimate axial strain. The initial response was linear. Immediately after the peak load, a drop in the curve occurred due to debonding of the outer-most fiber layer. Following the drop, the curve descended more gradually than the unconfined specimens due to the addition of the two-layer jacket (Figure 4.30). The average peak axial stress and average axial strain at peak stress for Group 6 specimens was 9.08 MPa (STD = 0.49 MPa) and 0.0073 mm/mm (STD = 0.0009 mm/mm), respectively. The average ultimate axial stress and average ultimate axial strain for Group 6 specimens was 7.67 MPa (STD = 0.37 MPa) and 0.0086 mm/mm (STD = 0.0010 mm/mm), respectively. The average increase in peak compressive stress compared to the control group was 37%, and the increase in ultimate axial strain was 12%. These results indicate that the addition of the confining system for Group 6 improved the strength and ductility of the column. Axial stress – axial strain responses for individual specimens are found in Appendix B, Figure B.29-B.28.

4.5. ENERGY ABSORPTION

The axial stress – axial strain responses presented in Section 4.4 were analyzed in terms of energy absorption of the masonry columns, and the results are summarized in Table 4.2. The absorbed energy, E_m, is determined for each unconfined and confined specimen as the area under the axial stress - axial strain curves, $\Sigma\ (df \cdot d\varepsilon)$. Values reported in Table 4.2 include the peak unconfined or confined energy, E_{mo} or E_{mc}; the total unconfined or confined energy, $E_{mo,u}$ or $E_{mc,u}$; the ratio of the average total confined

energy to the average peak confined energy $\frac{\overline{E_{mc,u}}}{\overline{E_{mc}}}$; and, the ratio of the average total confined energy to the average total unconfined energy, $\frac{\overline{E_{mc,u}}}{\overline{E_{mo,u}}}$. It is important to note that the total energy, confined or unconfined, was measured as the area under the axial stress - axial strain curve from the start of the curve to the ultimate point. The reasoning behind this measurement was that the ultimate point was a definitive "failure" point on all curves, while the point at which the test was terminated varied per column.

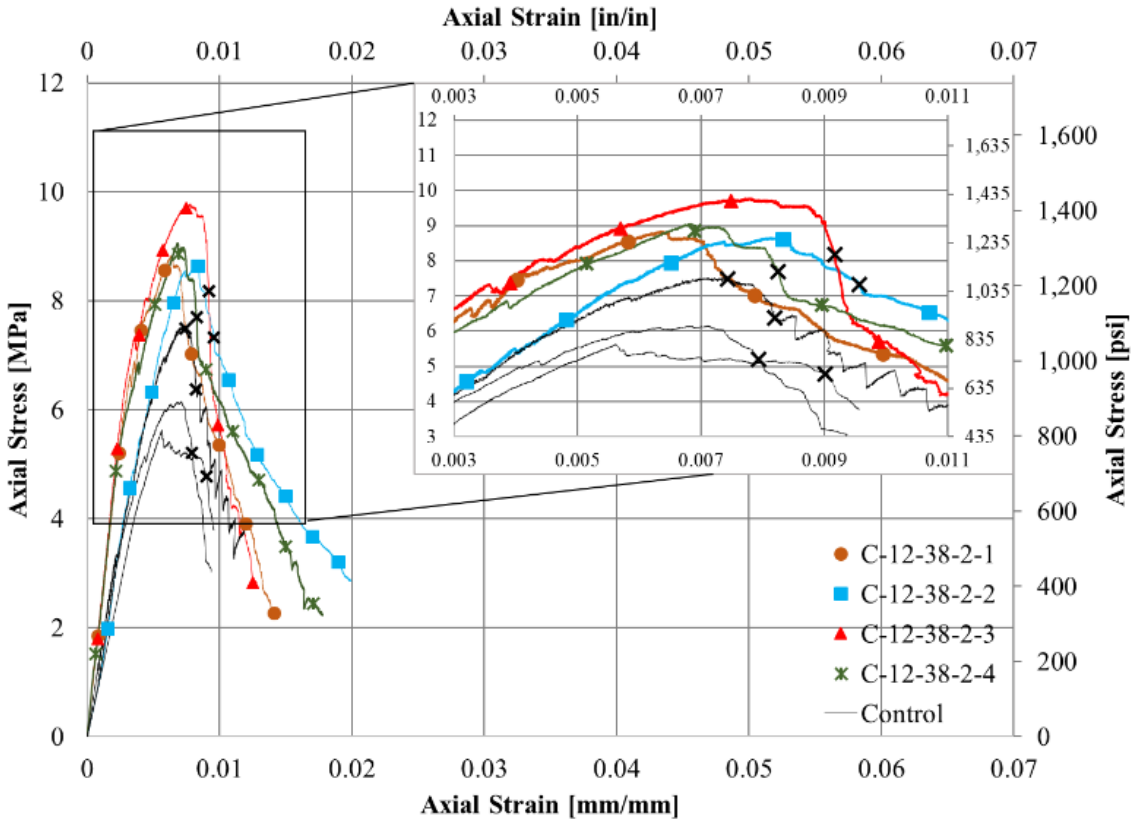

Figure 4.30. Group 6: Axial Stress – Axial Strain Response

The control group specimens had an average total energy absorbed, $\overline{E_{mo,u}}$, of 0.0333 MJ/m^3 (STD = 0.0074 MJ/m^3). Regarding the sharp cornered specimens (Group 1, 2, 3), the ratio $\frac{\overline{E_{mc,u}}}{\overline{E_{mo,u}}}$ ranged from 1.21 to 6.27 and increased with increasing number of fiber layers. This result indicates that additional jacket layers increase the total energy absorbed thus increasing the masonry column's ductility. Regarding the round cornered specimens (Group 4, 5, 6), the ratio $\frac{\overline{E_{mc,u}}}{\overline{E_{mo,u}}}$ ranged from 1.19 to 1.61. Comparing Groups 4 and 6 with one and two fiber layers, respectively, the results show that the energy absorbed increased with increasing number of fiber layers, but not as significantly as the sharp cornered columns. The energy absorbed was less significant for round cornered columns because the corners of the sharp cornered columns crushed due to the confining action of the composite, allowing for an increase in axial strain at ultimate stress and an increase in energy absorbed. The ratio $\frac{\overline{E_{mc,u}}}{\overline{E_{mo,u}}}$ is important because it depicts the increase in total absorbed energy compared to an unconfined column, proving the confinement system was activated and enhancing the columns strength and deformation capacity.

The ratio of the average ultimate energy to the average peak energy $\frac{\overline{E_{mc,u}}}{\overline{E_{mc}}}$, was compared for each group of specimens. The ratio is important because it shows the ductility of a column and its response after the peak load was reached. Regarding the sharp cornered specimens (Groups 1, 2, 3), the ratio ranged from 1.25 to 3.04 and increased with increasing number of fiber layers. This result indicates, that column ductility increases with the number of layers added. For the round cornered specimens (Groups 4, 5, 6), the ratio ranged from 1.29 to 1.46. Comparing Groups 4 and 6 with one

and two fiber layers, respectively, the results indicate that column ductility does not increase significantly with the addition of fiber layers. Comparing Groups 4 and 5 with one layer of fibers and one or two overlapping faces, respectively, the results show that by increasing the overlapping faces, the ductility increases. Comparing sharp and round cornered columns, sharp corned columns allowed for an increase in $\frac{\overline{E_{mc,u}}}{\overline{E_{mc}}}$ since the behavior of the descending branch of the axial stress-strain curves was more gradual, especially in the three-layered case. Rounded columns did not have a significant increase in this ratio since the axial stress – axial strain relationships reflected that of the unconfined specimens.

4.6. TRANSVERSE STRAIN – AXIAL STRAIN RESPONSE

Transverse strain measurements on the jacket fibers of four confined specimens included in this study were collected experimentally using strain gauges. Transverse strain responses were measured for two columns from Group 1 and two columns from Group 4. A single strain gauge was attached to each face of a specimen (four total per column) at the mid-height as discussed in Section 3.4.3. Individual strain readings of each face and average values considering all four readings were analyzed and are discussed in the sections that follow. Table 4.3 summarizes the strain reading at peak and ultimate points for each column. $\overline{\varepsilon_{mc,t}}$ and $\overline{\varepsilon_{mc,t,u}}$are the average transverse strain measurements of the four individual strain gauges per specimen at the peak and ultimate point, respectively. Tensile strains are indicated as negative. Found in Appendix B is a table summarizing the individual strain readings at the peak and ultimate points.

Table 4.2. Energy Absorption Capacity of Specimens

Specimen		E_{mo} or E_{mc}	$\overline{E_{mo}}$ or $\overline{E_{mc}}$	STD	$E_{mo,u}$ or $E_{mc,u}$	$\overline{E_{mo,u}}$ or $\overline{E_{mc,u}}$	STD	$\frac{\overline{E_{mc,u}}}{\overline{E_{mc}}}$	$\frac{\overline{E_{mc,u}}}{\overline{E_{mo,u}}}$
Group	**Name**	$\left(\frac{\mathbf{MJ}}{\mathbf{m^3}}\right)$	$\left(\frac{\mathbf{MJ}}{\mathbf{m^3}}\right)$	$\left(\frac{\mathbf{MJ}}{\mathbf{m^3}}\right)$	$\left(\frac{\mathbf{MJ}}{\mathbf{m^3}}\right)$	$\left(\frac{\mathbf{MJ}}{\mathbf{m^3}}\right)$	$\left(\frac{\mathbf{MJ}}{\mathbf{m^3}}\right)$	-	-
Control	UC-1	0.0287	0.0236	0.0061	0.0374	0.0333	0.0074	1.41	-
	UC-2	0.0288			0.0335				
	UC-3	0.0178			0.0184				
	UC-4	0.0200			0.0297				
	UC-5	0.0170			0.0349				
	UC-6	0.0209			0.0398				
	UC-7	0.0323			0.0393				
Group 1	C-12-0-1-1	0.0433	0.0322	0.0077	0.0490	0.0403	0.0066	1.25	1.21
	C-12-0-1-2	0.0281			0.0373				
	C-12-0-1-3	0.0260			0.0410				
	C-12-0-1-4	0.0312			0.0337				
Group 2	C-12-0-2-1	0.0470	0.0499	0.0120	0.0641	0.0773	0.0146	1.55	2.32
	C-12-0-2-2	0.0361			0.0704				
	C-12-0-2-3	0.0516			0.0977				
	C-12-0-2-4	0.0650			0.0769				
Group 3	C-12-0-3-1	0.0982	0.0685	0.0211	0.2958	0.2086	0.1076	3.04	6.27
	C-12-0-3-2	0.0500			0.1113				
	C-12-0-3-3	0.0678			0.1198				
	C-12-0-3-4	0.0581			0.3076				
Group 4	C-12-38-1-1	0.0315	0.0307	0.0026	0.0376	0.0396	0.0033	1.29	1.19
	C-12-38-1-2	0.0329			0.0406				
	C-12-38-1-3	0.0270			0.0364				
	C-12-38-1-4	0.0315			0.0437				
Group 5	C-12-38-1(2)-1	0.0486	0.0351	0.0099	0.0648	0.0514	0.0092	1.46	1.54
	C-12-38-1(2)-2	0.0258			0.0438				
	C-12-38-1(2)-3	0.0360			0.0479				
	C-12-38-1(2)-4	0.0299			0.0489				
Group 6	C-12-38-2-1	0.0359	0.0424	0.0065	0.0449	0.0534	0.0081	1.26	1.61
	C-12-38-2-2	0.0438			0.0531				
	C-12-38-2-3	0.0508			0.0644				
	C-12-38-2-4	0.0389			0.0513				

Shown in Figure 4.31 is the axial stress – strain response for each specimen. The curve to the right of the origin is the axial stress – axial strain relationship for each specimen as discussed previously. The curve to the left of the origin, indication as negative or tensile strain, the is average axial stress – transverse strain relationship for each specimen considered.

Table 4.3. Summary of Results - Transverse Strain Data

Specimen		f_{mc}	$f_{mc,u}$	ε_{mc}	$\varepsilon_{mc,u}$	$\overline{\varepsilon_{mc,t}}$	$\overline{\varepsilon_{mc,t,u}}$
Group	**Name**	**MPa**	**MPa**	**mm/mm**	**mm/mm**	**mm/mm**	**mm/mm**
Group 1	C-12-0-1-3	7.56	6.40	0.00524	0.00730	-0.00068	-0.00046
	C-12-0-1-4	7.55	6.39	0.00663	0.00698	-0.00045	-0.00022
Group 4	C-12-38-1-3	8.09	6.88	0.00556	0.00673	-0.00081	-0.00070
	C-12-38-1-4	7.12	5.97	0.00666	0.00843	-0.00030	-0.00031

4.6.1. Group 1 Specimens. Regarding the two specimens in Group 1 with transverse strain gages, values in Table 4.3 indicate that the peak axial stress and axial strain at peak stress had similar values (within 0.13% and 23%, respectively). Additionally, the ultimate point values are also similar (within 0.16% and 5%, respectively). However, at the peak and ultimate points, the average transverse strain reading for each specimen significantly differed (41% and 71% different, respectively). For both columns, the average transverse strain values at the ultimate axial stress were lower than at the peak axial stress, indicating more tension in the fibers at the peak axial point.

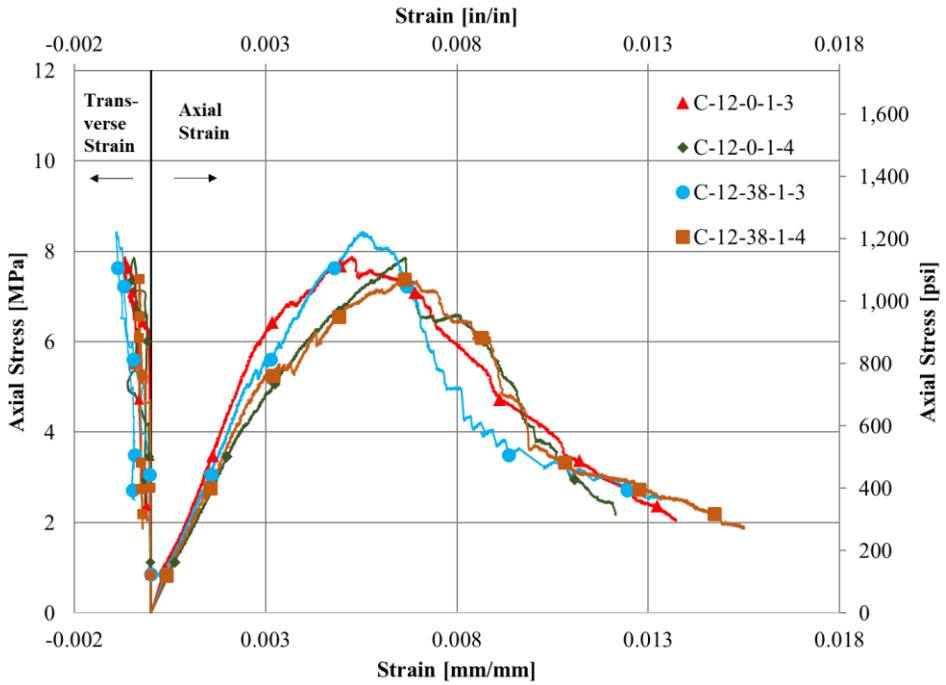

Figure 4.31. Average Axial Stress - Strain Relationship for Confined Columns with Strain Gages on Jacket Fibers

Regarding Specimen C-12-0-1-3, the axial stress – transverse strain behavior shown in Figure 4.32, indicates the point the confinement system began to engage (approximately 6 MPa in Figure 4.32). At this stress, the slope of the axial stress – axial strain response started to decrease. Markers in Figure 4.32 indicate the peak and ultimate stress points. Between the points, the average transverse strain reduced (or decreased in tension). The reduced tension was caused by the overlap fibers significantly debonding from the column or the crushing of the column corners.

Regarding the individual strain readings, all strain gages showed a significant increase in tensile strain before the peak stress was reached, indicating all faces were activated before this point. At the point of peak stress, found in Appendix B, Table B.2

and Figure 4.33, the face with the largest tensile strain was the left face. This indicates the left face is the most engaged at this point in time. After the point of ultimate stress, the transverse strain decreased in all gages correlating to the failure of the jacket through debonding.

Figure 4.33 shows the response of the individual gauges in terms of transverse strain verses time. The transverse strain values reported in Figure 4.33 are the absolute value of the tensile transverse strain measured. The following list is a discussion of key points in time or regions on the curves. Figures 4.34 and 4.35 show the corresponding damage to the specified column.

1. At this point in time during the test, the exterior matrix near the top, back face began to detach and crumble off the column. This caused a steep increase in strain for the front and left facing fibers due to the stress redistribution.
2. At this region, multiple horizontal cracks formed near the top of the left face of the specimen causing the transverse strain to rapidly decrease. This allowed the energy absorbed to be redistributed to the back and interior-most front face.
3. At this point in time, the front overlapping region of the fibers mostly detached. In addition, the applied stresses were redistributed to all other faces of the column causing an increase in tensile strain.
4. At this region, the matrix mortar continued to crumble on the back face and partially detach from the top of the specimen. This was evident because the steel fibers were exposed and detached from the column surface due to the exterior matrix mortar layer crumbling from the column. Due to the

detachment of the mortar and fibers, the energy absorbed was primarily redistributed to the left face.

5. At this region, a horizontal crack continued to form near the top and mid-height of the left face, and the exterior-most matrix began to crumble off. On the front face, the interior fiber layer began to detach from the face of the column. This started the process of detachment for the right face.
6. At this point in time, due to horizontal cracks forming and matrix crumbling from the back and left faces, applied stresses were redistributed to the right face. Soon after but before the ultimate axial stress was reached, the right face partially detached. At this point, multiple column faces had either completely or partially detached, causing a decrease in energy that could be absorbed by the confining system.

Appendix B, Figure B.36 shows the relationship between axial stress and transverse strain for this confined column. All curves showed an initial steeply sloped branch corresponding to negligible transverse strain values. After reaching the approximate unconfined masonry strength, the transverse strain increased as the confinement system was activated. After the peak load of the confined specimen was reached, the transverse strain measurements began to deviate from each other. This deviation was due to the location of the gages with respect to the fiber overlap. Throughout the response, the strain gage on the front face (overlap face) registered the smallest transverse strain values. In general, the strain gage on the left face registered the largest transverse strain, since it would be the last face to fully debond from the column, with the exception of the interior-most layer of the front face (underneath the overlap).

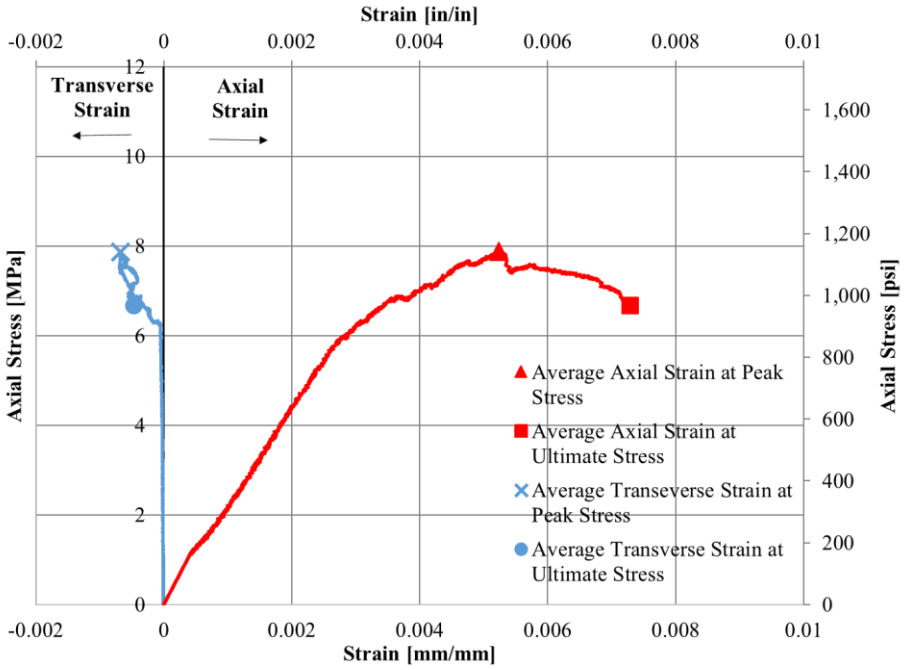

Figure 4.32. Specimen C-12-0-1-3: Axial Stress - Strain Curves

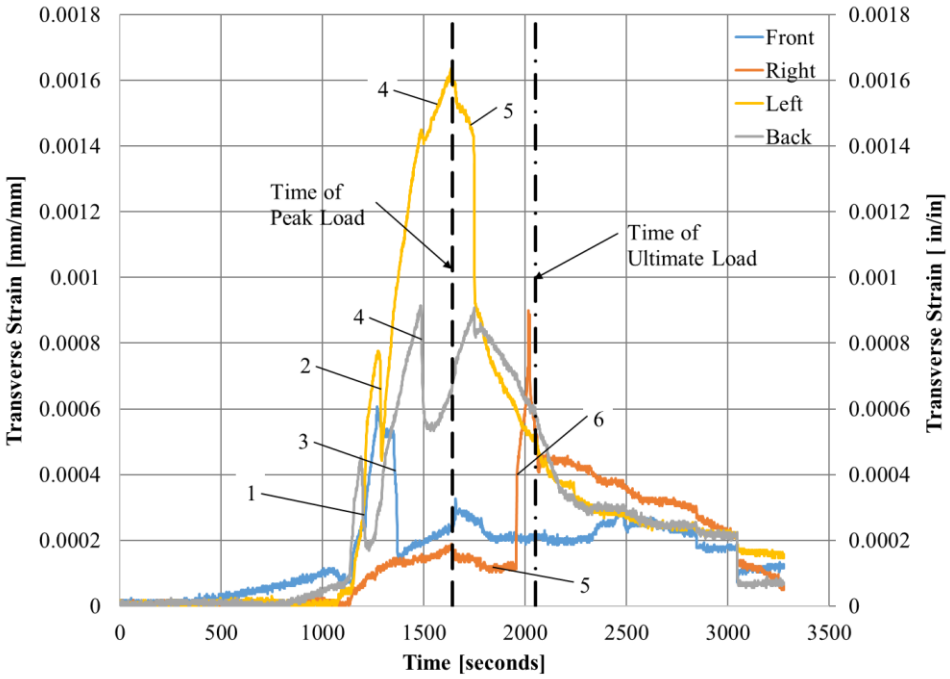

Figure 4.33. Specimen C-12-0-1-3: Transverse Strain vs. Time Response

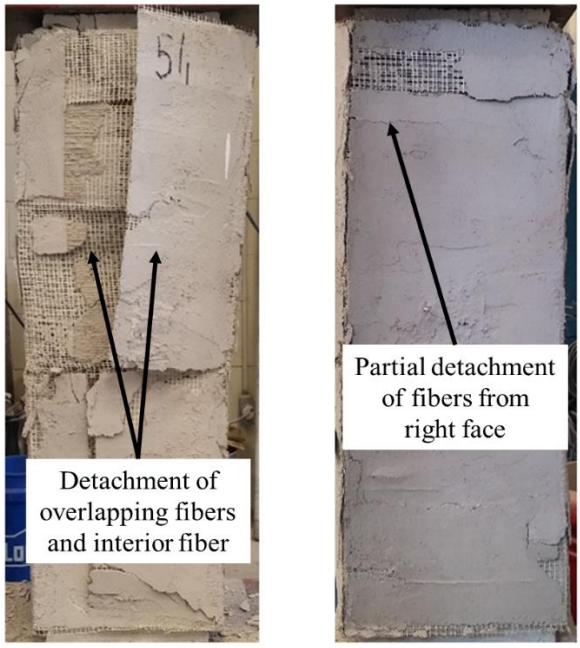

Figure 4.34. Specimen C-12-0-1-3 Damage After Testing: Front and Right Faces

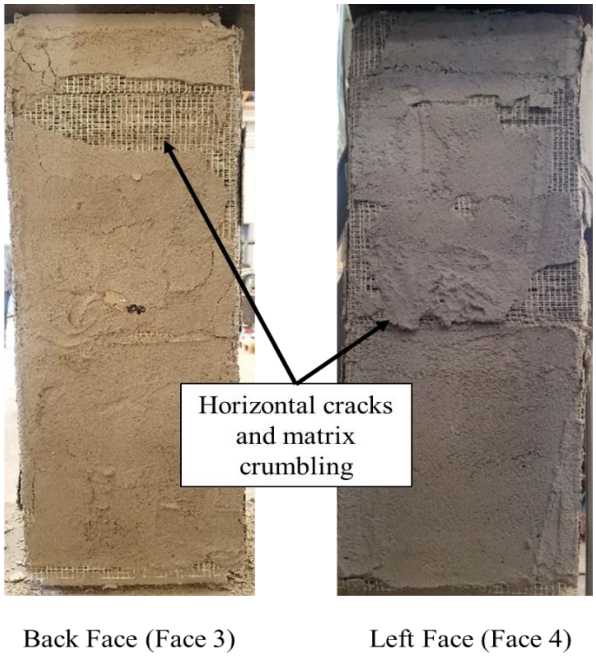

Figure 4.35. Specimen C-12-0-1-3 After Testing: Back and Left Faces

Regarding Specimen C-12-0-1-4, the axial stress – transverse strain behavior shown in Figure 4.36, indicates when the confinement system began to engage point (approximately 4 MPa in Figure 4.36). At this point, the tension began to increase within the fiber, while the matrix began to gradually detach from the first matrix layer. Between the average peak and ultimate stress points, the average transverse strain reduced (or decreased in tension). The reduced tension was caused by the overlap significantly debonding from the column or the crushing of the column corners.

Regarding the strain readings reported by the individual strain gages, significant increases in tensile strains were measured before the point of peak stress. This indicates that all faces of the jacket were active before this point. At the point of peak stress, the gage on the left column face shows that larges strain reading, indicating it was the most activated at this point in time. After the point of ultimate stress, strain readings on all faces decreased significantly due to the failure of the column through debonding. It is important to note that after the point of ultimate stress, the strain gage on the back face malfunctioned, indicated by a significant increase in tensile strain.

Shown in Figure 4.37 is the response of the individual gauges in terms of transverse strain verses time. The transverse strain values reported in Figure 4.37 are the absolute value of the tensile transverse strain measured. The following is a discussion of key points in time or region on the curves. Figures 4.38 and 4.39 show the corresponding damage to the specified column.

1. In this region, the fibers located on the left, back, and right face increased in tension more rapidly than the fibers on the front (overlapping) face indicating these fibers became more engaged than the outer-most overlap fibers.

2. At this point in time, horizontal and vertical cracks at the corners began to form on the left face. Stress applied was redistributed to other composed faces of the column for a short period of time.
3. Within this region, the three composite jacket levels detached individually, starting with the top jacket layer at the front face. Simultaneously, the top level detached from the right face causing a temporary decrease in energy absorption of the composite system.
4. At this point in the test, horizontal cracks formed at approximately mid-height on the right face near the fiber jacket joint.
5. At this point in time, multiple vertical and horizontal cracks formed on the back face of the specimen. The horizontal cracks correlated with mortar joint locations, but the vertical cracks were in arbitrary locations.
6. At this region, the middle fiber layer on the front overlap peeled from the specimen, leaving only the bottom overlap layers to be fully attached on the front face.
7. At the time when ultimate load was reached, the bottom layer of the front overlap started to detach from the specimen but did not fully detach. Simultaneously, on the right face, the middle fiber jacket started to detach near the top corner closest to the front face. Additionally, the exterior-most matrix crumbled from the specimen near the left and front face indicating that the interior-most layer of fiber was beginning to detach from the front face of the column.

Appendix B, Figure B.38 shows the relationship between the axial stress and transverse strain in which the relationship showed an initial steeply sloped branch, corresponding to negligible transverse strain values. The strain readings began to increase at an axial stress value less than the average unconfined strength. The response showed that the strain gauge located on the front face of the specimen began to engage prior to the other gages which was represented with a more gradual slope. The right, back, and left strain gages engaged soon after, still at a value less than the unconfined strength. This response could be a result of the formation of vertical cracks at the overlap, cracking of the matrix at the corners, or crushing of masonry. Throughout the response, the strain gage on the front face (overlap face) registered the smallest transverse strain values.

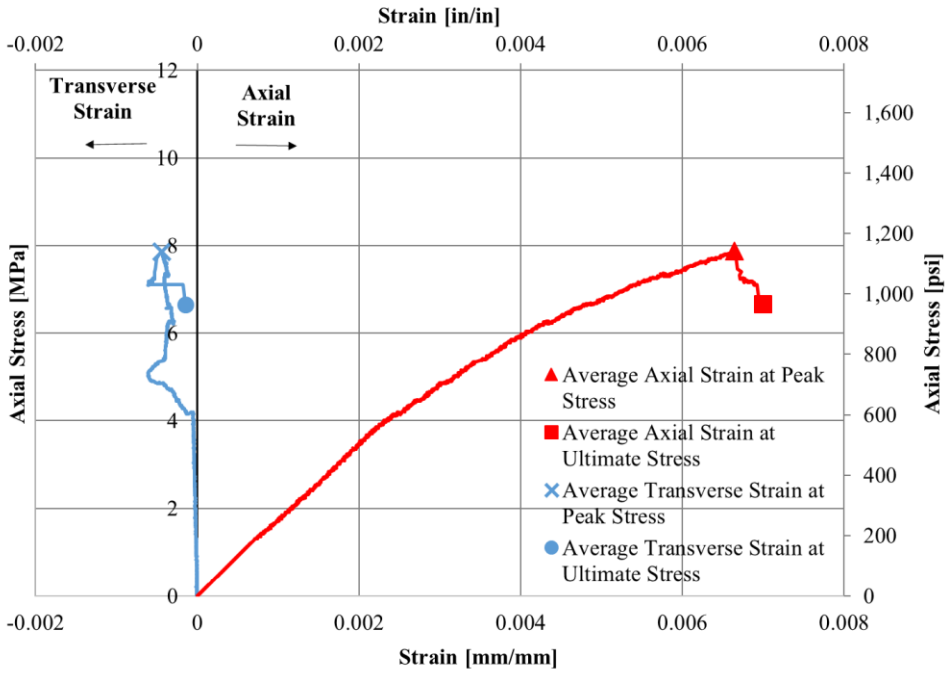

Figure 4.36. Specimen C-12-0-1-4: Axial Stress - Strain Response

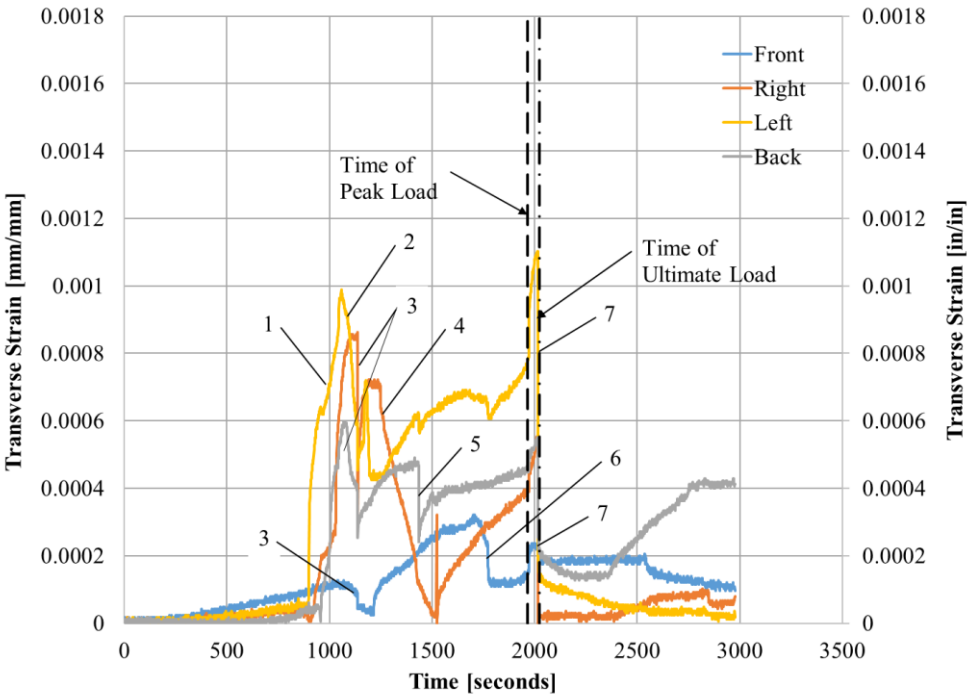

Figure 4.37. Specimen C-12-0-1-4: Transverse Strain vs. Time Response

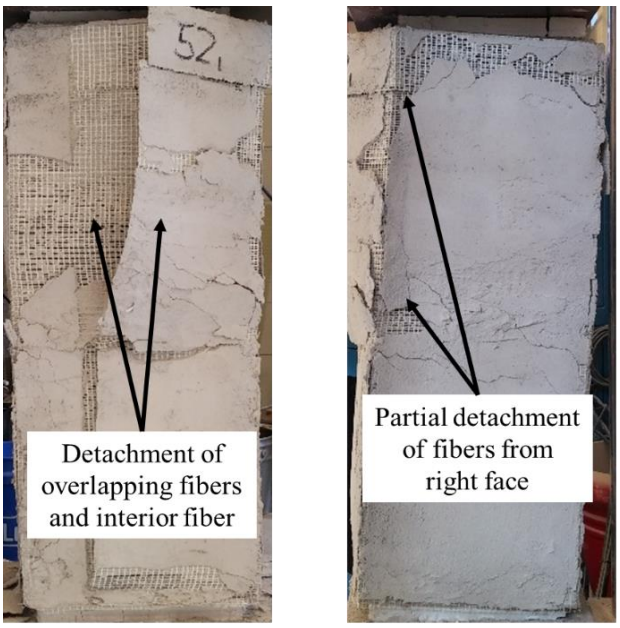

Front Face (Face 1) Right Face (Face 2)

Figure 4.38. Specimen C-12-0-1-4 After Testing: Front and Right Faces

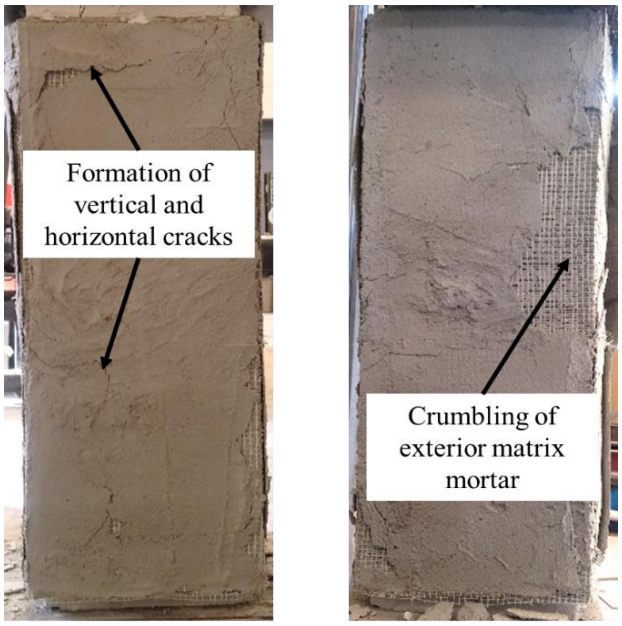

Figure 4.39. Specimen C-12-0-1-4 After Testing: Back and Left Faces

4.6.2. Group 4 Specimens. Regarding the two specimens in Group 4 with transverse strain gages, values in Table 4.3 indicate that the peak axial stress and axial strain at the peak stress differ by approximately 13%. Additionally, the ultimate point values differ the same approximate percentage. For both the average peak and ultimate stress points, the average transverse strains for each specimen vary significantly (with percent differences of 92% and 77%, respectively).

Regarding Specimen C-12-38-1-3, the axial stress – transverse strain behavior shown in Figure 4.40, indicates when the confinement system began to engage (approximately 5 MPa in Figure 4.40). At this stress, the slope of the axial stress – axial strain response started soften as a result of the matrix gradually detaching from the outer-most matrix layer. Figure 4.40 depict the peak and ultimate stress points. Between the

points, the average transverse strain reduced (or decreased in tension). The reduced tension in the fibers was caused by the overlap face significantly debonding from the specimen and the start of detachment of the other faces.

Regarding the individual strain readings, significant increases in tensile strain were measured before the peak stress was reached, indicating the jacket was engaged on each face before this point. At the point of peak stress, the strain gage on the right face reported the largest tensile strain, while at the point of ultimate stress, the strain gage of the back face reported the largest tensile strain. After the ultimate point, all gages reported a decrease in tensile strain due to the failure of the column. It is important to note that a malfunction occurred in the strain gage on the right face after the point of ultimate stress, shown by a significant increase in tensile strain.

Shown in Figure 4.41 is the response of the individual specimens in terms of transverse strain verses time. The transverse strain values reported in Figure 4.41 are the absolute value of the tensile transverse strain measured. The following list includes a discussion of key points in the curves. Figures 4.42 and 4.43 show the corresponding damage to the specified column.

1. At this region, the tension in the fibers on the back-face increased significantly after the formation of vertical cracks at the corners. The vertical cracks at the corners occurred due to the fiber jacket not being parallel with the masonry substrate when the confining system was applied causing the fibers to detach.
2. At this point during the test, popping noises were heard due to horizontal cracks forming at multiple locations on the back face of the specimen.

3. At this region, energy absorbed was redistributed to the front, back, and left faces due to a decrease in strain registered at the right face. Following this occurrence, the top and middle jackets detached from the front face (overlap face) completely. The result of this detachment included the interior-most fiber layers beginning to deform on the front-face, causing the left-faced fibers to begin to detach.
4. At this region, due to the complete detachment of the front face and the partial detachment of the left face, energy absorbed was redistributed to the right and back faces, causing an increase in strain.
5. At the time of peak stress, the right faced fiber jackets (top and middle layers) detached completely.
6. Between the time of peak axial stress and ultimate axial stress, large vertical cracks formed at the corners of the back face causing matrix mortar to crumble off in those regions. The back faced fibers began to detach near the point of ultimate axial stress.
7. At this point during the test, nearly all faces of the top and middle confining layers were detached or partially detached, causing the energy absorption to decrease significantly.

Appendix B, Figure B.40 shows the relationship between the axial stress and transverse strain for the confined specimens. The initial response for all strain gages was a steeply sloped branch indicating the transverse strain being negligible. It was shown that the strain gauge located on the back face was activated at a value less than one-half the unconfined compressive strength, which could correspond to the formation cracks or

the crushing of masonry. The other three strain gages were activated at a value less than the unconfined strength but were activated at approximately the same time. At this point, the confinement system was activated in the mid-region of the column. After this point, it is important to note that the strain gage found on the front face (overlap face) registered the smallest transverse strain value.

Regarding Specimen C-12-38-1-4, the axial stress – transverse strain behavior shown in Figure 4.44, indicates when the confinement system began to engage (approximately 4.5 MPa in Figure 4.44). At this stress, the slope of the axial stress – axial strain response and the axial stress – transverse strain started to decrease. At this point in time, the tension began to increase within the fiber and the matrix began to gradually detach from the outer-most matrix layer.

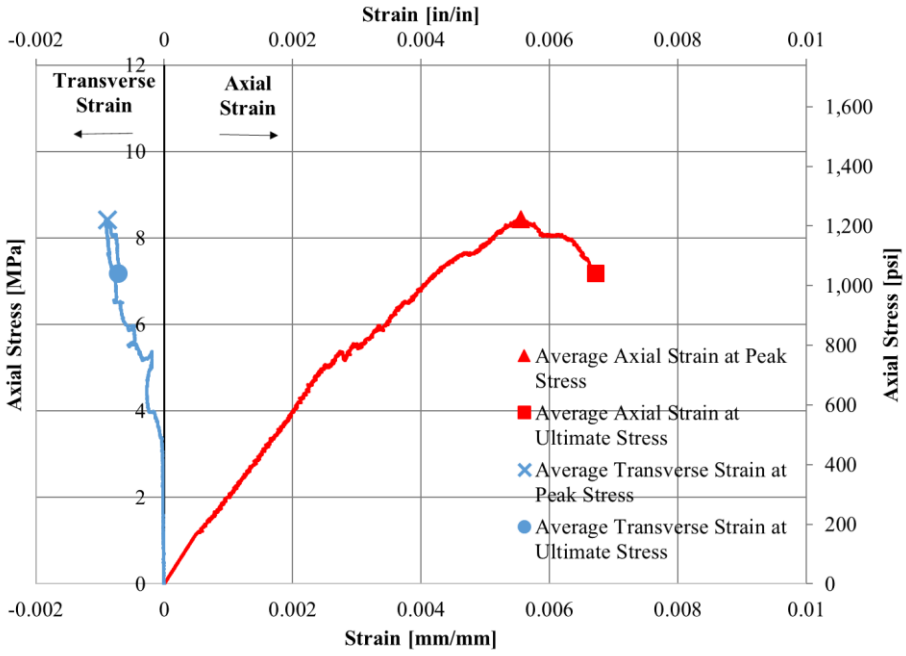

Figure 4.40. Specimen C-12-38-1-3: Axial Stress - Strain Response

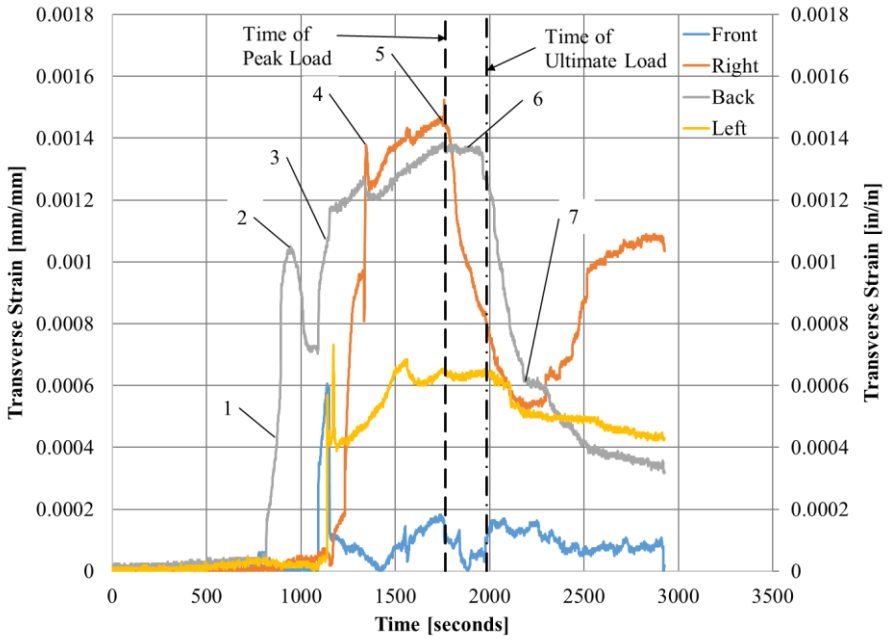

Figure 4.41. Specimen C-12-38-1-3: Transverse Strain vs. Time

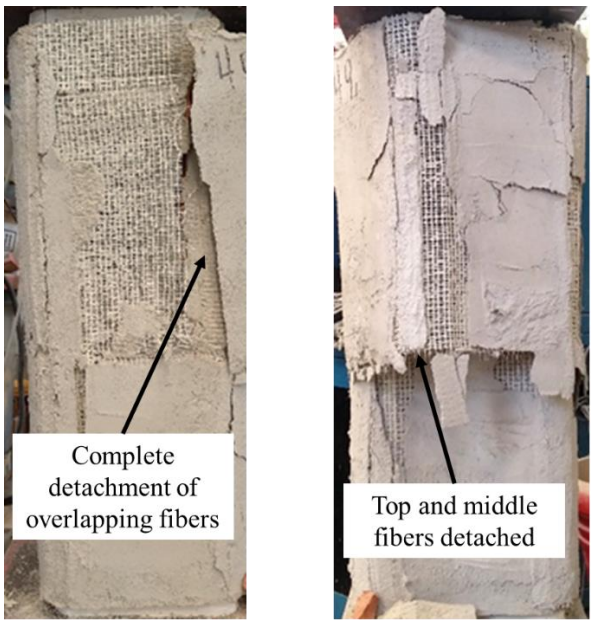

Front Face (Face 1) Right Face (Face 2)

Figure 4.42. Specimen C-12-38-1-3 After Testing: Front and Right Faces

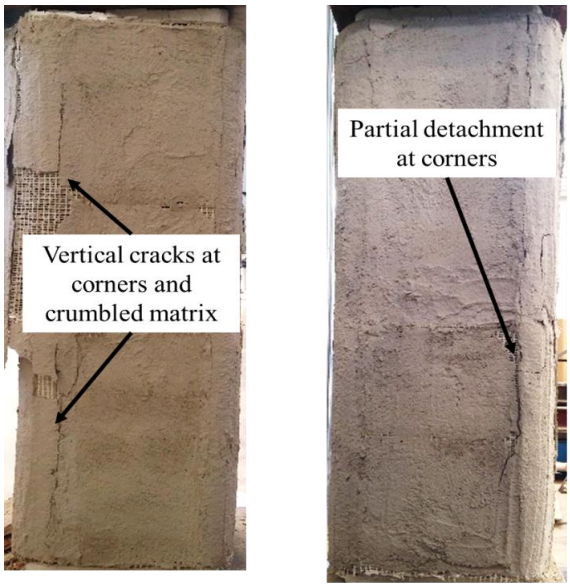

Figure 4.43. Specimen C-12-38-1-3 After Testing: Back and Left Faces

Figure 4.44 depicts the response between the peak and ultimate stress points in which the average transverse strain reduced (or decreased in tension). The reduced tension was caused by the overlap face debonding from the specimen while the other faces began detaching. Regarding the individual strain readings reported, prior to the point of peak stress all strain gages measured a significant increase in tensile strain indicating the jackets activation before this point. At the points of peak axial stress and ultimate stress, the strain gage on the back face reported the largest tensile strain. After the point of ultimate stress, tensile strain in all gages decreased but not significantly. The decrease in tensile strain was due to jacket detachment on multiple column faces.

Shown in Figure 4.45 is the response of the individual specimens in terms of the absolute value of transverse strain verses time. The following list includes a discussion of

key points in the curves. Figures 4.46 and 4.47 show the corresponding damage to the specified column.

1. During the region in which the slope of the transverse strain – time relationship for the back strain gage is steep, vertical cracks formed along the back corners of the column resulting in the stress to be redistributed to the composite on the front (overlap) face.
2. At this point in time, the top layer of fibers detached from the front face allowing for the applied energy to be absorbed by the left facing fibers.
3. At this region, the middle layer jacket detached from the front face followed by partial detachment on the left column face due to the interior-most fibers on the overlap face detaching from the masonry matrix layer. The energy absorbed was then redistributed to the right-facing fibers.
4. At this point in time, the matrix debonds at the corners at the right face prior to the formation of horizontal cracks. Soon after, the top and middle layer of jackets on the right face began to peel off the masonry column.
5. At this point during the test, the decrease in transverse strain for the back face was due to matrix debonding and crumbling from the column.
6. In the region between the time of peak and ultimate axial stress, it is evident that the fibers on the left and back faces are carrying more stress than the right and front facing fibers due to the slight increase in the curve's slope. By this point in the test, full or partial detachment of the front and right faced fiber jackets has occurred.

7. At these points during the test, the drops in transverse strain for the back facing fiber jacket was due to additional matrix mortar detaching and crumbling from the column.

Appendix B, Figure B.42 shows the axial stress – transverse strain response for this specimen. Like others, the initial response was a steeply sloped branch indicating negligible strain. The first strain gages to significantly increase in transverse strain was that of the front and back faces, correlating to the activation of the fiber jackets. Following, the right and left strain gages began register significant increases in transverse strain at an axial stress less than the unconfined strength. To note, the strain gage that registered the smallest amount of transverse strain was located on the right face. This could correspond to an error in the gage or early debonding of the right face to due to the construction limitation related to the corners.

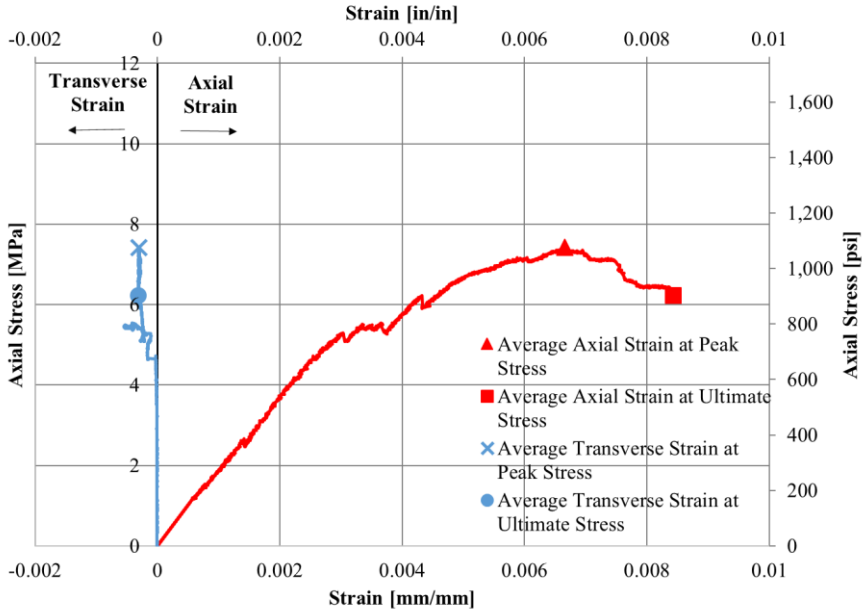

Figure 4.44. Specimen C-12-38-1-4: Axial Stress - Strain Response

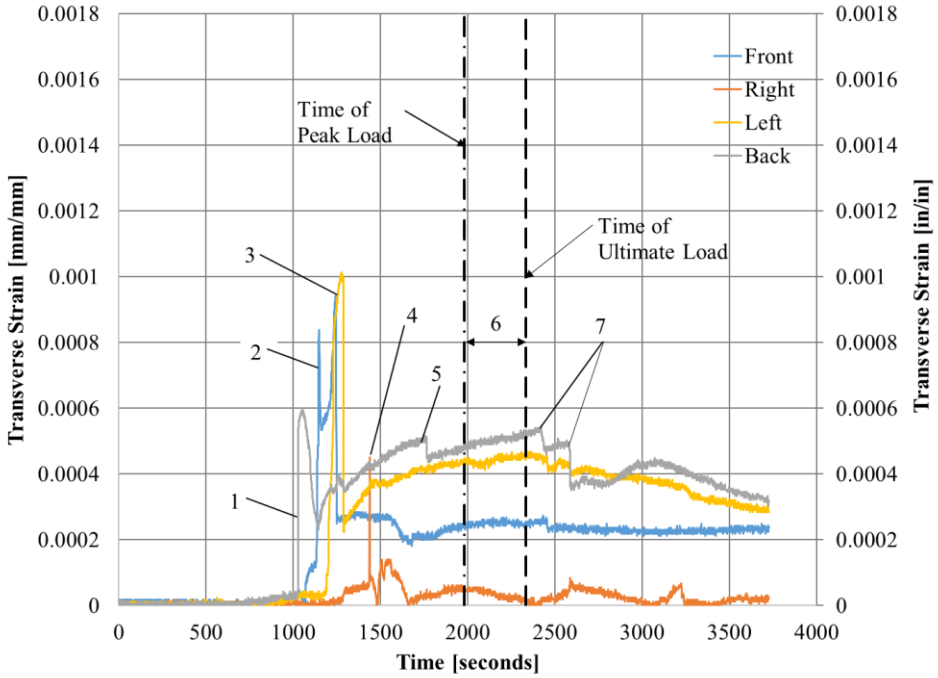

Figure 4.45. Specimen C-12-38-1-4: Transverse Strain vs. Time

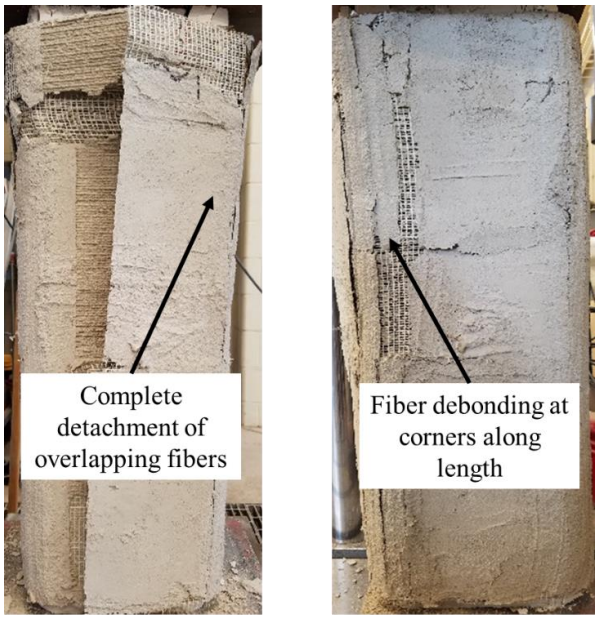

Figure 4.46. Specimen C-12-38-1-4 After Testing: Front and Right Faces

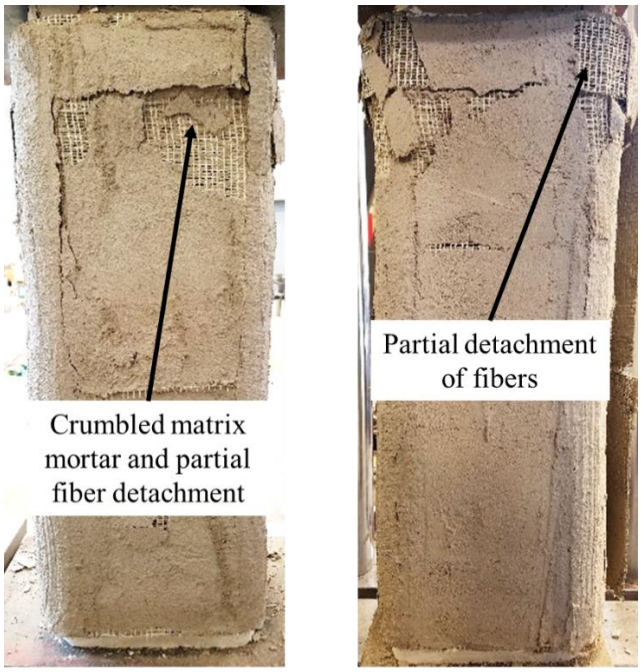

Figure 4.47. Specimen C-12-38-1-4 After Testing: Back and Left Faces

4.7. INFLUENCE OF PARAMETERS

The following section provides details regarding the influence of the different parameters in terms of the axial peak stress, ultimate strain at axial stress, and total energy absorbed.

4.7.1. Effect of Number of Fiber Layers. Analysis of the effects of varying fiber layers is divided into two series based on column geometry: sharp cornered columns and round cornered columns. For the sharp column series, the columns discussed are the control specimens, Group 1: C-12-0-1, Group 2: C-12-0-2, and Group 3: C-12-0-3. For the rounded column series, the columns discussed are the control specimens, Group 4: C-

12-38-1, and Group 6: C-12-38-2. The analysis is in terms of the axial stress - strain relationship, key values of axial stress and strain, and energy absorption.

4.7.1.1. Sharp cornered columns. Figure 4.48 plots the axial stress - axial strain curves for the confined column groups with sharp corners. Similar for plots of the axial stress – axial strain in the following section, markers on the curves identify the ultimate axial stress – axial strain point of the corresponding specimen. As shown in Figure 4.48, groups exhibited a response that is initially linear. In general, the slope of this linear portion increased with the number of fiber layers. The post-peak response for all groups includes a non-linear descending branch that became more gradual as the number of fiber layers increased. The shallower slope indicates the specimen was able to withstand an increased load for a duration of time while the strain continued to increase. In other words, the ductility and the energy absorbed by the column increased. Ductility is an important characteristic for building construction in geographical regions where extreme loading conditions may occur such as high seismic regions.

As discussed in Section 4.2, as the number of jacket layers increased, so did the deformation of the column at the sharp corners due to concentrated stresses. For the three-layered specimens, it was noticed at the termination of testing, the column corners were nearly rounded due to the confining action created by the jackets. However, the specimens with a single layer of fibers had minimal rounding of the corners with the limiting factor being fiber debonding at the overlap.

Regarding the axial displacement response of sharp cornered specimens, the displacement became more symmetric or uniform as the number of fiber layers increased. This is shown in the Axial Displacement column of Table 4.1.

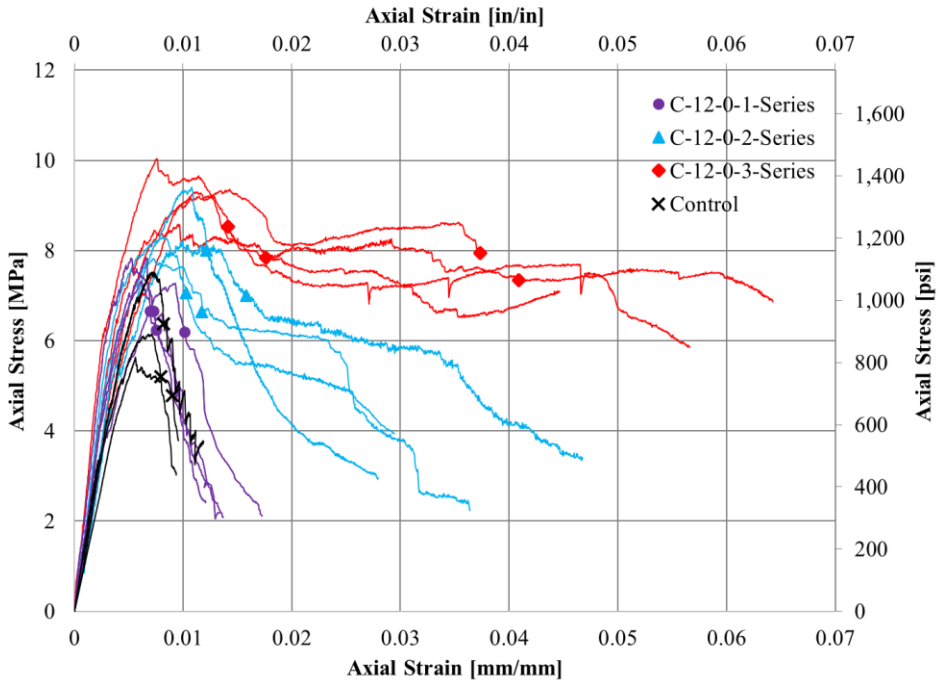

Figure 4.48. Axial Stress - Axial Strain Response of Sharp Cornered Columns

Figure 4.49 shows the average values of peak axial stress for each series in relation to the average unconfined stress and the ratio of the average confined peak stress to the average unconfined peak stress, $\frac{\overline{f_{mc}}}{f_{mo}}$. The average peak axial stress increased as the number of fiber layers increased. For each layer added, the average peak confinement stress increased between 13% - 15%. Individual specimen peak stress and ultimate stress depictions are found in Appendix C. In terms of the average ultimate strain achieved, this value increased in a non-linear fashion as the number of fiber layers increased, as shown in Figure 4.50. The ultimate strain for Group 1: C-12-0-1 provided a minimal increase in the ductility, with a value $\frac{\overline{\varepsilon_{mc,u}}}{\overline{\varepsilon_{mo,u}}}$ equal to 1.03. For Group 3: C-12-0-3, a significant

increase in ultimate axial strain was observed, with $\frac{\overline{\varepsilon_{mc,u}}}{\overline{\varepsilon_{mo,u}}}$ equal to 3.53. The significant increase in axial strain at ultimate stress was potentially due to the internal layers being restrained from opening by the external layer, especially since the overlapping layer was located on different column faces. As noted in Section 4.4.4, the experimental data for Group 3 specimens had a large standard deviation (43% of the average ultimate strain), and therefore the resulting values should be used with caution. Individual specimen depictions of axial strain at peak stress and ultimate stress are found in Appendix C.

Regarding the total energy absorbed by the sharp cornered columns, the energy absorbed increased as the number of fiber layers increased. The relationship between the different layer quantities is not linear. Figure 4.51 shows the average total energy absorbed which was defined as the energy absorbed until the ultimate axial stress – axial strain point was reached. Group 1 specimens provided an increase in total energy absorbed of 20% compared to the unconfined specimens, whereas Group 3 specimens provided a 527% increase in total energy absorbed. The significant increase can be attributed to the nature of multi-layered jackets and the variance of overlapping location for each jacket layer.

Three fiber layers provided a significant increase in the system's ability to redirect applied stresses. Once the outer-most overlapping fiber layer mostly or completely detached, the stresses were redistributed to the layers underneath or the region in which the outer-most layer had not debonded. This delayed the point of ultimate stress, therefore increasing the total energy absorbed by the confined columns.

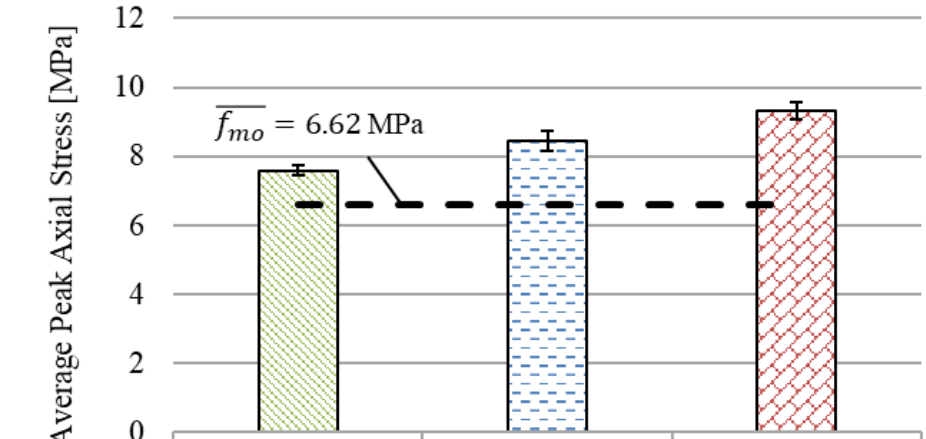

	C-12-0-1	C-12-0-2	C-12-0-3
$\overline{f_{mc}}$ [MPa]	7.59	8.45	9.32
$\overline{f_{mc}}/\overline{f_{mo}}$	1.15	1.28	1.41

Figure 4.49. Average Peak Axial Stress of Sharp Cornered Columns

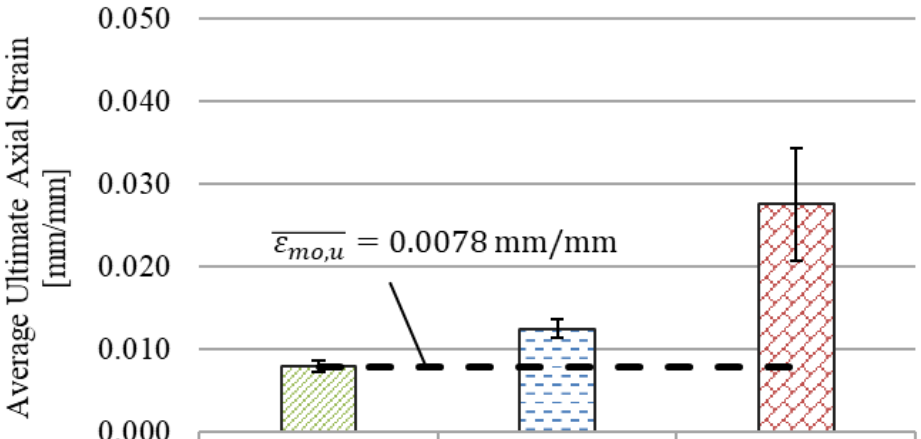

	C-12-0-1	C-12-0-2	C-12-0-3
$\overline{\varepsilon_{mc,u}}$	0.0080	0.0125	0.0275
$\overline{\varepsilon_{mc,u}}/\overline{\varepsilon_{mo,u}}$	1.03	1.60	3.53

Figure 4.50. Average Ultimate Axial Strain for Sharp Cornered Columns

Energy absorption can also be related to the quantity of damage to the interior masonry column. As the energy absorbed increased, the amount of damage to the columns increased. For the single-layered columns, the damage to the masonry column was similar to unconfined columns in which longitudinal cracks formed on all faces as discussed in Section 4.2.2.1. For the three-layered columns, once the jackets were opened after testing, much of the masonry column was destroyed or crushed as discussed in Section 4.2.2.3. The cross section of these specimens also exhibited visual arch effects due to the added confinement, as shown in Figure 4.7. Depictions of individual specimen responses of total energy absorbed are found in Appendix C.

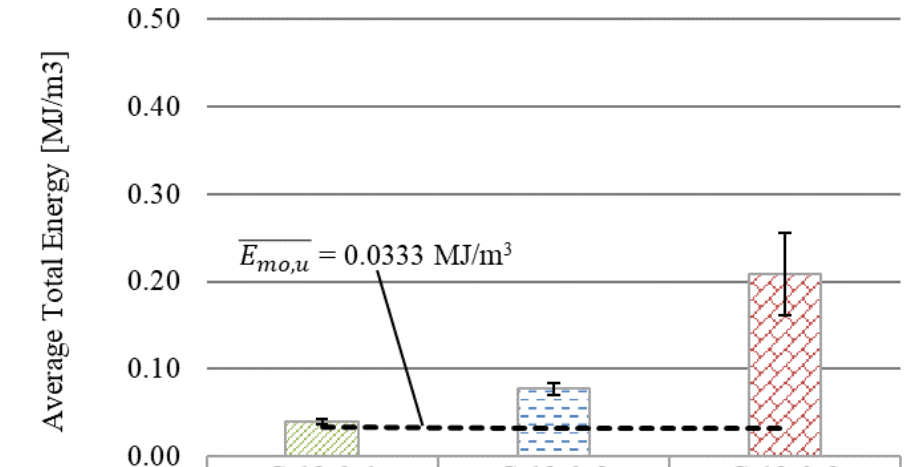

	C-12-0-1	C-12-0-2	C-12-0-3
$\overline{E_{mc,u}}$ [MJ/m³]	0.0403	0.0773	0.2086
$\overline{E_{mc,u}}/\overline{E_{mo,u}}$	1.21	2.32	6.27

Figure 4.51. Average Energy Absorbed of Sharp Cornered Columns

4.7.1.2. Round cornered columns. The groups analyzed for the round cornered series include the control specimens, Group 4, and Group 6. The axial stress - axial strain relationships (are shown in Figure 4.52). The basic responses of specimens in Groups 4 and 6 are similar to those of the unconfined specimens. The curves show an initial linear response, and the slope of the response increased as the number of fiber layers increased. After the peak load, a non-linear descending branch occurs for the rounded cornered specimens. Group 6 specimens exhibited a more gradual descent compared to the Group 4 specimens and the control specimens. Similar for all confined specimens in this discussion, the outer- most fiber layer began to open significantly once the peak load was reached, causing a drop in the axial stress – axial strain curve. Regarding the axial stress – axial strain responses, the markers indicate the ultimate stress point for each specimen under consideration.

Concerning the axial displacement response of round cornered columns, all round cornered specimens were asymmetrically displaced, however the responses did not indicate a particular trend as the number of fiber layers increased.

Figure 4.53 shows the average values of peak axial stress for each series in relation to the average unconfined stress. Figure 4.53 also shows the ratio of the average confined peak stress to the average unconfined peak stress $\frac{\overline{f_{mc}}}{\overline{f_{mo}}}$ which ranged in magnitude from 1.17 to 1.37. Individual specimen peak axial stress and ultimate stress depictions are found in Appendix C.

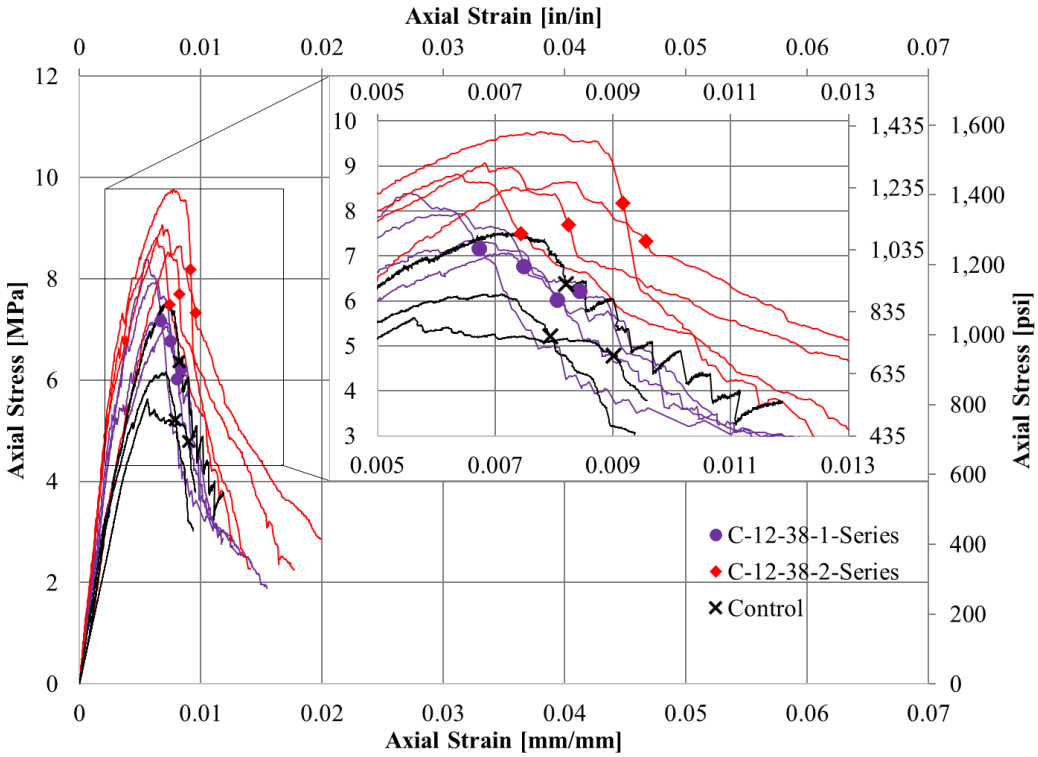

Figure 4.52. Group 4 and 6: Axial Stress - Axial Strain Response

In terms of average ultimate axial strain, Figure 4.54 shows the relationship between confined specimens of Group 4 and 6, and the unconfined specimens. Group 4 specimens did not exhibit an increase in average ultimate strain which in turn, did not improve the ductility of the masonry column effectively. Group 6 specimens did provide an increase in the ductility of the columns, since $\frac{\overline{\varepsilon_{mc,u}}}{\overline{\varepsilon_{mo,u}}}$ was 1.10. Individual specimen depictions of axial strain at peak stress and ultimate stress are found in Appendix C.

In general, the addition of fiber layers to round cornered columns did not improve the masonry columns ductility significantly but did increase the columns confining strength. It is important to note that after the termination of testing for confined

specimens, the corners of the columns remained intact, meaning the concentrated stresses at the corners were not significant. Due to limitations of the confinement preparation, the fibers were not perfectly rounded at the corners. As discussed in Section 3.3.2, the fibers were prepared by bending the jacket at three points for each corner. When the columns were confined, the fibers were not perfectly parallel to the corners of the columns, causing the bond at each of those three locations to be weakened. The tensile forces created in the jackets caused the matrix mortar to begin to debond near the column corners.

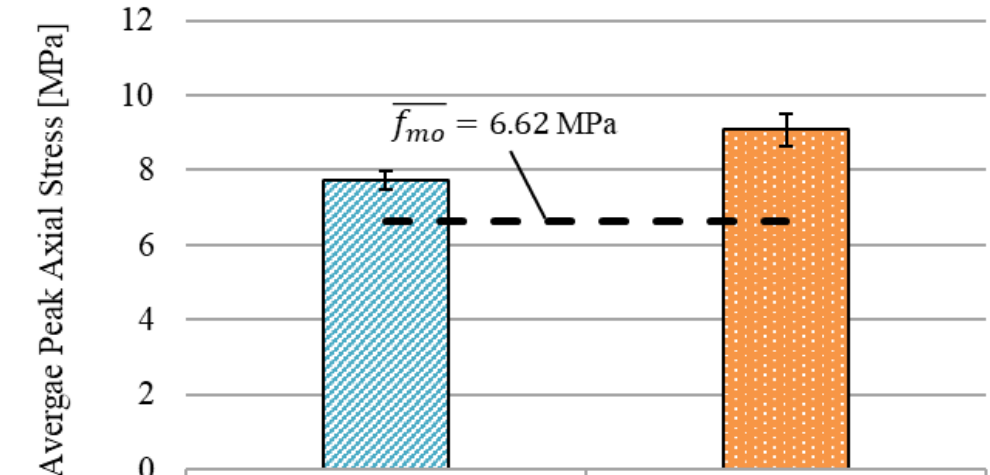

	C-12-38-1	C-12-38-2
$\overline{f_{mc}}$ [MPa]	7.73	9.08
$\overline{f_{mc}}/\overline{f_{mo}}$	1.17	1.37

Figure 4.53. Average Peak Axial Stress of Round Cornered Columns

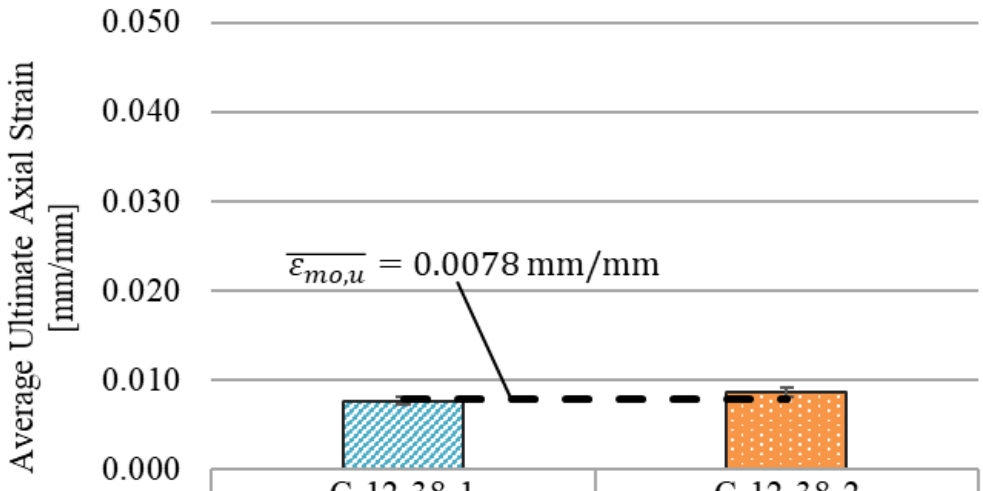

	C-12-38-1	C-12-38-2
$\overline{\varepsilon_{mc,u}}$	0.0077	0.0086
$\overline{\varepsilon_{mc,u}}/\overline{\varepsilon_{mo,u}}$	0.98	1.10

Figure 4.54. Average Ultimate Axial Strain of Rounded Cornered Columns

Regarding the energy absorbed by the rounded columns, the total energy absorbed relative to the unconfined columns increased in a non-linear fashion as the number of fiber layers increased. Figure 4.55 shows the average total energy absorbed in comparison with the average total energy of the control specimens. Group 4 specimens exhibited an increase of absorbed energy of 19% compared to the control group, while Group 6 provided a 60% increase. Similar to the sharp cornered columns, the increase in energy can be attributed to the redistribution of stress when the outer-most fiber layer detached. For the two-layered columns, once the outer-most fiber layer debonded, the stresses were redistributed to the region that did not debond or to the area with a single fiber layer. Unlike the sharp cornered columns, the energy absorbed is not as easily attributed to the destruction of the corners of the masonry columns, but it can be related

to the visible arching effect. The cross section of the two layered specimens exhibited symmetric or asymmetric arching effect once the composite layers were removed, while the single layered specimens showed little of this effect (Section 4.2.2.4 and 4.2.2.6). The total energy absorbed for Group 6 specimens had a relatively high standard deviation of 0.0081 MJ/m^3, and therefore the resulting values should be used with caution.

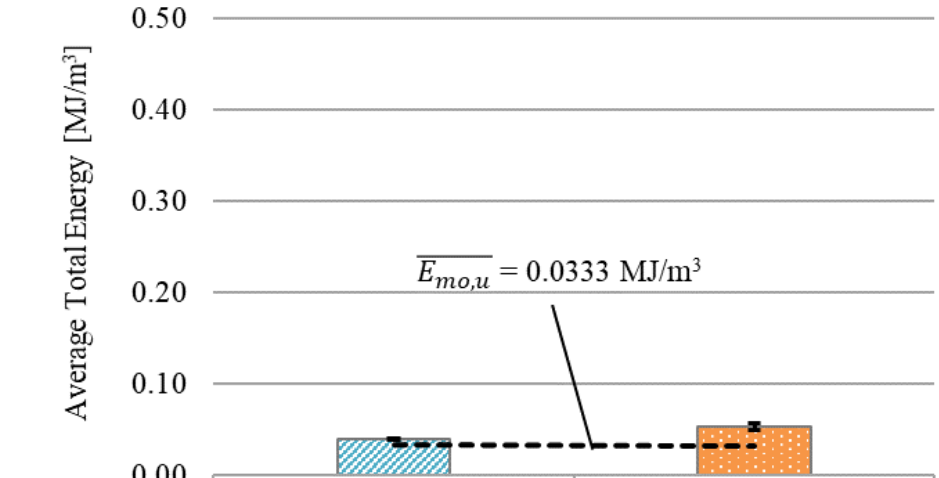

	C-12-38-1	C-12-38-2
$\overline{E_{mc,u}}$ [MJ/m³]	0.0396	0.0534
$\overline{E_{mc,u}}/\overline{E_{mo,u}}$	1.19	1.61

Figure 4.55. Average Energy Absorbed of Round Cornered Columns

4.7.2. Effect of Corner Radius. Analysis of the effects of column corner radius focuses on the pairings of Groups 1 and 4, and Groups 2 and 6. Groups 1 and 4 include specimens with a single fiber layer, with one overlap face, but with different column corner radii. Groups 2 and 6 include specimens with two fiber layers, with one overlap

face, and different corner radii. The pairing is analyzed in terms of the axial stress-strain relationships, key values of axial stress and strain, energy absorption, and transverse strain.

4.7.2.1. Comparison of Group 1 and Group 4. The axial stress – strain relationships of Group 1: C-12-0-1 and Group 4: C-12-38-1, along with the control specimens, are shown in Figure 4.56. As discussed in Section 4.3, specimens in Group 1 and Group 4 have similar axial stress – axial strain behavior as the unconfined columns. Both groups exhibited an initial linear response followed by immediate drops after the peak load. The drops in the curves represent the debonding of the fibers at the overlap. The post-peak responses include a rapid drop in the curve corresponding to the composite debonding and widening of interior cracks on the masonry. The responses of Group 1 and 4 specimens are similar except the descending branches of Group 1 specimens were, on average, more gradual than those of the Group 4 specimens (Figure 4.56). Regarding the axial displacement response of the columns in Groups 1 and 4, Group 1 specimens were primarily case A1 or asymmetric before the peak axial stress was reached and Group 4 specimens were primarily case A2, asymmetric after the peak axial stress.

In terms of average peak axial stress, the magnitude did not significantly increase as the corner radius increased (Figure 4.57). The respective average values for specimens in Group 1 and Group 4 were 7.59 MPa (STD =0.32 MPa) and 7.73 MPa (STD = 0.59 MPa). The average confined peak stress over the average unconfined peak stress ratio, $\frac{\overline{f_{mc}}}{\overline{f_{mo}}}$, varies from 1.15-1.17. The specimens of Group 1 and 4 provided little increase in peak axial stress due to the initiation of fiber debonding at the overlap prior to the peak load.

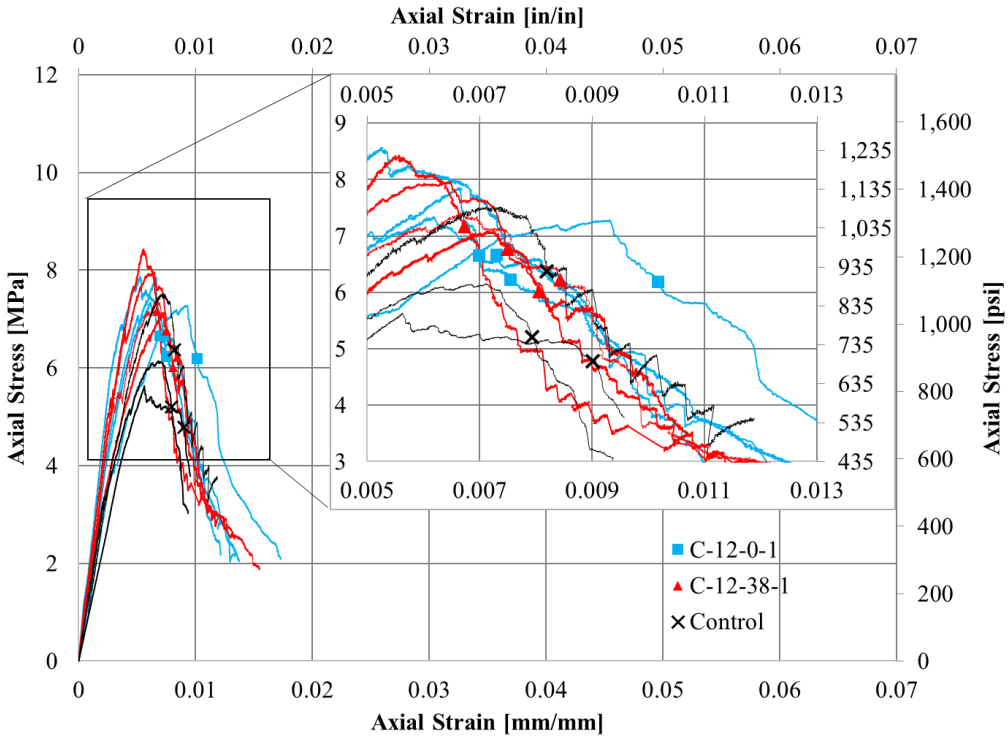

Figure 4.56. Groups 1 and 4: Axial Stress - Axial Strain Response

The point of ultimate axial stress-strain is denoted on each of the curves in Figure 4.56 which an "**X**" marker. The average ultimate axial stress values are similar for the specimens in Groups 1 and 4, with corresponding values of 6.43 MPa (STD = 0.26 MPa) and 6.54 MPa (STD = 0.52 MPa), respectively. The average ultimate axial strain values differ by approximately 3.8%, with values of 0.0080 mm/mm (STD = 0.0015 mm/mm) for Group 1 and 0.0077 mm/mm (STD = 0.0007 mm/mm) for Group 4 (Figure 4.58). The ultimate axial strain for Group 1 specimens could be larger due to the presence of sharp corners. Due to the confining action of the composite system, the corners began to crush during testing, allowing these specimens to absorb more energy. This enabled more axial strain and delayed the ultimate point due to the engagement of the confining system after

the peak stress point. However, it should be noted that the standard deviations of the values indicate that there is high uncertainty. The ratio $\frac{\overline{\varepsilon_{mc,u}}}{\overline{\varepsilon_{mo,u}}}$ for specimens in Groups 1 and 4 is 1.03 and 0.98, respectively. This suggests that for a single-layer jacket, the confinement is slightly more effective for columns with sharp corners than with rounded corners. However, both types of specimens under consideration did not provide a significant increases in peak axial stress and ultimate axial strain compared to the unconfined specimens, indicating that rounding of the column corners had little effect.

Regarding the energy absorbed by Group 1 and 4 specimens, the average amount of energy absorbed is nearly equal (Figure 4.59). Both series provide an approximate 20% average increase in energy absorbed compared to the unconfined specimens. These results indicate that rounding of the column corners had little effect on the jacket's effectiveness in terms of energy absorbed

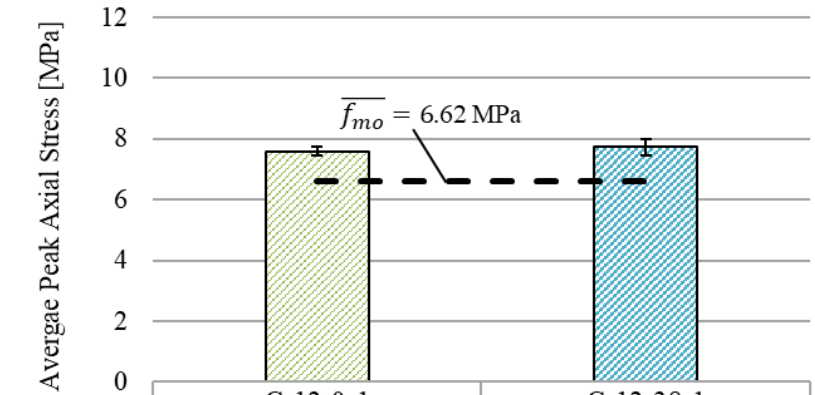

Figure 4.57. Average Peak Axial Stress of Columns with a Single Fiber Layer

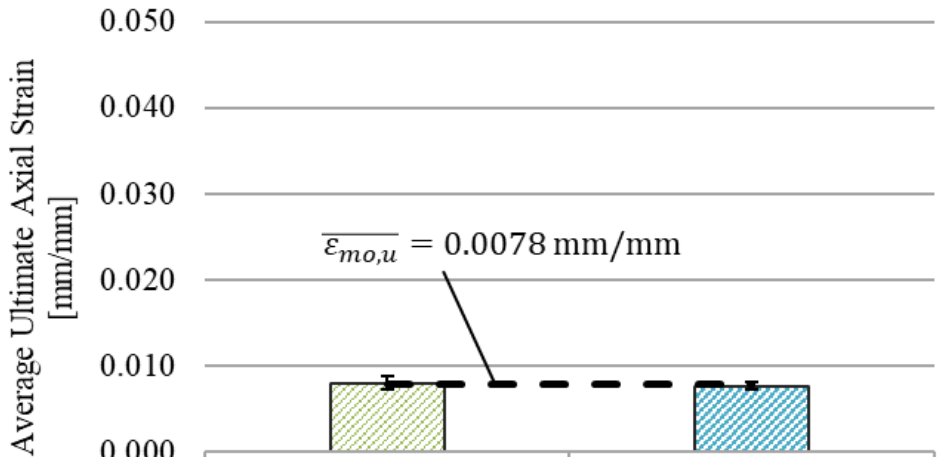

	C-12-0-1	C-12-38-1
$\overline{\varepsilon_{mc,u}}$	0.0080	0.0077
$\overline{\varepsilon_{mc,u}}/\overline{\varepsilon_{mo,u}}$	1.03	0.98

Figure 4.58. Average Ultimate Axial Strain of Columns with a Single Fiber Layer

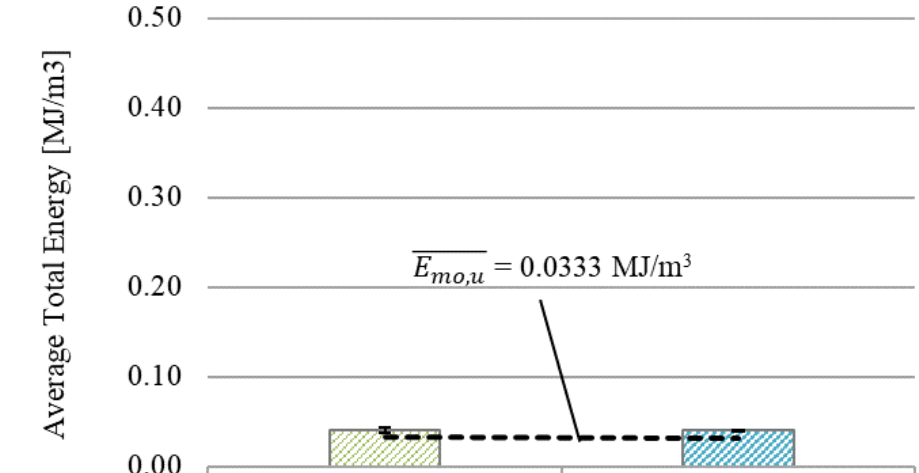

	C-12-0-1	C-12-38-1
$\overline{E_{mc,u}}$ [MJ/m³]	0.0403	0.0396
$\overline{E_{mc,u}}/\overline{E_{mo,u}}$	1.21	1.19

Figure 4.59 Energy Absorbed of Columns with a Single Fiber Layer

Table 4.4 reports changes in axial stress between the peak axial stress and ultimate axial stress points (f_{mc} - $f_{mc,u}$) and the difference between the average transverse strain between the peak axial stress point and the ultimate axial stress point ($\overline{\varepsilon_{mc,t}} - \overline{\varepsilon_{mc,t,u}}$). Negative values of axial stress indicate a decrease in (compressive) stress between the points considered. Positive values of average transverse strain indicate an increase in (tensile) strain between the considered points.

The change in axial stress for specimens with sharp (Group 1) and round (Group 4) cornered columns are within 5% of one another. However, the change in average transverse strain differs greatly both in magnitude and sign. Average transverse strain measured in column (C-12-38-1-4) increased in tension between the peak and ultimate stress points, unlike the other columns with strain gages applied. The increase in tension indicates that the fibers were more engaged at the point of ultimate stress than at the peak axial stress. For the other three specimens, the average transverse strain values were smaller at the ultimate axial stress point indicating the engagement of the fibers reduced after the peak point. This observation can be confirmed by the general behavior of the columns since the formation of cracks would increase after the point of peak axial stress, and the fibers on the overlap face would begin to debond significantly.

Regarding the individual transverse strain – time responses of the strain gages attached to the fibers on the indicated columns, the initial responses were similar for all faces with the exception of the strain gages on the front faces of sharp cornered columns. The slope of the responses of the strain gages on the front faces was more inclined than those on the other three column faces, indicating increased fiber engagement prior to the other faces. This activation was also indicated by the formation of vertical cracks at the

fiber overlap. For all specimens, the confinement system engaged prior to the peak axial stress indicated by the increased values of transverse strain at the point in time of peak stress. The drops in the individual transverse strain reading are attributed to cracking of the matrix mortar or debonding of the fiber overlap. In general, single-layered specimens with sharp or round cornered columns show similar behavior in transverse strain measurements and redistribution of applied stress around the column cross-section.

Table 4.4. Changes in Transverse Strain

Specimen		f_{mc} - $f_{mc,u}$	$\overline{\varepsilon_{mc,t,u}} - \overline{\varepsilon_{mc,t}}$
Group	**Name**	**MPa**	**mm/mm**
Group 1	C-12-0-1-3	-1.17	-0.00022
	C-12-0-1-4	-1.16	-0.00023
Group 4	C-12-38-1-3	-1.21	-0.00011
	C-12-38-1-4	-1.15	0.00001

4.7.2.2. Comparison of Group 2 and Group 6. As discussed in Section 4.3, specimens in Group 2: C-12-0-2 and Group 6: C-12-38-2 had similar axial stress-strain behavior as the unconfined specimens (Figure 4.60 and 4.61). All specimens exhibited an initial linear response followed by immediate drops in the curves. The drops in the curves represent the debonding of the outer-most fiber overlap for the confined columns. The post-peak response for Group 6 specimens include abrupt drops of the curve corresponding to the composite debonding. The process was more gradual than the descending branch of the unconfined specimens but not as gradual compared with Group

2 specimens. The descending branch of Group 2 specimens was more gradual due to the concentrated stresses acting at the column corners. Drops later in the post-peak branch correspond with the outer-most fiber layer debonding on multiple column faces. Regarding the axial displacement response of specimens in Group 2 and 6, Group 2 specimens displaced primarily symmetrically, while Group 6 specimens displaced asymmetrically after the peak axial stress had been reached.

Regarding the average peak axial stress, the magnitude increased as the corner radius increased (Figure 4.62). Values of average peak axial stress for Group 2 and Group 6 specimens are 8.45 MPa (STD = 0.68 MPa) and 9.08 MPa (STD = 0.49 MPa), respectively.

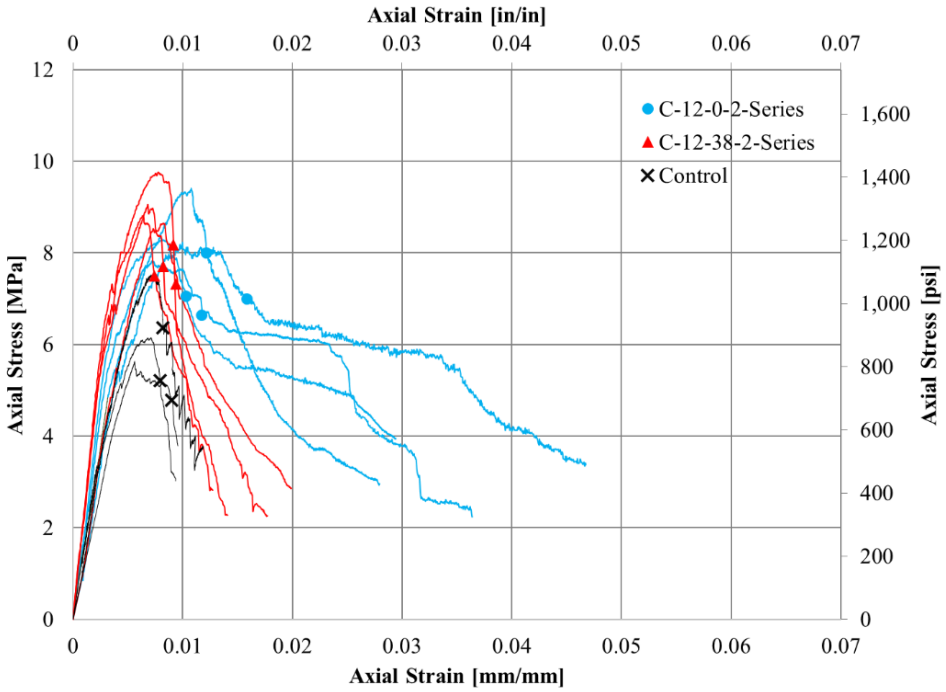

Figure 4.60. Axial Stress - Axial Strain Response of Columns with Two Fiber Layers

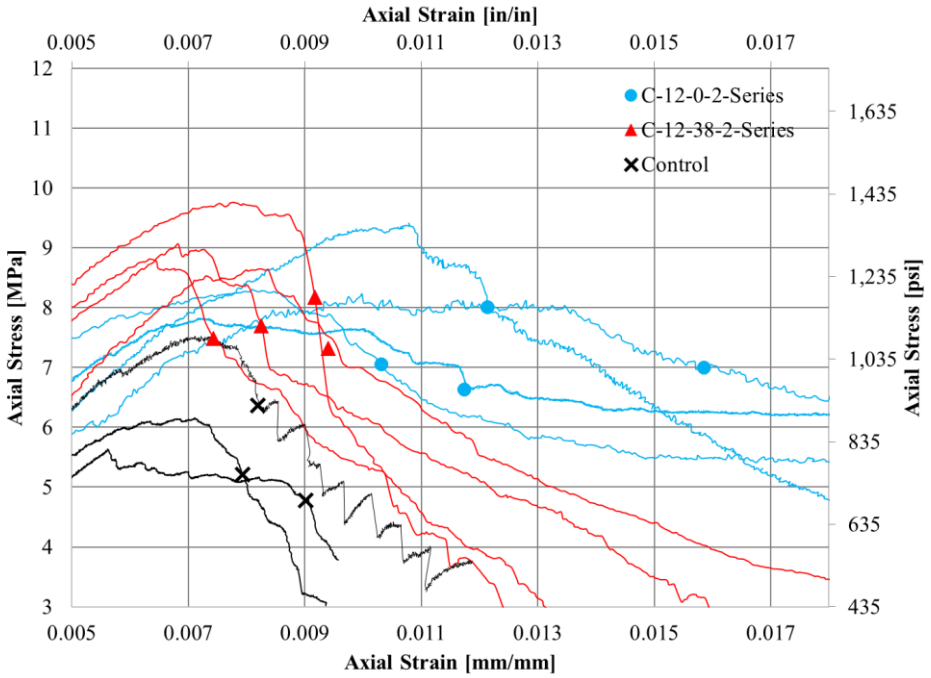

Figure 4.61. Axial Stress - Axial Strain Response of Columns with Two Fiber Layers (Revised Scale)

The ratio of the average confined peak stress to the average unconfined peak stress, $\frac{\overline{f_{mc}}}{\overline{f_{mo}}}$, varies from 1.28-1.37 and increased with increasing number of fiber layers. With the sharp cornered columns, the fiber jacket was not able to fully engage until nearly the peak load, when the corners started to crush due to stress concentrations. The round cornered columns fiber jackets were able to engage sooner since crushing of the bricks did not have to occur before activating the confinement and thus increasing its efficacy.

Regarding the average ultimate axial strain, the magnitude increased as the corner radius decreased (Figure 4.63). The respective values for Groups 2 and 6 are 0.0125 mm/mm (STD = 0.0024 mm/mm) and 0.0086 mm/mm (STD = 0.0010 mm/mm). The

increase in ultimate axial strain compared to the unconfined axial strain for the Group 2 specimens is 60%. Overall, Group 2 specimens provided more ductility in terms of axial strain but a lesser increase in peak axial stress compared to Group 6 specimens. However, it should be noted that ultimate strain values for Group 2 specimens also had larger standard deviations than those of the Group 6 specimens.

Regarding the total energy absorbed, this attribute increased as the corner radius decreased (Figure 4.64). Group 2 specimens provided a 132% increase in average unconfined total energy absorbed (relative to the unconfined specimens), while Group 6 provided a 60% increase. The increase in total energy absorbed is primarily related to the ultimate axial strain in this case, where the sharp cornered specimens exhibited a larger ultimate axial strain compared to the round cornered specimens. It is important to note that the damage to the masonry columns was more significant for the sharp cornered specimens compared to the rounded specimens, as discussed in Section 4.2.2.2 and 4.2.2.6. The cross section of the sharp cornered specimens showed symmetric and more distinct arching effects. Figure 4.65 and 4.66 show cross sections of representative specimens from the groups to compare the different arching effects observed.

4.7.3. Effect of Number of Fiber Overlapping Faces. Analysis of the effects of number of fiber overlapping faces focuses on the rounded columns in Groups 4 and 5 in comparison with the unconfined group. Group 4 includes specimens that have rounded corners, a single fiber layer, and one side of overlap. Group 5 includes specimens that have rounded corners, a single fiber layer, and two faces of overlap. The analysis of the groups is in terms of the axial stress-strain response, key values of stress and strain, and energy absorbed.

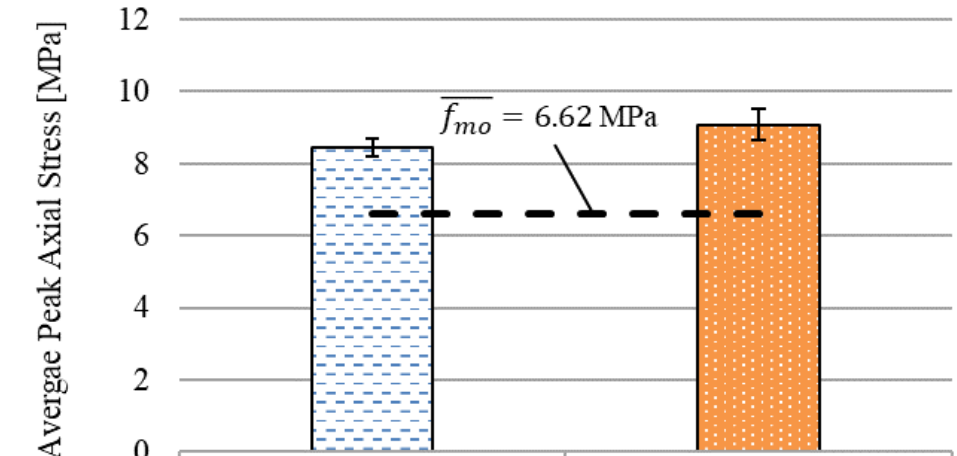

	C-12-0-2	C-12-38-2
$\overline{f_{mc}}$ [MPa]	8.45	9.08
$\overline{f_{mc}}/\overline{f_{mo}}$	1.28	1.37

Figure 4.62. Average Peak Axial Stress of Columns with Two Fiber Layers

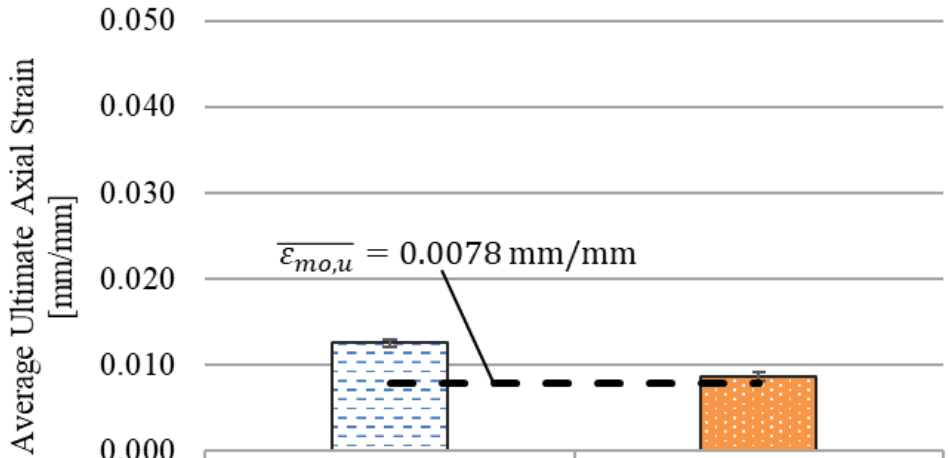

	C-12-0-2	C-12-38-2
$\overline{\varepsilon_{mc,u}}$	0.0125	0.0086
$\overline{\varepsilon_{mc,u}}/\overline{\varepsilon_{mo,u}}$	1.60	1.10

Figure 4.63. Average Ultimate Axial Strain of Columns with Two Fiber Layers

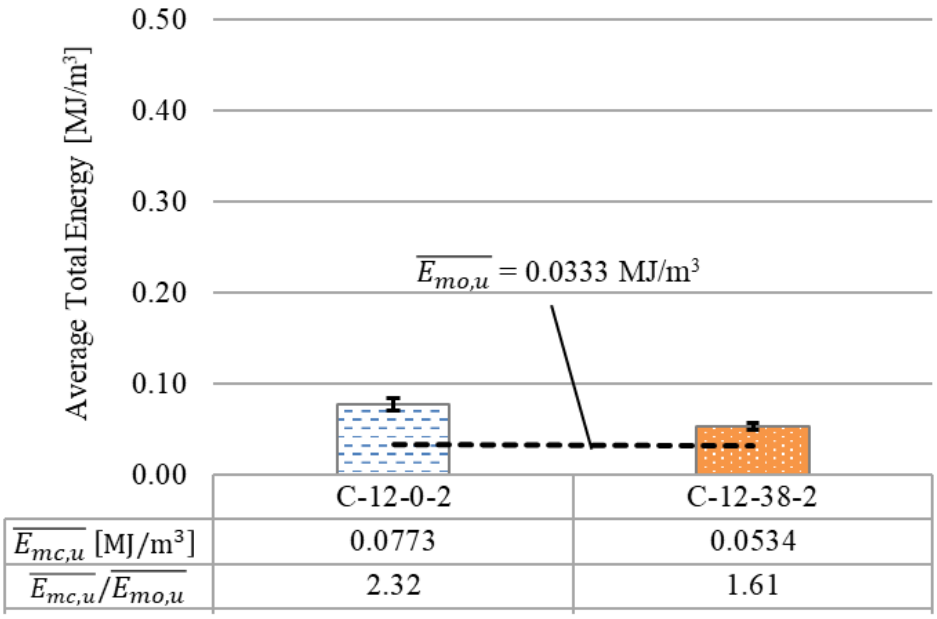

	C-12-0-2	C-12-38-2
$\overline{E_{mc,u}}$ [MJ/m³]	0.0773	0.0534
$\overline{E_{mc,u}}/\overline{E_{mo,u}}$	2.32	1.61

Figure 4.64. Energy Absorbed of Columns with Two Fiber Layers

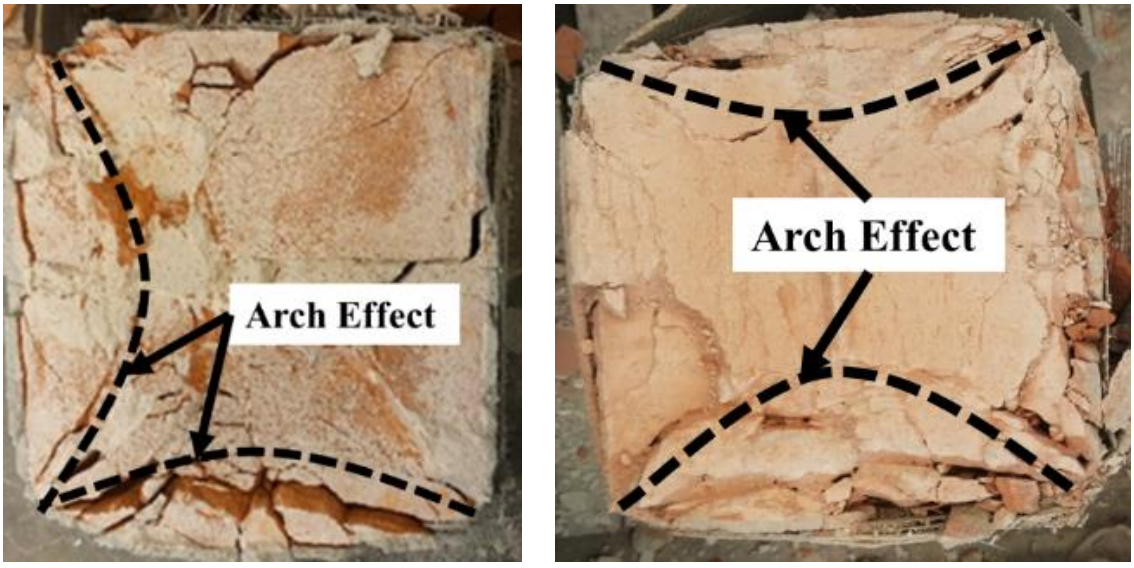

Figure 4.65. Examples of Arching Effect of Group 2: C-12-0-2 Specimens

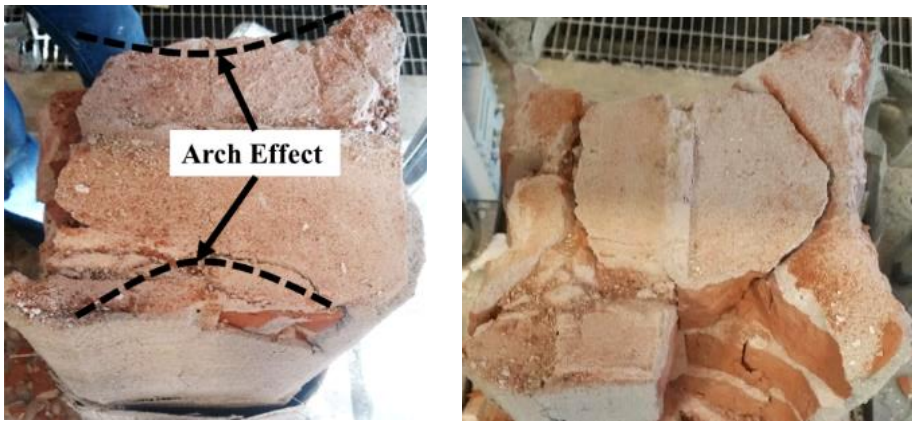

Figure 4.66. Examples of Arching Effect of Group 6: C-12-38-2 Specimens

The axial stress – axial strain curves are shown in Figures 4.67 and 4.68. Specimens in Groups 4 and 5 show similar overall behavior with one another, with an initial linear relationship. After the peak load, the curves show immediate drops due to debonding of the outer-most fiber layer. The drops are followed by a non-linear descending branch. For specimens in Groups 4 and 5, this descending branch was similar to that of the unconfined specimens but with a different slope. Figure 4.67 shows a focused view of the axial stress-strain response and the ultimate axial stress-strain point indicated by symbols along the curves. For specimens in Groups 4 and 5, the ultimate points are similar in axial stress, but Group 5 specimens show larger ultimate strains. The difference in behavior comparing Groups 4 and 5 is evident in the descending branch, where the average ultimate strain is larger for Group 5 specimens, as shown in Figure 4.68. The larger average peak axial stress and average ultimate strain value of Group 5 indicates the column ductility increases with increasing number of overlap faces.

Regarding the average peak axial stress, the magnitude increased as the number of overlapping faces increased. Figure 4.69 shows the average peak axial stress for specimens in Groups 4 and 5 as related to the average unconfined axial stress. Specimens in Group 5 provided greater axial strength increases than those in Group 4. The increase in axial stress relative to the unconfined specimens was 17% and 32% for Groups 4 and 5, respectively.

Regarding the average ultimate strain, the values increased with the number of overlapping faces, resulting in a 12% difference in average ultimate strain values of Group 4 and 5 specimens. Group 5, with the single fiber layer and two overlapping faces, provided the largest increase in average ultimate axial strain in relation to the average unconfined strain (Figure 4.70).

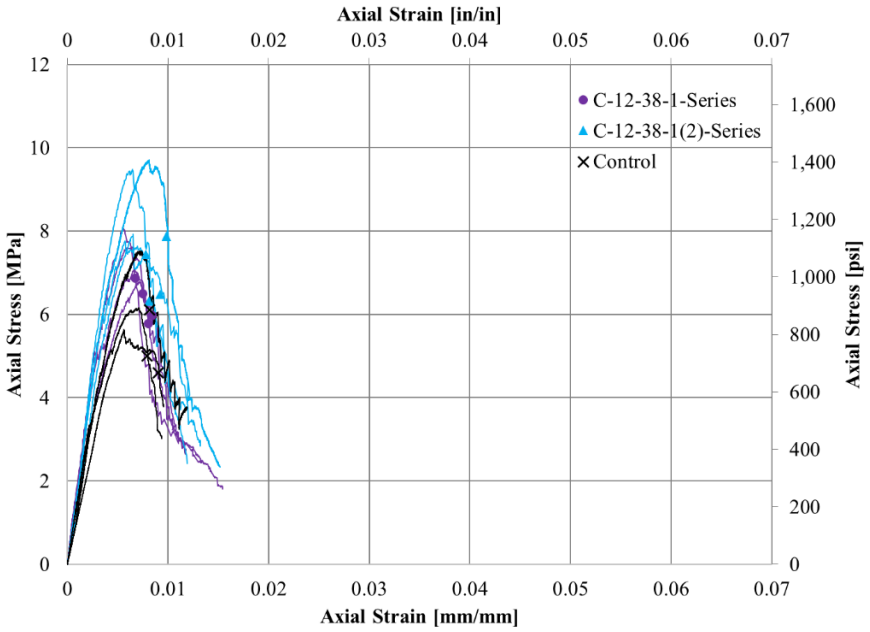

Figure 4.67. Axial Stress - Axial Strain Response of Round Cornered Columns

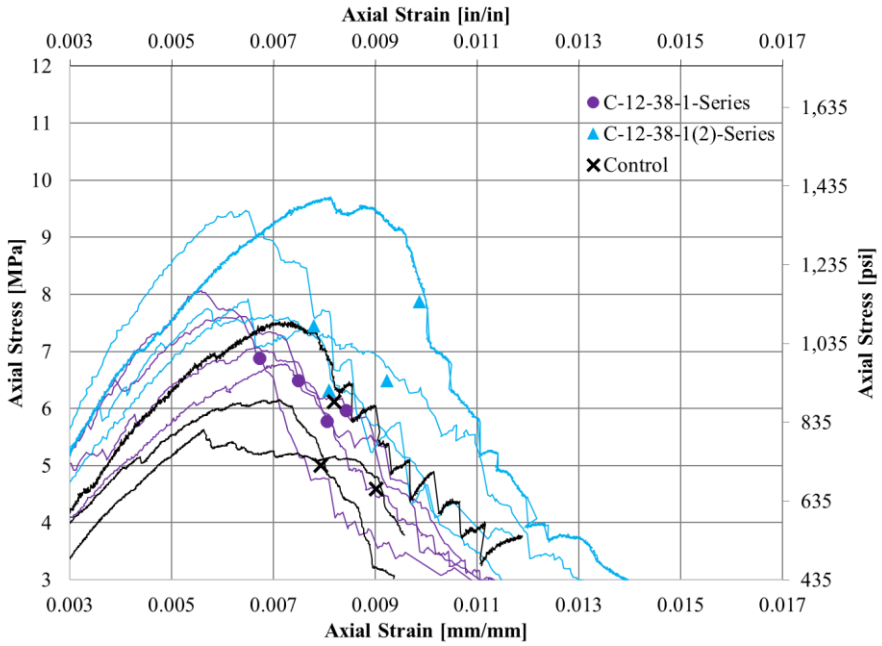

Figure 4.68. Axial Stress - Axial Strain Response of Round Cornered Columns (Revised Axis)

Regarding the total energy absorbed, this attribute increased with the number of overlapping faces as shown in Figure 4.71. Group 5 specimens provided a 54% average increase in total energy absorbed compared to the unconfined specimens, while Group 4 specimens provided a 19% average increase. This trend is primarily related to the ultimate axial strain, which increases as the number of overlapping faces increase.

Table 4.2 shows that the average values of the ratio $\frac{\overline{E_{mc,u}}}{\overline{E_{mc}}}$, which relates the total energy absorbed to the energy absorbed at the peak load, are 1.46 for Group 5 specimens and 1.29 for Group 4 specimens. Overall, Groups 5 specimens had larger values of peak axial stress, ultimate axial strain, and total energy absorbed. Group 5 specimens exhibited more ductile behavior as discusse.

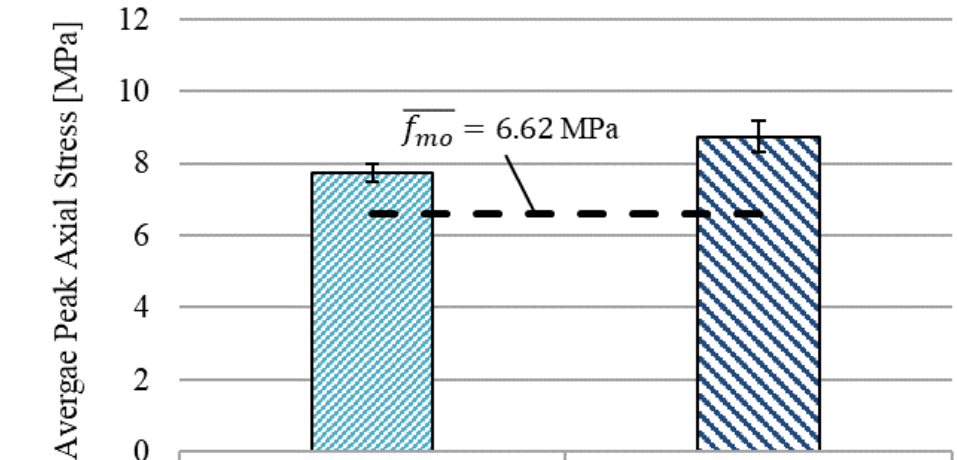

	C-12-38-1	C-12-38-1(2)
$\overline{f_{mc}}$ [MPa]	7.73	8.73
$\overline{f_{mc}}/\overline{f_{mo}}$	1.17	1.32

Figure 4.69. Average Peak Axial Stress of Round Cornered Columns

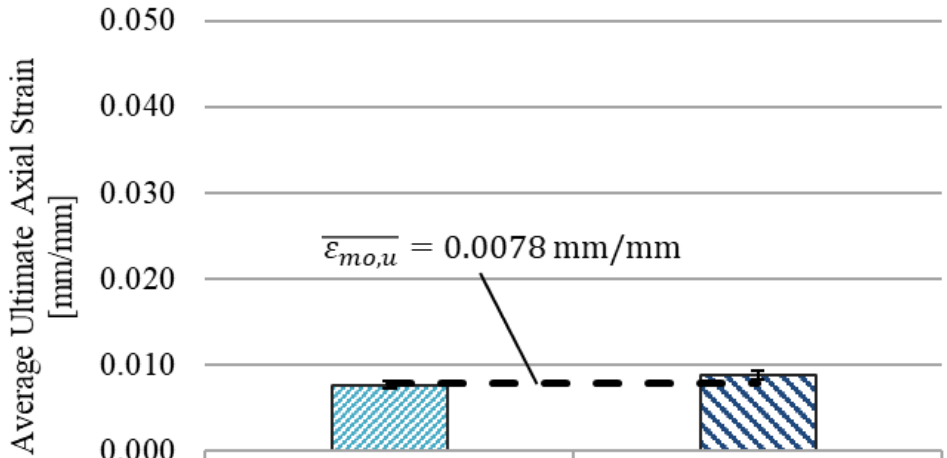

	C-12-38-1	C-12-38-1(2)
$\overline{\varepsilon_{mc,u}}$	0.0077	0.0087
$\overline{\varepsilon_{mc,u}}/\overline{\varepsilon_{mo,u}}$	0.98	1.12

Figure 4.70. Average Ultimate Axial Strain of Round Cornered Columns

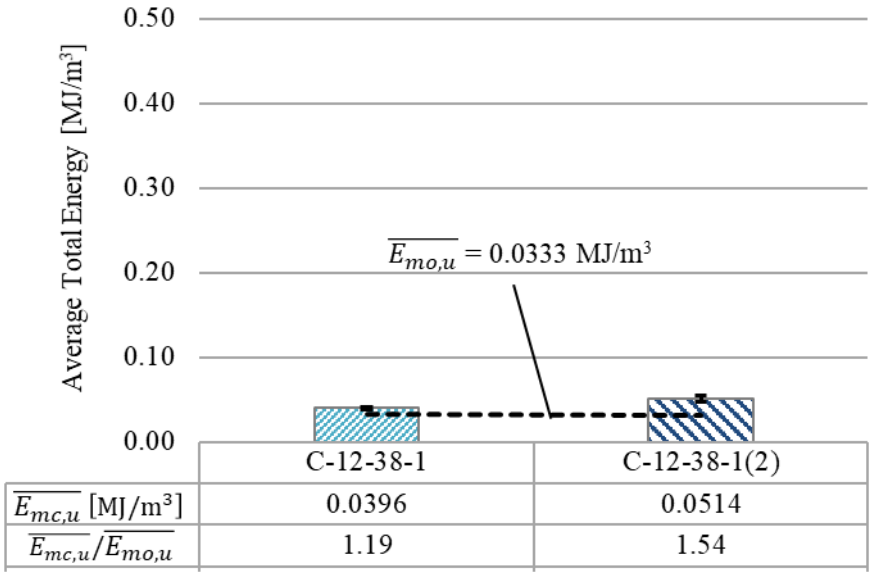

	C-12-38-1	C-12-38-1(2)
$\overline{E_{mc,u}}$ [MJ/m³]	0.0396	0.0514
$\overline{E_{mc,u}}/\overline{E_{mo,u}}$	1.19	1.54

Figure 4.71. Average Total Energy Absorbed of Round Cornered Columns

It is interesting to note that specimens with a single fiber layer and two overlapping faces (Group 5) had similar axial stress – axial strain responses as specimens with two fiber layers and one overlapping face (Group 6), as shown in Figure 4.72. Group 5 specimens have similar peak axial stress values as Group 6 specimens, with average values differing by less than 5%. The respective values of peak axial stress are given in Table 4.1. In addition, the average ultimate axial strain values for Groups 5 and 6 are similar, equaling 0.0087 mm/mm and 0.0086 mm/mm, respectively. Although no direct conclusions can be drawn from the comparison of these two groups due to multiple differing variables, this is merely a qualitative observation that requires further study, especially on bond behavior of the SRG composite and the overlapping length required.

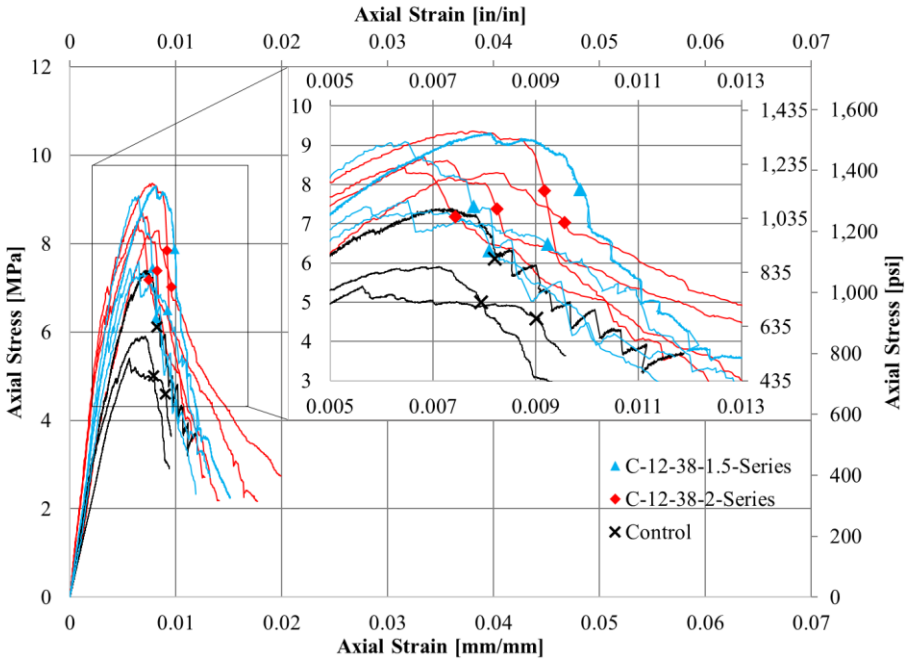

Figure 4.72. Axial Stress – Axial Strain Responses of Round Cornered Specimens (Groups 5 and 6)

4.8. CONCLUDING REMARKS

The following section includes concluding remarks based on the observed results. Remarks in terms of column behavior are discussed briefly followed by results of the influence of the test parameters considered in this study.

4.8.1. General Behavior. The general behavior of unconfined specimens, in terms of the axial stress – axial strain response, can be described as having an initial linear response. At the peak load, vertical (longitudinal) cracks along the length of each face can be observed. Following the peak load, the descending branch rapidly declined or declined in sudden drops due to the formation of additional cracks. The general behavior of confined specimens, in terms of the axial stress – axial strain response, can be

described as having an initial linear response that follows the unconfined behavior. Generally, before the unconfined strength was achieved, the relationship becomes non-linear, and the axial stress continues to increase until the peak stress is reached. After the peak stress, a descending branch is observed until failure occurs. The slope of the descending branch varied based on the parameters of the confinement system. In many cases, the descending branch plateaued until a sudden drop in the response caused by the formation of cracks, detachment of the composite jacket, or the disintegration of the masonry occurred.

4.8.2. Effects of Number of Fiber Layers. For confined specimens with sharp corners, increasing the number of fiber layers increases the compressive strength of the confined masonry columns. In addition, the average ultimate axial strain and total energy absorbed by the column increases, in turn, increasing the column's ductility. The increase was not linearly proportional to the increase in number of fiber layers.

For specimens with sharp corners, the addition of a single fiber layer to a masonry column results in a similar axial stress – axial strain relationship as that of unconfined specimens. The axial stress – axial strain responses had similar initial slopes followed by drops in the curve after the peak load was reached due to the formation of large vertical cracks in the masonry and confinement.

Regarding confined specimens with rounded corners, increasing the number of fiber layers increases the compressive strength and axial strain at ultimate stress of the confined masonry columns. In other word, the energy absorbed by the columns increased with the number of fiber layers, but the increase was not linearly proportional to the increase in fiber layers.

4.8.3. Effects of Corner Radius. Regarding confined specimens with a single fiber layer, no significant differences occurred as the corner radius increased. Both cross-sectional geometries of columns (with sharp corners and with rounded-corners) produced an increase in compressive strength and ultimate axial strain compared to the unconfined specimens. Both had similar axial stress – axial strain responses as unconfined specimens, with a rapid descending branch after the peak load was achieved. Columns with sharp corners produced larger changes in average transverse strain between the peak axial stress and ultimate stress points than columns with rounded corners.

Regarding specimens with two fiber layers, the peak axial stress increased with increasing corner radius; however the ultimate axial strain decreased with the increased corner radius. Both geometries of specimen provided an increase in the total energy absorbed compared to the unconfined columns. The total energy absorbed by the confined columns decreased with the increase in corner radius primarily due to the rapid descending branch of the axial stress – axial strain response, resulting in a lesser average ultimate axial strain value than sharp cornered specimens.

4.8.4. Effects of Fiber Overlap. Increasing the number of overlapping faces at the end of the fiber strip increases the confined column compressive strength and axial strain at ultimate stress. Specimens with overlapping fiber on two faces showed a similar response to specimens confined with two fiber layers. In terms of the axial stress – axial strain response, columns with two layers had a gradual descending branch after the peak load compared to specimens with overlapping fiber on two faces, which responded similar to unconfined specimens.

5. ANALYSIS OF RESULTS AND MODEL

5.1. EXPERIMENTAL RESULTS COMPARISON

As discussed in Section 1, the experiments presented in Section 3 and 4 of this thesis work were part of a larger study on confinement of masonry with SRG that was conducted in two phases. At the time of this thesis, the tests in these two phases were the only known tests on SRG-confined masonry columns. In this section, the test results from this thesis work are supplemented with those from both phases of this study to examine overall trends and determine the effectiveness of SRG confinement of masonry using a larger data set. Section 5.2 compares the test results from this thesis work to those of the other specimens in Phases I and II. Section 5.3 examines the applicability of existing models for FRP and FRCM confined masonry to predict the increase in compressive strength provided by SRG confinement considering the test results from both phases. Section 5.4 summarizes the key findings from this section.

5.2. COMPRARISON WITH OTHER TEST RESULTS

This section compares the experimental results obtained within this thesis work to other experimental results collected within this overall study (Phase I and Phase II).

5.2.1. Comparison of Phase II Specimens. The second phase of this study included masonry columns that were confined with multi-layered SRG jackets with different densities of steel fiber sheet (670 g/m^2 and 1,200 g/m^2, labeled as G600 and G1200, respectively, by Kerakoll). The different sheet densities were achieved by different fiber cord spacings. All specimens in Phase II were constructed from the same

masonry materials and were constructed and tested by the same researchers. Specimens confined with steel fiber of density 1,200 g/m^2 are included in this thesis work and are labeled Groups 1-6 (shown in Table 5.1). Specimens confined with steel fiber of density 670 g/m^2 are labeled Groups 7-12 and were reported by Senesi (2018). The combination of test parameters for specimens in each group is summarized in Table 5.1. Specimen groups are compared in terms of average peak strength, normalized compressive strength relative to the average unconfined compressive strength, axial strain at peak stress, and axial strain at ultimate stress, where the values are summarized in Table 5.2.

Specimens with sharp corners and confined with a single fiber layer (Groups 1 and 7) showed that the higher density steel fiber provided a larger increase in compressive strength than the lower density fiber (see Table 5.2). The confined compressive strength for specimens in Group 1 had a relatively small coefficient of variation (4.23 %). The confined compressive strength of specimens in Group 7 had a larger coefficient of variation (11.59%) indicating that the results had more scatter. The larger coefficient of variation could be due to the experience level of the researchers who constructed the specimens. The first two specimens in Group 7 were constructed while the researchers were gaining experience, while the final two specimens were constructed towards the end of the construction phase. Regarding the average axial strain at peak stress, specimens in Group 7 had a larger value than those of Group 1. Because the failure mode of these specimens was jack opening, this result suggests that the 670 g/m^2 fiber sheets (G600) had better bond with the masonry substrate than the 1,200 g/m^2 (G1200) fiber sheets. The better bond could be attributed to the steel fiber cord spacing, in which the larger spacing of the G600 fiber sheets allowed for better penetration of the matrix

between the fiber cords to bond to the substrate. In terms of the average axial strain at ultimate stress, specimens in Group 7 had a larger value than specimens in Group 1, with a resulting difference of 44% between the average results.

Regarding the sharp cornered specimens with multi-layered jackets (Groups 2 and 8; Groups 3 and 9), the results show that the normalized compressive strength for specimens confined with higher density fibers was slightly larger than that of specimens confined with lower density fibers. However, the increase in confined strength between the different steel fiber densities decreased as the number of fiber layers increased, as shown in Table 5.2. Therefore, even though the reinforcement ratio of specimens in Groups 2 and 3 was nearly 1.8 times greater than the ratio for specimens in Groups 8 and 9, the average increase in compressive strength was not significant (3.5%). Regarding axial strain at peak stress, the average value for specimens with the higher density steel fiber (Groups 2 and 3) was larger than that of specimens with the lower density steel (Groups 8 and 9), as shown in Table 5.2. This is contrary to the results provided by specimens with a single fiber layer in which the axial strain at peak stress was less for specimens confined with the higher density fiber. Similarly, the average axial strain at ultimate stress was larger for specimens confined with higher density fiber jackets. This result suggests that the bond behavior of sharp cornered specimens confined with higher density steel improves as the number of layers increases, which may be due to the fact that the internal layers of multi-layers jackets may be restrained from opening by the external layers, especially since the overlapping layer was located on different faces (see Sections 3.3.2.4 and 4.7.1.1).

Regarding specimens with rounded corners, the results showed a slight increase in compressive strength for the specimens confined with higher density steel fibers (Groups 4-6) than those confined with lower density steel fibers (Groups 10-12). Comparing specimens of Groups 4 and 10, the specimens confined with lower density fibers showed larger compressive strength (see Table 5.2). However, the specimens in Groups 4 and 10 had large coefficients of variation (CoV = 7.67% and 7.05%, respectively) indicating that the data collected in these groups had large scatter. Similar to the sharp cornered specimens, the increase in confined strength between the different steel fiber densities decreased as the number of fiber layers increased, as shown in Table 5.2. This indicates that the composite effectiveness in terms of increase in confined strength was slightly larger for the higher density steel fibers than the lower density fibers. However, regarding the average axial strain at peak stress, specimens confined with lower density fiber provided larger values than specimens confined with higher density fibers. This reveals that the bond behavior of low density steel fiber was better than that of the higher density fiber as explained previously. Similarly, the axial strain at ultimate stress was larger for specimens with lower density fiber jackets. This reveals that the better bond of the lower density steel fiber jackets allowed the columns to withstand greater compressive deformation, thereby increasing the ductility.

5.2.2. Comparison of Phase I and Phase II Specimens. The first phase of this study included masonry columns that were confined with a single-layer SRG jacket where the SRG composite was made from different types of matrix (lime-based mortar and cementitious mortar). Other test variables included the steel fiber sheet density (670 g/m^2 and 1,200 g/m^2) and corner radius (r = 0, 9.5, or 38.1 mm). All specimens in Phase I

were constructed from the same masonry materials and were constructed and tested by the same researchers. Specimens confined with SRG jackets with lime-based mortar (GeoCalce mortar by Kerakoll, average compressive strength = 13.1 MPa) were reported by Fraioli (2017) and are labeled Groups 13-16 in Table 5.1. Specimens confined with SRG jackets with cementitious mortar (GeoLite mortar by Kerakoll, compressive strength = 47.1 MPa) are labeled Groups 17-20 and were reported by Baietti (2017). The combination of test parameters for specimens in each group is summarized in Table 5.1.

Results from the Phase I study suggests that the compressive strength of the matrix mortar did not significantly influence the confined strength of the masonry columns (Baietti, 2017; Fraioli, 2017). Therefore, even though the SRG matrix was different than the matrix used in the Phase II study, the results of Groups 17-20 are included in the comparisons in this section

It should be noted that the unconfined compressive strength of the unreinforced masonry specimens was not the same for the two phases. The average unconfined compressive strength of specimens in Phases I and II were 7.38 MPa and 6.62 MPa, respectively. The percent difference between these compressive strength values is approximately 11%. The bricks and masonry mortar were provided from the same supplier; however, the average compressive strength of the masonry mortar used was 4.3 MPa and 3.4 MPa for Phase I and II specimens, respectively. The large variance was likely the result of the quantity of water used in the masonry mortar (1.10 kg of water per 25 kg bag of mortar in Phase I and 1.15 kg of water per 25 kg bag of mortar in Phase II). As discussed in Section 3.2.1.3, the addition of the water in Phase II was to improve the workability for the construction of the columns. The difference in the masonry mortar

compressive strengths is likely the reason for the variance of the average unconfined compressive strength for the specimens within the two phases of the study. In addition, seven unconfined (control) specimens were included in Phase II, whereas three were included in Phase I. Values of compressive strength determine from the three Phase I specimens had a larger coefficient of variation (CoV = 15.8%) than the seven Phase II specimens (CoV = 11.0%), indicating a larger scatter and higher degree of uncertainty.

Specimen groups that included sharp cornered columns confined with a single layer of steel fiber with a density of 670 g/m^2 (Group 7, 13, and 17) were compared in terms of normalized compressive strength, average peak stress, axial strain at peak stress, and axial strain at ultimate stress. Table 5.2 shows that the average normalized compressive strength of Group 7 specimens was significantly lower than those of Groups 13 and 17. In terms of average peak axial stress, the percent difference between specimens in Group 7 and Groups 13 and 17 was approximately 33%. This variation does not correlate with results in literature, that the confining action is more effective for lower strength columns (El-Hacha & Mashrik, 2012; Ombres, 2014; Napoli et al., 2016). Reasons for this could be due to the thickness of the matrix mortar layers and the failure mode observed. Specimens in the first phase of this study had individual matrix layers of approximately 5 mm, allowing for a total matrix thickness of 10 mm for specimens confined with a single fiber jacket layer. Specimens in the second phase of this study had matrix layers that ranged from 2 mm to 4 mm in thickness, as described in Section 3.3.2.4. The total thickness of the matrix with a single fiber jacket was 6 mm. The thickness of the matrix layers could change the overall compressive behavior of the confined column because jacket opening governed the failure mode, and jacket opening

is a function of the bond behavior. It is hypothesized that a thicker matrix resulted in a better bond, thus delaying the failure and resulting in larger normalized peak stress values for the Phase I specimens.

Similar to the trend in average compressive strength values, the average axial strain at peak stress was lower for specimens in Group 7 compared to specimens of Groups 13 and 17, as shown in Table 5.2. The average percent difference between the axial strain values in Group 7 and Groups 13 and 17 is approximately 12%. In terms of average axial strain at ultimate stress, specimens in Group 7 had significantly lower values compared to specimens in Group 13 and 17, with percent differences of 53% and 85%, respectively. This indicates that the SRG jackets in Phase I of the study had better bond behavior than those in Phase II.

A similar response was evident for specimens with rounded corners and confined with a single fiber layer (density equal to 670 g/m^2). The average normalized compressive strength for Group 10 specimens was significantly lower than those of Groups 15 and 19, indicating the confining action was greater in the specimens in the first phase, as shown in Table 5.2. The average percent difference between the average peak axial stress values of Group 10 and Groups 15 and 19 is approximately 28% and 26%, respectively. In terms of axial strain at peak stress, specimens in Group 10 had significantly lower values compared to those in Groups 15 and 19, as shown in Table 5.2. Similarly, the axial strain at ultimate stress for specimens in Group 10 was lower than that for specimens in Groups 15 and 19, resulting in percent difference of 51% and 80%, respectively. Again, these results indicate that the SRG jackets in Phase I of the study had

better bond behavior than those in Phase II, possibly a results of the different matrix mortar thickness as discussed previously.

Similar to results found in this thesis work, the confined specimens in Phase I of this study with rounded corners had larger increases in peak axial stress compared to specimens with sharp corners, indicating better confining action by the composite system. On the other hand, specimens with sharp corners provided an increase in axial strain at ultimate stress compared to those with rounded corners. This indicates, due to the crushing of the corners, specimens with sharp corners were able to withstand an increased axial strain and an increased amount of total energy absorbed by the confined column.

Regarding the specimens confined with a single steel fiber layer with a sheet density of 1,200 g/m^2, Group 16 and Group 20 specimens had rounded corners with a radius of 9.5 mm. Specimens in Groups 1 and 4 had corner radii of 0 mm and 38.1 mm, respectively, as shown in Table 5.1. Therefore, the normalized compressive strength of specimens in Groups 16 and 20 would be expected to fall in the range of the normalized compressive strength of specimens in Groups 1 and 4. However, as shown in Table 5.2, the normalized compressive strength for specimens in Groups 16 and 20 is larger than both the normalized compressive strength of Groups 1 and 4. Again, these results indicate that the SRG jackets of specimens in Phase I of this study had better bond and confining action than those of Phase II.

5.3. COMPARISON WITH EXISTING MODELS

This section compared the increase in compressive strength predicted by existing models to those determined by the experiment program of this thesis work.

Table 5.1. Specimen Parameters

Phase	Ref.	Specimen Group	Fiber Density	Matrix Type	Corner Radius	Number of Fiber Layers	Number of Overlapping Faces
			g/m^2	[1]	mm	-	-
I	-	Group 1	1,200	1	0	1	1
I	-	Group 2	1,200	1	0	2	1
I	-	Group 3	1,200	1	0	3	1
I	-	Group 4	1,200	1	38.1	1	1
I	-	Group 5	1,200	1	38.1	1	2
I	-	Group 6	1,200	1	38.1	2	1
I	Senesi (2018)	Group 7	670	1	0	1	1
I	Senesi (2018)	Group 8	670	1	0	2	1
I	Senesi (2018)	Group 9	670	1	0	3	1
I	Senesi (2018)	Group 10	670	1	38.1	1	1
I	Senesi (2018)	Group 11	670	1	38.1	1	2
I	Senesi (2018)	Group 12	670	1	38.1	2	1
II	Fraioli (2017)	Group 13	670	1	0	1	1
II	Fraioli (2017)	Group 14	670	1	9.5	1	1
II	Fraioli (2017)	Group 15	670	1	38.1	1	1
II	Fraioli (2017)	Group 16	1,200	1	9.5	1	1
II	Baietti (2017)	Group 17	670	2	0	1	1
II	Baietti (2017)	Group 18	670	2	9.5	1	1
II	Baietti (2017)	Group 19	670	2	38.1	1	1
II	Baietti (2017)	Group 20	1,200	2	9.5	1	1

Note: [1] Matrix Type 1: GeoCalce Mortar; Matrix Type 2: GeoLite Mortar

Table 5.2. Phase I and Phase II: Summary of Results

Ref.	Specimen		f_{mo} or f_{mc}	$\overline{f_{mo}}$ or $\overline{f_{mc}}$	STD	CoV	$\frac{\overline{f_{mc}}}{\overline{f_{mo}}}$	$f_{mo,u}$ or $f_{mc,u}$	$\overline{f_{mo,u}}$ or $\overline{f_{mc,u}}$	ε_{mo} or ε_{mc}	$\overline{\varepsilon_{mo}}$ or $\overline{\varepsilon_{mc}}$	$\varepsilon_{mo,u}$ or $\varepsilon_{mc,u}$	$\overline{\varepsilon_{mo,u}}$ or $\overline{\varepsilon_{mc,u}}$	STD	CoV	Failure Mode	Axial Disp.
-	Group	Name	MPa	MPa	MPa	%	-	MPa	MPa	mm / mm	mm / mm	mm / mm	mm / mm	mm / mm	%	C/O[1]	S/A1/ A2[2]
Jemison / Senesi (2018)	Control	UC-1	7.65	6.62	0.73	11.0	-	6.50	5.59	0.0061	0.0061	0.0074	0.0078	0.0013	16.6	C	A1
		UC-2	6.16					5.21		0.0071		0.0079				C	S
		UC-3	6.47					5.48		0.0050		0.0051				C	A2
		UC-4	6.28					5.33		0.0063		0.0080				C	S
		UC-5	5.64					4.78		0.0056		0.0090				C	A1
		UC-6	6.61					5.48		0.0056		0.0087				C	A2
		UC-7	7.52					6.37		0.0072		0.0082				C	A2
-	Group 1	C-12-0-1-1	7.28	7.59	0.32	4.2	1.15	6.19	6.43	0.0093	0.0068	0.0102	0.0080	0.0015	18.3	O	S
		C-12-0-1-2	7.34					6.23		0.0062		0.0075				O	A1
		C-12-0-1-3	7.87					6.66		0.0052		0.0073				O	A1
		C-12-0-1-4	7.86					6.65		0.0066		0.0070				O	A1
-	Group 2	C-12-0-2-1	8.31	8.45	0.68	8.1	1.28	7.05	7.17	0.0081	0.0090	0.0103	0.0125	0.0024	18.9	O	S
		C-12-0-2-2	7.83					6.63		0.0072		0.0117				O	A1
		C-12-0-2-3	8.23					7.00		0.0099		0.0158				O	S
		C-12-0-2-4	9.42					8.00		0.0108		0.0121				O	S
-	Group 3	C-12-0-3-1	9.36	9.32	0.59	6.3	1.41	7.95	7.92	0.0112	0.0099	0.0374	0.0275	0.0136	49.4	O	S
		C-12-0-3-2	10.05					8.53		0.0076		0.0142				O	S
		C-12-0-3-3	9.22					7.84		0.0114		0.0176				O	S

Table 5.2. Phase I and Phase II: Summary of Results (Cont.)

		C-12-0-3-4	8.63					7.35		0.0095		0.0409				O	S
-	**Group 4**	C-12-38-1-1	7.09	7.73	0.59	7.7	1.17	6.02	6.54	0.0071	0.0065	0.0081	0.0077	0.0007	9.6	O	A2
		C-12-38-1-2	7.96					6.76		0.0065		0.0075				O	A2
		C-12-38-1-3	8.43					7.17		0.0056		0.0067				O	A2
		C-12-38-1-4	7.42					6.22		0.0067		0.0084				O	A1
-	**Group 5**	C-12-38-1(2)-1	9.70	8.73	1.01	11.5	1.32	8.20	7.32	0.0081	0.0066	0.0099	0.0087	0.0010	11.1	O	A2
		C-12-38-1(2)-2	7.78					6.58		0.0057		0.0081				O	A1
		C-12-38-1(2)-3	9.50					7.76		0.0062		0.0078				O	A2
		C-12-38-1(2)-4	7.95					6.76		0.0066		0.0092				O	A2
-	**Group 6**	C-12-38-2-1	8.83	9.08	0.49	5.4	1.37	7.49	7.67	0.0064	0.0073	0.0074	0.0086	0.0010	11.1	O	A2
		C-12-38-2-2	8.66					7.32		0.0084		0.0096				O	A1
		C-12-38-2-3	9.77					8.18		0.0078		0.0092				O	A2
		C-12-38-2-4	9.06					7.70		0.0068		0.0082				O	A1
Senesi (2018)	**Group 7**	C-6-0-1-1	6.17	6.95	0.81	11.6	1.05	5.24	5.87	0.0096	0.0086	0.0135	0.0125	0.0017	13.7	O	S
		C-6-0-1-2	6.41					5.44		0.0083		0.0140				O	A2
		C-6-0-1-3	7.90					6.71		0.0091		0.0122				O	A2
		C-6-0-1-4	7.33					6.08		0.0076		0.0102				O	A1
Senesi (2018)	**Group 8**	C-6-0-2-1	8.61	8.23	0.58	7.1	1.24	7.31	6.99	0.0101	0.0078	0.0134	0.0114	0.0021	18.6	O	S
		C-6-0-2-2	8.58					7.29		0.0079		0.0127				O	S

Table 5.2. Phase I and Phase II: Summary of Results (Cont.)

		C-6-0-2-3	8.37					7.11		0.0066		0.0109				O	A1
		C-6-0-2-4	7.37					6.25		0.0066		0.0087				O	A1
Senesi (2018)	**Group 9**	C-6-0-3-1	9.14	9.16	0.53	5.8	1.38	7.76	7.78	0.0103	0.0089	0.0148	0.0133	0.0014	10.6	O	S
		C-6-0-3-2	9.48					8.04		0.0091		0.0124				O	S
		C-6-0-3-3	8.42					7.16		0.0090		0.0141				O	S
		C-12-0-3-4	9.60					8.16		0.0070		0.0118				O	S
Senesi (2018)	**Group 10**	C-6-38-1-1	7.90	8.22	0.58	7.1	1.24	6.67	6.96	0.0069	0.0069	0.0083	0.0085	0.0008	9.5	O	A2
		C-6-38-1-2	8.13					6.90		0.0078		0.0097				O	A1
		C-6-38-1-3	7.79					6.59		0.0063		0.0083				O	A2
		C-6-38-1-4	9.06					7.68		0.0067		0.0078				O	A1/2
Senesi (2018)	**Group 11**	C-6-38-1(2)-1	8.10	8.41	0.33	4.0	1.27	6.89	7.14	0.0084	0.0078	0.0091	0.0094	0.0003	2.8	O	A2
		C-6-38-1(2)-2	8.14					6.91		0.0075		0.0093				O	A1
		C-6-38-1(2)-3	8.71					7.40		0.0073		0.0097				O	A2
		C-6-38-1(2)-4	8.68					7.35		0.0080		0.0095				O	A2
Senesi (2018)	**Group 12**	C-6-38-2-1	9.82	8.81	0.75	8.6	1.33	8.34	7.47	0.0090	0.0084	0.0123	0.0109	0.0017	15.6	O	S
		C-6-38-2-2	8.39					7.07		0.0079		0.0097				O	A2
		C-6-38-2-3	8.10					6.88		0.0070		0.0092				O	A1/2
		C-6-38-2-4	8.93					7.58		0.0098		0.0125				O	A2

Table 5.2. Phase I and Phase II: Summary of Results (Cont.)

Baietti / Fraioli (2017)	**Control**	UC-1	8.72	7.38	1.16	15.8	-	7.41	6.27	0.0051	0.0058	0.0055	0.0096	0.0038	39.2	C	-
		UC-2	6.64					5.64		0.0062		0.0129				C	-
		UC-3	6.78					5.76		0.0061		0.0103				C	-
Fraioli (2017)	**Group 13**	C-1-6-0-1	10.28	9.36	0.73	7.8	1.41	8.74	7.95	0.0099	0.0099	0.0210	0.0214	0.0005	2.4	O	-
		C-1-6-0-2	9.46					8.04		0.0103		0.0217				O	-
		C-1-6-0-3	9.14					7.77		0.0101		0.0220				O	-
		C-1-6-0-4	8.54					7.26		0.0095		0.0210				O	-
Fraioli (2017)	**Group 14**	C-1-6-9-1	9.21	9.41	0.48	5.1	1.42	7.83	8.00	0.0114	0.0116	0.0115	0.0144	0.0056	38.6	O	-
		C-1-6-9-2	9.07					7.71		0.0142		0.0208				O	-
		C-1-6-9-3	9.96					8.47		0.0092		0.0109				O	-
Fraioli (2017)	**Group 15**	C-1-6-38-1	9.74	10.41	0.52	5.0	1.57	8.28	8.84	0.0131	0.0107	0.0171	0.0143	0.0028	19.4	O	-
		C-1-6-38-2	10.40					8.84		0.0080		0.0110				O	-
		C-1-6-38-3	11.00					9.35		0.0098		0.0130				O	-
		C-1-6-38-4	10.48					8.91		0.0119		0.0160				O	-
Fraioli (2017)	**Group 16**	C-1-12-9-1	10.42	10.00	0.34	3.4	1.51	8.86	8.50	0.0095	0.0076	0.0110	0.0098	0.0009	9.0	O	-
		C-1-12-9-2	9.70					8.25		0.0061		0.0090				O	-
		C-1-12-9-3	9.75					8.29		0.0085		0.0100				O	-
		C-1-12-9-4	10.11					8.59		0.0064		0.0093				O	-
Baietti (2017)	**Group 17**	C-2-6-0-1	9.13	9.31	0.60	6.4	1.41	7.76	7.92	0.0139	0.0096	0.0250	0.0310	0.0050	16.0	O	-

Table 5.2. Phase I and Phase II: Summary of Results (Cont.)

		C-2-6-0-2	10.09					8.58		0.0078		0.0290				O	-
		C-2-6-0-3	9.37					7.96		0.0072		0.0340				O	-
		C-2-6-0-4	8.66					7.36		0.0094		0.0360				O/R	-
Baietti (2017)	**Group 18**	C-2-6-9-1	9.50	9.85	0.27	2.7	1.49	8.08	8.37	0.0113	0.0112	0.0197	0.0224	0.0051	22.8	O	-
		C-2-6-9-2	10.13					8.61		0.0106		0.0300				O	-
		C-2-6-9-3	9.83					8.36		0.0101		0.0197				O	-
		C-2-6-9-4	9.95					8.46		0.0130		0.0200				O	-
Baietti (2017)	**Group 19**	C-2-6-38-1	9.75	10.26	0.69	6.7	1.55	8.29	8.72	0.0139	0.0112	0.0200	0.0199	0.0003	1.7	O	-
		C-2-6-38-2	11.21					9.53		0.0094		0.0194				O/R	-
		C-2-6-38-3	10.32					8.77		0.0092		0.0202				O	-
		C-2-6-38-4	9.75					8.29		0.0125		0.0198				O	-
Baietti (2017)	**Group 20**	C-2-12-9-1	10.74	10.49	0.48	4.6	1.59	9.13	8.92	0.0084	0.0095	0.0099	0.0116	0.0016	13.7	O	-
		C-2-12-9-2	11.05					9.39		0.0100		0.0130				O	-
		C-2-12-9-3	10.11					8.59		0.0098		0.0129				O	-
		C-2-12-9-4	10.07					8.56		0.0100		0.0106				O	-

Note:
(1) C = masonry crushing, O = jacketing opening, R = fiber rupture
(2) S = All Corners Symmetric, A1 = Asymmetric before peak axial stress was reached, A2 = Asymmetric after peak axial stress
Conversions: 1 MPa = 145.038 psi, 1 mm/mm = 1 in/in

Table 5.3. Predicted Strength of Confined Specimen Groups

Ref.	Specimen Group	Exp.	Krevaikas and Triantafillou (2005)			Di Ludovico et al. (2010)			CNR DT200 R1 (2013)			Cascardi et al. (2017)		
		$\frac{\overline{f_{mc}}}{\overline{f_{mo}}}$	$\frac{f_{l,eff}}{f_{mo}}$	$\frac{f_{mc}}{f_{mo}}$	Calc. / Exp	$\frac{f_{l,eff}}{f_{mo}}$	$\frac{f_{mc}}{f_{mo}}$	Calc. / Exp	$\frac{f_{l,eff}}{f_{mo}}$	$\frac{f_{mc}}{f_{mo}}$	Calc. / Exp	$\frac{f_{l,eff}}{f_{mo}}$	$\frac{f_{mc}}{f_{mo}}$	Calc. / Exp
-	Group 1	1.15	0.20	1.00	0.87	0.20	1.37	1.19	0.06	1.38	1.21	0.22	1.37	1.20
-	Group 2	1.28	0.41	1.28	1.00	0.41	1.68	1.32	0.12	1.54	1.21	0.87	1.99	1.56
-	Group 3	1.41	0.61	1.61	1.15	0.61	1.99	1.41	0.17	1.67	1.18	1.95	2.86	2.03
-	Group 4	1.17	0.42	1.29	1.10	0.42	1.69	1.45	0.12	1.55	1.33	0.24	1.43	1.22
-	Group 5	1.32	0.42	1.29	0.97	0.42	1.69	1.28	0.12	1.55	1.17	0.24	1.43	1.08
-	Group 6	1.37	0.83	1.97	1.44	0.83	2.29	1.67	0.23	1.78	1.29	0.95	2.14	1.56
Senesi (2018)	Group 7	1.05	0.10	1.00	0.95	0.10	1.19	1.14	0.03	1.27	1.21	0.11	1.26	1.20
Senesi (2018)	Group 8	1.24	0.20	1.00	0.80	0.20	1.36	1.10	0.06	1.38	1.11	0.43	1.69	1.36
Senesi (2018)	Group 9	1.38	0.30	1.10	0.79	0.30	1.52	1.10	0.09	1.47	1.06	0.96	2.30	1.66
Senesi (2018)	Group 10	1.24	0.20	1.00	0.81	0.20	1.37	1.10	0.06	1.38	1.12	0.12	1.30	1.05
Senesi (2018)	Group 11	1.27	0.20	1.00	0.79	0.20	1.37	1.08	0.06	1.38	1.09	0.12	1.30	1.02
Senesi (2018)	Group 12	1.33	0.41	1.27	0.96	0.41	1.68	1.27	0.12	1.54	1.16	0.47	1.80	1.35
Fraioli (2017)	Group 13	1.27	0.09	1.00	0.79	0.09	1.18	0.93	0.03	1.26	0.99	0.10	1.38	1.09
Fraioli (2017)	Group 14	1.28	0.12	1.00	0.78	0.12	1.22	0.96	0.03	1.29	1.01	0.10	1.39	1.09

Table 5.3. Predicted Strength of Confined Specimen Groups (Cont.)

Fraioli (2017)	Group 15	1.41	0.18	1.00	0.71	0.18	1.33	0.94	0.05	1.36	0.97	0.11	1.44	1.02
Fraioli (2017)	Group 16	1.36	0.24	1.00	0.74	0.24	1.42	1.05	0.07	1.41	1.04	0.20	1.56	1.15
Baietti (2017)	Group 17	1.26	0.09	1.00	0.79	0.09	1.18	0.93	0.03	1.26	1.00	0.10	2.37	1.88
Baietti (2017)	Group 18	1.33	0.12	1.00	0.75	0.12	1.22	0.92	0.03	1.29	0.97	0.10	2.42	1.81
Baietti (2017)	Group 19	1.39	0.18	1.00	0.72	0.18	1.33	0.96	0.05	1.36	0.98	0.11	2.58	1.86
Baietti (2017)	Group 20	1.42	0.24	1.00	0.70	0.24	1.42	1.00	0.07	1.41	1.00	0.20	3.02	2.12

5.3.1. Overview. This section compares the increase in compressive strength of masonry columns provided by SRG confinement with values calculated using different models from literature. Several design models have been developed to determine the strength of FRP-confined masonry columns (e.g., CNR-DT 200 R1/2013), but currently no models have been developed to predict the strength enhancement provided by SRG confinement to masonry columns. This issue was noted by Fossetti and Minafo (2017), who studied the effectiveness of various types of strengthening systems on masonry columns, one of which included the use of high-strength steel wires within the mortar joints and bonded with a cementitious mortar matrix (discussed in Section 2.2.2.5). Due to the lack of existing models, Fossetti and Minafo (2017) evaluated the applicability of expressions for FRP-confined masonry for this type of confinement. A similar procedure is adopted herein to evaluate the applicability of different expressions for SRG confined masonry. A recent study by Cascardi et al. (2017), which proposed models for FRCM confined masonry, is also included in this section.

The following sections describe the models considered, along with the formulations and the parameters included.

Many of the models calculate the confined compressive strength (f_{mc}) based on the well-known formula typically adopted for FRP-confined concrete columns given in the general form in Equation 5.1:

$$f_{mc} = f_{mo}\left[\alpha + k'\left(\frac{f_{l,eff}}{f_{mo}}\right)^{\beta}\right] \qquad \text{Eq. 5.1}$$

where:

f_{mc} = compressive strength of confined masonry

f_{mo} = compressive strength of unconfined masonry

k' = non-dimensional coefficient (defined in each model)

α and β = empirical constants (defined in each model)

$f_{l,eff}$ = effective confinement pressure

$$f_{l,eff} = k_e f_l = k_H k_v f_l \quad \text{Eq. 5.2}$$

f_l = equivalient confinement stress

k_H = horizontal efficiency coefficient given in Equation 5.4

k_V = vertical efficiency coefficient, equal to 1.0 for columns continuously confined along the length

$$f_l = \frac{(b+h)}{bh} t_f E_f \varepsilon_f \quad \text{Eq. 5.3}$$

$$k_H = 1 - \frac{b'^2 + h'^2}{3A_g} \quad \text{Eq. 5.4}$$

where:

b = column width

h = column depth

t_f = thickness of fiber

E_f = Elastic Modulus of fiber

ε_f = circumferential strain of fiber

A_g = total cross-sectional area

$b' = b - 2*r$

$h' = h - 2*r$

r = corner radius

It is important to note that the general model in Equation 5.1 takes into account the influence of the transverse cross-sectional geometry in Equations 5.3 and 5.4. The model can be used for columns with multiple confining layers by multiplying the thickness of the fiber by the quantity of layers. The general model and the models discussed in this section assume the column is homogeneous and symmetric at each transverse cross section. In addition, the models assume uniform stress distribution along the length of the column.

5.3.2. Description of Models Evaluated. This section provides details regarding the process used to develop the compressive strength models.

5.3.2.1. Krevaikas and Triantafillou Model (2005). Krevaidas and Triantafillou proposed a model for the compressive strength (f_{mc}) of FRP-confined masonry columns based on the model previously described that is typically adopted for FRP-confined concrete. The authors calibrated the model for masonry columns confined with FRP systems while varying the following parameters: number of fiber layers, column corner radius, and cross-sectional aspect ratio.

From the general model, the empirical constant α, was determined to be less than 1.0. For both concrete and masonry confined specimens with low volumetric fractions of transverse confining reinforcement, experimental evidence suggests that for low values of confining stress, the confined compressive strength does not exceed the unconfined value (Krevaikas & Triantafillou, 2005). The volumetric fraction of reinforcement is defined as the ratio of the total fiber area to the total cross-sectional area in the direction of interest. Given the experimental results considered, the ratio of the confined to unconfined strength, $\frac{f_{mc}}{f_{mo}}$, versus the normalized confining stress, $\frac{f_{l,eff}}{f_{mo}}$, are shown in Figure 5.1. Using a best-fit analysis, the empirical constants were determined to be α = 0.60, β = 1.0, k' = 1.65 for the experimental results considered.

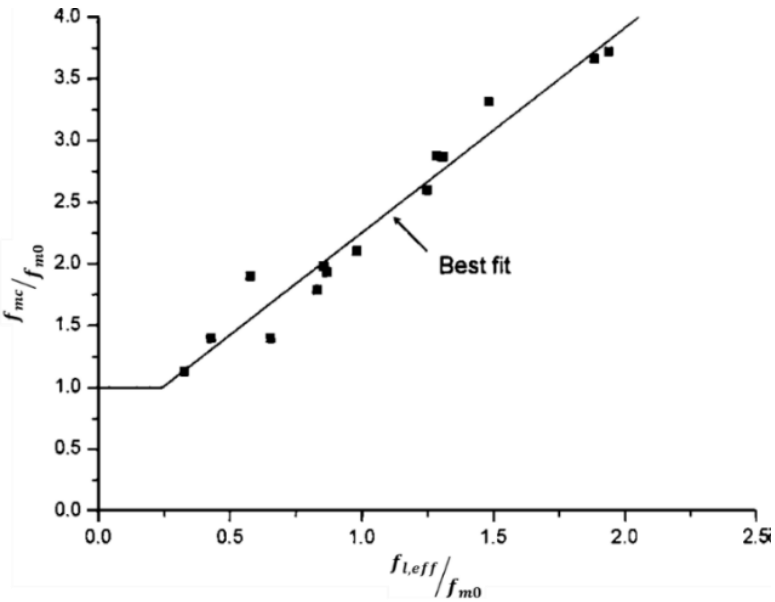

Figure 5.1. Normalized Compressive Strength of Confined Masonry verses the Normalized Confining Stress (Krevaikas & Triantafillou, 2005)

Following, the authors substituted the values into Equation 5.1 and set the ratio $\frac{f_{mc}}{f_{mo}}$ equal to 1.0, and the ratio of $\frac{f_{l,eff}}{f_{mo}}$ was computed to be 0.24. The proposed model for the confined compressive strength of masonry is given in Equation 5.5 and 5.6:

$$f_{mc} = f_{mo}\ ;\ if\ \frac{f_{l,eff}}{f_{m0}} \leq 0.24 \qquad \text{Eq. 5.5}$$

$$f_{mc} = f_{mo}\left(0.6 + 1.65\frac{f_{l,eff}}{f_{mo}}\right);\ \ if\ \frac{f_{l,eff}}{f_{mo}} > 0.24 \qquad \text{Eq. 5.6}$$

where the nomenclature is discussed in Section 2.2.1.1.

5.3.2.2. Di Ludovico et al. Model (2010). The authors performed a comparative study of existing formulations in the literature and calibrated the adopted model for FRP-confined concrete for the experimental data collected on FRP-confined masonry. The specimens of the experimental program were solid clay brick masonry columns having a constant corner radius and were confined with an FRP system with different fiber types. The effectiveness of GFRP, CFRP, and BFRP confining systems were included. The authors used the general formulations to determine the effective lateral pressure($f_{l,eff}$) and coefficient (k_H), then they proposed an expression to calculate the effectiveness coefficient (k'). The authors used the formulation developed by Toutanji and Deng (2002) for k' proposed for concrete compression members:

$$k' = k_1\left(\frac{f_{l,eff}}{f_{mo}}\right)^{\tau} \qquad \text{Eq. 5.7}$$

in which the parameters calibrated in Equation 5.7 were:

k_1 = ideal confinement coefficient = 1.53

τ = shape parameter based on plastic characteristics of the material = - 0.10

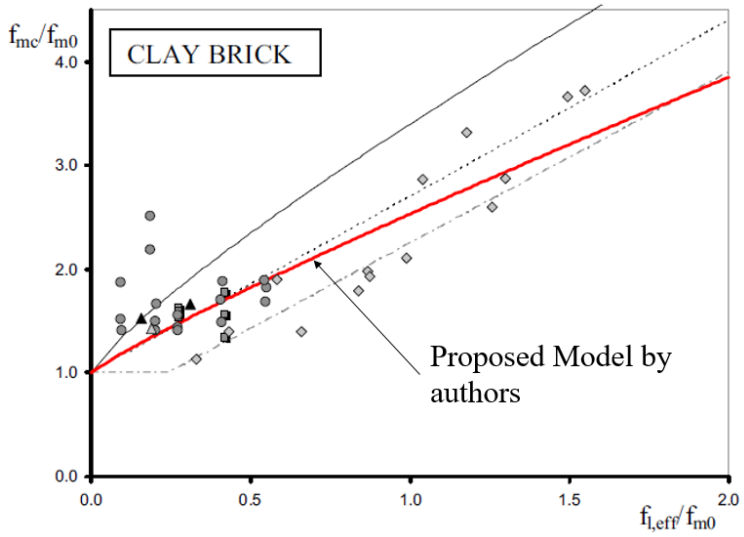

Figure 5.2. Proposed Model for Experimental Results of FRP-Confined Masonry (Di Ludovico et al, 2010)

As shown in Figure 5.2, the authors calibrated the coefficients using the same technique described in Section 5.3.2.1 for the experimental results. The resulting expression to predict the confined strength of masonry columns is:

$$f_{mc} = f_{mo}\left[1.0 + k'\frac{f_{l,eff}}{f_{mo}}\right] \quad \text{Eq. 5.8}$$

$$k' = 1.53\left(\frac{f_{l,eff}}{f_{mo}}\right)^{-0.10} \quad \text{Eq. 5.9}$$

where α and β in Equation 5.1 are equal to 1.0. For details on the other variables stated, see Section 2.2.1.5.

5.3.2.3. CNR – DT 200 R1 Model (2013). The Italian CNR-DT 200 code uses the same general model described in Equation 5.1 to determine the confined compressive strength of masonry members. The empirical constants α and β were set to 1.0 and 0.5, respectively. The equation is different from others in literature in the formulation developed for k' and $f_{l,eff}$ in terms of f_l.

$$k' = \alpha_2 * \left(\frac{g_m}{1000}\right)^{\alpha_3} \quad \text{Eq. 5.10}$$

where g_m is the masonry mass-density (g_m is taken as 1,600 kg/m^3 in this study), and α_2 and α_3 are coefficients equal to 1.0. For the case of rectangular cross-sections columns wrapped continuously, f_l is:

$$f_l = \frac{2t_f}{max\{b, h\}} * E_f \varepsilon_{fd,rid} \quad \text{Eq. 5.11}$$

where:

$\varepsilon_{fd,rid}$ = 0.004 mm/mm as a conventional strain limitation

E_f = elastic modulus for the fiber material.

The resulting expression to determine the confined strength in accordance with CNR-DT 200 R1 (2013) is:

$$f_{mc} = f_{mo}\left[1.0 + \frac{g_m}{1000}\left(\frac{f_{l,eff}}{f_{mo}}\right)^{0.5}\right] \quad \text{Eq. 5.12}$$

5.3.2.4. Cascardi et al. Model (2017). The authors proposed both a detailed and simplified model to determine the compressive strength of concrete and masonry compression elements confined with FRCM composite. Both models were formulated using a statistical evaluation of a database of test results collected from the literature. FRCM with different fiber types and matrix properties were included, however no tests were included on SRG confined masonry since none were available at the time. The simplified model is included in this discussion since it is easier to implement for practical applications (Cascardi et al., 2017). Previous literature suggested that the compressive strength is equal to the unconfined compressive strength plus a contribution provided by the jacket, depending on the confining pressure modified by a non-dimensional coefficient (k') (Guler & Ashour, 2015). The aim of the proposed models was to define a function considering the contribution from the fiber jacket and the inorganic matrix used for FRCM systems. A multiple linear regression was used to calculate the non-

dimensional coefficients. This function was used for a database of confined masonry columns to develop a regression surface shown in Figure 5.3. It was determined that the matrix of the FRCM jacket played a significant role in the confined stress. The author surmised that if a poor-quality matrix (in terms of compressive strength) was used, premature cracking of the mortar would occur, causing the effectiveness of the confinement system to decrease.

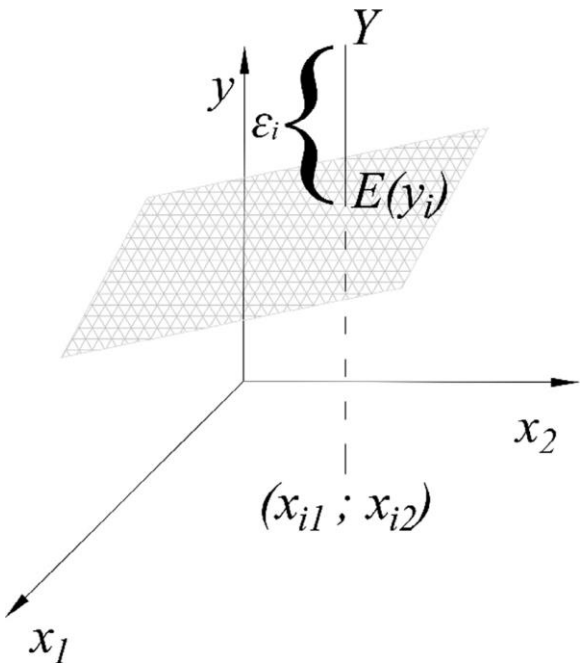

Figure 5.3. Scheme of the Multiple Linear Regression Surface $E(y_i)$ (Cascardi et al., 2017)

The simplified model proposed for masonry columns confined with a FRCM systems is:

$$f_{mc} = f_{mo}\left(1.0 + k'\left(\frac{f_l}{f_{mo}}\right)^{\frac{1}{2}}\right) \quad \text{Eq. 5.13}$$

$$k' = 6\rho_{mat}\frac{f_{c,mat}}{f_{mo}} \quad \text{Eq. 5.14}$$

$$f_l = \frac{nt_f E_f \varepsilon_f}{D'} \quad \text{Eq. 5.15}$$

$$\rho_{mat} = \frac{4t_{mat}}{D'} \quad \text{Eq. 5.16}$$

where the nomenclature is discussed in Section 2.2.2.6.

The proposed models can be used for columns with the following parameters: transverse cross-section (circular or rectangular), number of confinement layers, type of fiber reinforcement, unconfined compressive strength, and matrix compressive strength. Interestingly, the model does not include a factor to account for corner radius of rectangular cross-sections. The approach used in this research work was to determine the diagonal of the rectangular-section from the center of the rounded corners, shown in Figure 5.4. Figure 5.5 describes the relationship between the detailed and the simplified models proposed. As shown in the figures, the simplified model provides less accurate results, but results that are generally conservative considering the data used to calibrate the model.

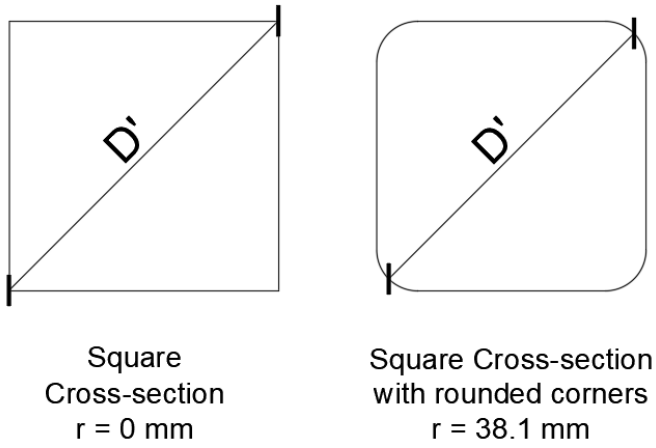

Figure 5.4. Measurement of Diagonal for Rectangular Cross-Sections

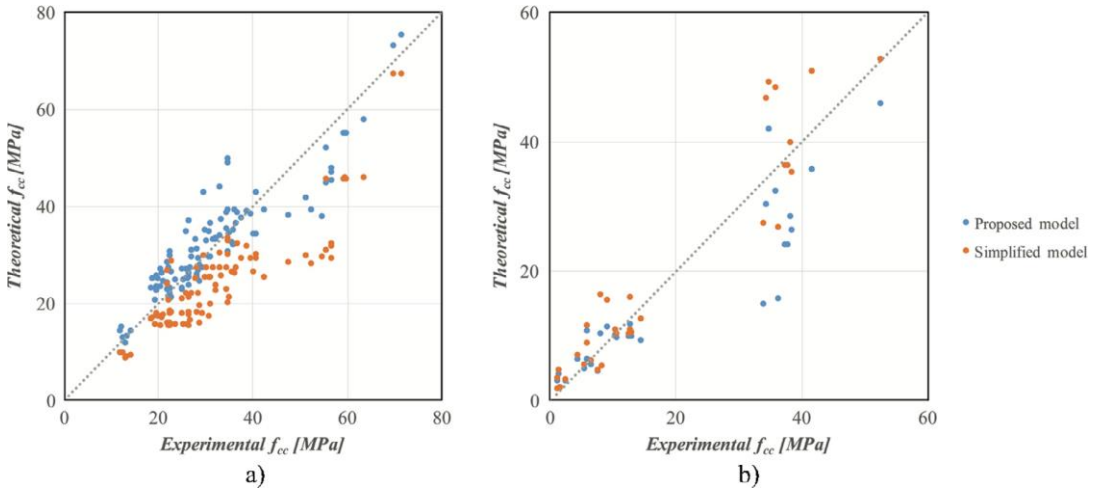

Figure 5.5. Proposed Detailed Models vs. Simplified Models (a) concrete, (b) masonry (Cascardi et al., 2017)

5.3.3. Discussion of Model Results. The results of the models presented in Section 5.3.2 are discussed in this section. Table 5.3 summarizes the predicted (Calc.) and experimental (Exp.) values of the compressive strength increase normalized by the

unconfined compressive strength, $\frac{f_{mc}}{f_{mo}}$, for specimens discussed in this thesis supplemented by those from Senesi (2018), Fraioli (2017), and Baietti (2017). Experimental values given in Table 5.3 are the average values of the specimens in the corresponding group, $\frac{\overline{f_{mc}}}{\overline{f_{mo}}}$.

5.3.3.1. Krevaikas and Triantafillou (2005). Results in Table 5.3 for the specimens discussed in this thesis show that the model proposed by Krevaikas & Triantafillou (2005) provided reasonable results, for Groups 1-5 (± 15%). The model overestimated the compressive strength increase by 44% for specimens in Group 6, which had two SRG confinement layers and rounded corners.

The proposed model by Krevaikas and Triantifillo does take into account the cross-section geometry through the horizontal effectiveness coefficient, k_H. Throughout the literature it has been found that the cross-section geometry is an important factor when determining the compressive strength of FRCM confined columns. Properties of the confinement fiber is also considered when determining the lateral confinement pressure. Properties of the fiber could vary greatly depending on the fiber used such as steel fiber or carbon fiber. In addition, the specimens used by the authors to calibrate the coefficients (α, β, and k') in the model also considered the aspect ratio (ranging from 1.0 to 2.0) of the cross-sectional geometry, which greatly affected the compressive strength of the confined columns in the experimental study. The proposed model does not take into account the fiber development length provided by the overlapping length and the number of overlapping faces, which is an important characteristic as it relates to bond of

FRCM systems. With the exception of Group 6, this model predicted reasonable values for specimens with varying number of confinement layers and various corner radii.

On the other hand, the model underestimated the effect of the SRG confinement for all other groups (Groups 7-20). With the exception of Group 12, this was due to the fact that the controlling equation of the predicted strength was Equation 5.5, which indicates no strength enhancement provided by the confinement. Groups 7-20 had lower density fibers (670 g/m^2) and/or a jacket with either one or two layers. Therefore, it appears that this model does not accurately predict the strength enhancement for relatively low values of lateral confining stress.

5.3.3.2. Di Ludovico et al. Model (2010). Values in Table 5.3 show that the model by Di Ludovico et al. (2010) overestimated the compressive strength increase for all specimen groups with higher density fiber (1,200 g/m^2), and for all groups with multiple jacket layers. The largest variance was for Group 6 with higher density fibers, two confining layers, and rounded corners. The authors who proposed this model considered the non-dimensional coefficient (k') to be a polynomial function instead of a constant value determined using experimental data, which is commonly used in other models in literature. Using the proposed formulation shown in Equation 5.9, the non-dimensional coefficient reduced as $\frac{f_{l,eff}}{f_{mo}}$ increased. Therefore, the coefficient reduced the overall predicted effectiveness of the confining system as the effective lateral confining pressure increased, assuming the unconfined compressive strength is constant. The experimental results showed that the effective lateral confining pressure increased as the number of SRG confinement layers increased, but the increase was not linearly

proportional to the number of confining layers. In turn, the composites effectiveness reduced as the number of layers increased, but in a non-linear fashion.

The model proposed by Di Ludovico et al. considered the transverse cross-sectional geometry by using the general horizontal efficiency coefficient k_H when calculating the effective lateral confining pressure. It is important to note that the model does consider the mechanical properties of the fiber in the calculation of the effective lateral confining pressure, however the coefficients (k_1 and τ) were calibrated using clay brick specimens confined with basalt, carbon, and glass fiber reinforced polymers, which provide different mechanical and bond characteristics than SRG systems. In addition, the model does not consider the development length of the composite. Overall, the proposed model by Di Ludovico et. al. overestimated the increase in compressive strength provided by the SRG jacket, especially for multi-layer jackets of higher density fibers (1,200 g/m^2).

5.3.3.3. CNR-DT 200 Model (2013). The model by CNR-DT 200 (2013) predicted reasonable results for the compressive strength increase for the masonry columns confined with different configurations of SRG systems, within 0.97-1.33 times the experimental values. It should be noted that the predicted values were determined using an estimated mass density of masonry of 1,600 kg/m^3. This value varies based on the proportions of the masonry components, which could range from 1,444 to 1,640 kg/m^3, based on volumetric proportion. The model does consider the cross-section geometry through the horizontal effectiveness coefficient (k_H) and the mechanical properties of the fiber. Similar to the other models, the CNR-DT 200 model does not take

into account the fiber development length, which can significantly affect the compressive strength of the confined columns.

5.3.3.4. Cascardi et al. (2016). The model proposed by Cascardi et al. overestimated the compressive strength values for all groups by 2%-112%. This model provided better results for groups with rounded corners than for those with sharp corners. However, the model did not directly account for rounded corners, only using the corner-to-corner diagonal (*D'* shown in Equation 5.15 and 5.16) as a proxy for the cross-sectional area. Specimens with rounded corners were considered to have a smaller diameter than the specimens with sharp corners, which reduced the predicted compressive strength. The model highly overestimated the compressive strength for sharp cornered specimens and multi-layer jackets (Groups 2 and 3), as well as those with high strength matrix (Groups 17-20). The calculated model values did not have the trend as the experimental results for peak compressive stress versus corner radius. The model predicted a decrease in compressive strength with increase in corner radius, the opposite of these experimental results. This model does consider the compressive strength of the matrix in turn, considering the matrix tensile strength. For Groups 1-16, the average compressive strength of the matrix mortar determined experimentally was below the value provided by the manufacturer; however, if the matrix compressive strength were the minimum compressive strength stated by the manufacturer (Kerakoll, 2017), the predicted value would have increased, with larger overestimations in the strength. Overall, the model proposed by Cascardi et al. did not provide accurate results given the experimental parameters. Explanation regarding how to take the column corner condition and the matrix mortar compressive strength into account should be further studied.

5.4. CONCLUDING REMARKS

This section summarizes the key aspects from the comparisons in Sections 5.2 and 5.3.

5.4.1. Comparison with Other Test Results. Experimental results of specimens in this thesis work were compared to others within the same phase of this study (Phase II) since they were constructed and tested by the same researchers. Specimens in this thesis work were confined with SRG jackets having a steel fiber sheet density of 1,200 g/m^2, while other specimens were confined with SRG jackets with a steel fiber sheet density of 670 g/m^2. Regarding sharp cornered specimens confined with a single fiber layer, the peak axial stress increased as the fiber density increased. However, the axial strain at peak stress decreased with the increase in steel fiber density. This suggests that the bond behavior of the composite improved as the density of the steel fiber jacket decreased. Contrary to the single layered specimens, sharp cornered columns confined with multiple fiber layers showed increasing axial strain at peak stress as the steel fiber density increased. The peak axial stress also increased as the density of the fibers increased, however the confinement effectiveness decreased with the increase in fiber layers.

Regarding the specimens with rounded corners and confined with a single fiber layer, the peak axial stress increased as the steel fiber density decreased. However, the specimens confined with the lower density steel fiber had a large coefficient of variation indicating a higher degree of uncertainty. Specimens with rounded column corners confined with multiple fiber layers and multiple fiber overlapping faces increased in peak axial stress as the fiber density increased. Regarding the axial strain at peak and ultimate

stress points, the values increased as the steel fiber density decreased, indicating better bond for composites with lower fiber density.

Comparing the specimens within Phases I and II of this study, it was noted that the unconfined compressive strength of the masonry columns varied significantly (11%). In addition, the thickness of the matrix layers between the two phases differed (10 mm vs. 6 mm). Sharp cornered specimens confined with a single layer of G600 steel fibers were directly compared between the phases. Larger increases in compressive strength (relative to the unconfined strength) were achieved by the SRG confinement in Phase I of the study than in Phase II, even though the unconfined compressive strength of the columns in Phase I was larger than in Phase II. This phenomenon disagrees with other results found in literature, however the different matrix thicknesses between the confinement systems could play a role in this observation (El-Hacha & Mashrik, 2012) (Ombres, 2014) (Napoli et al., 2016). In addition, sharp cornered specimens confined with a single layer of G600 in Phase I of the study provided increased axial strain at peak stress and axial strain at ultimate stress than specimens in Phase II, suggesting that these specimens provided increased ductility in terms of increase strength and axial strain at key points.

A similar response was evident for specimens with rounded corners and confined with a single layer of G600 steel fibers. Results determined by Fraioli (2017), Baietti (2017), and Senesi (2018) shared similar trends to those in this thesis work. Columns with rounded corners provided an increased peak axial stress compared to specimens with sharp corners, indicating better initial confining action by the confinement system. In addition, columns with sharp corners provided an increased axial strain at peak stress

compared to specimens with rounded corners. This indicates that specimens with sharp corners provided increased column ductility shown by the crushing of the column corners, allowing for increased axial strain and total energy absorbed compared to specimens with rounded corners.

5.4.2. Comparison with Existing Models. The compressive strength increase provided by the SRG jackets determined experimentally was compared to the predicted values calculated using models developed for FRP confined masonry by Krevaikas and Triantafillou (2005), Di Ludovico et al. (2010), CNR-DT 200 (2013), and for FRCM confined masonry by Cascardi et al. (2016). For the specimens within this thesis work, the model used by CNR-DT 200 (2013) provided the most accurate predictions. This result is also true for the experimental results found by Fraioli (2017), Baietti (2017), and Senesi (2018). More work is needed to improve the predictions for SRG jackets, and also to predict the stress-strain response of SRG-confined masonry.

6. SUMMARY, CONCLUSIONS, AND RECOMMENDATIONS

6.1. SUMMARY

This thesis work studied the behavior of unreinforced clay brick masonry columns confined by SRG jackets and subjected to monolithic, concentric axial loading. In particular, the effects of column corner radius, number of fiber layers, and number of overlapping faces were examined. This study was intended to expand the results obtained from a previous study by Baietti (2017) and Fraioli (2017) and a concurrent study by Senesi (2018). These tests are the first in the literature on confinement of masonry using SRG jackets.

This thesis presents the results of 31 columns constructed using solid clay brick units bonded using a natural hydraulic lime masonry mortar. Of the 31 specimens, seven were unconfined so that the strength and deformability enhancement provided by the SRG jacket could be determined. The 24 confined specimens in this thesis work were divided into six different groups based on their unique combination of test parameters. The parameter varied for sharp cornered columns was the number of fiber layers (ranging from 1-3 layers) in which each layer was bonded using a 2 mm thick layer of matrix mortar. The parameters varied for round cornered columns include the number of fiber layers (ranging from 1-2 layers) and the number of fiber overlap faces (either 1 or 2 column faces).

Data presented for all specimens included the axial stress – axial strain response, total energy absorbed, axial displacement type, and failure mode. In addition, key points were discussed for each specimen including the peak axial stress, ultimate axial strain,

and transverse strain at peak and ultimate stress points (where applicable). The influence of the various test parameters considered in this study was analyzed. Existing analytical models to predict the strength increase provided by confinement were discussed in terms of the compressive behavior. In addition, considering the specimens included in this thesis work and supplemented with others collected from the literature (Fraioli 2017, Baietti 2017, Senesi, 2018), models were evaluated to determine their applicability to predict the strength increase provided by SRG confinement system.

6.2. CONCLUSIONS

The following section includes concluding remarks based on the observed experimental and model results. Remarks in terms of column behavior are discussed briefly followed by the influence of the test parameters considered in this study. Remarks of the experimental results compared to additional specimens in Phases I and II of this study are discussed as well as the results of existing models to predict the increase in strength provided by SRG confinement.

1. The general behavior of unconfined specimens, in terms of the axial stress – axial strain response, can be described as having an initial linear response followed by non-linear response until the peak stress is reached. Thereafter, a rapid descending branch occurred due to the formation of large, longitudinal cracks. The general behavior of confined specimens, in terms of the axial stress – axial strain response, can be described as having an initial linear response that follows the unconfined behavior. Generally, after the unconfined strength is achieved, the axial stress continues to increase until the peak stress

is reached. After the peak stress, a descending branch is observed until failure occurs. The slope of the descending branch varied depending on the parameters of the confined specimen.

2. Regarding the effects of the number of fiber layers, increasing the number of fiber layers increased the compressive strength, average ultimate axial strain, and total energy absorbed by columns with sharp corners. This in turn, increased the column's ductility. The increase was not linearly proportional to the increase in number of fiber layers. Similarly, for specimens with rounded corners, increasing the number of fiber layers increased the compressive strength, average ultimate axial strain, and total energy absorbed by the column, in turn, increasing the column's ductility. The increase was not linearly proportional to the increase in number of fiber layers.
3. Regarding the effects of corner radius, no significant difference in confined compressive strength occurred as the corner radius increased for specimens with a single fiber layer. Both sharp and rounded cornered cross-sectional geometries produced an increase in compressive strength and ultimate axial strain compared to the unconfined specimens. For specimens with two fiber layers, the peak axial stress increased with increasing corner radius, however the ultimate strain decreased with the increase in corner radius. The total energy absorbed by the confined columns decreased with the increase in corner radius primarily due to the rapid descending branch shown in the axial stress- axial strain responses.

4. Increasing the number of overlapping faces at the end of the fiber strip slightly increased the compressive strength and ultimate axial strain. Specimens with the fiber overlap on two faces showed a similar response to specimens confined with two fiber layers.
5. Comparing the experimental results reported in this thesis work to other results collected within the second phase of the study, the results showed that increasing the fiber density increases the peak axial stress of the confined specimens. For sharp cornered specimens confined with a single layer of fibers, the axial strain at peak stress increased with the decrease in fiber density. On the contrary, for sharp cornered columns confined with multiple fiber layers, the axial strain at peak stress decreased with the decrease in fiber density.
6. Regarding specimens with rounded corners in the second phase of this study, as the density of the steel fibers increased the peak axial stress increased, however the axial strain at peak and ultimate stress points decreased. This indicates that the bond behavior becomes more enhanced as the steel density decreases for specimens with rounded corners.
7. Comparing sharp cornered specimens within Phases I and II of this study showed that specimens within Phase I had larger increases in peak axial stress, axial strain at peak stress, and axial strain at ultimate stress relative to specimens within Phase II. The increased results could be related to the increased thickness of the matrix layers of the confined specimens within the first phase or the increased unconfined compressive strength of the masonry

columns with in the first phase of this study. This phenomenon disagrees with other results found in literature for confining action of composite systems generally increases as the unconfined compressive strength decreases.

8. For specimens confined with a single layer of fiber (density = 670 g/m^2), the peak axial stress increased with the increase in corner radius. The axial strain at peak and ultimate stress points increased with the decrease in corner radius, indicating that specimens with sharp corners provide an increase in columns ductility due to the crushing of the corners, allowing for an increase in axial strain and total energy absorbed compared to round cornered specimens.
9. The model that provided the most accurate predictions for the increase in compressive strength provided by SRG jackets compared to specimens within this thesis work was the model by CNR-DT 200 (2013), followed by the model developed by Krevaikas and Triantafillou (2005). Considering all specimens in Phases I and II, the model by CNR-DT 200 (2013) was found to provide the most accurate predictions.

6.3. RECOMMENDATIONS FOR FUTURE WORK

Based on the findings and lessons learned from this study, other considerations in the study of the compressive behavior of masonry columns confined with SRG composite that are recommended to be incorporated in future work include the following:

1. Based on conclusions made in this thesis work and those of (Senesi, 2018), the density of the steel fiber jackets that should be focused on in future work is 670 g/m^2. It was found that using steel fiber jackets with sheet density of

1,200 g/m^2 did not provide a significant increase in the compressive strength in relation to the specimens confined with steel of sheet density 670 g/m^2.

2. Based on conclusions made in this thesis work and in literature, the effect of the matrix thickness should be analyzed to study the composite's bond to the substrate and other fiber layers. To study the bond behavior of the composite system, it is recommended to increase the interior matrix layer bonding the steel fiber to the substrate to 5 mm and increase the other layers to 4 mm.
3. The steel fiber development length should continue to be studied by performing tensile coupon tests with varying development lengths of the composite system and varying the quantity of fiber overlapping faces on column specimens. To continue the study of confined column specimens, the number of overlapping faces should be varied for sharp cornered and round cornered specimens.
4. Strengthening using SRG confinement on masonry columns constructed using a historic technique which involves grouting hollow elements using a combination of grout and damaged pieces of the masonry bricks, could be explored.
5. Regarding the analytical models, more work is needed to improve the predictions of the increase in compressive strength provided by SRG jackets and to predict other key elements of the axial stress – axial strain response.

APPENDIX A.

IMAGES OF TESTED COLUMNS

Table A.1. UC – 1 Failure Mode

	Face 1	Face 2	Face 3	Face 4	Details	Failure Mode
UC-1	 	 	 	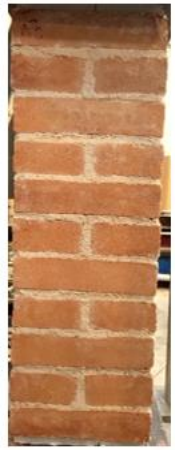 	Longitudinal vertical crack formed on each face near the middle of the width. The cracks run through solid brick and mortar joints. Formation of other vertical cracks besides the ones running mid-width on faces 1 and 3.	Formation of vertical cracks through the vertical joints of the bricks.

Table A.2. UC – 2 Failure Mode

	Face 1	Face 2	Face 3	Face 4	Details	Failure Mode
UC-2	 	 	 	 	Longitudinal vertical crack formed on each face near the middle of the width. The cracks run through solid brick and mortar joints. Formation of other vertical cracks besides the ones running mid-width on all faces.	Formation of vertical cracks through the vertical joints of the bricks.

Table A.3. UC – 3 Failure Mode

	Face 1	Face 2	Face 3	Face 4	Details	Failure Mode
UC-3	 	 	 	 	Longitudinal vertical crack formed on each face near the middle of the width. The cracks run through solid brick and mortar joints. Formation of other vertical cracks besides the ones running mid-width on faces 1 and 4. The corner between face 1 and 4 fell off during the testing. 	Formation of vertical cracks through the vertical joints of the bricks.

Table A.4. UC – 4 Failure Mode

	Face 1	Face 2	Face 3	Face 4	Details	Failure Mode
UC-4	 	 	 	 	Longitudinal vertical crack formed on each face near the middle of the width. The cracks run through solid brick and mortar joints. Formation of other vertical cracks besides the ones running mid-width on all faces. The corner between face 3 and 4 fell off during the testing. 	Formation of vertical cracks through the vertical joints of the bricks.

Table A.5. UC – 5 Failure Mode

	Face 1	Face 2	Face 3	Face 4	Details	Failure Mode
UC-5	 	 	 	 	Longitudinal vertical crack formed on each face near the middle of the width. The cracks run through solid brick and mortar joints. Formation of other vertical cracks besides the ones running mid-width on all faces. The corner between face 3 and 4 fell off during the testing.	Formation of vertical cracks through the vertical joints of the bricks.

Table A.6. UC – 6 Failure Mode

	Face 1	Face 2	Face 3	Face 4	Details	Failure Mode
UC-6	 	 	 	 	Longitudinal vertical crack formed on each face near the middle of the width. The cracks run through solid brick and mortar joints. Formation of other vertical cracks besides the ones running mid-width on all faces.	Formation of vertical cracks through the vertical joints of the bricks.

Table A.7. UC – 7 Failure Mode

	Face 1	Face 2	Face 3	Face 4	Details	Failure Mode
UC-7	 	 	 	 	Longitudinal vertical crack formed on each face near the middle of the width. The cracks run through solid brick and mortar joints. Formation of other vertical cracks besides the ones running mid-width on all faces, focusing at the bottom.	Formation of vertical cracks through the vertical joints of the bricks.

Table A.8. C-12-0-1-1 Failure Mode

	Face 1 (External overlap face)	Face 2	Face 3	Face 4	Remarks	Failure mode
C-12-0-1-1					The side between face 1 and face 4 showed an increased displacement, resulting in a more extensive crushing of a portion of the cross section. 	Opening of the reinforcement happened on the whole overlap; crushing of the mortar happened on two layers mid-height (visible horizontal cracks on face 3 and face 4).

le A.9. C-12-0-1-2 Failure Mode

	Face 1 (External overlap face)	Face 2	Face 3	Face 4	Remarks	Failure mode
C-12-0-1-2					Removing the reinforcement caused one the side between face 1 and face 4 to crumble. 	Opening of the reinforcement happened on the whole overlap; crushing of the mortar happened below the 1st brick (horizontal cracks visible on faces 1,2 and 3).

Table A.10. C-12-0-1-3 Failure Mode

	Face 1 (overlap)	Face 2	Face 3	Face 4	Details	Failure Mode
C-12-0-1-3	 	 	 	 	The cross sections didn't show significant arch effect. 	Opening of the reinforcement happened on the whole overlap, the detachment being more evident starting from the top.

Table A.11. C-12-0-1-4 Failure Mode

	Face 1 (overlap)	Face 2	Face 3	Face 4	Details	Failure Mode
C-12-0-1-4	 	 	 	 	The cross sections showed partial arch effect on faces 2 and 4. 	Opening of the reinforcement happened on the whole overlap, the detachment being more evident starting from the top.

Table A.12. C-12-0-2-1 Failure Mode

	Face 1 (External overlap face)	Face 2	Face 3	Face 4	Remarks	Failure mode
C-12-0-2-1					The cross sections showed visible arch effect on all sides. 	Opening of the reinforcement happened at the top of the overlap, with a length of 550mm, the detachment being more evident at the top and middle sheet.

Table A.13. C-12-0-2-2 Failure Mode

	Face 1 (External overlap face)	Face 2	Face 3	Face 4	Remarks	Failure mode
C-12-0-2-2					The cross sections showed visible arch effect on all sides, less remarkable on face 2. 	Opening of the reinforcement happened at the bottom of the overlap, with a length of 600mm: crushing of the mortar happened below the 3rd and 5th bricks (horizontal cracks visible on faces 3 and 4).

Table A.14. C-12-0-2-3 Failure Mode

	Face 1 (External overlap face)	Face 2	Face 3	Face 4	Remarks	Failure mode
C-12-0-2-3					The cross sections showed visible arch effect on all sides, less remarkable on face 3. 	Opening of the reinforcement happened at the top of the overlap, with a length of 455mm; crushing of the mortar happened below the 4th and 5th bricks (horizontal cracks visible on all faces).

Table A.15. C-12-0-2-4 Failure Mode

	Face 1 (External overlap face)	Face 2	Face 3	Face 4	Remarks	Failure mode
C-12-0-2-4					The cross sections showed visible arch effect on all sides. 	Opening of the reinforcement happened at the top of the overlap, with a length of 405mm; crushing of the mortar happened below the 4th, 6thand 7th bricks (horizontal cracks visible on faces 2, 3and 4).

Table A.16. C-12-0-3-1 Failure Mode

	Face 1 (External overlap face)	Face 2	Face 3	Face 4	Remarks	Failure mode
C-12-0-3-1					The cross sections showed slight arch effect on faces 3 and 4. 	Opening of the reinforcement happened at the top and at the bottom of the overlap, with a length of 355mm and 255mm respectively; crushing of the mortar happened below the 5th, 6th, 7th, and 8th bricks (horizontal cracks visible on all faces).

Table A.17. C-12-0-3-2 Failure Mode

	Face 1 (External overlap face)	Face 2	Face 3	Face 4	Remarks	Failure mode
C-12-0-3-2					The cross sections showed visible arch effect on all faces. 	Opening of the reinforcement happened in the middle of the overlap with a length of 550mm; crushing of the mortar happened below the 3rd, 6th, 10th bricks (visible horizontal cracks on all faces).

Table A.18. C-12-0-3-3 Failure Mode

	Face 1 (External overlap face)	Face 2	Face 3	Face 4	Remarks	Failure mode
C-12-0-3-3					The mid-height cross section showed visible arch effect on all faces.  Top half cross sections showed arch effect on two symmetrical faces. 	Opening of the reinforcement happened at the bottom of the overlap with a length of 300mm; crushing of the mortar happened below the 5th, 6th, and 8th bricks (visible horizontal cracks on faces 3 and 4).

Table A.19. C-12-0-3-4 Failure Mode

	Face 1 (External overlap face)	Face 2	Face 3	Face 4	Remarks	Failure mode
C-12-0-3-4					The cross sections showed visible arch effect on all faces. 	Opening of the reinforcement happened at the top of the overlap with a length of 400mm; crushing of the mortar happened below the 3rd, 5th and 8th bricks (visible horizontal cracks on faces 2, 3 and 4).

Table A.20. C-12-38-1-1 Failure Mode

	Face 1 (overlap)	Face 2	Face 3	Face 4	Details	Failure Mode
C-12-38-1-1	 	 	 	 	Vertical cracks on all 4 faces. Portions of bricks and mortar remained bonded to the corners of the fibers.	The detachment of the reinforcement happened on the whole height.

Table A.21. C-12-38-1-2 Failure Mode

	Face 1 (overlap)	Face 2	Face 3	Face 4	Details	Failure Mode
C-12-38-1-2	 	 	 	 	Vertical cracks on all 4 faces; face 1and 2 showed various cracks in addition to the one running mid-width; face 3 showed the thinnest mid-width crack.	The detachment of the reinforcement happened at the top of the overlap, with a length of 405mm, on 2 faces; the bottom reinforcement showed an opening only in the overlap face.

Table A.22. C-12-38-1-3 Failure Mode

	Face 1 (overlap)	Face 2	Face 3	Face 4	Details	Failure Mode
C-12-38-1-3	 	 	 	 	Vertical cracks on all 4 faces; faces 1 and 2 showed various cracks in addition to the one running mid-width.	The detachment of the reinforcement happened at the top of the overlap, with a length of 400mm; the bottom sheet only opened on face 1.

Table A.23. C-12-38-1-4 Failure Mode

	Face 1 (overlap)	Face 2	Face 3	Face 4	Details	Failure Mode
C-12-38-1-4	 	 	 	 	Vertical cracks on all 4 faces; face 1 and 2 showed various cracks in addition to the one running mid-width.	The detachment of the reinforcement happened on the whole height; the top sheet detached from all sides, the middle and bottom layer detached from face 1 and 2.

Table A.24. C-12-38-1(2)-1 Failure Mode

	Face 1 (overlap)	Face 2	Face 3	Face 4	Details	Failure Mode
C-12-38-1.5-1	 	 	 	 	Vertical cracks on all 4 faces; face 2 and face 3 showed various cracks in addition to the one running mid-width.	The detachment of the reinforcement happened at the top, with a length of 405mm, on 3 faces; the bottom reinforcement showed an opening only in the overlap face.

Table A.25. C-12-38-1(2)-2 Failure Mode

	Face 1 (overlap)	Face 2	Face 3	Face 4	Details	Failure Mode
C-12-38-1.5-2	 	 	 	 	Vertical cracks on all 4 faces; face 1, face 2 and face 3 showed various cracks in addition to the one running mid-width; face 4 showed the thinnest mid-width crack.	The detachment of the reinforcement happened at the top of the overlap, with a length of 405mm, on 2 faces; the bottom reinforcement showed an opening only in the overlap face.

Table A.26. C-12-38-1(2)-3 Failure Mode

	Face 1 (overlap)	Face 2	Face 3	Face 4	Details	Failure Mode
C-12-38-1.5-3	 	 	 	 	Vertical cracks on all 4 faces; face 3 and face 4 showed various cracks in addition to the one running mid-width; face 1 showed the thinnest mid-width crack.	The detachment of the reinforcement happened on the whole height, starting from the bottom; crushing of the mortar happened below the 1st and 3rd brick (visible horizontal cracks on all faces).

Table A.27. C-12-38-1(2)-4 Failure Mode

	Face 1 (overlap)	Face 2	Face 3	Face 4	Details	Failure Mode
C-12-38-1.5-4	 	 	 	 	Vertical cracks on all 4 faces; face 2 and face 4 showed various cracks in addition to the one running mid-width; face 1 showed the thinnest mid-width crack.	The detachment of the reinforcement happened on the whole height, starting from the bottom.

Table A.28. C-12-38-2-1 Failure Mode

	Face 1 (overlap)	Face 2	Face 3	Face 4	Details	Failure Mode
C-12-38-2-1	 	 	 	 	Vertical cracks on all four faces, the corner between face 3 and 4 was crushed the most. The cross sections showed symmetrical arch effect on all faces. 	Opening of the reinforcement happened at the top of the overlap, with a length of 405mm; the top and middle sheet detached from all sides, the bottom sheet detached from face 1.

Table A.29. C-12-38-2-2 Failure Mode

	Face 1 (overlap)	Face 2	Face 3	Face 4	Details	Failure Mode
C-12-38-2-2	 	 	 	 	Vertical cracks on all four faces; face 3 showed the thinnest mid-width crack. The cross sections didn't show any arch effect, opening the column showed orthogonal cracks along the middle of the bricks.	Opening of the reinforcement happened on the whole height.

Table A.30. C-12-38-2-3 Failure Mode

	Face 1 (overlap)	Face 2	Face 3	Face 4	Details	Failure Mode
C-12-38-2-3	 	 	 	 	Vertical cracks on all four faces; face 4 showed various cracks in addition to the one running mid-width. The cross sections showed asymmetrical arch effect on faces 2, 3 and 4. 	Opening of the reinforcement happened on the whole height, the sheets detached on faces 1, 2 and 4.

Table A.31. C-12-38-2-4 Failure Mode

	Face 1 (overlap)	Face 2	Face 3	Face 4	Details	Failure Mode
C-12-38-2-4	 	 	 	 	Vertical cracks on all four faces; face 4 showed the widest crack, that caused the corner between face 4 and face 1 to detach. 	Opening of the reinforcement happened on the whole height, the sheets detached on faces 1, 2 and 4.

APPENDIX B.

AXIAL STRESS – STRAIN RELATIONSHIPS

Unconfined Series (Control Series) Axial Stress – Axial Strain Responses

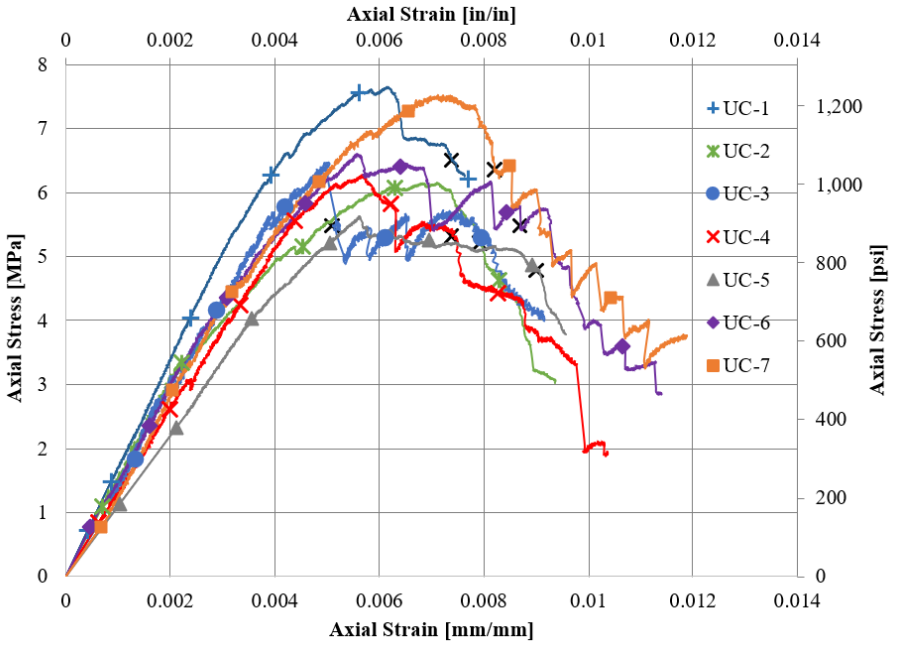

Figure B.1. Axial Stress - Axial Strain Response Unconfined Series (UC) (Revised Axis)

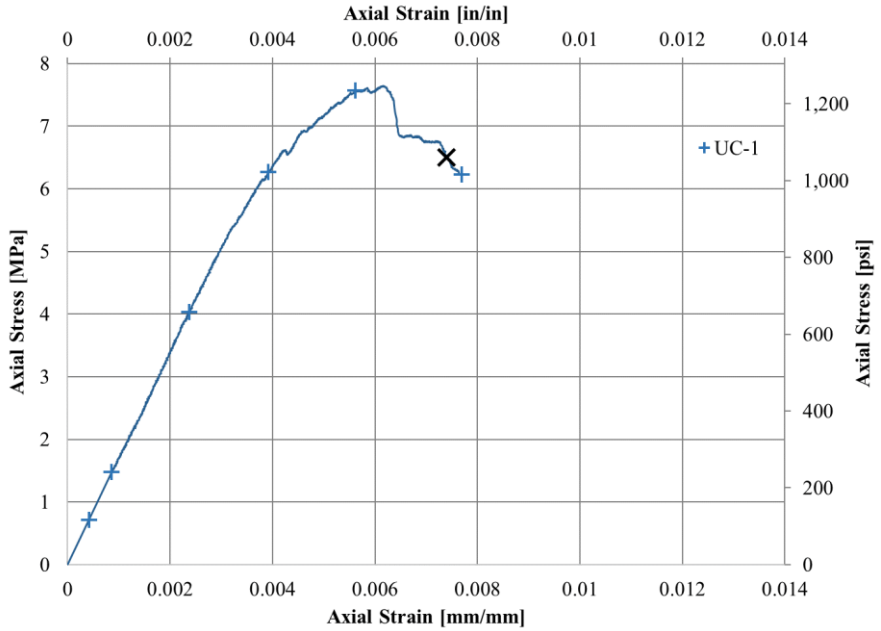

Figure B.2. UC-1: Axial Stress - Axial Strain Response

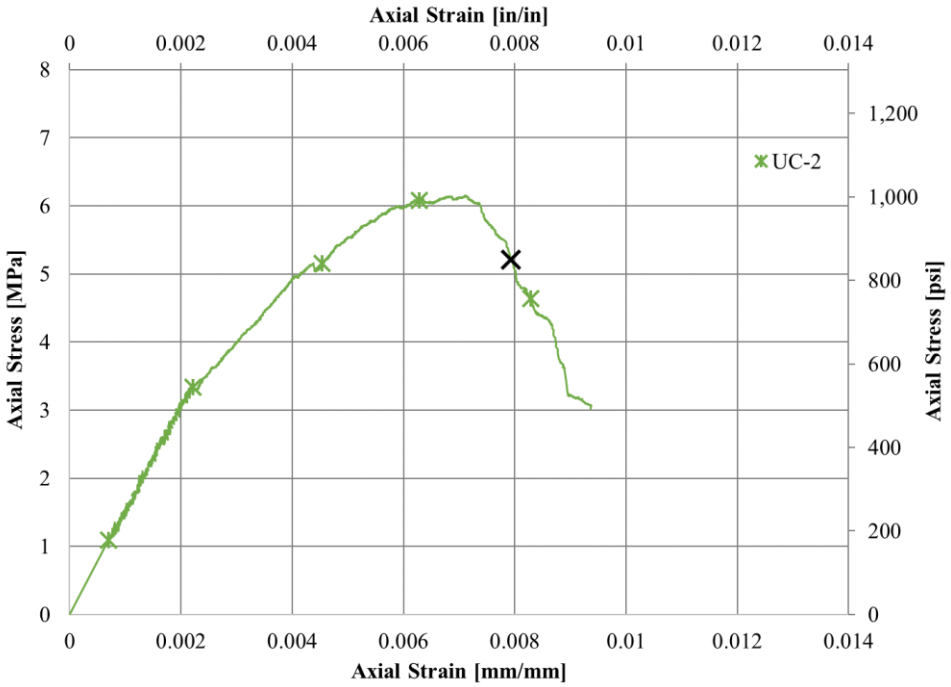

Figure B.3. UC-2: Axial Stress - Axial Strain Response

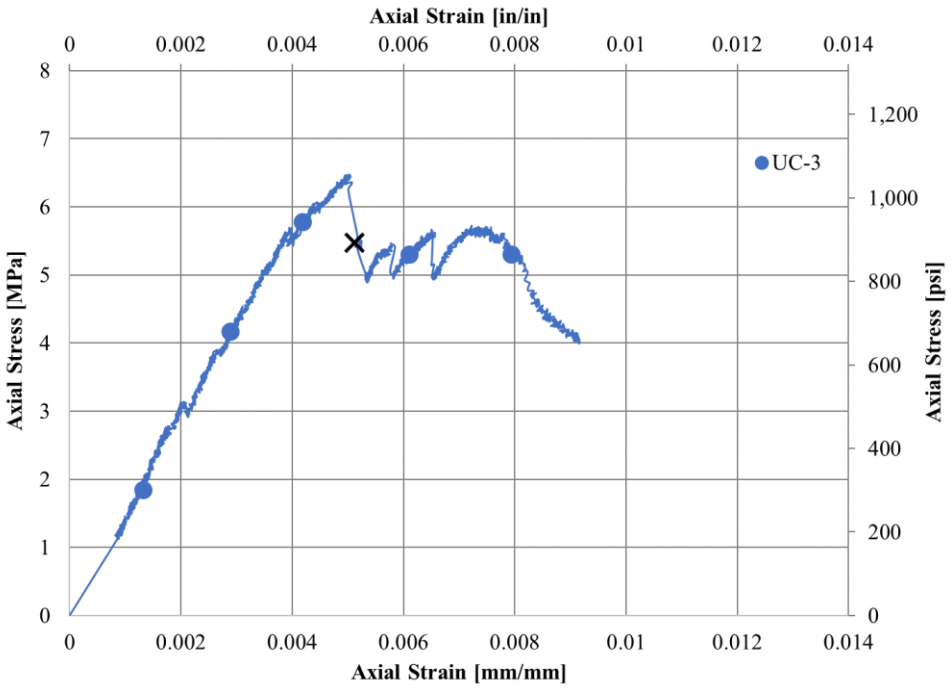

Figure B.4. UC-3: Axial Stress - Axial Strain Response

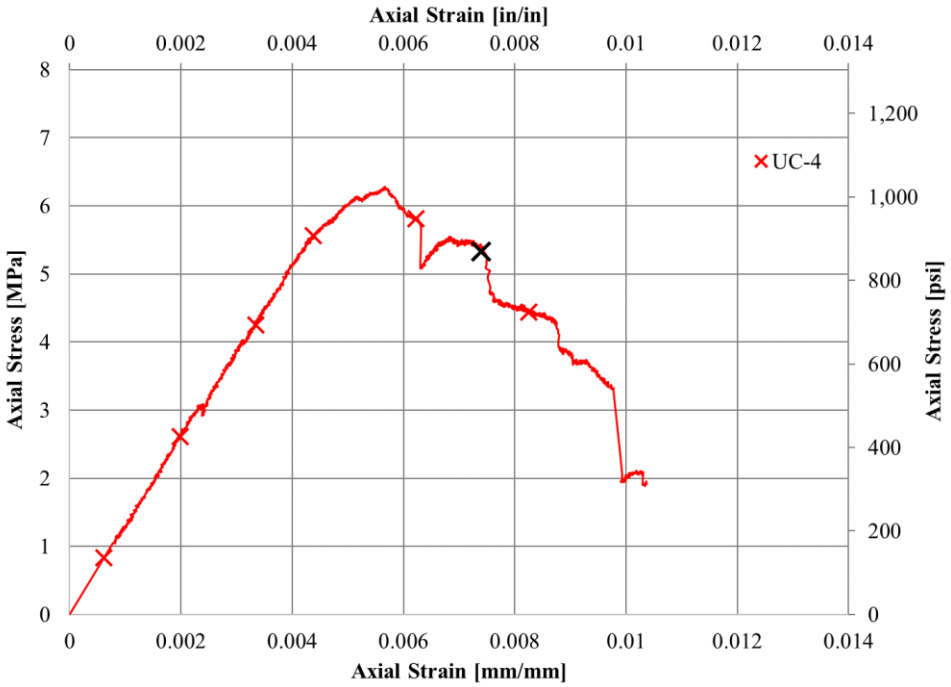

Figure B.5. UC-4: Axial Stress - Axial Strain Response

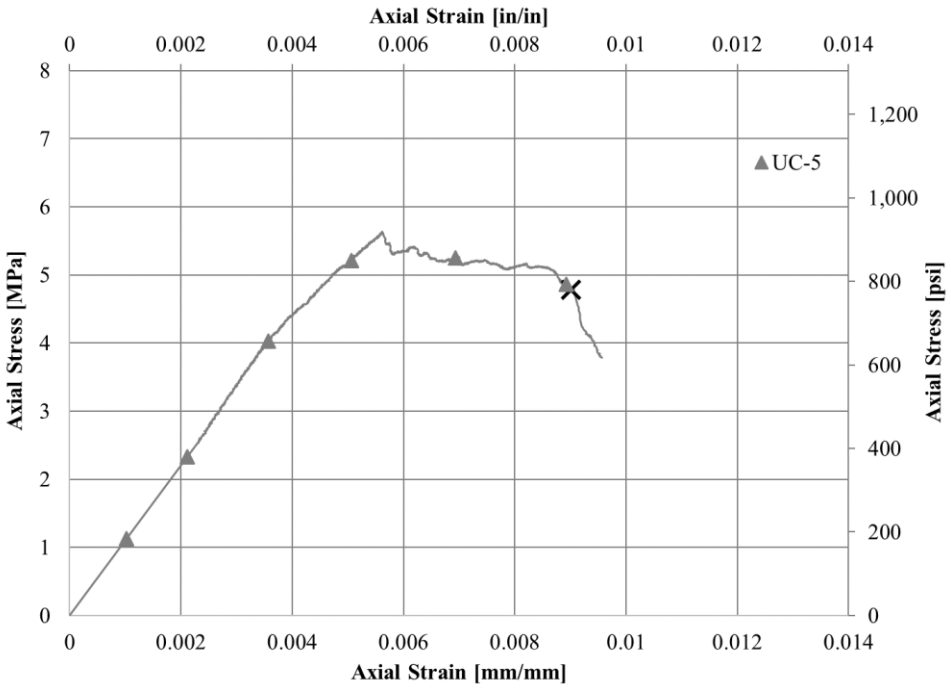

Figure B.6. UC-5: Axial Stress - Axial Strain Response

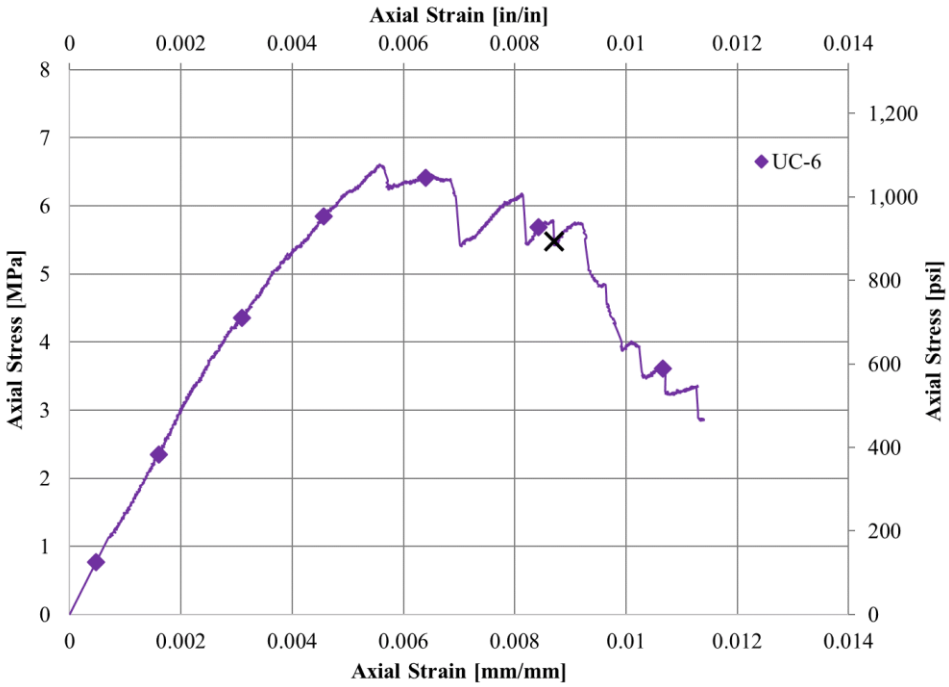

Figure B.7. UC-6: Axial Stress - Axial Strain Response

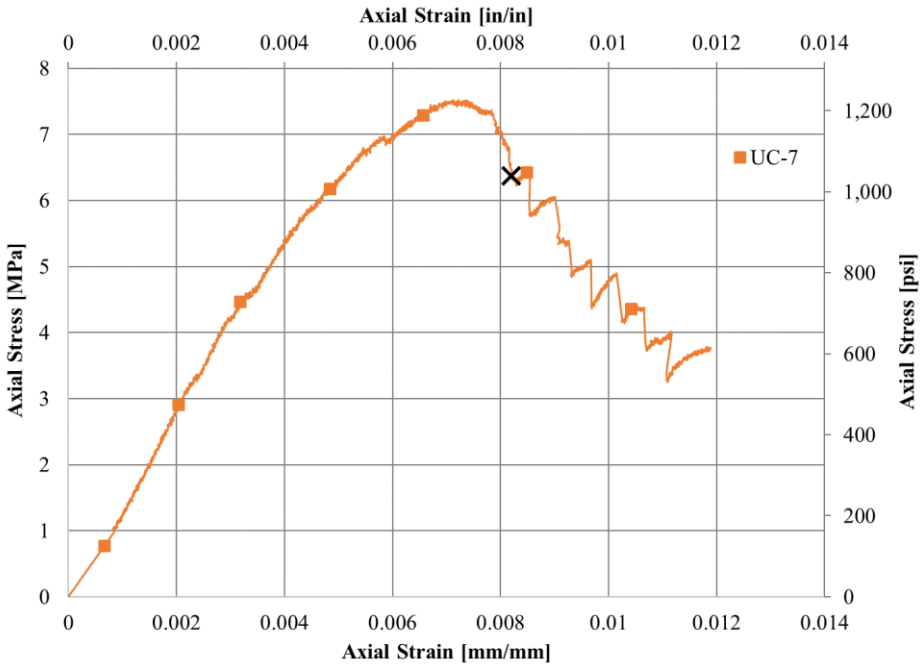

Figure B.8. UC-7: Axial Stress - Axial Strain Response

Group 1 (C-12-0-1-Series) Axial Stress – Axial Strain Responses

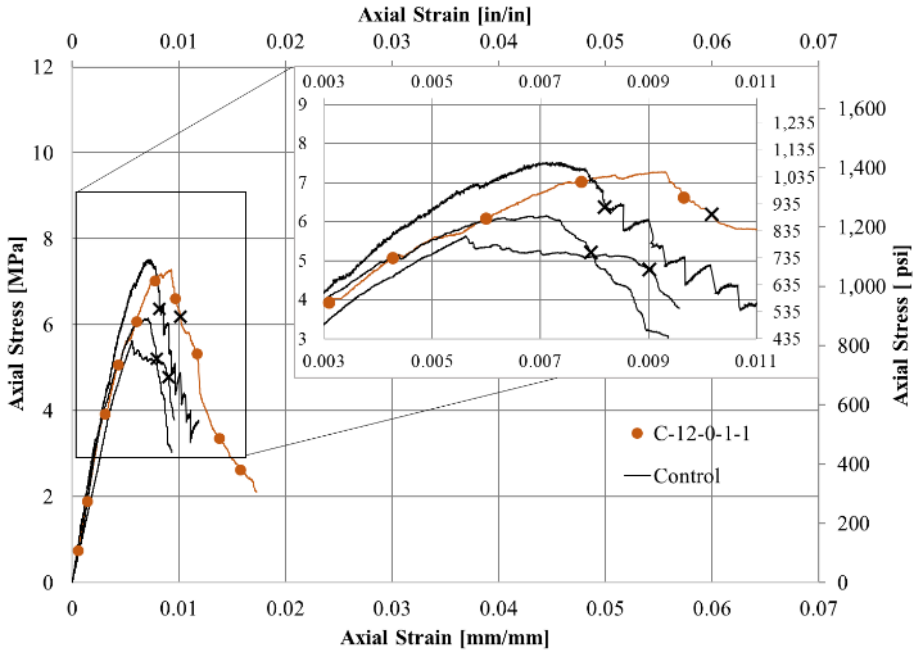

Figure B.9. C-12-0-1-1: Axial Stress - Axial Strain Response

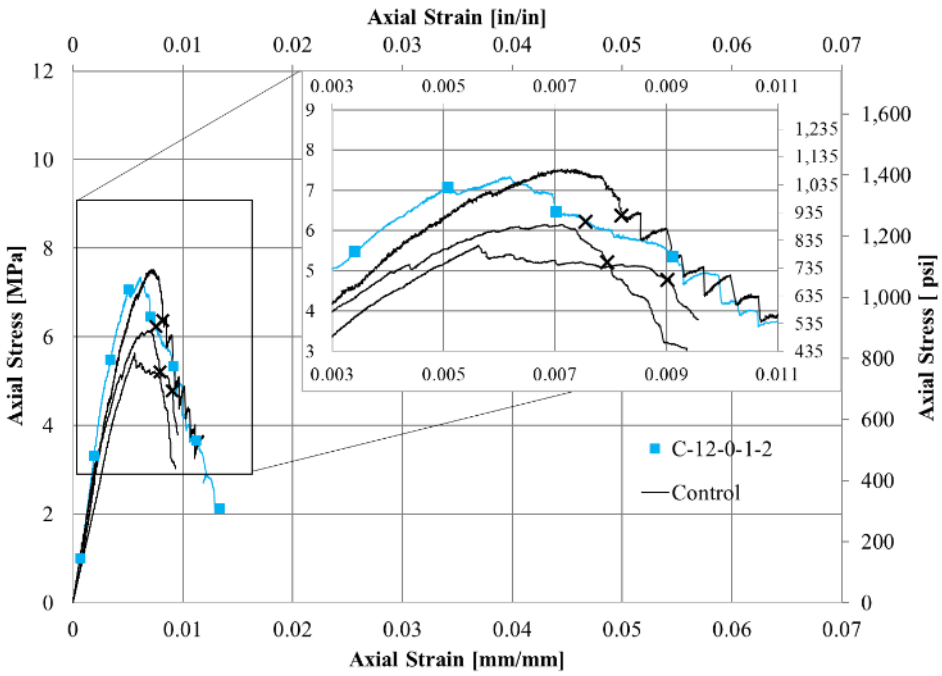

Figure B.10. C-12-0-1-2: Axial Stress - Axial Strain Response

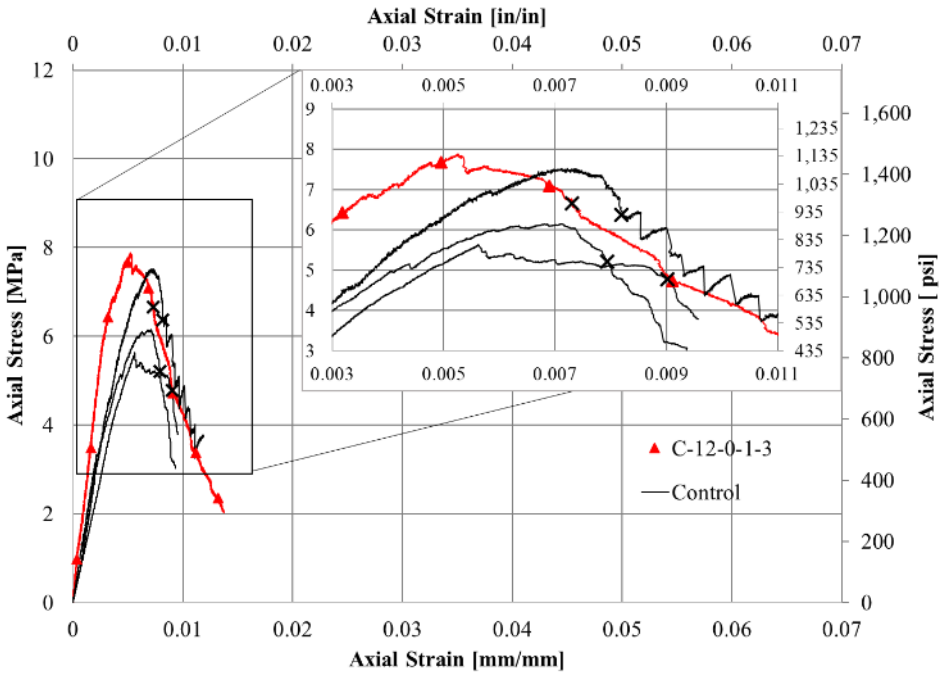

Figure B.11. C-12-0-1-3: Axial Stress - Axial Strain Response

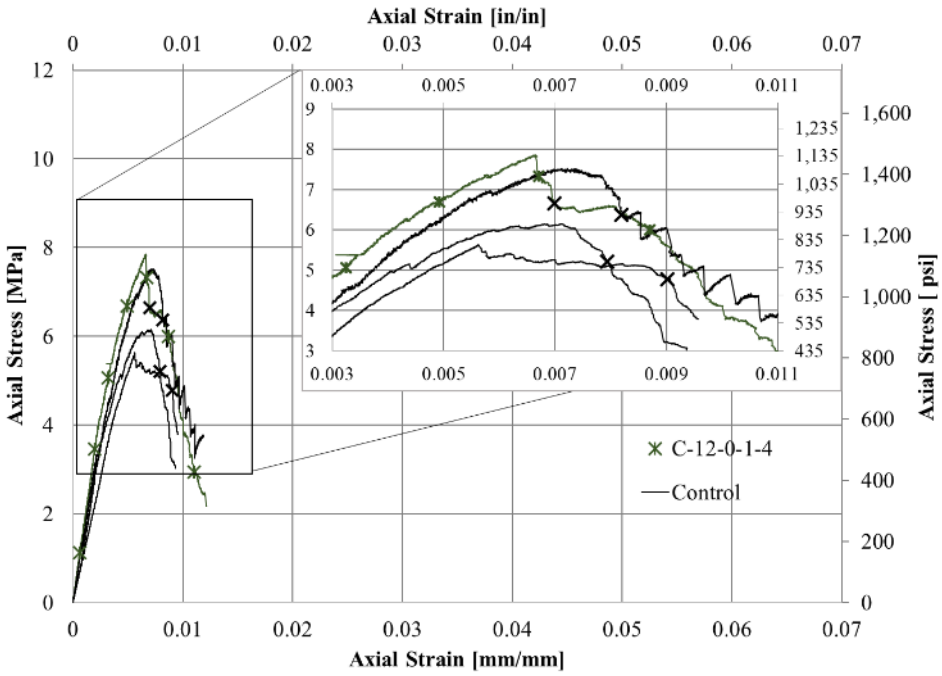

Figure B.12. C-12-0-1-4: Axial Stress - Axial Strain Response

Group 2 (C-12-0-2-Series) Axial Stress – Axial Strain Responses

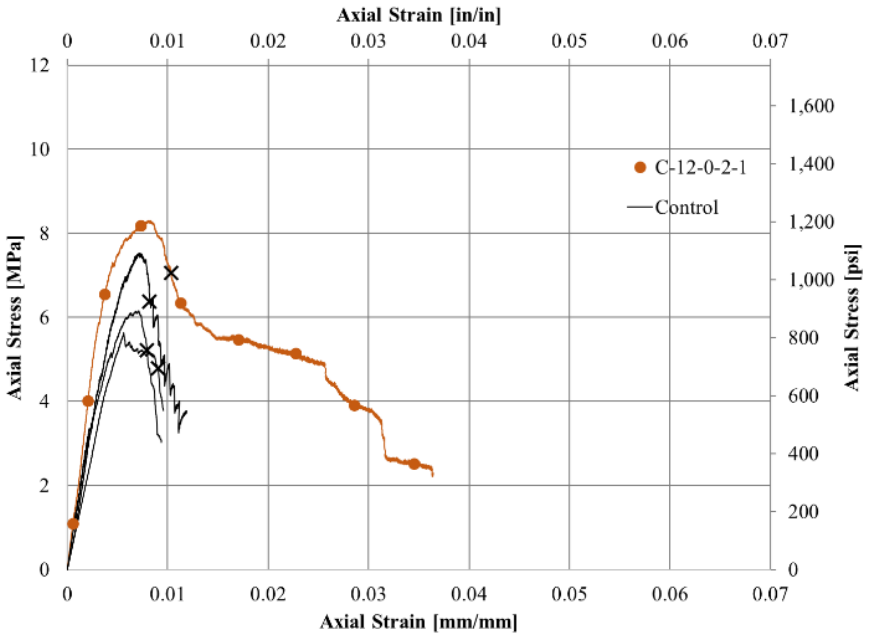

Figure B.13. C-12-0-2-1: Axial Stress - Axial Strain Response

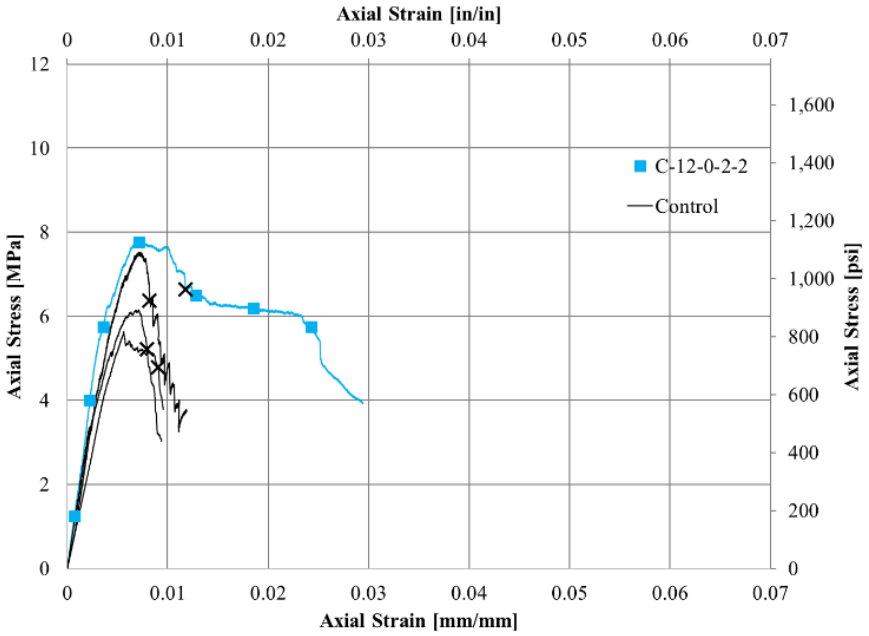

Figure B.14. C-12-0-2-2: Axial Stress - Axial Strain Response

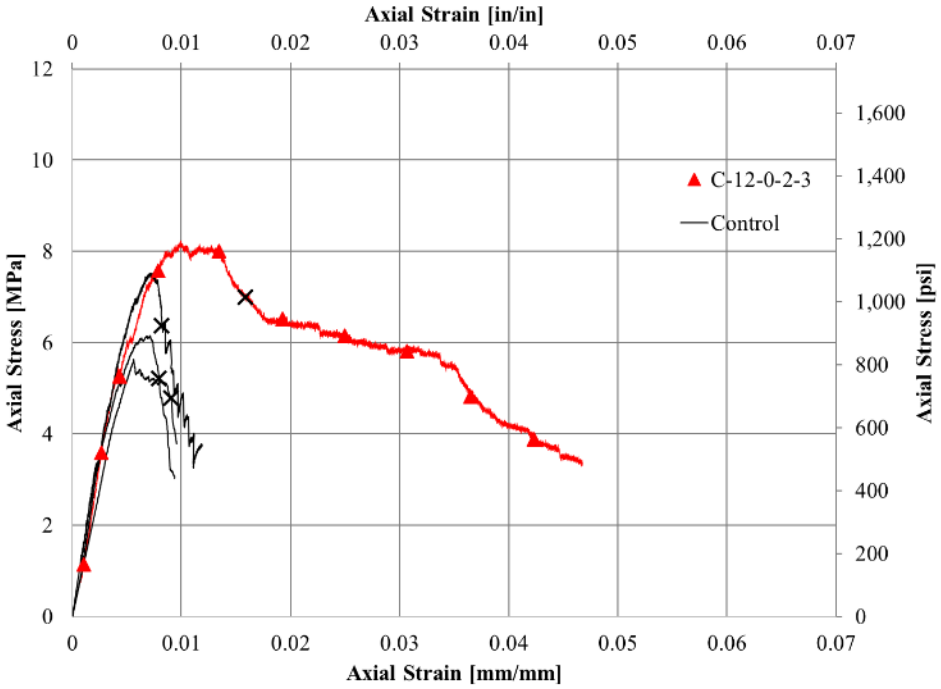

Figure B.15. C-12-0-2-3: Axial Stress - Axial Strain Response

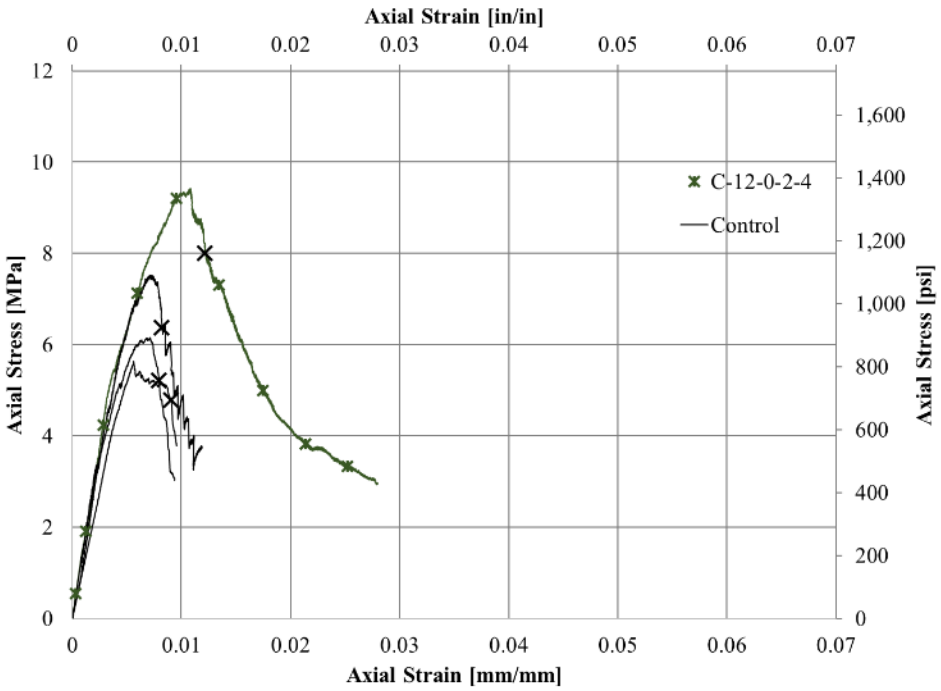

Figure B.16. C-12-0-2-4: Axial Stress - Axial Strain Response

Group 3 (C-12-0-3-Series) Axial Stress – Axial Strain Responses

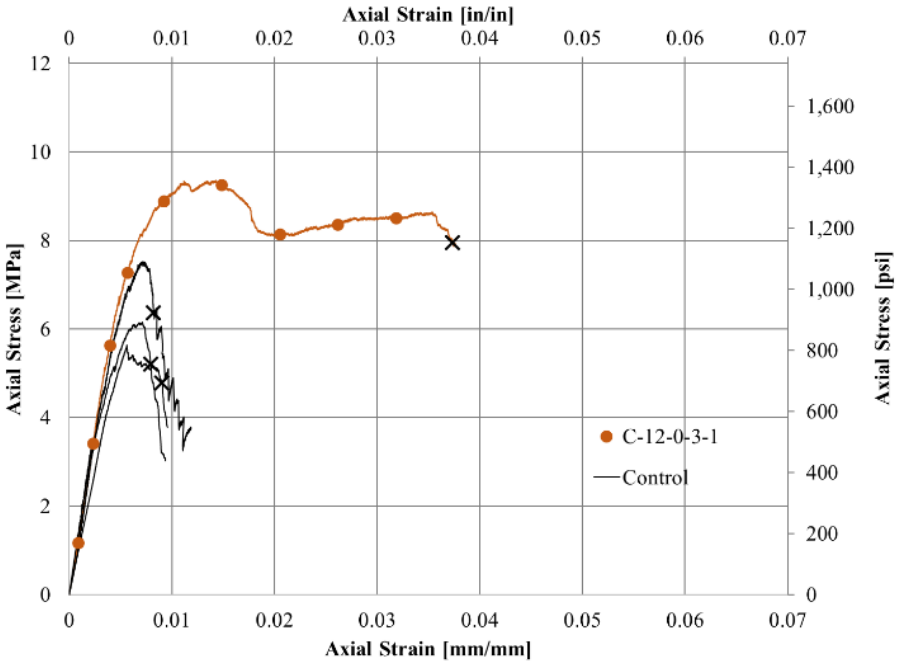

Figure B.17. C-12-0-3-1: Axial Stress - Axial Strain Response

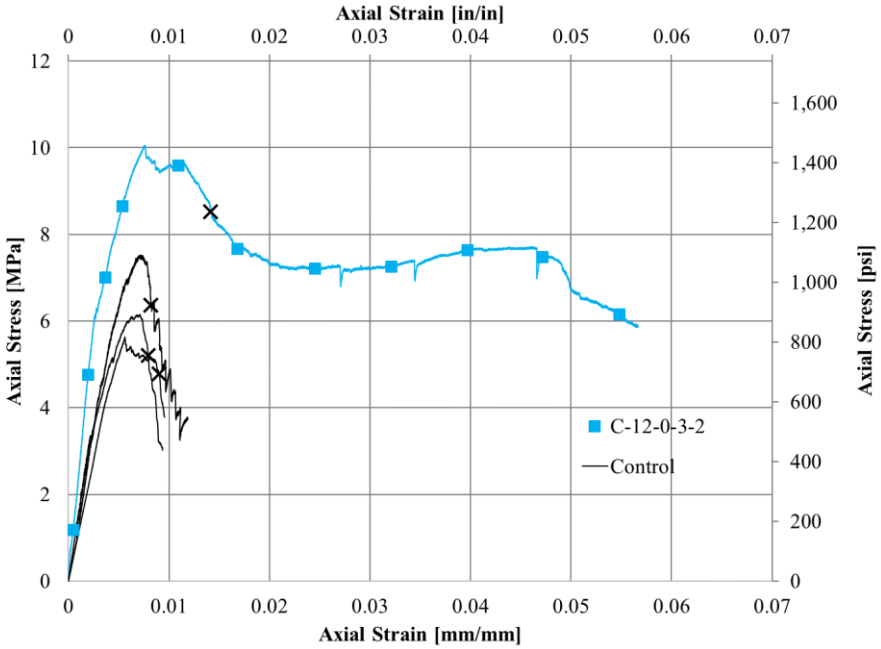

Figure B.18. C-12-0-3-2: Axial Stress - Axial Strain Response

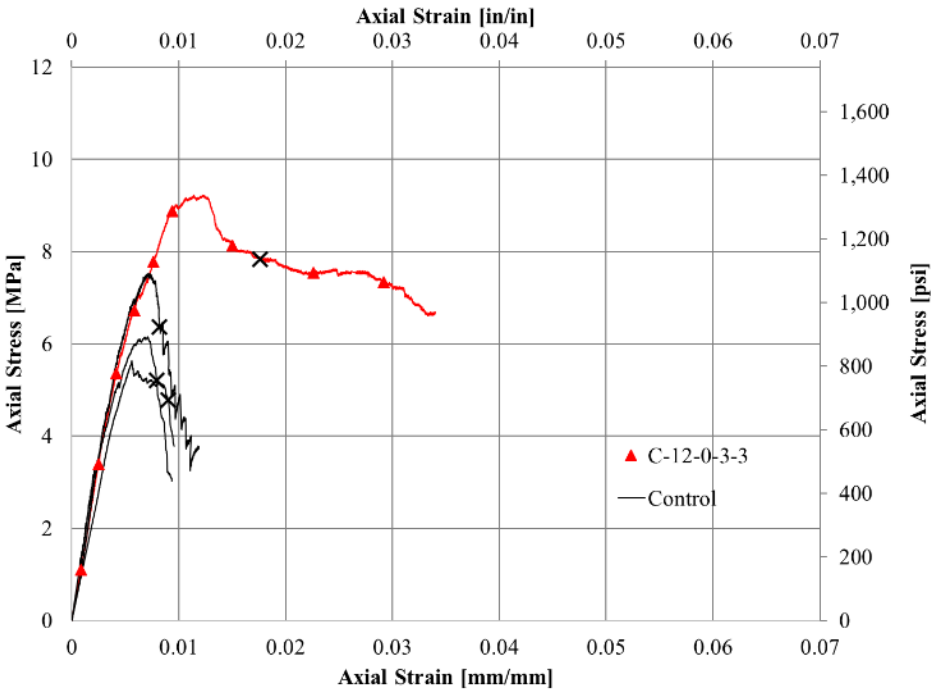

Figure B.19. C-12-0-3-3: Axial Stress - Axial Strain Response

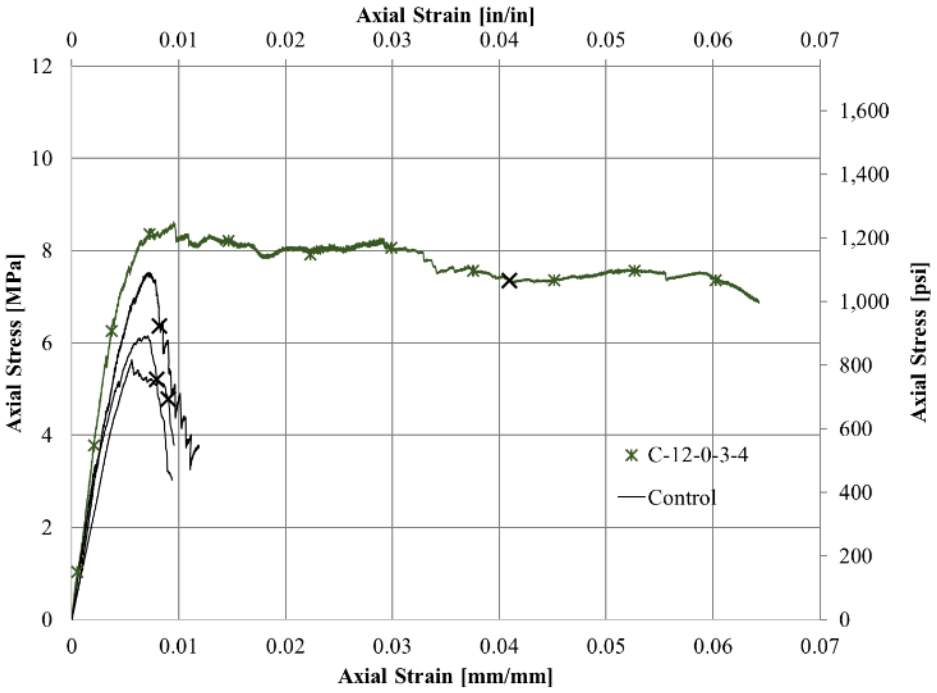

Figure B.20. C-12-0-3-4: Axial Stress - Axial Strain Response

Group 4 (C-12-38-1-Series) Axial Stress - Axial Strain Responses

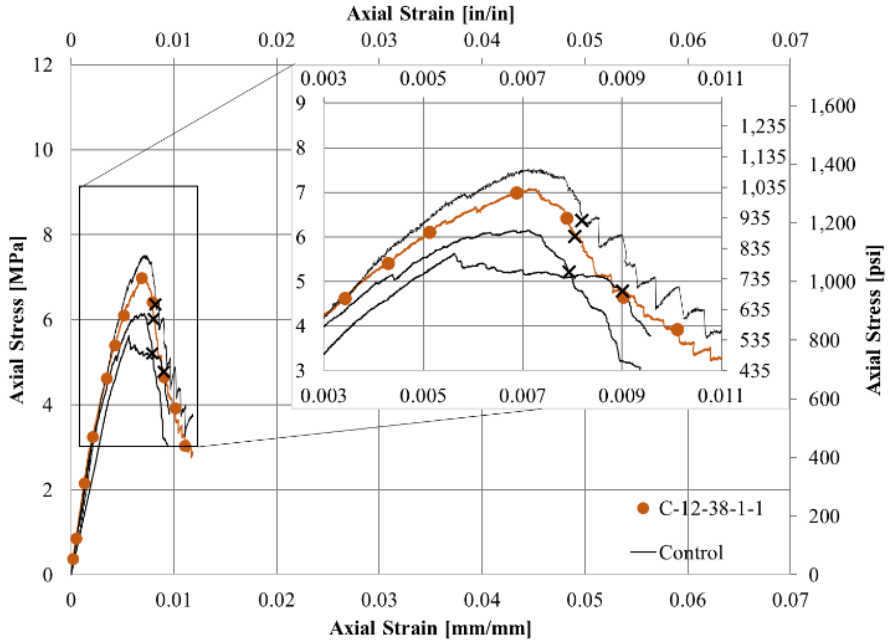

Figure B.21. C-12-38-1-1: Axial Stress - Axial Strain Response

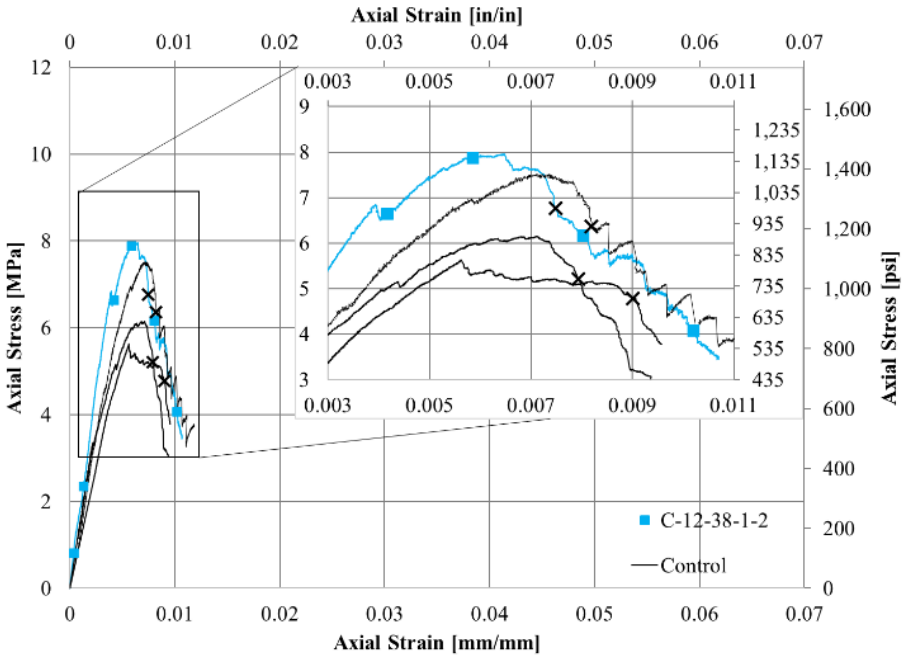

Figure B.22. C-12-38-1-2: Axial Stress - Axial Strain Response

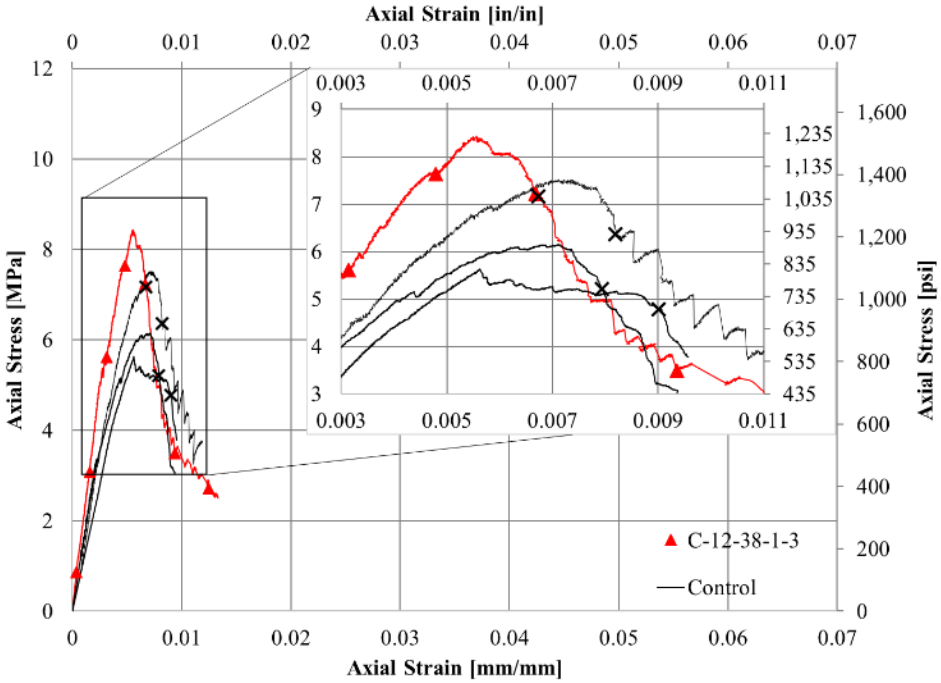

Figure B.23. C-12-38-1-3: Axial Stress - Axial Strain Response

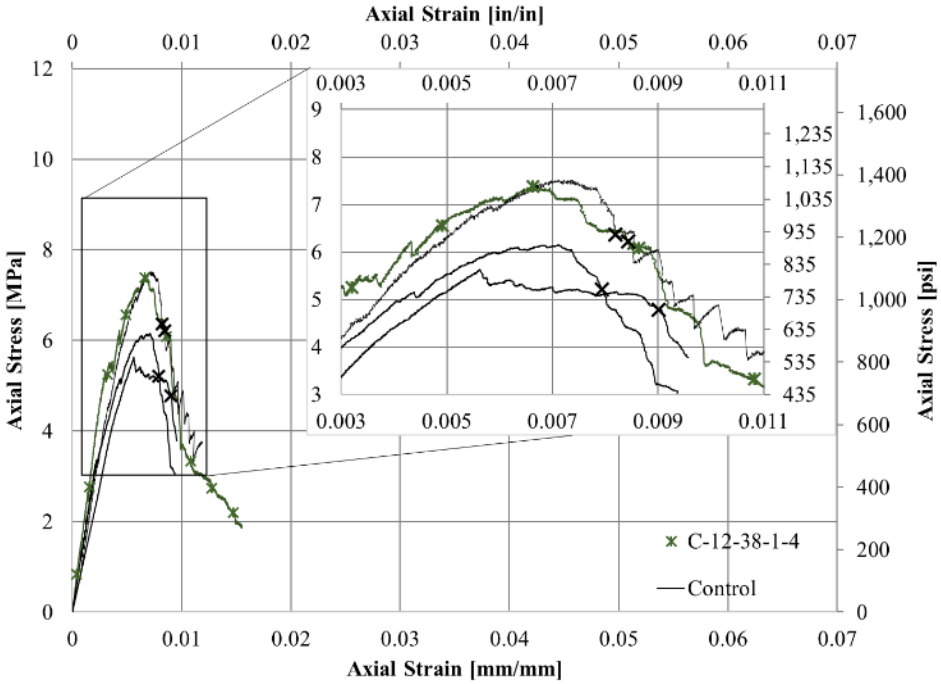

Figure B.24. C-12-38-1-4: Axial Stress - Axial Strain Response

Group 5 (C-12-38-1.5-Series) Axial Stress - Axial Strain Responses

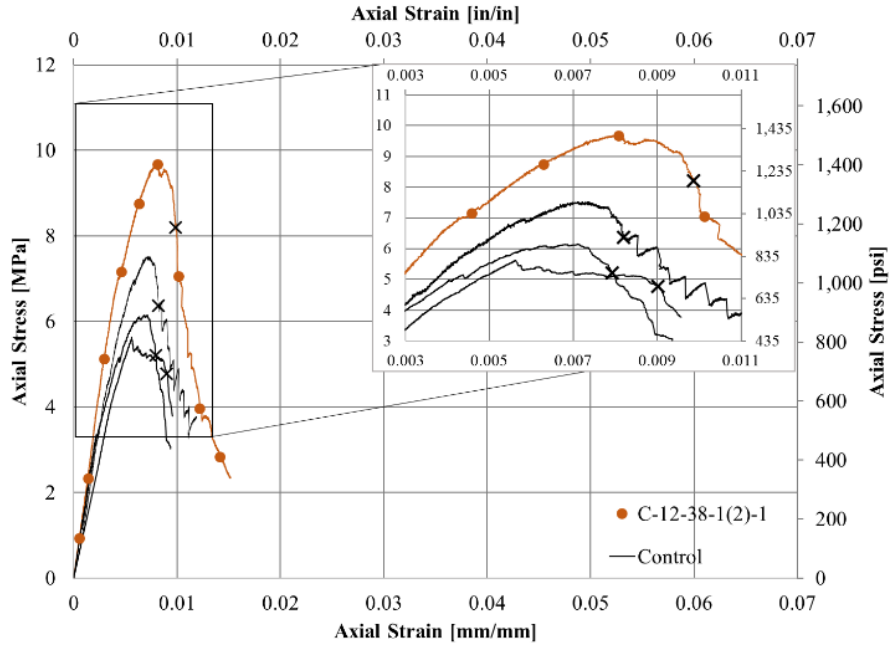

Figure B.25. C-12-38-1(2)-1: Axial Stress - Axial Strain Response

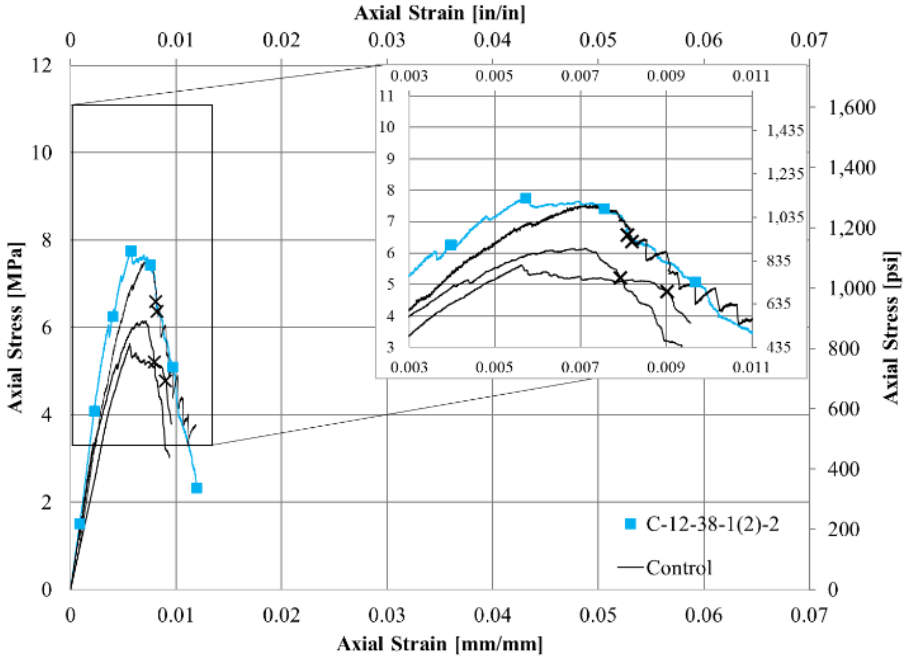

Figure B.26. C-12-38-1.5-2: Axial Stress - Axial Strain Response

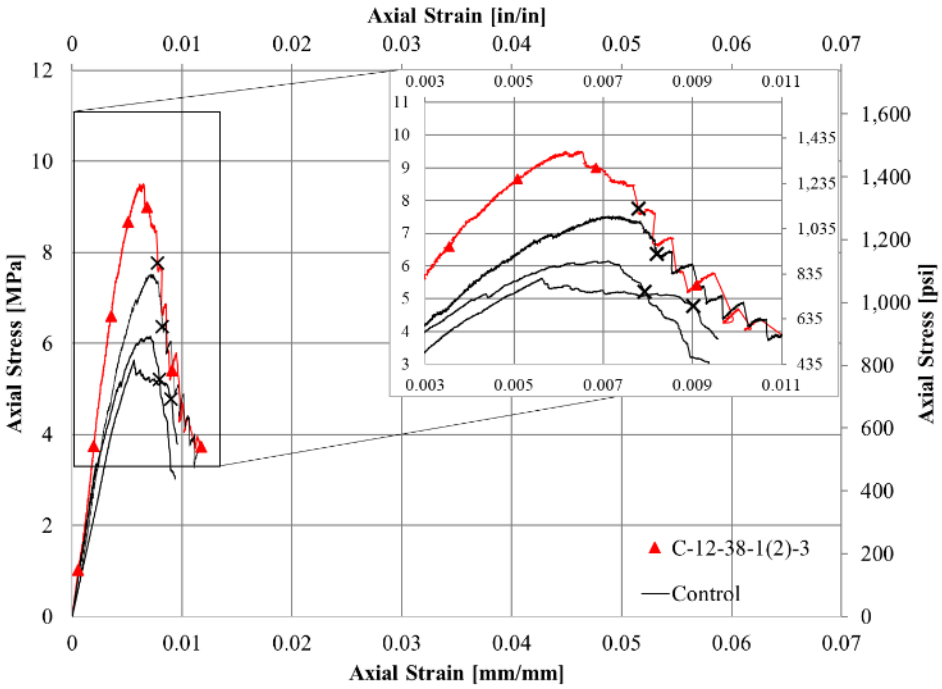

Figure B.27. C-12-38-1.5-3: Axial Stress - Axial Strain Response

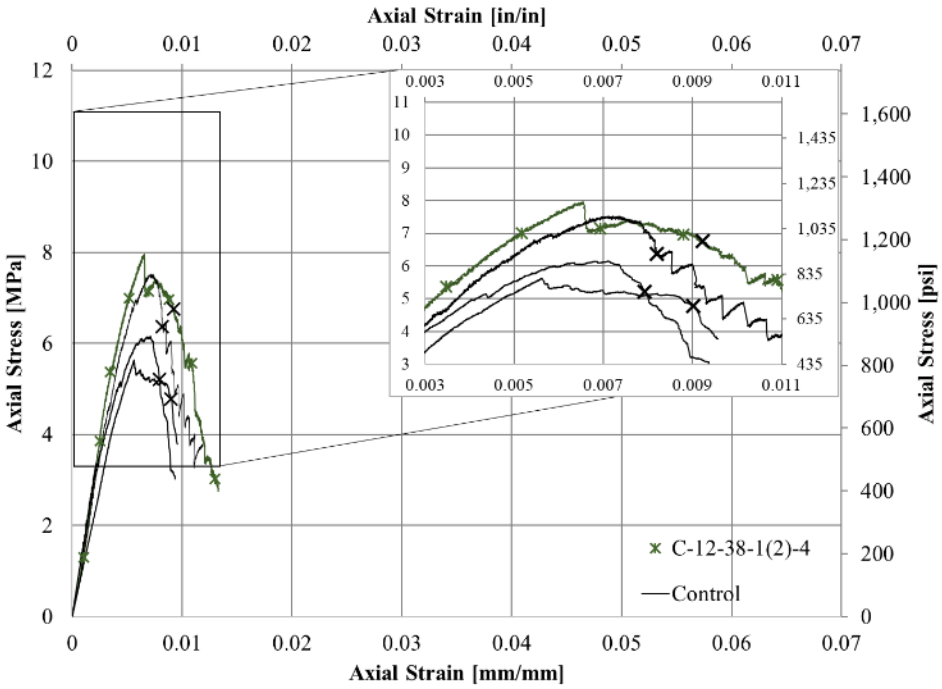

Figure B.28. C-12-38-1.5-4: Axial Stress - Axial Strain Response

Group 6 (C-12-38-2-Series) Axial Stress - Axial Strain Responses

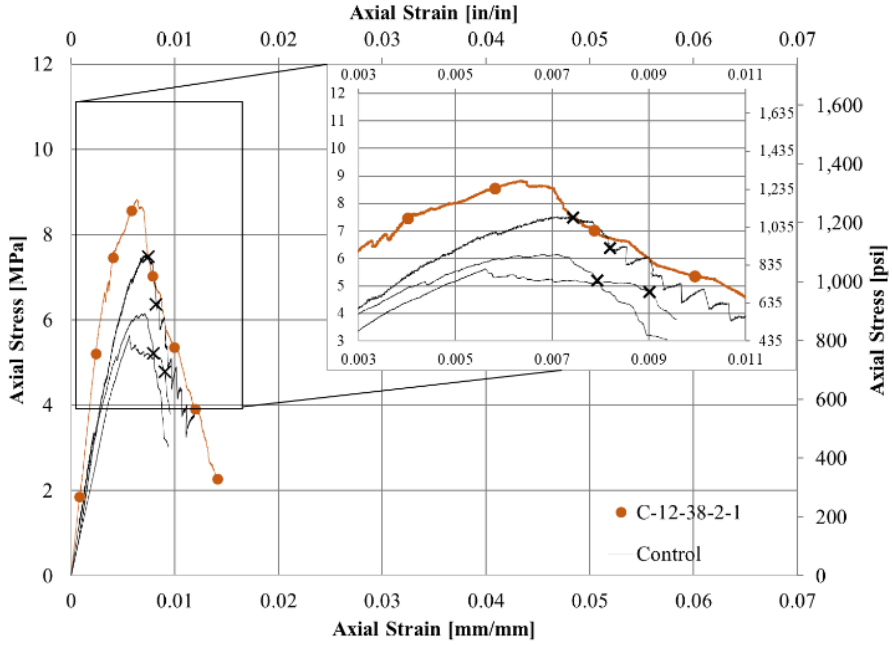

Figure B.29. C-12-38-2-1: Axial Stress - Axial Strain Response

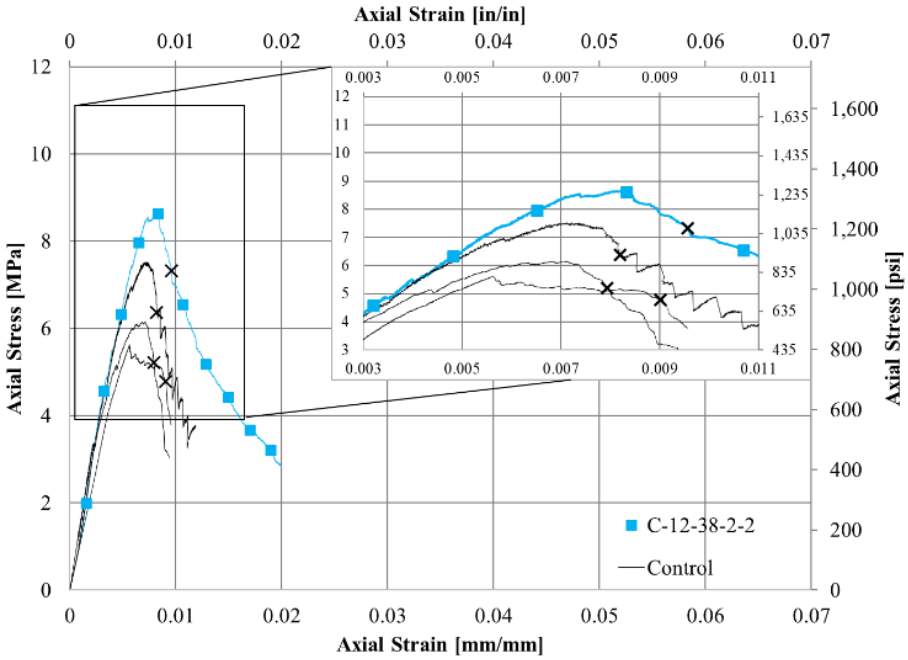

Figure B.30. C-12-38-2-2: Axial Stress - Axial Strain Response

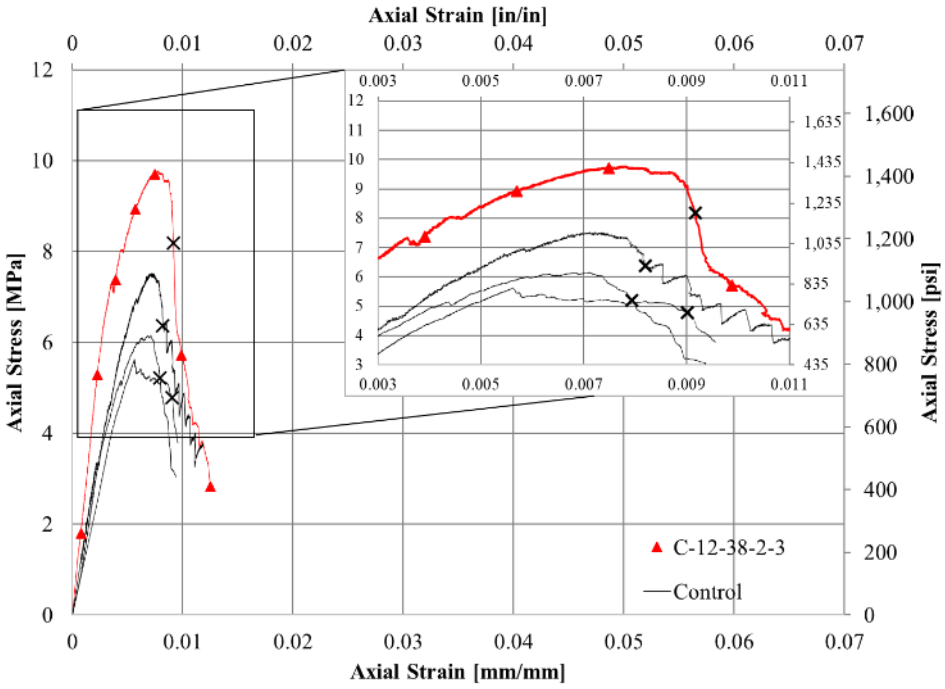

Figure B.31. C-12-38-2-3: Axial Stress - Axial Strain Response

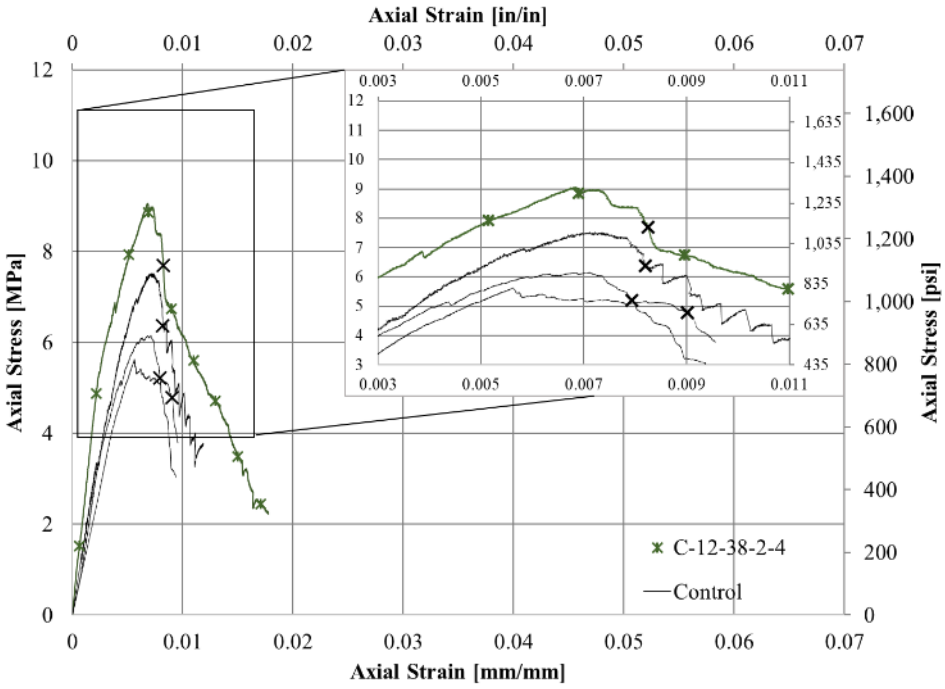

Figure B.32. C-12-38-2-4: Axial Stress - Axial Strain Response

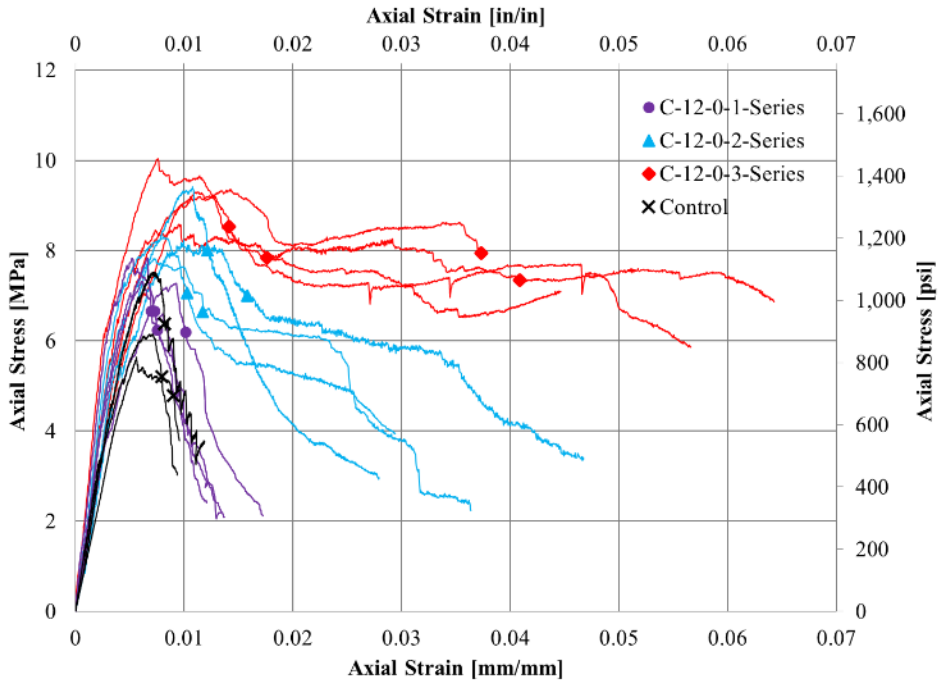

Figure B.33. Axial Stress - Axial Strain Response of Sharp Cornered Columns

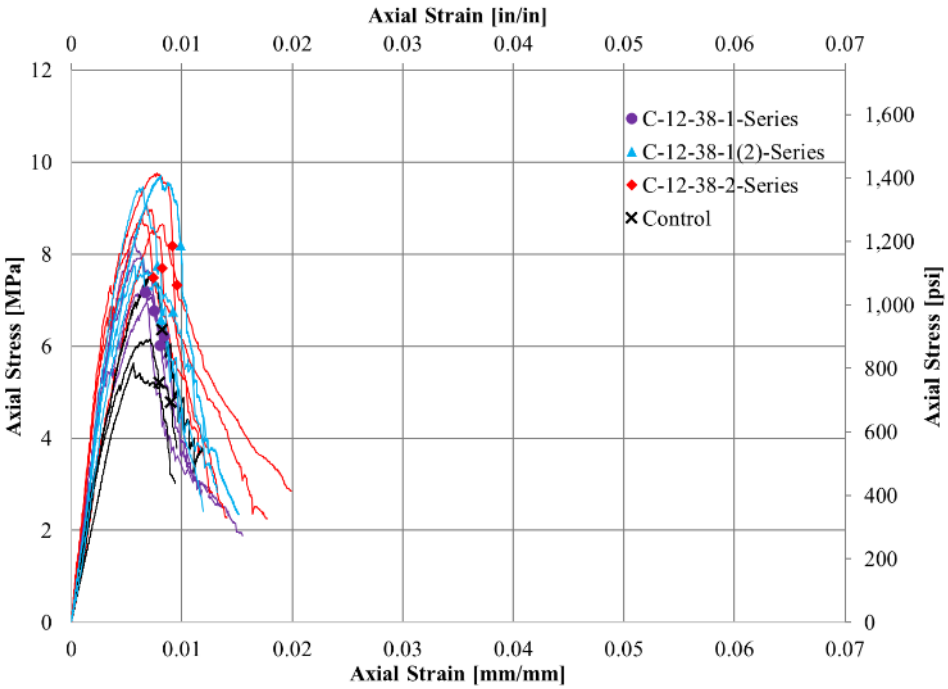

Figure B.34. Axial Stress - Axial Strain Response of Round Cornered Columns

Table B.1. Reported Transverse Strain for Individual Column Faces

Specimen		f_{mc}	$f_{mc,u}$	$\varepsilon_{mc,t}$ Face 1	$\varepsilon_{mc,t}$ Face 2	$\varepsilon_{mc,t}$ Face 3	$\varepsilon_{mc,t}$ Face 4	$\overline{\varepsilon_{mc,t}}$	$\varepsilon_{mc,t,u}$ Face 1	$\varepsilon_{mc,t,u}$ Face 2	$\varepsilon_{mc,t,u}$ Face 3	$\varepsilon_{mc,t,u}$ Face 4	$\overline{\varepsilon_{mc,t,u}}$
Group	**Name**	**MPa**	**MPa**	**mm/mm**	**mm/mm**	**mm/mm**	**mm/mm**	**mm/mm**	**mm/mm**	**mm/mm**	**mm/mm**	**mm/mm**	**mm/mm**
Group 1	C-12-0-1-3	7.56	6.40	-0.00023	-0.00018	-0.00067	-0.00164	-0.00068	-0.00021	-0.00052	-0.00059	-0.00050	-0.00046
	C-12-0-1-4	7.55	6.39	-0.00015	-0.00039	-0.00047	-0.00078	-0.00045	-0.00018	-0.00002	-0.00022	-0.00045	-0.00022
Group 4	C-12-38-1-3	8.09	6.88	-0.00011	-0.00144	-0.00136	-0.00034	-0.00081	-0.00010	-0.00079	-0.00126	-0.00064	-0.00070
	C-12-38-1-4	7.12	5.97	-0.00024	-0.00004	-0.00049	-0.00044	-0.00030	-0.00024	-0.00001	-0.00052	-0.00046	-0.00031

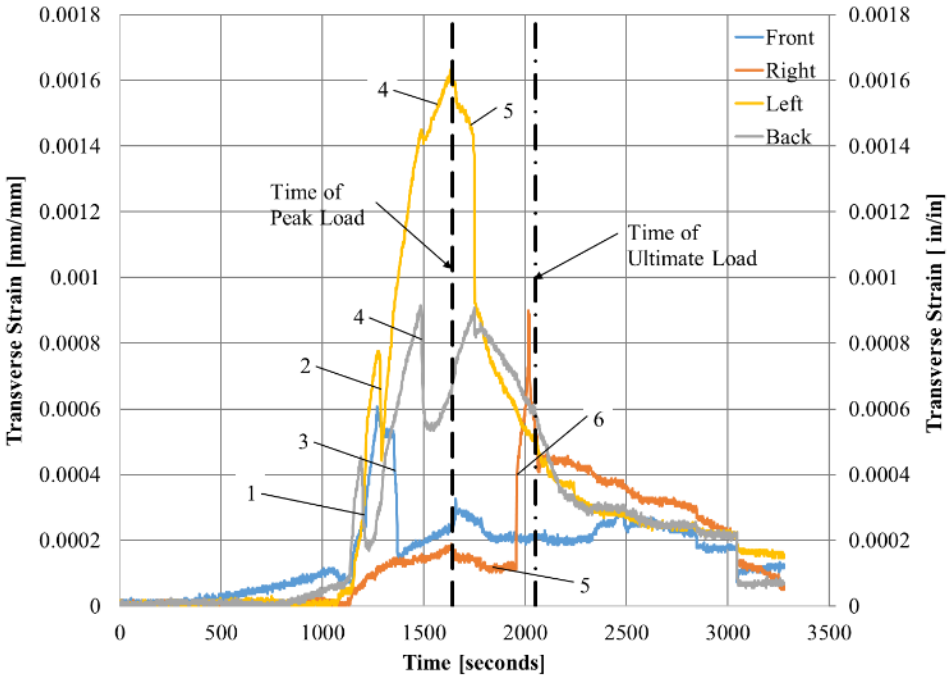

Figure B.35. Transverse Strain - Time Response of Specimen C-12-0-1-3

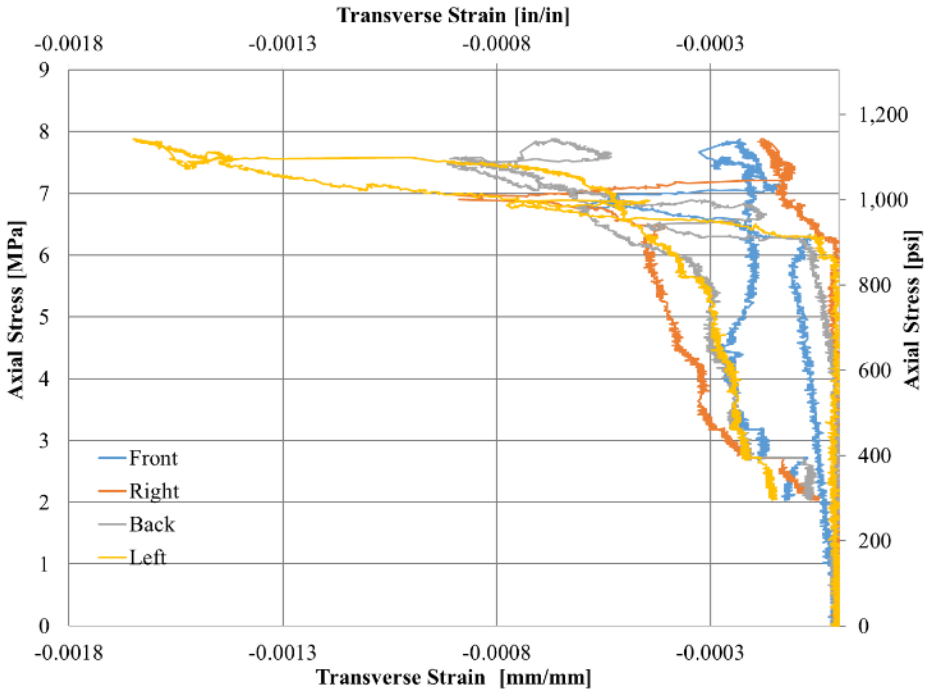

Figure B.36. Axial Stress - Transverse Strain Response of Specimen C-12-0-1-3

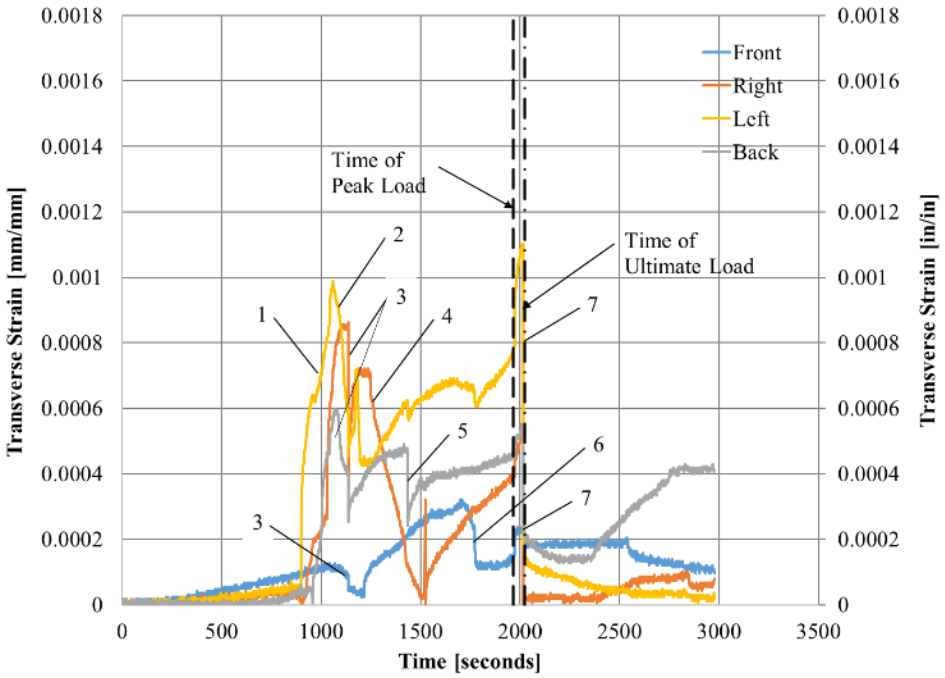

Figure B.37. Transverse Strain - Time Response of Specimen C-12-0-1-4

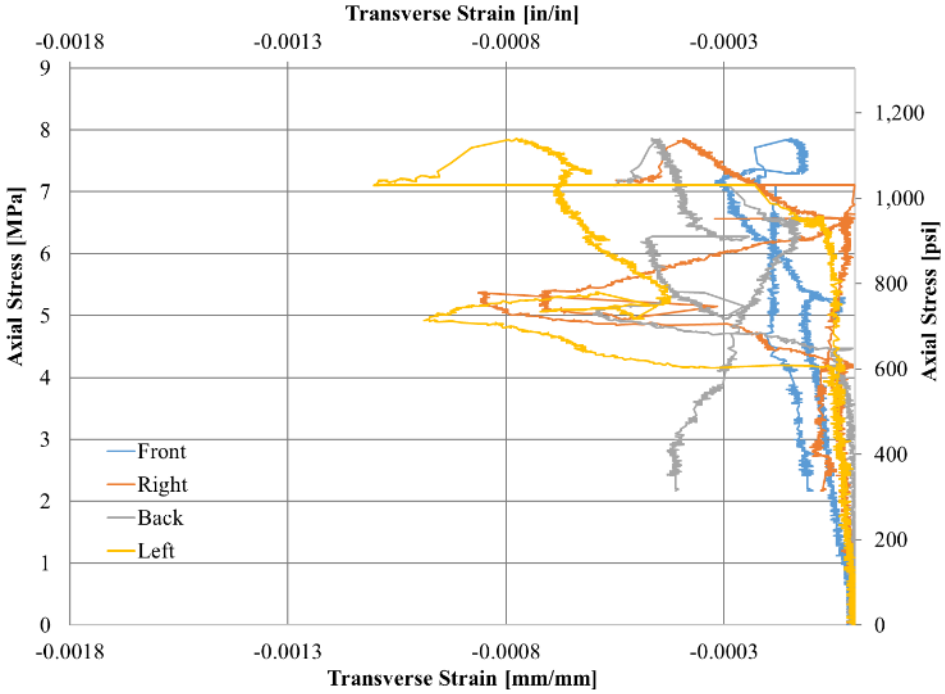

Figure B.38. Axial Stress - Transverse Strain Response of Specimen C-12-0-1-4

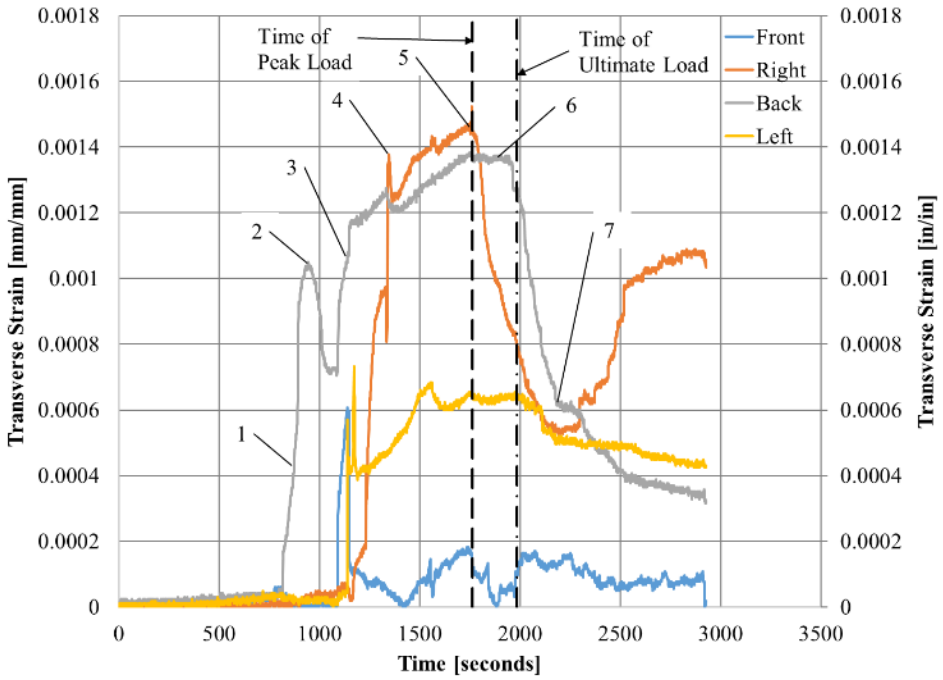

Figure B.39. Transverse Strain - Time Response of Specimen C-12-38-1-3

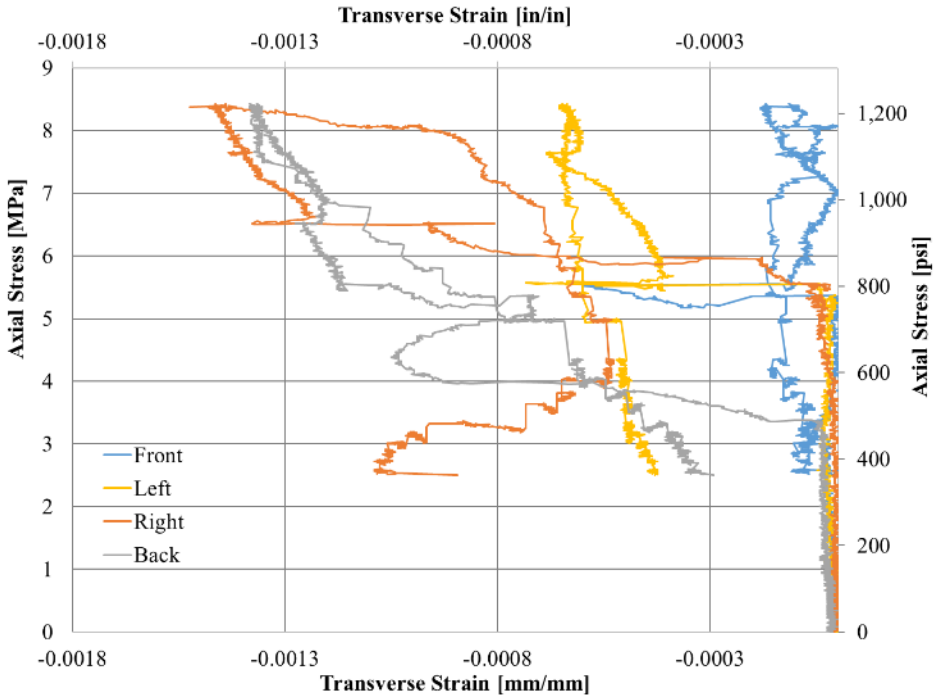

Figure B.40. Axial Stress - Transverse Strain Response of Specimen C-12-38-1-3

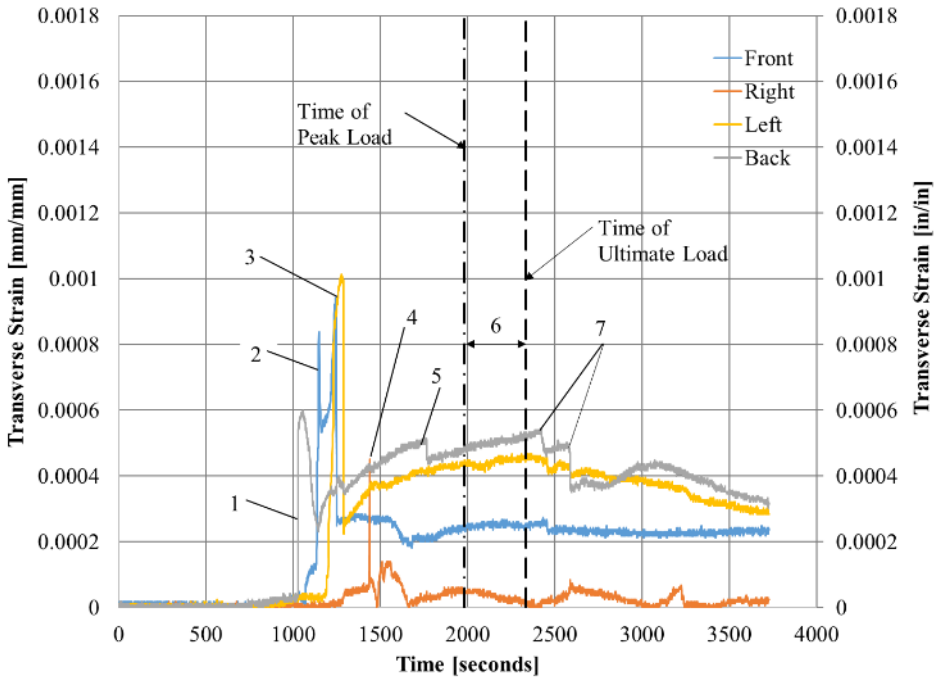

Figure B.41. Transverse Strain - Time Response of Specimen C-12-38-1-4

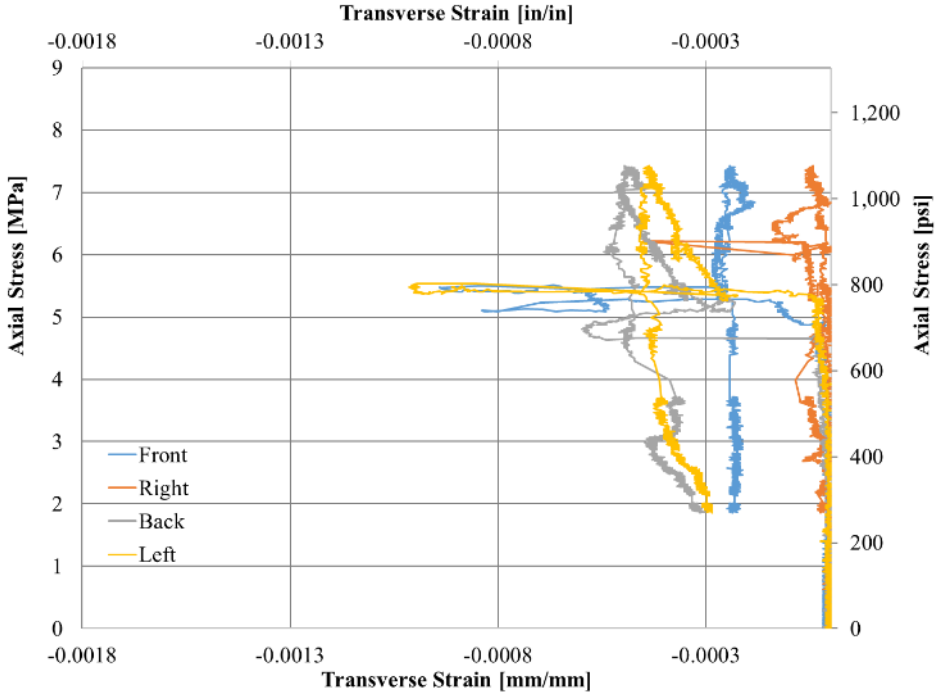

Figure B.42. Axial Stress - Transverse Strain Response of Specimen C-12-38-1-4

APPENDIX C.

SUMMARY OF RESULTS

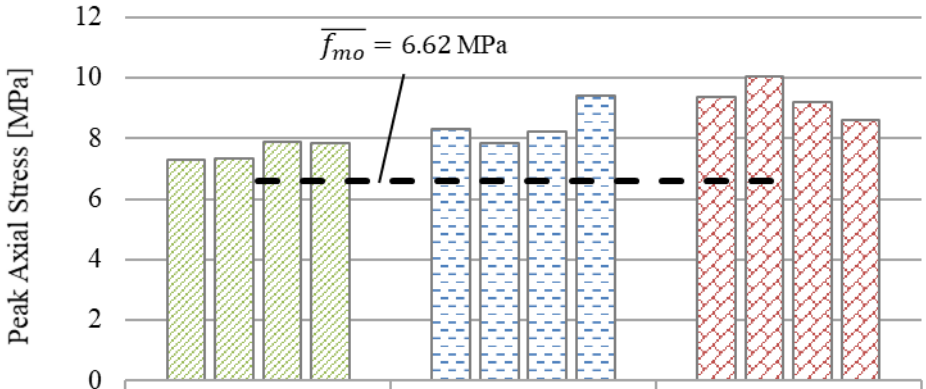

	C-12-0-1	C-12-0-2	C-12-0-3
$f_{mc,1}$ [MPa]	7.28	8.31	9.36
$f_{mc,2}$ [MPa]	7.34	7.83	10.05
$f_{mc,3}$ [MPa]	7.87	8.23	9.22
$f_{mc,4}$ [MPa]	7.86	9.42	8.63

Figure C.1. Peak Axial Stress of Sharp Cornered Specimens

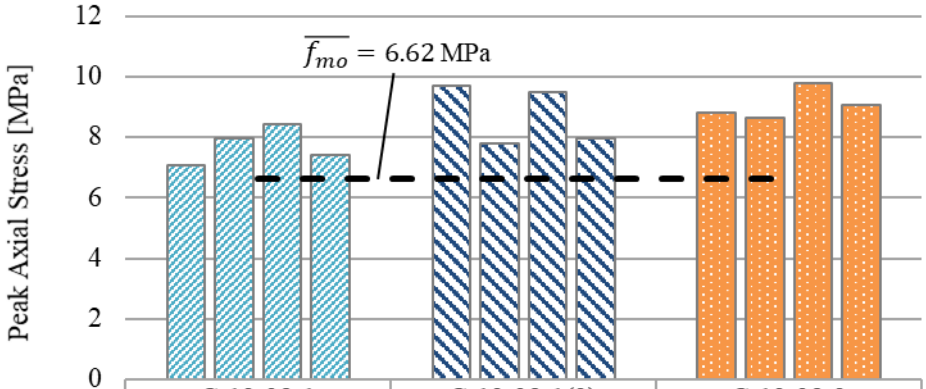

	C-12-38-1	C-12-38-1(2)	C-12-38-2
$f_{mc,1}$ [MPa]	7.09	9.70	8.83
$f_{mc,2}$ [MPa]	7.96	7.78	8.66
$f_{mc,3}$ [MPa]	8.43	9.50	9.77
$f_{mc,4}$ [MPa]	7.42	7.95	9.06

Figure C.2. Peak Axial Stress of Round Cornered Specimens

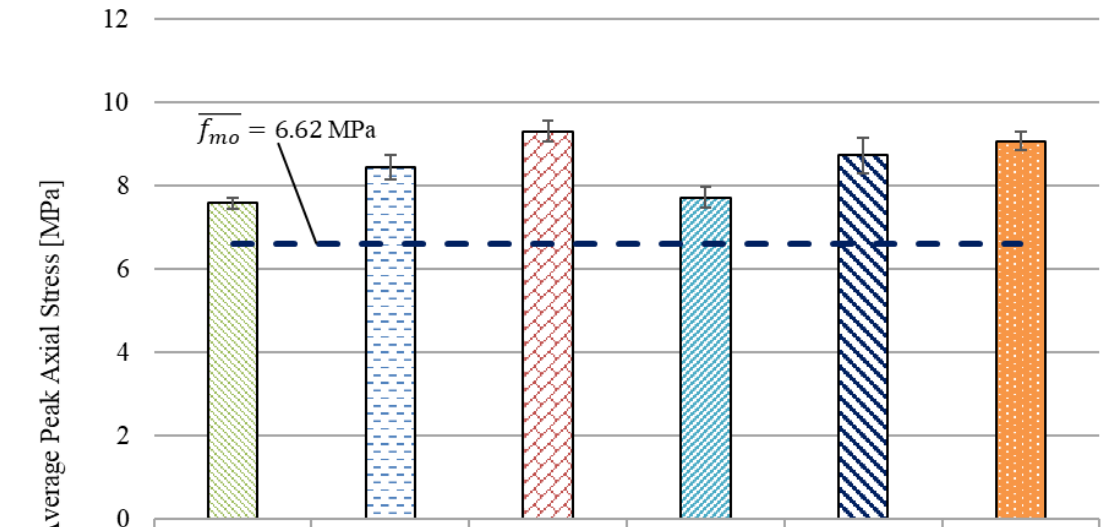

	C-12-0-1	C-12-0-2	C-12-0-3	C-12-38-1	C-12-38-1(2)	C-12-38-2
$\overline{f_{mc}}$ [MPa]	7.59	8.45	9.32	7.73	8.73	9.08
$\overline{f_{mc}}/\overline{f_{mo}}$	1.15	1.28	1.41	1.17	1.32	1.37

Figure C.3. Average Peak Axial Stress of Confined Specimens

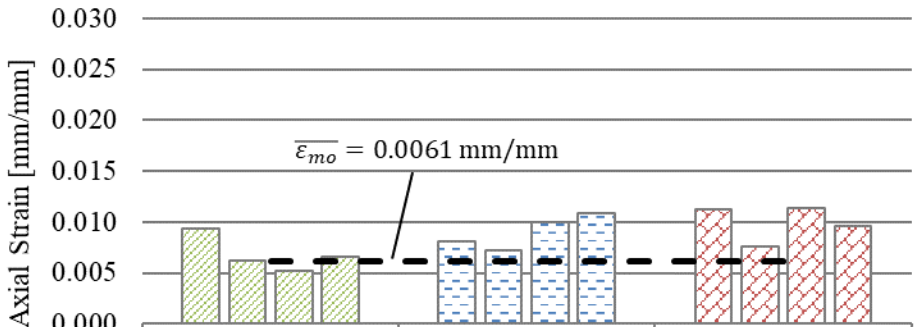

	C-12-0-1	C-12-0-2	C-12-0-3
$\varepsilon_{mc,1}$	0.0093	0.0081	0.0112
$\varepsilon_{mc,2}$	0.0062	0.0072	0.0076
$\varepsilon_{mc,3}$	0.0052	0.0099	0.0114
$\varepsilon_{mc,4}$	0.0066	0.0108	0.0095

Figure C.4. Peak Axial Strain of Sharp Cornered Specimens

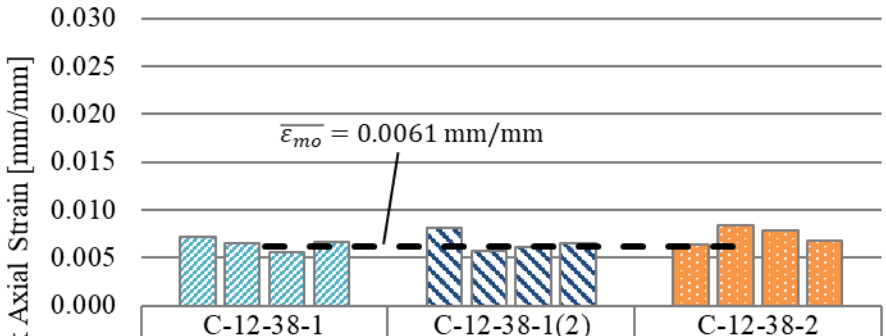

	C-12-38-1	C-12-38-1(2)	C-12-38-2
$\varepsilon_{mc,1}$	0.0071	0.0081	0.0064
$\varepsilon_{mc,2}$	0.0065	0.0057	0.0084
$\varepsilon_{mc,3}$	0.0056	0.0062	0.0078
$\varepsilon_{mc,4}$	0.0067	0.0066	0.0068

Figure C.5. Peak Axial Strain of Round Cornered Specimens

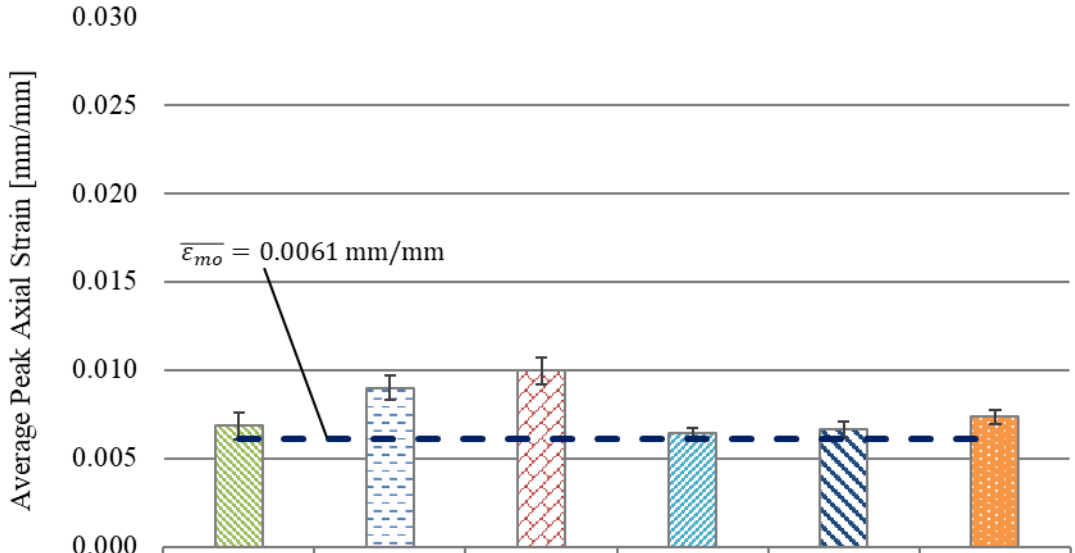

	C-12-0-1	C-12-0-2	C-12-0-3	C-12-38-1	C-12-38-1(2)	C-12-38-2
$\overline{\varepsilon_{mc}}$	0.0068	0.0090	0.0099	0.0065	0.0066	0.0073
$\overline{\varepsilon_{mc}}/\varepsilon_{mo}$	1.12	1.47	1.62	1.05	1.08	1.20

Figure C.6. Average Peak Axial Strain of Confined Specimens

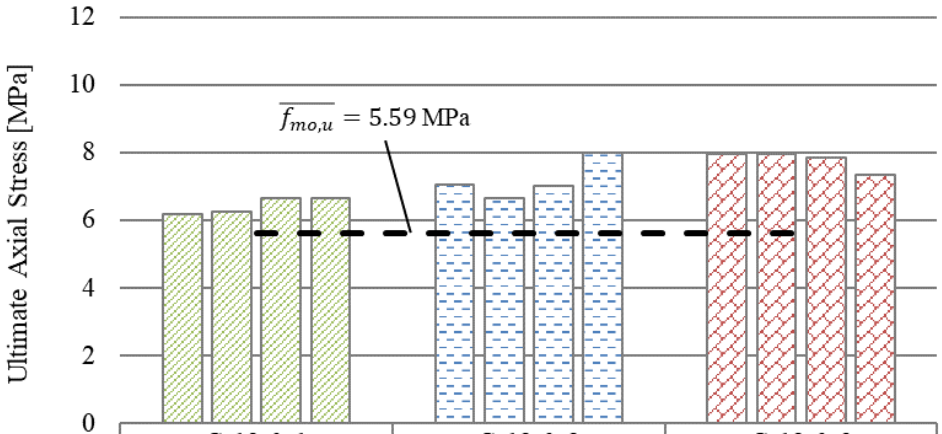

	C-12-0-1	C-12-0-2	C-12-0-3
$f_{mc,u,1}$ [MPa]	6.19	7.05	7.95
$f_{mc,u,2}$ [MPa]	6.23	6.63	7.95
$f_{mc,u,3}$ [MPa]	6.66	7.00	7.84
$f_{mc,u,4}$ [MPa]	6.65	8.00	7.35

Figure C.7. Ultimate Axial Stress of Sharp Cornered Specimens

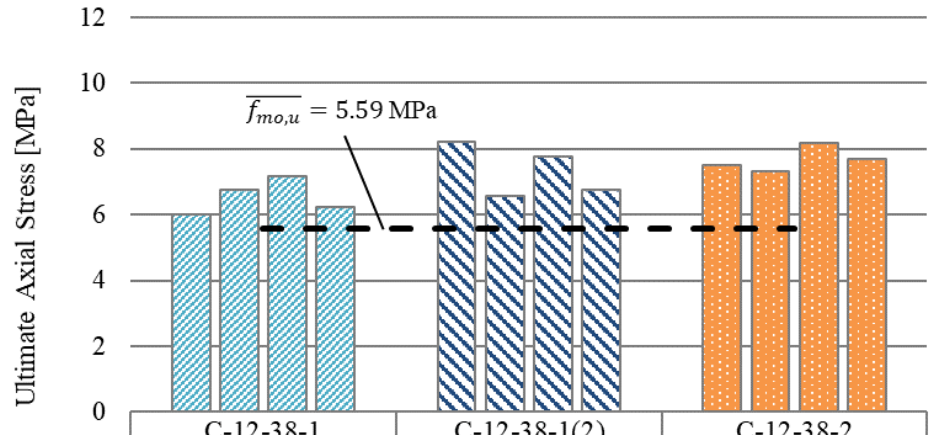

	C-12-38-1	C-12-38-1(2)	C-12-38-2
$f_{mc,u,1}$ [MPa]	6.02	8.20	7.49
$f_{mc,u,2}$ [MPa]	6.76	6.58	7.32
$f_{mc,u,3}$ [MPa]	7.17	7.76	8.18
$f_{mc,u,4}$ [MPa]	6.22	6.76	7.70

Figure C.8. Ultimate Axial Stress of Round Cornered Specimens

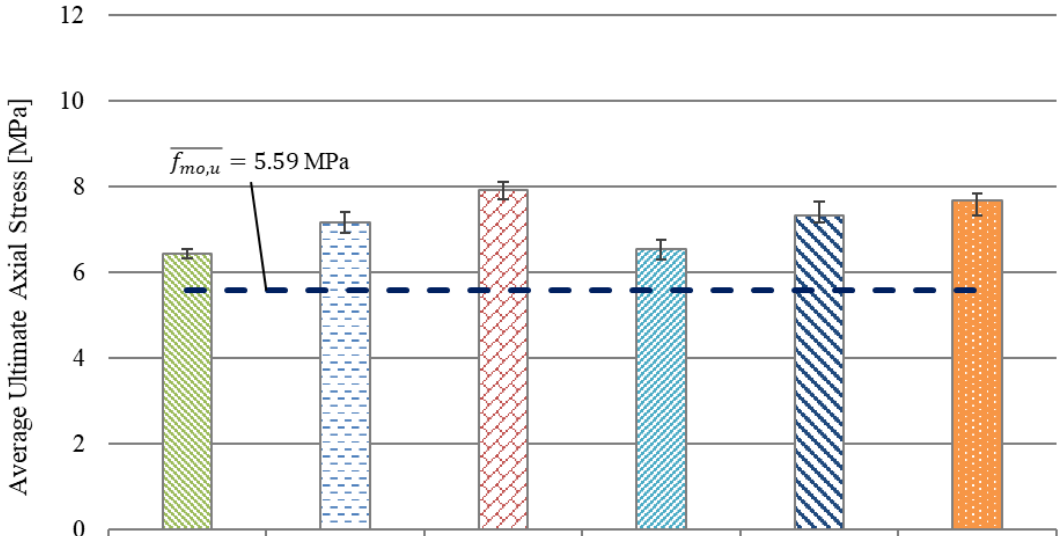

	C-12-0-1	C-12-0-2	C-12-0-3	C-12-38-1	C-12-38-1(2)	C-12-38-2
$\overline{f_{mc,u}}$ [MPa]	6.43	7.17	7.92	6.54	7.32	7.67
$\overline{f_{mc,u}}/\overline{f_{mo,u}}$	1.15	1.28	1.42	1.17	1.31	1.37

Figure C.9. Average Ultimate Axial Stress of Confined Specimens

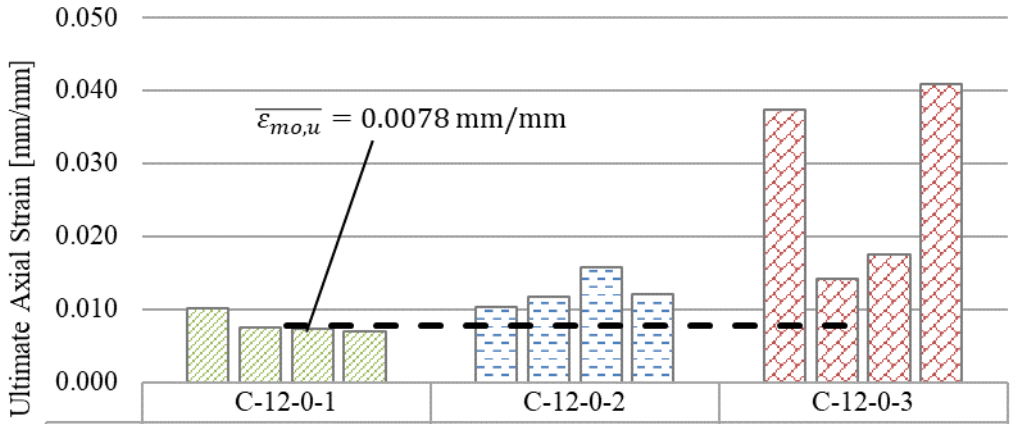

	C-12-0-1	C-12-0-2	C-12-0-3
$\varepsilon_{mc,u,1}$	0.0102	0.0103	0.0374
$\varepsilon_{mc,u,2}$	0.0075	0.0117	0.0142
$\varepsilon_{mc,u,3}$	0.0073	0.0158	0.0176
$\varepsilon_{mc,u,4}$	0.0070	0.0121	0.0409

Figure C.10. Ultimate Axial Strain of Sharp Cornered Specimens

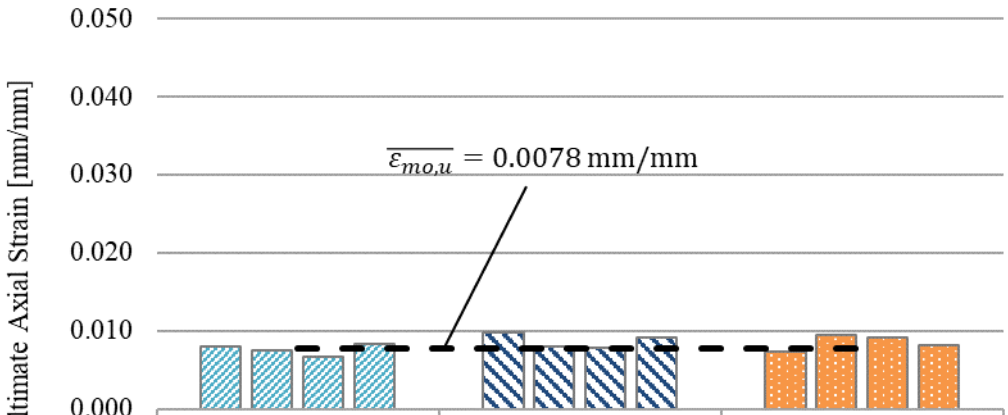

	C-12-38-1	C-12-38-1(2)	C-12-38-2
$\varepsilon_{mc,u,1}$	0.0081	0.0099	0.0074
$\varepsilon_{mc,u,2}$	0.0075	0.0081	0.0096
$\varepsilon_{mc,u,3}$	0.0067	0.0078	0.0092
$\varepsilon_{mc,u,4}$	0.0084	0.0092	0.0082

Figure C.11. Ultimate Axial Strain of Round Cornered Specimens

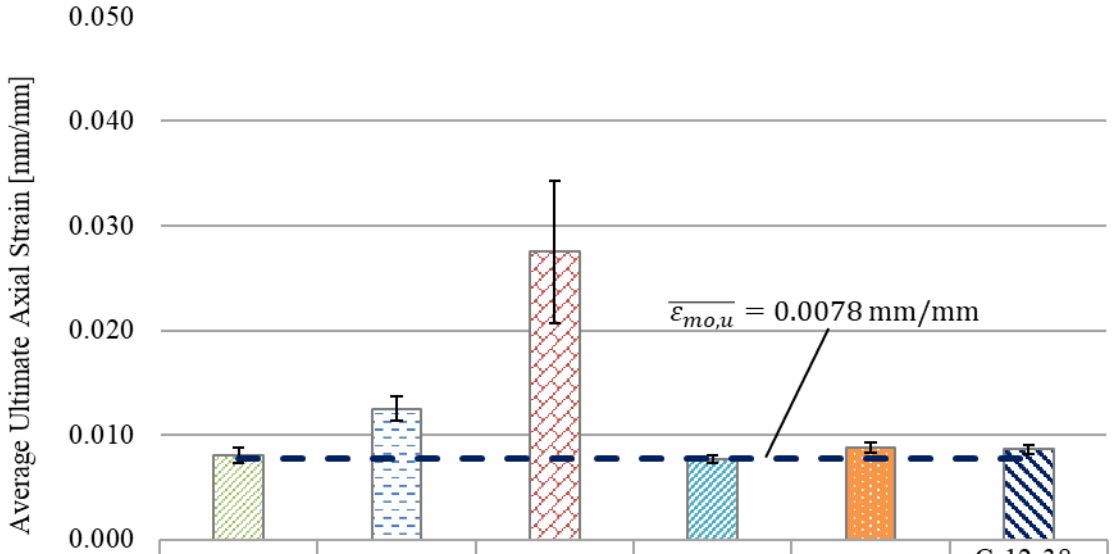

	C-12-0-1	C-12-0-2	C-12-0-3	C-12-38-1	C-12-38-2	C-12-38-1(2)
$\overline{\varepsilon_{mc,u}}$	0.0080	0.0125	0.0275	0.0077	0.0087	0.0086
$\overline{\varepsilon_{mc,u}}/\overline{\varepsilon_{mo,u}}$	1.03	1.60	3.53	0.98	1.12	1.10

Figure C.12. Average Ultimate Axial Strain of Confined Specimens

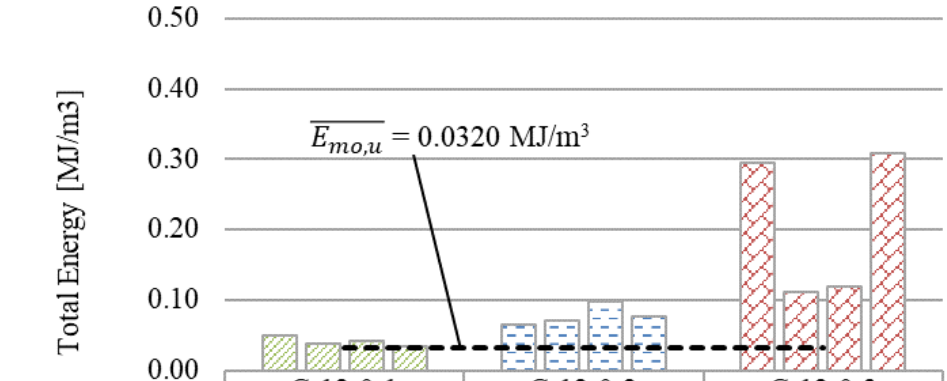

	C-12-0-1	C-12-0-2	C-12-0-3
$E_{mc,u,1}$ [MJ/m³]	0.0490	0.0641	0.2958
$E_{mc,u,2}$ [MJ/m³]	0.0373	0.0704	0.1113
$E_{mc,u,3}$ [MJ/m³]	0.0410	0.0977	0.1198
$E_{mc,u,4}$ [MJ/m³]	0.0337	0.0769	0.3076

Figure C.13. Total Energy of Sharp Cornered Specimens

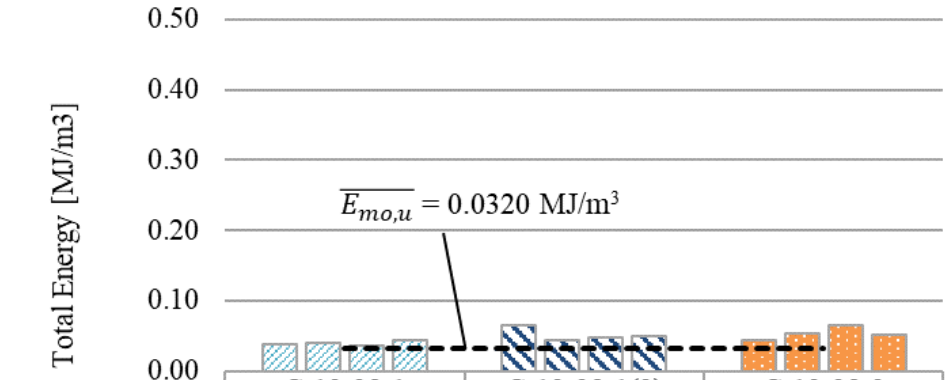

	C-12-38-1	C-12-38-1(2)	C-12-38-2
$E_{mc,u,1}$ [MJ/m³]	0.0376	0.0648	0.0449
$E_{mc,u,2}$ [MJ/m³]	0.0406	0.0438	0.0531
$E_{mc,u,3}$ [MJ/m³]	0.0364	0.0479	0.0644
$E_{mc,u,4}$ [MJ/m³]	0.0437	0.0489	0.0513

Figure C.14. Total Energy of Round Cornered Specimens

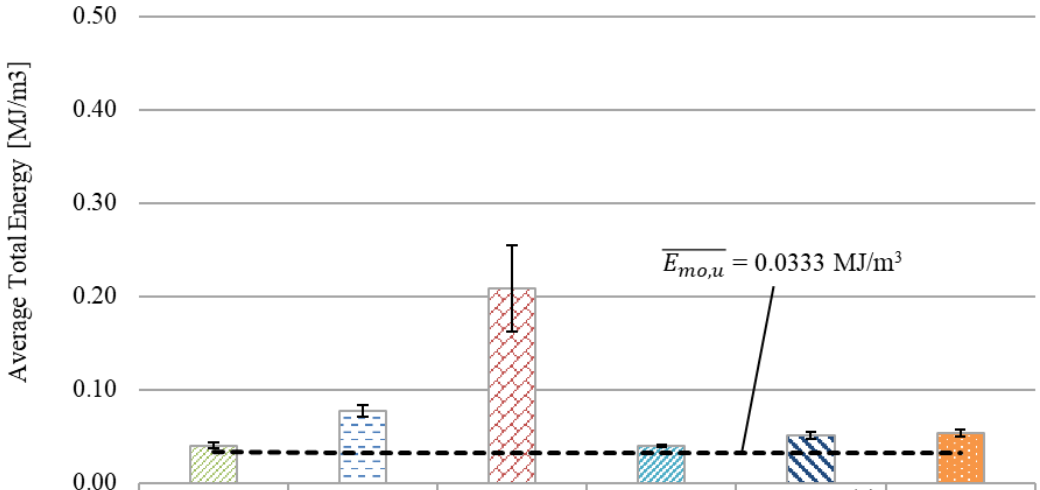

	C-12-0-1	C-12-0-2	C-12-0-3	C-12-38-1	C-12-38-1(2)	C-12-38-2
$\overline{E_{mc,u}}$ [MJ/m³]	0.0403	0.0773	0.2086	0.0396	0.0514	0.0534
$\overline{E_{mc,u}}/\overline{E_{mo,u}}$	1.21	2.32	6.27	1.19	1.54	1.61

Figure C.15. Average Total Energy of Confined Specimens

BIBLIOGRAPHY

Aiello, M. A., Micelli, F., & Valente, L. (2007). Structural Upgrading of Masonry Columns by Using Composite Reinforcements. *Journal of Compoistes for Construction, Vol. 11*, 650-658.

Aiello, M., Micelli, F., & Valente, L. (2009). FRP Confinement of Square Masonry Columns. *Composites for Construction, Vol. 13*, 148-158.

American Concrete Institute, A. (2008). ACI 440.2R. *Guide test methods for fiber-reinforced polymers for reinforcing or strengthening concrete structures*. Detroit, Michigan, United States of America.

American Society for Testing and Materials (ASTM). (2016). *C109 - 16a. Standard Test Method for Compressive Strength of Hydraulic Cement Mortars.* West Conshohocken, PA: ASTM International.

American Society for Testing and Materials (ASTM). (2016). *C192-16a Standard Practice for Making and Curing Concrete Test Specimens in the Laboratory.* West Conshohocken, PA: ASTM International.

Baietti, G. (2017). *Compressive Behavior of Masonry Columns Confined with Fiber Reinforced Cementitious Matrix (FRCM) Composites.* Master's Thesis, Bologna, Italy.

Borri, A., Castori, G., & Carradi, M. (2011). Masonry Columns Confined by Steel Fiber Composite Wraps. *Materials, Vol. 4*, 311-326.

Borri, A., Castori, G., & Corradi, M. (2013). Masonry Confinement Using Steel Cords. *Journal of Materials in Civil Engineering*, 1910-1919.

Bournas, D., Lontou, P., Papanicolaou, C., & Triantafillou, T. (2007). Textile-Reinforced Mortar versus Fiber-Reinforced Polymer Confinment in Reinforced Concrete Columns. *ACI Structural Journal*, 740-748.

Bournas, D., Triantafillou, T., Zygouris, K., & Stavropoulos, F. (2009). Textile-Reinforced Mortar versus FRP Jacketing in Seismic Retrofitting of RC Columns with Continuous or Lap-Spliced Deformed Bars. *Conposites for Construction, Vol. 13*, 360-371.

Campione, & Miraglia. (2003). Strength and Strain Capacities of Concrete Compression Members Reinforced with FRP. *Cement & Concrete Composites, Vol. 25*, 31-41.

Campione, G., Cavaleri, L., & Papia, M. (2016). Stainless Steel Grids for Confinement of Clay Brick Masonry Columns. *Journal of Structural Engineering, ASCE, Vol. 142*, 1-8.

Carloni, C., Mazzotti, C., Savoia, M., & Subramaniam, K. (2013). Confinement of Masonry Columns with PBO-FRCM Composites. *Key Engineering Materials, Vol. 624*, 644-651.

Cascardi, A., Longo, F., Micelli, F., & Aiello, M. (2017). Compressive Strenght of Confined Column wiht Fiber Reinforced Mortar (FRM): New Design-Oriented-Models. *Construciton and Building Materials, Vol. 156*, 387-401.

Cevallos, O., Olivito, R., & Codispoti, R. (2015). Experimental Analysis of Repaired Masonry Elements with Flax-FRCM and PBO-FRCM Composites Subjected to Axial Bending Loads. *Fibers, Vol. 3*, 491-503.

Corradi, M., Grazini, A., & Borri, A. (2007). Confinement of brick masonry columns with CFRP materials. *Composites Science and Technology, 67*, 1772-1783.

Di Ludovico, M., D'Ambra, C., Prota, A., & Manfredi, G. (2010). FRP Confinement of Tuff and Clay Brick Columns: Experimental Study and Assessment of Analytical Models. *Journal of Composites for Construction, Vol. 14*, 583-596.

Di Ludovico, M., Prota, A., & Manfredi, G. (2010). Structural Upgrade Using Basalt Fibers for Concrete Confinement. *Composites for Construction, Vol. 14*, 541-552.

El-Hacha, R., & Mashrik, M. (2012). Effect of SFRP Confinement on Circular and Square Croncrete Columns. *Engineering Structures, Vol. 36*, 379-393.

Fossetti, M., & Minafo, G. (2017). Comparative Experimental Analysis on the Compressive Behaviour of Masonry Columns Strengthened by FRP, BFRCM, or Steel Wires. *Composites Part B, Vol. 112*, 112-124.

Fraioli, G. (2017). *Experiment study of the compressive behavior of masonry columns confined with SRG composites.* Bologna, Italy.

Guler, S., & Ashour, A. (2015). Review of current design guidelines for circular FRP-wrapped plain concrete cylinders. *Composites for Construction, Vol. 20*.

Italian Council of Research, C. (2004). CNR-DT 200. *Guide for the design and construciton of externally bonded FRP systems for strengthening existing structures*. Rome, Italy.

Italian Council of Research, C. (2013). CNR-DT 200 R1. *Guide for the design and construciton of externally bonded FRP systems for strengthening existing structures*. Rome, Italy.

Kaushik, H., Rai, D., & Jain, S. (2007). Stress-Strain Characteristics of Clay Brick Masonry Under Uniaxial Compression. *Journal of Material Civil Engineering, Vol. 19*, 9728-9739.

Kerakoll. (2017). *Biocalce Intonachino Fino.* Retrieved 05 2018, from Kerakoll Bio Products.

Kerakoll. (2017). *GeoCalce F Antisismico.* Retrieved from Kerakoll Geo Products: http://products.kerakoll.com/catalogo_dett.asp?idp=10181

Kerakoll. (2017). *GeoSteel G1200.* Retrieved from Kerakoll: http://products.kerakoll.com/catalogo_dett.asp?idp=10178

Krevaikas, T. D., & Triantafillou, T. C. (2005). Masonry Confinement with Fiber-Reinforced Polymers. *Journal of Composites for Construction, Vol. 9*, 128-135.

Mander, J., MJN, P., & Park, R. (1988). Theoretical Stress-Strain Model for Confined Concrete. *ASCE Journal of Structual Engineering, Vol. 114*, 1804-1826.

Napoli, A., Realfonzo, & Roberto. (2016). *Compressive Behavior of Concrete Confined by SRP Wraps.* Retrieved from Construction and Building Materials: http://dx.doi.org/10.1016/j.conbuildmat.2016.01.005

Ombres, L. (2015). Confinement Effectiveness in Eccentrically Loaded Masonry Columns Strengthened by Fiber Reinforced Cementitious Matrix (FRCM) Jackets. *Key Engineering Materials Vol. 624*, 551-558.

SanMarco, T. (n.d.). *Vivo - San Marco.* Retrieved 05 2018, from San Marco.

Santandrea, M., Quartarone, G., Carloni, C., & Gu, X. (2017). Confinement of Masonry Columns with Steel and Basalt FRCM Composites. *Key Engineering Materials, Vol. 747*, 342-349.

Senesi, C. (2018). *Confinement of masonry columns with SRG composites: an experimental investigation on the effect of the number of layers and corner condition.* Bologna, Italy.

Sneed, L. H., Carloni, C., Baietti, G., & Fraioli, G. (2017). Confinement of Clay Masonry Columns with SRG. *Key Engineering Materials, Vol. 747*, 350-357.

Sneed, L., Ravazdezh, F., Santandrea, M., Imohamed, I., & Carloni, C. (2017). A Study of the Compressive Behavior of Concrete Columns Confined with SRP Jackets using Digital Image Analysis. *Composite Structures, Vol. 179*, 195-207.

Triantafillou, T., Pappanicolaou, C., Zissimopoulos, P., & Laourdekis, T. (2006). Concrete Confiemnt with Textile-Reinforced Mortar Jackets. *ACI Structural Journal*, 28-37.

Vishap Precision Group. (2014). *Solders, Fluxes, Kits, and Soldering Unit.* Retrieved from VPG Micro-Measurements: http://www.vishaypg.com/micro-measurements/list/product-11023/

Wang, D., Z.Y, W., Smith, S., & Yu, T. (2016). Size Effect on Axial Stress-Strain Behavior of CFRP-Confined Square Concrete Columns. *Construction and Building Materials*, 116-126.

Wight, J. K. (2016). *Reinforced Concrete Mechanics and Design, 7th Ed.* Hoboken, NJ: Pearson Education, Inc.

VITA

Sarah Elizabeth Jemison was born to parents Thomas and Sandra Jemison of Nixa, Missouri. She received her Bachelor of Science in Civil Engineering and Bachelor of Science in Architectural Engineering with structural emphasis from Missouri University of Science and Technology in Rolla, Missouri in May 2018. She graduated summa cum laude with a GPA of 3.95. She started her Master of Science in Civil Engineering at Missouri University of Science and Technology in August of 2017 by dual enrolling into graduate courses. She received her Master of Science in Civil Engineering from Missouri University of Science and Technology in December 2018.